DEVELOPMENT OF A LATTICE BOLTZMANN MODEL TO INVESTIGATE THE INTERACTION MECHANISM OF SURFACE ACOUSTIC WAVE ON A SESSILE DROPLET

Stephen Burrell Burnside

Submitted for the degree of Doctor of Philosophy

Heriot-Watt University

Institute of Mechanical, Process and Energy Engineering

School of Engineering and Physical Sciences

March 2022

ABSTRACT

This study focuses on the development of a three dimensional numerical model, based on the lattice Boltzmann method (LBM), for two-phase fluid flow dynamics employing a multiple-relaxation-time (MRT) pseudopotential scheme. The numerical model is applied in the investigation of acoustic interactions with microscale sessile droplets (1-10 μl), under surface acoustic wave (SAW) excitation, through the introduction of additonal forcing terms in the LBM scheme. In the study, a range of resonant frequencies (61.7 - 250.1 MHz) are studied and quantatively compared to existing studies and experimental findings to verify the proposed model. The modelling predictions on the roles of forces (SAW, interfacial tension, inertia and viscosity) on the dynamics of mixing, pumping and jetting of a droplet are in good agreement with observations and experimental data.

Further examination of the model, through parameter study, identified that the relaxation parameters considered free to tune in the MRT, play an important role in model stability, providing large reductions in spurious velocities, in both the liquid and gas phases, when the values are specified correctly. It has also been discovered that employing a dynamic contact angle hysteresis model increased the adhesion between the liquid droplet and the substrate, improving the agreement with experimental findings by up to 20%. Lastly, an investigation of various equation of state implementations revealed some fascinating differences in droplet dynamics and behaviours, owing primarily to the physical underpinning of which each is based upon.

The developed model is successfully applied in the examination of various scenarios including SAW-droplet interactions on an inclined slope, droplet impact on flat (horizontal) and inclined surfaces with and without SAW interactions, and dual SAW interactions on a droplet at several configurations. The findings indicate the importance of applied SAW power, especially in inclined slope scenarios, to overcome the inertia and gravitational forces which act to counteract the droplet motion initiated by the acoustic wave direction of travel.

Furthermore, a new multi-component multi-phase multi-pseudopotential (MCMP MPI) LB model is proposed. The study details initial model development and verification for classical benchmark cases, comparing to both the single-component (SCMP MPI) and publicised data. Similar to its SCMP MPI counterpart, the model displays excellent

stability, even at high density ratios, and thermodynamic consistency. Comparison to the SCMP MPI model reveals lower spurious velocities are generated in the proposed MCMP model, approximately one order of magnitude lower. Close inspection of the interaction force implementation shows they are analogous whilst similar surface tension values are presented for both models. The proposed scheme signifies a new class of MPI model capable of simulating realistic fluid compositions for use in applications of scientific and engineering interest.

DEDICATION

Dedicated to my beautiful partner Amy for always believing in me and showing me love. And to my wonderful parents, Gwen and James, for their unconditional love and support throughout my life.

ACKNOWLEDGEMENT

I would like to thank my supervisor Dr Baixin Chen for his guidance and support throughout my PhD studies. His encouragement over the past four years has been invaluable during my research work.

I express my gratitude to the members of our research group; Dr Marius Dewar, Dr Sorush Khajepor, Dr Mubbashar Mehmood, Dr Kamil Pasieczynski, Dr Umer Saleem, Amin Zarareh and Nidal Saab, for their valued discussions and suggestions during our meetings.

A special thanks goes to my close friends and family for their patience, encouragement, understanding and support. I will be forever grateful.

DECLARATION STATEMENT

Research Thesis Submission

Name*:*	Stephen Burrell Burnside		
School:	School of Engineering and Physical Sciences		
Version: *(i.e. First, Resubmission, Final)*	Final	Degree Sought:	PhD Mechanical Engineering

Declaration

In accordance with the appropriate regulations, I hereby submit my thesis and I declare that:

1. The thesis embodies the results of my own work and has been composed by myself
2. Where appropriate, I have made acknowledgement of the work of others
3. The thesis is the correct version for submission and is the same version as any electronic versions submitted*.
4. My thesis for the award referred to, deposited in the Heriot-Watt University Library, should be made available for loan or photocopying and be available via the Institutional Repository, subject to such conditions as the Librarian may require
5. I understand that as a student of the University I am required to abide by the Regulations of the University and to conform to its discipline.
6. I confirm that the thesis has been verified against plagiarism via an approved plagiarism detection application e.g. Turnitin.

* *Please note that it is the responsibility of the candidate to ensure that the correct version of the thesis is submitted.*

Signature of Candidate*:*	S Burnside	Date:	08/03/22

Submission

Submitted By *(name in capitals):*	STEPHEN BURRELL BURNSIDE
Signature of Individual Submitting:	S Burnside
Date Submitted:	08/03/22

For Completion in the Student Service Centre (SSC)

Limited Access	Requested	Yes		No		Approved	Yes		No	
E-thesis Submitted *(mandatory for final theses)*										
Received in the SSC by *(name in capitals):*						Date:				

TABLE OF CONTENTS

LIST OF TABLES

LIST OF FIGURES

NOMENCLATURE

θ_R	Rayleigh angle
V_f	Longitudinal sound wave velocity in liquid
V_R	Rayleigh sound wave velocity in solid substrate
ρ	Density
p	Pressure
u	Velocity
$\boldsymbol{F}$	Forces including intermolecular, adhesive, gravity, and surface acoustic wave
τ	Relaxation-time / Viscous stress
A	Wave amplitude
ω	Angular frequency
k_i	Wave number (imaginary part)
α	Attenuation constant / Slope inclination
λ	Wavelength
f_i	Particle distribution function
c_i	Lattice velocities
w_i	Lattice weights
c_s	Lattice speed of sound
υ	Kinematic viscosity
μ	Dynamic viscosity
ψ	Pseudopotential
G	Strength of interaction
T_R	Reduced temperature
θ	Static contact angle
θ_A	Advancing contact angle
θ_R	Receding contact angle
g	Gravitational acceleration

$\boldsymbol{M}$	Transformation matrix
$\boldsymbol{S}$	Relaxation matrix
σ	Mechanical stability tuning parameter
γ	Interfacial tension
κ	Interfacial tension adjustment parameter
C_l	Length scale conversion
C_t	Time scale conversion
C_u	Velocity scale conversion

Non-dimensional Numbers

Eo	Eotvos number
Re	Reynolds number
We	Weber number
Ca	Capillary number

LIST OF ABBREVIATIONS

LBM	Lattice Boltzmann Method
SAW	Surface Acoustic Wave
IDT	Interdigital Transducer
CFD	Computational Fluid Dynamics
BGK	Bhatnagar-Gross-Krook
SRT	Single-Relaxation-Time
MRT	Multiple-Relaxation-Time
TRT	Two-Relaxation-Time
SCMP	Single Component Multiphase
MCMP	Multiple Component Multiphase
EOS	Equation of State
YS	Yuan-Schaefer
MPI	Multiple Pseudopotential Interactions
EDM	Exact Difference Model
CS	Carnahan-Starling
PR	Peng-Robinson
CAH	Contact Angle Hysteresis
FID	Free Impact Droplet
SID	SAW Interaction Droplet
SD	Standard Deviation

LIST OF PUBLICATIONS

1. **Burnside, S. B**., Pasieczynski, K., Zarareh, A., Mehmood, M., Fu, Y. Q and Chen, B., Simulations of surface acoustic wave interactions on a sessile droplet using a three-dimensional multiphase lattice Boltzmann model. Phys. Rev. E, 2021. 104, 045301. DOI: 10.1103/PhysRevE.104.045301

2. Zarareh, A., Khajepor, S., **Burnside, S. B** and Chen, B., Improving the staircase approximation for wettability implementation of phase-field model: Part 1 - Static contact angle. Computers & Mathematics with Applications, 2021. 98, 218-238. DOI: 10.1016/j.camwa.2021.07.013.

3. Mehmood, M., Chaudhary, T. N., **Burnside, S. B**., Khan, U, F., Fu, Y. Q and Chen, B., Coupling mechanism of kinetic and thermal impacts of Rayleigh surface acoustic waves on the microdroplet. Experimental Thermal and Fluid Science, 2022. 133, 110580. DOI: 10.1016 /j.expthermflusci.2021.110580.

4. Zarareh, A., **Burnside, S. B**., Khajepor, S. and Chen, B., Improving the staircase approximation for wettability implementation of phase-field model: Part 2 - Three-component permeation. Computers & Mathematics with Applications, 2022. 109, 100-124. DOI: 10.1016/j.camwa.2022.01.005.

Chapter 1 – Introduction

1.1 Perspective

In recent years, due to technological advances, there has been a move towards incorporating complete laboratory analysis procedures on to the surface of a microfluidic device, known as Lab-on-a-Chip (LOC) [1]. The objective being that analysis processes such as DNA detection or sequencing [2], which conventionally occurs in a laboratory setting consisting of multiple pieces of equipment, can be simplified in scale and lead-time, allowing for evaluation to be conducted in the field. The shorter processing time would also provide more instantaneous outcomes to potential patients hence diagnosis could be quicker. In the literature, a microfluidic "platform" is described as providing a set of fluidic operations which are designed to be easily incorporated into defined fabrication practices to set a basis for miniaturisation, integration and automation of bio-chemical processes [3].

The performance and control of chemical and biological processes in a microscale system can throw up some challenges, for example, mixing processes are generally required to be fast and effective, however mixing by diffusion, at this scale, is inherently slow and requires relatively long channels to achieve sufficient mixing due to low Reynolds number [4,5]. Additionally, the reduced volume of fluid being examined can be technically difficult since, at the microscale, pumping becomes more difficult due to a significant increase in viscous and capillary forces [6].

Recently, surface acoustic waves (SAW) have been shown to demonstrate features that could have positive implications for the development of microfluidic devices [7]. Pumping, mixing, jetting and nebulisation of microdroplets can all be induced through manipulation of the applied power of the SAW [8]. As the acoustic wave propagates in the path of a liquid droplet, the energy is transferred into the liquid medium causing the aforementioned phenomena to occur. This interaction coupling mechanism between the SAW and the fluid is not yet fully understood, hence further investigation is required [9–11].

1.2 Research Objectives

The focus of this thesis is to provide understanding of the underlying mechanisms which dictate droplet behaviours in the presence of SAW interaction. A three-dimensional

numerical model has been constructed to study the hydrodynamic effects of SAW-droplet coupling, with the aim of providing insight and guidance to the microfluidics community. A comprehensive analysis of SAW parameters and configurations has been investigated for droplets on horizontal and inclined substrates, and droplet impact on horizontal substrates.

It is also the objective of this thesis to examine the choice of numerical schemes and provide insight into its influence on model stability, applicability, and performance for SAW-droplet interactions.

1.3 Thesis structure

The thesis has been arranged into chapters described below:

Chapter 1 – Introduction: Provides a brief introduction to the research topic and an overview of the objectives.

Chapter 2 – Literature Review: Reviews the current research centred around SAW-based microfluidics themes, highlighting background theories and fundamentals. Experimental and numerical studies are introduced, with any research or knowledge gaps being emphasised.

Chapter 3 – Pseudopotential LB Multiphase Models: Introduces the theory of the pseudopotential LB and provides analysis on the current models. Fluid-solid interactions are studied with some recommendations provided to the community.

Chapter 4 – Development of lattice Boltzmann model for surface acoustic wave interactions in sessile droplets: Reports the construction and development of a numerical model for examining the interactions between SAW and microscale sessile droplets. SAW and LB parameters are investigated and their outcome on droplet behaviours and dynamics is described.

Chapter 5 – Influence of configuration parameters on SAW-droplet interactions: Further examination of the effect model configuration parameters have on droplet dynamics during SAW-droplet coupling.

Chapter 6 – Investigation of the dynamics of surface acoustic wave interactions in sessile droplets: Studies on droplet behaviours during SAW interactions for different

applications; droplet on inclined slope, droplet impact on flat slope with/without SAW, and dual SAW interactions from opposing sides of the droplet.

Chapter 7 – Multi-component Multi-phase Multi-Pseudopotential lattice Boltzmann model: Introduces a newly proposed numerical model for multi-component fluids with multiple phases using the multi-pseudopotential LB framework.

Chapter 8 – Conclusions and Future Work: Provides a summary of the research work completed as part of the thesis and indicates potential avenues for future work.

Chapter 2 – Literature Review

2.1 Introduction

Fluids are essentially substances which cannot withstand shear forces when at rest, and when subject to external stresses, undergo continuous deformation. Liquids (water) and gases (air) are typical examples. Fluids are constructed from a large number of atoms or molecules which can move around and interact with one another. At the microscopic scale ($<10^{-3}$ m), the dynamics of the fluid molecules can be extremely complex due to fluctuations and strong inhomogeneity. Conversely, at the macroscopic scale ($\sim10^{1}$ m) the opposite is demonstrated. The dynamics are achieved through averaging the motion of the molecules, culminating in a continuous, homogeneous system.

The manipulation of droplets at small scale has been a field of study which has had widespread popularity in scientific and engineering contexts [12–15]. Advances in technology and computational resources have unlocked new possibilities which could have positive repercussions in fields such as chemical and biological analysis. Major advancements in the field of microfluidics (the manipulation of fluids at length scales less than a millimetre [16,17]) gave rise to the production of miniaturised devices, enabling areas such as DNA analysis to become integrated into the device [18]. A popular area of research within the community is concentrated around micro-Total Analysis Systems (μ-TAS) where the objective is to integrate whole laboratory processes on to a single chip. This has also been termed LOC [3,19]. The precise manipulation of small volumes of liquids requires the network of channels within the device to be on the scale of typically 10 to 100 μm. The channels are normally fabricated on the surface of substrates, ranging from glass, silicon and piezoelectric crystal. Although it may seem as though a LOC device is merely a network of microchannels, it does however serve other functions depending on the intended application. It should then be seen as a multifaceted microsystem involving mechanical, electronic and fluid functions [20].

It is the objective of this thesis to explore, understand and develop new modelling techniques for SAW interactions on microscale sessile droplets, ranging in diameter 1 to 10 mm. Consequently, it is only appropriate that the basic concepts are presented in order to provide the necessary understanding of acoustic wave propagation and excitation in the presence of liquid droplets.

2.2 Surface Acoustic Wave Generation and Propagation in Solid, Liquid and Solid-Liquid Interfaces

Surface acoustic waves can be categorised depending on their mode. Conditional on the type of substrate and resonant frequency, SAWs can be defined as Rayleigh, Sezawa, Shear-horizontal and Love wave [21]. The most widely known form is the Rayleigh SAW. It was first postulated by Lord Rayleigh in 1885 where he described the behaviour of waves entering an isotropic elastic solid [22]. It was discovered that the wave energy was confined to a region close to the free surface, decaying with depth inside the substrate until it becomes negligible in a few wavelengths of the surface [23]. Generally, this type of surface acoustic wave is generated using an interdigital transducer (IDT) where the electrical field generated is coupled to a piezoelectric substrate. This is commonly known as a SAW device consisting of an IDT and a piezoelectric substrate. The IDT fingers are arranged resembling a comb shape and are usually produced in pairs; one to act as a transmitter, connected to an excitation source, and the other as a receiver. The electrical signal applied to the transmitter is converted to mechanical energy, producing the SAW along the substrate. The mechanical energy is then converted back to electrical energy at the receiver.

There are various IDT shapes and designs depending on the intended application. Straight IDT's are conventionally used in SAW devices where the fingers are organised in parallel, presented in Figure 2-1 (a), however focused devices use curved IDT's to concentrate the SAW energy to a single point in the device, illustrated in Figure 2-1 (b). Other forms include tapered and flexible devices [24].

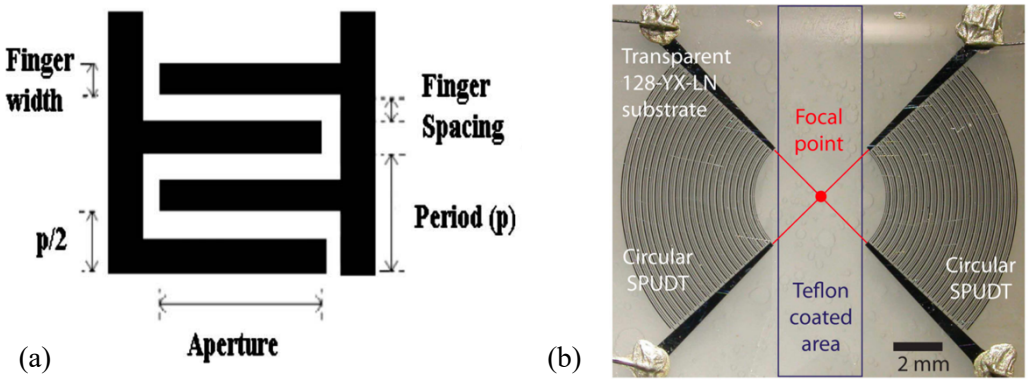

Figure 2-1. Illustration of different IDT shapes; (a) straight IDT for coventional SAW device [25] (b) curved IDT for focused SAW device [26]

Similarly, there are a multitude of substrate materials commonly used in the manufacture of SAW devices. The most commonly used include lithium niobate ($LiNbO_3$) and quartz. Additionally, devices incorporating thin-film piezoelectric materials such as zinc oxide (ZnO) and aluminium nitride (AlN) can be utilised to modify the sound wave velocities and hence alter the Rayleigh angle [27].

2.2.1 Rayleigh wave characteristics

A Rayleigh wave consists of two translational components; one is longitudinal which causes horizontal displacement, and the other is transverse producing vertical translation of the SAW. Propagation in the lateral direction is assumed uniform. It is found that for a typical isotropic material (i.e., piezoelectric) the motion of the material particles is elliptical in shape. The rotation direction of the surface particles is anticlockwise which is in contrast to the propagation direction. Interestingly, the rotation direction is reversed at a depth of approximately one fifth from the surface [28].

As indicated in Figure 2-2, the motion of the surface particles is elliptical in a Rayleigh wave. When a liquid medium is loaded on to the free surface of the piezoelectric substrate the vertical component of the acoustic wave couples with the liquid layer adjacent to the surface.

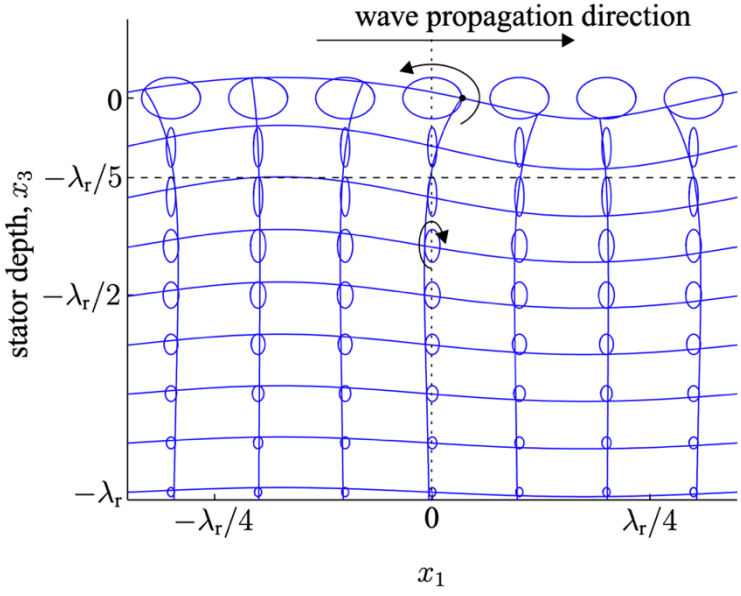

Figure 2-2. Rayleigh wave characteristics in a piezoelectric material. Displacement field distribution as a function of depth [28]

This coupling leads to the emission of longitudinal waves into the liquid, known as the Leaky Rayleigh wave or Leaky SAW (LSAW), as shown in Figure 2-3. Due to a difference in velocity of the longitudinal sound wave V_f and the Rayleigh wave in the solid substrate V_R, the resultant wave is radiated in the fluid at an angle, known as the Rayleigh angle θ_R [9]

$$\theta_R = \sin^{-1}\frac{V_f}{V_R} \qquad 2\text{–}1$$

For a 128º YX-$LiNbO_3$ substrate, the SAW velocity is about 3994 ms^{-1} and the velocity of the water is approximately 1500 ms^{-1} resulting in a Rayleigh angle is roughly 23º [29].

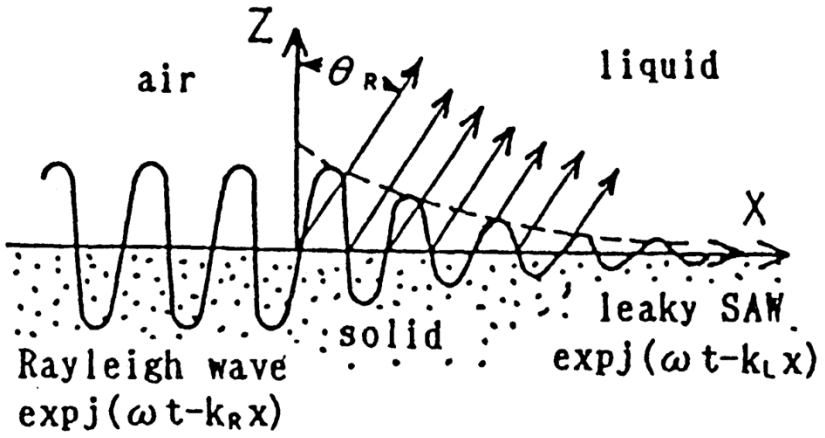

Figure 2-3. Sketch of acoustic wave attenuation from solid substrate into liquid at Rayleigh angle θ_R [30]

2.3 Experimental Principles and Observations of SAW in Microfluidics

Over the past few years there have been many studies employing SAW devices for various scientific applications. In the subsequent sections, a review of the current experimental progress and insights in SAW driven microfluidics is presented, with special interest in SAW-based microfluidics applications focused on deformation and translation of sessile droplets.

2.3.1 SAW Streaming, Pumping, Jetting and Atomisation

The term streaming is defined as the internal circulation generated inside the liquid medium due to the leakage of acoustic energy from the SAW, as depicted in Figure 2-4.

The acoustic reflections within the droplet translate into a hydrodynamic circulatory motion which is driven by the leaky SAW.

SAW-driven acoustic mixing in sessile droplets can be difficult due to the small volumes of liquid involved [31]. At the microscale, capillary and viscous forces become more dominant over gravitational and inertial forces, leading to less efficient mixing as the diffusion timescale is increased significantly. The work of Shilton et al. [31] revealed evidence of chaotic advection in a SAW-driven system through tracking particles trajectories. It was observed that an increase in fluid viscosity leads to a less chaotic flow, with the particle trajectories exhibiting a bulk rotational flow pattern.

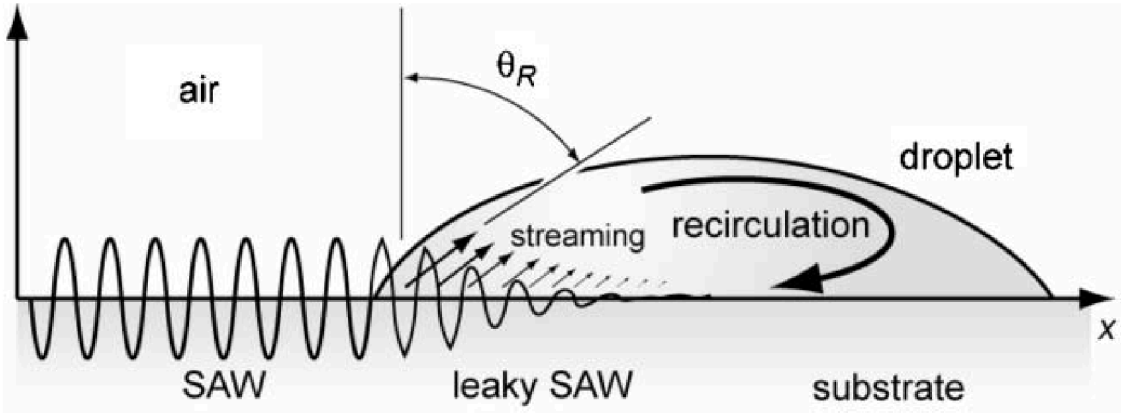

Figure 2-4. Illustration of acoustic streaming induced by SAW due to leakage of the acoustic energy into the liquid at the Rayleigh angle [32]

SAW streaming is also found to be dependent on several other factors, including; SAW power, frequency, liquid volume and surface condition [29]. Du et al. [21] demonstrated that the applied voltage has a direct impact on the magnitude of streaming velocity within the droplet, approximately linear for both wave modes, Rayleigh and Sezawa, for ZnO thin film devices. Shilton et al. [33] present a new approach for the miniaturisation of nanoscale microreactors. They demonstrated that in order to achieve effective vortical streaming in nanolitre volume droplets, frequency plays an important role. At lower frequency ranges, the outcome is standing wave formations, with a ring pattern emerging as presented in Figure 2-5 (a). To restore the vortical streaming pattern, high frequencies are required, on the order of GHz, illustrated in Figure 2-5 (b).

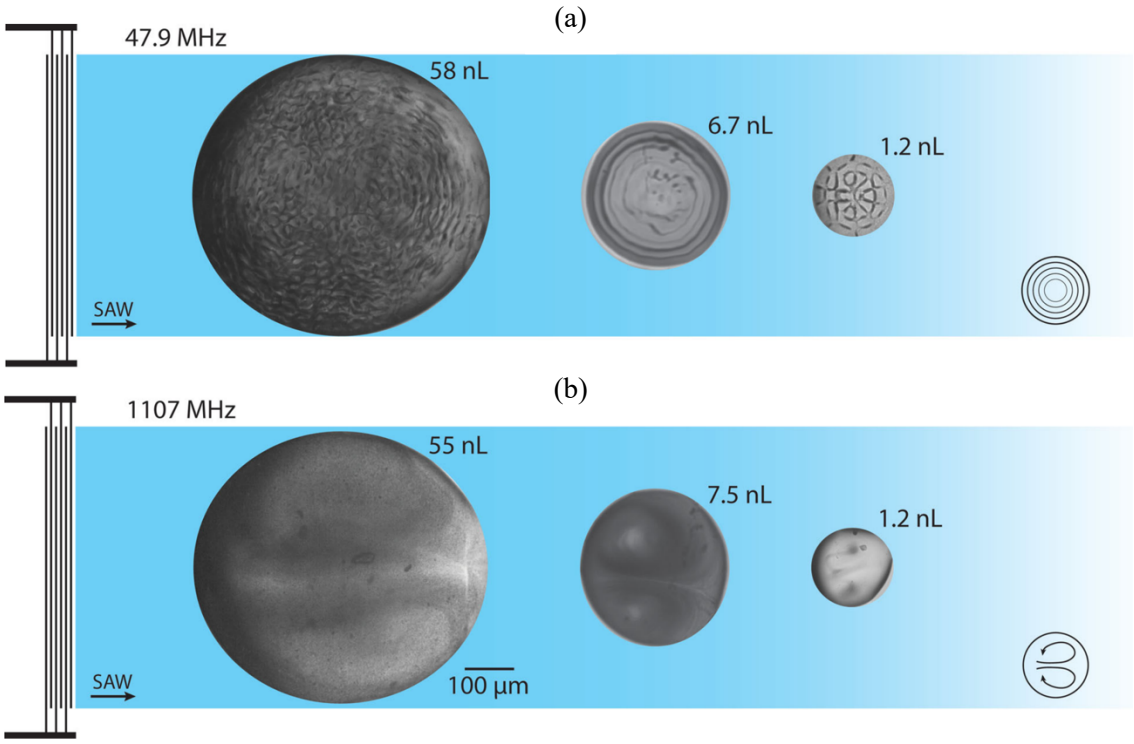

Figure 2-5. Acoustic streaming in nanolitre droplets; (a) 47.9 MHz case demonstrates a ring-like pattern emerging due to standing wave formations (b) 1107 MHz case illustrates streaming pairs forming in each droplet size [33]

SAW streaming and mixing is generated at relatively low radio frequency (RF) powers, ranging from milliwatt (mW) to low watts (W), which can be beneficial for mixing chemical or biological reactants. Further increase of RF power can initiate deformation and translation of the droplet along the substrate if the surface has been chemically treated. This mode, frequently referred to as pumping, may seem like a relatively simple process however it involves complex interfacial dynamics and intricate internal streaming patterns. Guo et al. [34] investigated the effects of SAW frequency, power and substrate material to characterise the microfluidic performance of SAW devices. The results reveal that an increase in resonant frequency raises the threshold power required to achieve specified modes (i.e., streaming, pumping, and jetting). For pumping mode this is increased from 0.7 W at 61.7 MHz to 4.8 W at 250.1 MHz for a $LiNbO_3$ substrate. Additionally, it is shown that a $LiNbO_3$ substrate demands significantly less power than a ZnO/Si substrate to initiate the respective modes [34].

Additionally, Brunet et al. [35] experimentally studied the effects of SAW on droplets composed of different liquids (deionised water and water/glycerol mixtures) on $LiNbO_3$ substrate. The findings reveal the importance of viscosity on droplet velocity, with an

increased viscosity resulting in a lower velocity due to viscous dissipation [35]. Tan et al. [32] explored the possibility of utilising the movement of sessile droplets to collect microparticles deposited on a contaminated surface, as shown in Figure 2-6. They report collection efficiencies of up to 68% for pollen and 70% for E. coli bacteria, compared to 55% for synthetic particles. The reasoning for this disparity has been partially attributed to the surface roughness of pollen and the spiked surface of the bacteria enhancing the collection capacity over the artificial particles. It has been envisioned that this type of device could be beneficial in the collection of airborne microorganisms owing to the irregularity of the surface bioparticles [32].

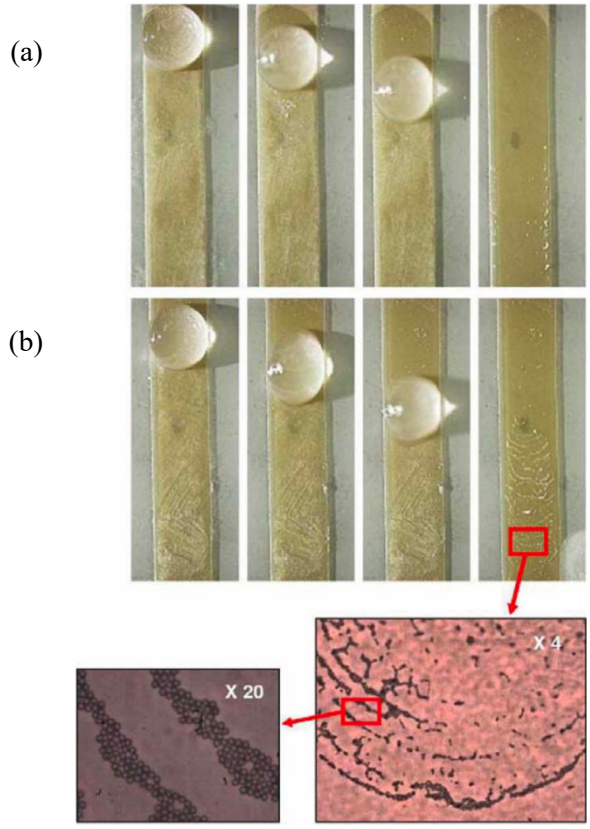

Figure 2-6. Sequential images showing particle collection using droplet movement over surface; (a) melamine (hydrophilic) particles (b) polystyrene (hydrophobic) particles. Droplet movement is from top to bottom. Further magnification (bottom images) shows polystyrene particles left behind gathered in ring-like structures rather than in random clusters [32]

The movement of droplets can be carefully manipulated to allow it to follow a predetermined path on the chip. Wixforth [7] demonstrated that several droplets of different fluids (or reagents) can be acoustically guided along chemically defined tracks

on the chip where they can be merged, split or mixed depending on the desired application. Zhang et al. [36] present a method for contactless droplet transport and processing using programmable, acoustic-based devices. The technology allows for precise droplet manipulation via a trap and release mechanism where a pre-programmed sequence is executed, see Figure 2-7, allowing for multi-step reactions where it is imperative that reactants are added sequentially.

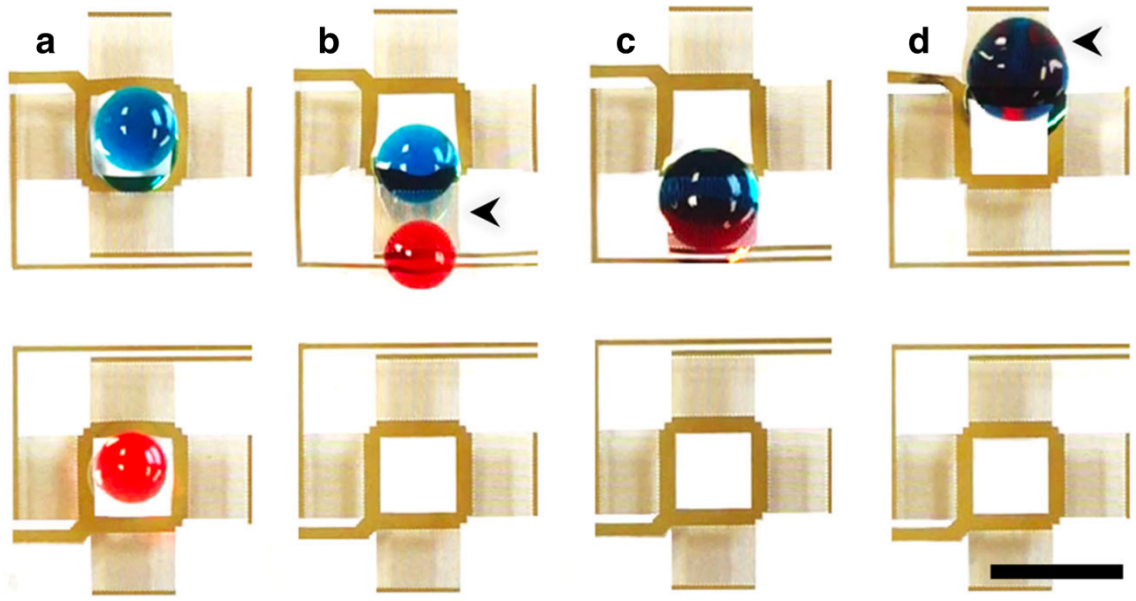

Figure 2-7. Sequencial images of droplet merging using a digital acoustic-based device; **a-d** merging of two droplets [36]

Droplet jetting is achievable when the acoustic radiation is large enough to overcome the surface tension of the droplet. A large surface acceleration is produced which serves to destabilise the air-liquid interface, culminating in an elongated column of fluid emerging [26]. Shiokawa et al. [30] reported jet streams with SAW excitation where the water is continuously ejected from the substrate, along the Rayleigh angle, until all the fluid has been depleted. Jetting phenomenon can be achieved from a single propagating SAW, where the acoustic wave travels along the device from left to right for example. Moreover, the use of focused SAW devices has been exploited in this area as the energy is concentrated to a single point [26]. Two opposing acoustic waves focused towards the liquid droplet at the centre of the device causes deformation in a consistent manner, with an extended column being produced normal to the surface, illustrated in Figure 2-8. Tan et al. [26] experimentally investigated the nature of jetting phenomena in a bid to provide a greater understanding of the fluid behaviour to the microfluidics community. The study

reveals the existence of various regimes, as a consequence the acoustic energy radiated to the droplet, which can result in pinch-off of single or multiple droplets, leading to total drop breakup. Additionally, the author present a derivation for predictive jet velocity, based on a jet momentum balance derived by Eggers [37], comparing it to experimental findings. The results demonstrate a good agreement with the measure values; hence a new predictive approach has been developed. This type of device could be have advantages in ink-jet or soft biological printing applications where there is no longer any need for a nozzle [38].

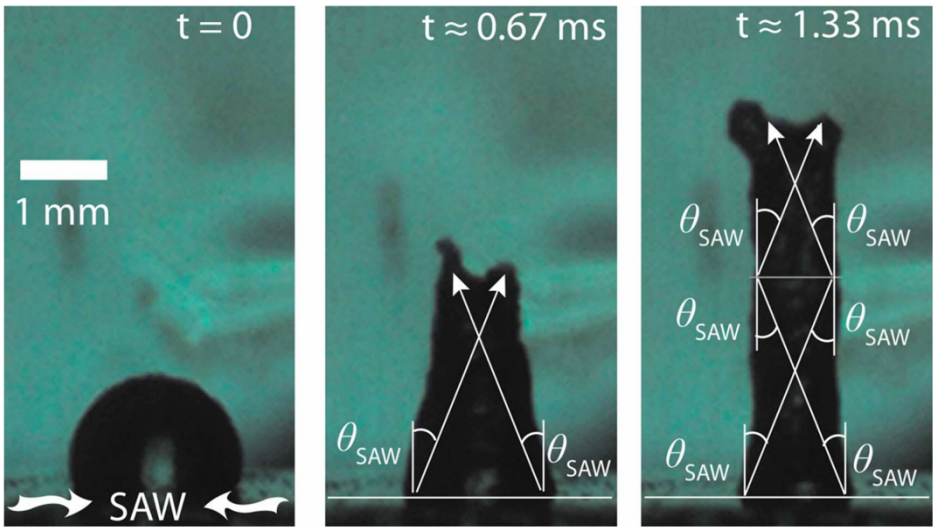

Figure 2-8. Initial jet formation sequence due to concentrated acoustic radiation arising as a consequence of the convergence of two SAWs produced by curved focused IDTs placed on both sides of the drop [26]

Atomisation or nebulisation of fluids has a wide range of applications including agriculture [39,40], medical [41,42] and automotive [43–45]. The obliteration of liquids into miniscule particles is beneficial in the delivery of drugs into the lungs, in asthma patients for example, where particle size is important in being able to penetrate the lung cavity more effectively to dispense the intended dosage [46].

The SAW atomiser was first proposed by Kurosawa et al. [47] in the 1990's, where owing to advances in material technologies, they were able to increase the operational frequency of their device to 10 MHz. The authors observe a coupling between the Rayleigh wave and the thin liquid film, which when the power is intensified, the vibrating surface transfers into the liquid, triggering capillary waves at the free surface. An atomised mist is then detected at the crest of the capillary waves once the intensity is high enough [47].

Recently, Qi et al. [48] proposed a device capable of extracting protein molecules and live yeast cells through an 'extraction of fluid from paper' technique. The process involves extracting fluid from narrow strips of paper, through SAW atomisation, which could have promising applications in mass spectrometry, medical diagnosis and drug delivery [48]. The contribution by Ho et al. [49] substantiated the application of a paper-based SAW atomisation device to mass spectrometry as they were able to successfully detect low levels of heavy metals in tap water as well as drugs in whole human blood. Alvarez et al. [50] investigated the use of a SAW atomiser for drug delivery purposes, where microparticles are encapsulated inside Poly-ε-caprolactone (PCL). The findings reveal that frequency and concentration of PCL have a strong influence on final microparticle size, with smaller particles (~3 μm) being generated at lower evaporation rates which are suitable for effective respiratory drug delivery.

2.3.2 SAW Devices for Particle Concentration and Sorting

Besides droplet manipulation on a SAW device, acoustic internal streaming has been used to concentrate microparticles to a specific region within the liquid. Li et al. [51] revealed that by inducing a bulk azimuthal circulatory flow via asymmetrical positioning of the droplet in the path of the propagating SAW radiation, particles can be focused towards the centre of the droplet, as can be seen Figure 2-9. Redispersion of particles can also be achieved when the input power is intensified further such that shear-induced migration is overcome by outwardly orientated centripetal acceleration [51].

Many other studies have reported exploiting SAW-driven induced internal streaming for the concentration of microparticles in droplets [52–54]. However, there has been much interest in the development of efficient and effective particle and cell actuation devices utilising microfluidic channels. Shi et al. [55] presented a novel manipulation technique for focusing particles in microfluidic channels using standing SAWs (SSAW). SSAWs can be generated when a pair of IDTs, aligned on either side of the channel, propagate acoustic waves towards the centre, from opposing directions. The interference of the two waves culminates in a standing wave, together with the periodic distribution of pressure nodes and anti-nodes, shown in Figure 2-10. The fluctuating pressure generates an acoustic radiation (along the X axis) which drives the suspended particles towards either pressure nodes or anti-nodes, depending on the density and the compressibility between particles and the fluid [56]. Devices can be specifically designed in order to focus

particles to the channel centre, through careful consideration of the channel width to encapsulate only a single pressure node. This allows the distributed particles entering the channel to be funnelled towards the channel centre once they pass the SSAW interaction area between the opposing IDTs (Figure 2-10).

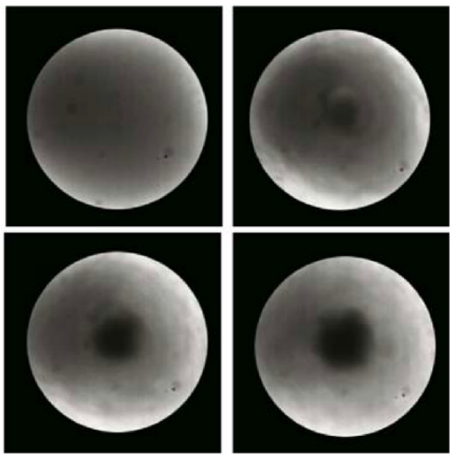

Figure 2-9. Images showing rapid concentration of 1 μm spherical fluorescent polystyrene particles at RF power 330 mW [51]

More recently, Wu et al. [57] demonstrated that nanoparticles can be successfully separated, in a continuous flow, based on volume through tilting the angle of the IDTs on the microfluidic device. The results show that, at a constant input power, the larger particles are moved further from the original stream whilst the smaller particles are moved less, allowing for the collection of each at opposing outlets.

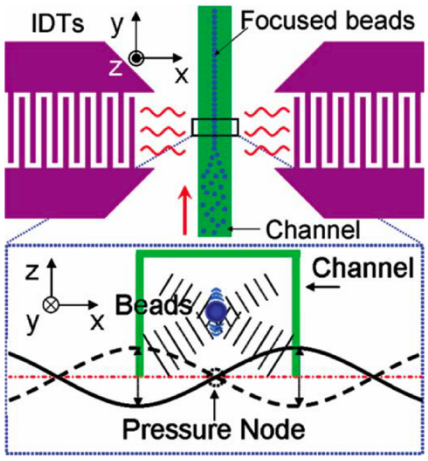

Figure 2-10. Schematic of SSAW particle focusing device. Insert demonstrates working principle of SSAW [55]

2.3.3 Thermal Impact Induced by SAW

Although thermodynamic heating effects is a widely known problem in SAW microfluidics, there has been very limited research dedicated to the topic. The consensus from the community is that the thermal effect is a consequence of both losses in the substrate and viscous dissipation of acoustic energy in the liquid [58]. These effects are exacerbated as the RF power of the IDT is increased which can cause issues, especially in applications involving biological matter such as tissue or cells where they are particularly sensitive to temperature [59].

Recently, an experimental study by Mehmood [60] investigated the connection between kinetic and thermal impacts of SAW-droplet interactions for a thin-film piezoelectric substrate. The author proposed an analytical model, based on mass, momentum, and energy conservation, to describe a coupling mechanism between the internal streaming and the temperature distribution within the droplet. As illustrated in Figure 2-11, in the model kinetic sources from streaming, K_{st}, and friction, K_f, are considered whilst thermal sources include heat transfer from the substrate to the droplet, Q_s, radiated energy at the SAW interaction point, Q_r, and heat transfer from the droplet to the surroundings, Q_{air}.

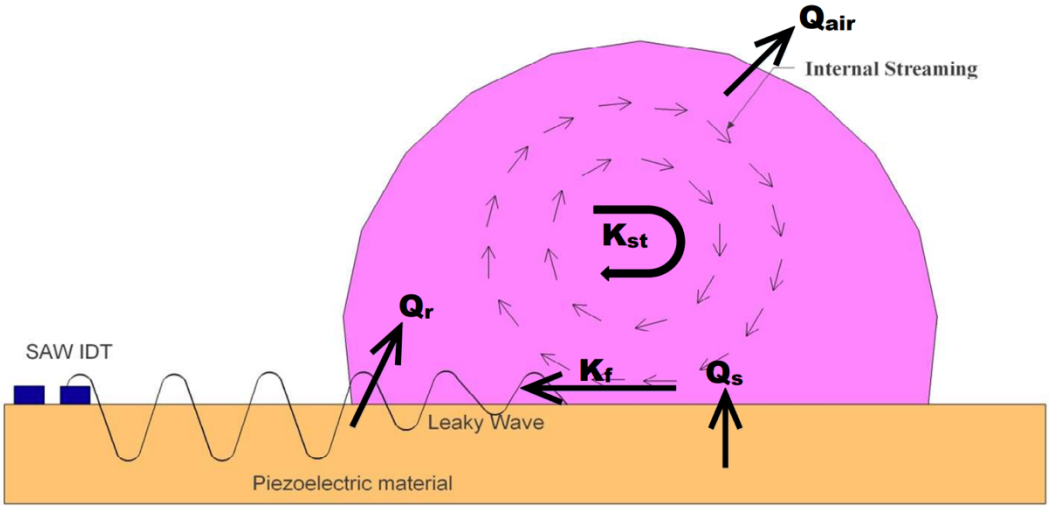

Figure 2-11. Schematic explaining thermodynamic energy conservation of SAW-droplet interactions indicating heat transfers and kinetic change inside the droplet [60]

The findings from the study reveal that the temperature rise inside the droplet is directly proportional to the reasonant frequency of the SAW device. Depending on the applied power, wave (Rayleigh or Sezawa) and time during experiment, there can be heat transfer from the droplet back to the substrate as the temperature of the bottom layer of fluid in

the droplet is greater than that of the substrate. Lastly, the contribution of thermal energy within the droplet is found to vastly exceed that of the kinetic energy, hence the majority of input power from the IDT is converted to heat.

2.4 Numerical Techniques for SAW-Liquid Interactions

As previously shown, experimental studies of SAW-liquid coupling have allowed for mixing, pumping, jetting and atomisation of microfluids to be achieved through careful manipulation of the input parameters [38]. Recently, computational modelling has been employed to aid in the understanding of underlying hydrodynamic mechanisms and behaviours. Numerical studies can be an effective tool in the manufacturer of microfluidic devices since behaviours can be predicted and mechanisms can be revealed, allowing for more effective and efficient utilisation of device design.

Numerical modelling can be categorised according to scale, progressing from the Continuum scale down to the nano scale where particles or molecules are simulated. Beyond this scale, a quantum mechanics approach is required where individual atoms are considered and the distinction between solid and liquid no longer applies [61]. Well established computational techniques, centred around the Continuum scale, have been widely available for several years. On the other hand, modelling based on microscopic interactions of particles has seen less popularity and thus minimal exposure. In the following, acoustic streaming theory is introduced followed by a review of numerical modelling techniques, with special interest in studies focused on SAW interactions in microfluidics, detailing novelty and findings which have progressed the overall understanding of the field.

2.4.1 Acoustic streaming theory

The flow (momentum) of continuum fluids can be represented by equations based on the Navier-Stokes (N-S) equations,

$$\rho \frac{\partial \boldsymbol{u}}{\partial t} + \rho(\boldsymbol{u} \cdot \nabla)\boldsymbol{u} = -\nabla \boldsymbol{P} + \mu \nabla^2 \boldsymbol{u} + \left(\eta + \frac{1}{3}\mu\right)\nabla(\nabla \cdot \boldsymbol{u}) \qquad 2\text{–}2$$

where ρ is the density of the fluid, $\boldsymbol{P}$ is the pressure, $\boldsymbol{u}$ is the velocity, η and μ are the bulk and shear viscosities, respectively. Mass conservation is satisfied by the continuity equation,

$$\frac{\partial \rho}{\partial t} + \nabla \cdot \rho \boldsymbol{u} = 0 \qquad 2\text{–}3$$

Assuming wave propagation is an adiabatic process [62] and after expansion, through conservation of momentum Eq. 2–2 may be written as

$$\frac{\partial(\rho \boldsymbol{u})}{\partial t} + \rho(\boldsymbol{u} \cdot \nabla)\boldsymbol{u} + \boldsymbol{u}\nabla \cdot \rho \mathbf{u} = -\nabla \boldsymbol{P} + \left(\eta + \frac{4}{3}\mu\right)\nabla(\nabla \cdot \boldsymbol{u}) - \mu\nabla^2 \boldsymbol{u} \qquad 2\text{–}4$$

Taking the time average of Eq. 2–4, the acoustic streaming equation, derived by Nyborg [63,64] for an incompressible fluid, is then defined as,

$$\mu\nabla^2 \boldsymbol{u} - \nabla \boldsymbol{P} + F = 0 \qquad 2\text{–}5$$

where $F = -\rho\langle(\boldsymbol{u} \cdot \nabla)\boldsymbol{u} + \boldsymbol{u}(\nabla \cdot \mathbf{u})\rangle$, is the acoustic streaming force, $\boldsymbol{u}$ is the velocity of the Rayleigh wave in the fluid and $\langle\cdot\rangle$ represents the time-averaged mean value over a large number of cycles. From Eq. 2–5, it is clear that once the velocity is known, the non-linear streaming force can be calculated.

A propagating SAW will change its mode to LSAW when it comes into contact with a liquid medium. A longitudinal wave, established from the conversion of SAW to LSAW, is transmitted in the fluid along the Rayleigh angle, as described in Figure 2-3. The particle displacement (u_x, u_z) can be represented by [29],

$$\begin{aligned} u_x &= Aexp(j\omega t) \cdot exp(-jk_L x) \cdot exp(\alpha k_L z) \\ u_z &= -j\alpha Aexp(j\omega t) \cdot exp(-jk_L x) \cdot exp(\alpha k_L z) \end{aligned} \qquad 2\text{–}6$$

where A is the SAW amplitude and $\omega = 2\pi f$ is the angular frequency. The Rayleigh wave number k_R is a real number while the Leaky SAW k_L is complex, with the imaginary part representing energy dissipation in the liquid. According to [30], k_L can be calculated by extending the method of Campbell and Jones [65] to liquid/solid structures assuming that the boundary conditions of stress and displacement at z = 0 are continuous. The attenuation constant, α, is found from,

$$\alpha^2 = 1 - \left(\frac{V_L}{V_f}\right)^2 \qquad 2\text{–}7$$

with V_L and V_f symbolising the Leaky SAW velocity and sound velocity in the liquid, respectively.

Through replacing the particle displacement (u_x, u_z) with the particle velocity $v = \delta u/\delta t$, and substituting into Eq. 2–5, the components of streaming force (F_x, F_z) can be expressed as [29],

$$F_x = -\rho(1+\alpha_1^2)A^2\omega^2 k_i \, exp\, 2(k_i x + \alpha_1 k_i z)$$
$$F_z = -\rho(1+\alpha_1^2)A^2\omega^2 \alpha_1 k_i \, exp\, 2(k_i x + \alpha_1 k_i z) \qquad 2–8$$

where $\alpha = j\alpha_1$ and $k_L = k_r + jk_i$. Since the total SAW streaming force is given by $F_{SAW} = \sqrt{F_x^2 + F_z^2}$, it can be shown that the derivation of the force is equal to [29],

$$F_{SAW} = -\rho(1+\alpha_1^2)^{3/2}A^2\omega^2 k_i \, exp\, 2(k_i x + \alpha_1 k_i z) \qquad 2–9$$

The direction of the SAW force in the liquid is similar to the radiation of the LSAW, along the Rayleigh angle. The exponential decay of the longitudinal wave restricts the impact of the SAW force in the fluid to a few microns of the interface point between the SAW and the liquid medium. The above theory and derivation provide a framework from which SAW induced acoustic streaming, within a liquid medium (droplet), can be numerically predicted with or without the implementation of the dynamics of the acoustic field. In this research, the SAW transportation is decoupled in the solid and liquid, hence no acoustic field is applied, instead a body force (modelled according to Eq. 2–9) is employed. Further details can be found in Section 4.2.

2.4.2 Continuum scale models

With the advent of computational technologies in the early 20th Century, methodologies providing solutions to the above set of equations was vastly accelerated. Since its inception, computational fluid dynamics (CFD) [66] has grown to become the most successful and popular method for simulating fluid dynamics. Numerical approaches such as Finite Volume (FV) [67,68], Finite Difference (FD) [69,70] and Finite Element (FE) [71,72] discretise space and time to approximately solve the system of governing equations.

Multiphase flow models at the continuum scale aim to solve the governing equations whilst differentiating between phases. To satisfy these conditions there have been several methodologies proposed such as volume-of-fluid (VOF) [73], level set method (LSM) [74] and phase field (PF) [75].

To date, there have been many studies concerning the interaction between SAW's and a liquid medium to investigate the dynamic behaviour of the fluid. Köster [76] presented a mathematical model to study the coupling mechanism between the LSAW and the fluid. The basic premise is to define to sub-categories; one based on the acoustic field and the other on the streaming field, to elevate the problem of extreme disparity between timescales (i.e., approximately 10^{-8} s for acoustics and 10^{-3} s for streaming). The author briefly describes a method to capture surface deformation in sessile drops which preserves the volume, however this is a very restricted study, consisting of only one special case. Antil et al. [77] similarly performed numerical simulations associated with acoustic streaming in microfluidic biochips. They corroborated the mathematical procedure with qualitative and quantitative comparison against experimental data, demonstrating good agreement for acoustic streaming behaviour. More recently, Alghane and co-workers [78–80] comprehensively studied the effects SAW-driven acoustic streaming in sessile droplets on a 128° YX-$LiNbO_3$ substrate experimentally and numerically, by means of a three dimensional FV modelling scheme (see Figure 2-12).

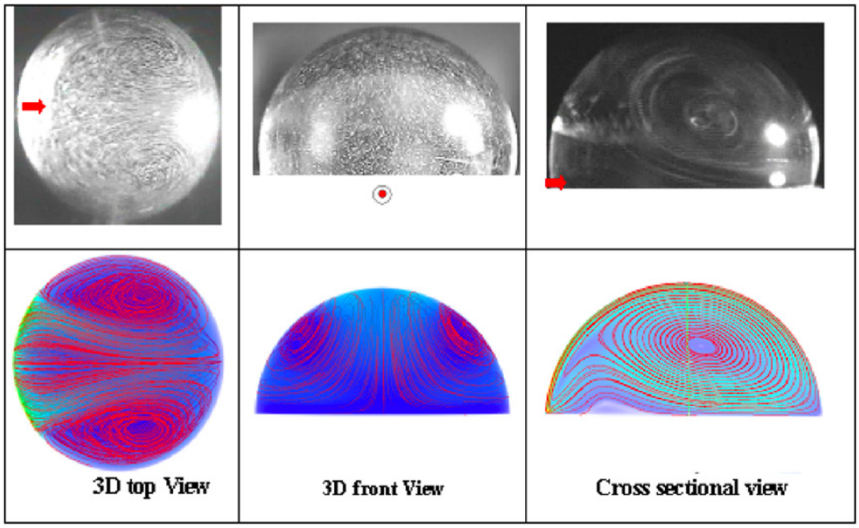

Figure 2-12. Comparison of experimental and numerical modelling for 30 µl droplet. Top row depicts trajectories of particles inside drop. Bottom row shows streaming patterns from numerical simulations. Arrow denotes SAW propagation direction [78]

The authors provide a numerical correlation between SAW amplitude, A (required in calculating the SAW streaming force in the numerical model), SAW wavelength, λ, and the applied experimental RF powers (in Watts), P_D, by matching the streaming velocities [78].

$$\frac{A}{\lambda} = 8.15 \times 10^{-6} P_D^{0.225} + 5 \times 10^{-6} P_D^{0.8} \qquad 2\text{–}10$$

The proposed relationship provides a tool to link the simulated input parameters to actual RF powers used in the experiments. Additionally, the findings reveal the importance of SAW width to droplet radius, concluding that the maximum streaming velocities are achieved when this aspect ratio is approximately equal to half [79]. Moreover, the authors report strong nonlinearity in the flow inertia, suggesting the Stokes model is only valid for very small acoustic powers [80]. Unlike multiphase flow models, the interface region is considered rigid in their study, hence it was restricted to low power regimes where droplet deformation was insignificant. Riaud et al. [81] investigated the influence of viscosity and caustics on acoustic streaming in droplets both experimentally and numerically. The findings from the study suggest viscosity influences the flow structure as well as the velocity magnitude, whereas caustics appear to drive the flow.

Lately, Biroun and co-workers [82–85] have studied both experimentally and numerically droplet deformation and jetting on a ZnO/Si thin film device, excited by SAW, over a range of resonant frequencies. The numerical model, based on a coupled level set volume of fluid (CLSVOF) method, is validated against experimental data, with an empirical correlation for A/λ, similar to Alghane et al. [78], presented for ZnO/Si substrates. The developed model captures complex multiphase fluid interactions which span a broad range of SAW powers, allowing for intricate droplet deformation as a direct consequence of SAW induced internal flow, to be captured, as shown in Figure 2-13. Interestingly, it has been demonstrated that SAWs can be implemented to reduce the contact time (up to 35%) of droplets impacting a surface [84]. When an inclined surface is employed, the droplet rebound direction can also be manipulated through careful consideration of the SAW propagation [83].

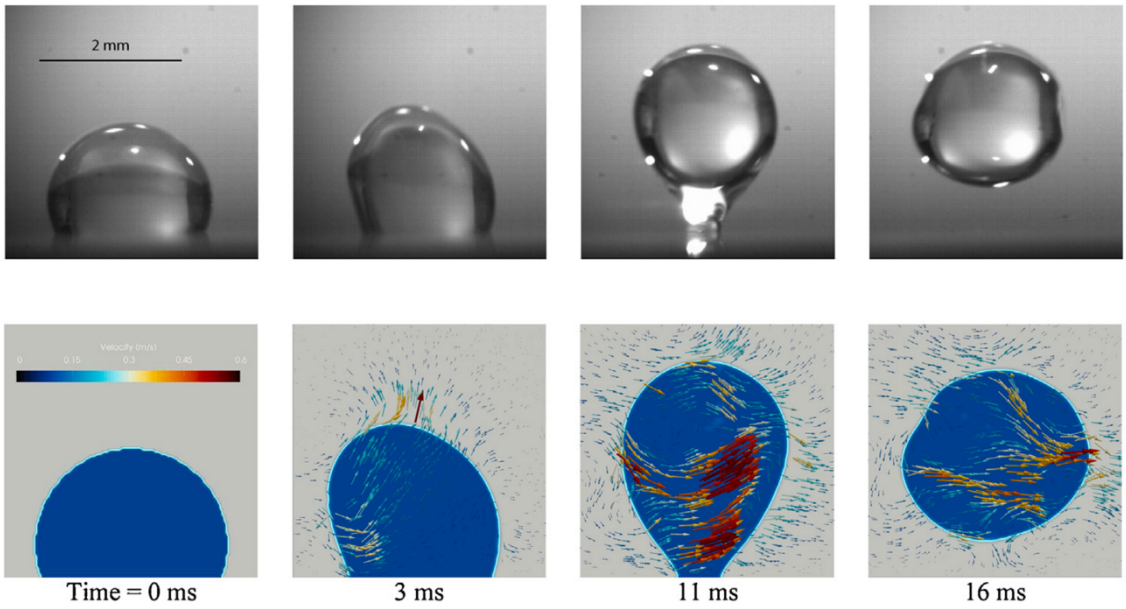

Figure 2-13. Comparison between experimental and numerical results for droplet jetting at frequency 271.32 MHz [82]

2.4.3 Particle-based models

In the field of numerical modelling and simulation of SAW induced streaming and mixing of fluids in microchannels and droplets, there exist very limited studies utilising particle-based dynamics models. The lattice Boltzmann (LB) methodology, a mesoscopic modelling technique, has been used in the study of acoustic streaming and attenuation-driven acoustic streaming for single phase fluids [86,87]. Tan and Yeo [88] studied acoustic streaming in micro and nanochannels under SAW excitation by means of a hybrid numerical scheme comprising of FD for elastic solid and LB method for fluid flows. The findings show good agreement with the analytical solutions, demonstrating a viability of using the LB in the exploration of SAW effects on liquids. More recently, Sheikholeslam Noori et al. [89] developed a two-dimensional (2D) two-component droplet-based SAW interaction model using the colour-gradient LB methodology. The study reported the minimum amplitude required to initiate streaming, pumping and jetting states for a $LiNbO_3$ substrate at various resonant frequencies (20 MHz to 200 MHz). In a further study, the authors investigated numerically the comparison between ZnO/Si and $LiNbO_3$ devices, revealing that the former is more suited to pumping/transport applications due to a shorter wet length and hence faster movement along the substrate [90].

In the proceeding section, the LB methodology will be introduced, focussing on the concepts and underlying theories from which the foundations are based upon.

2.5 Lattice Boltzmann method

The lattice Boltzmann method (LBM) has, in recent years, gained increased interest in the scientific community as a viable alternative for simulating complex hydrodynamic phenomena. LBM lies at the interface between continuum and particle-based dynamics, resulting in a scheme which has a relatively high computational demand but also a high physical insight.

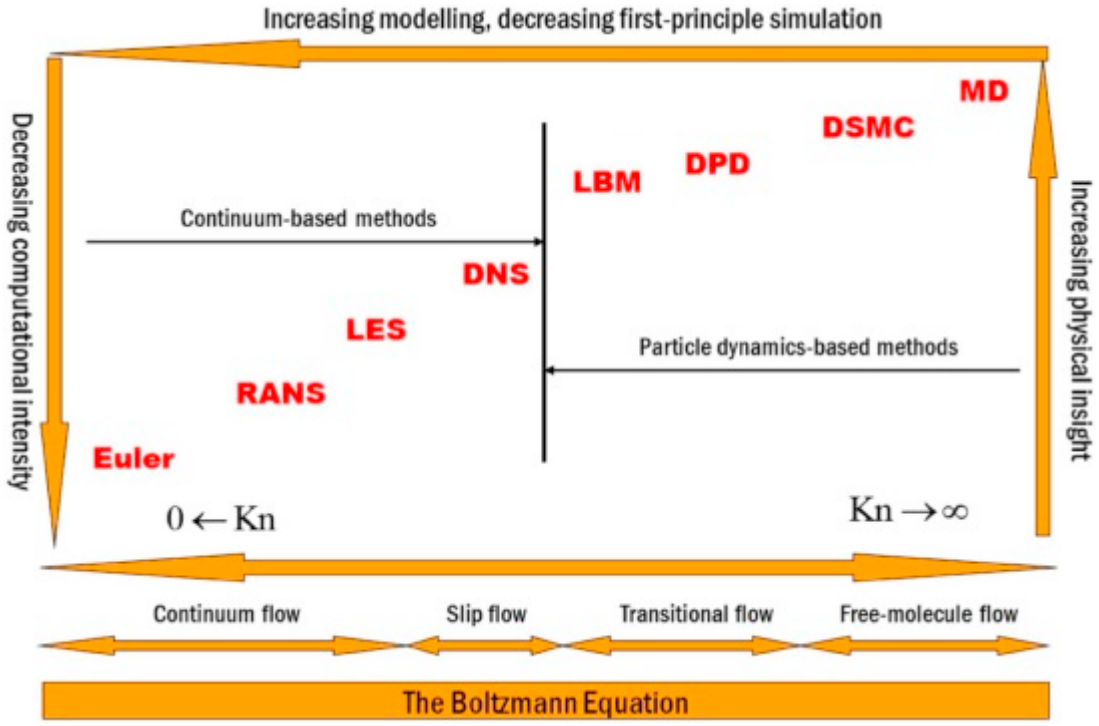

Figure 2-14. A hierarchy of modelling and simulation approaches, providing definition of Knudsen number Kn [91]

LBM has been able to successfully simulate various regimes comprising; porous media [92–94], multiphase flows [95–97], turbulence [98–100] and compressible flows [101–103] amongst others. Before proceeding further, it is only appropriate that a theoretical background is presented primarily in order to provide an understanding of main concepts and fundamentals of the methodology.

Essentially, the LBM is a description of a *collide* and *stream* process where fictious particles continuously interact and propagate along discrete pathways, on a lattice

structure, to reproduce hydrodynamic behaviour. Distribution functions $f_i(\boldsymbol{x}, t)$ provide a quantification of the likelihood of finding a particular particle, with a particular speed, at a particular location and a particular time. Particles can move from their initial position $\boldsymbol{x}$ along discrete lattice velocities c_i to neighbouring positions $\boldsymbol{x} + c_i$. The evolution of the distribution functions leads to the lattice Boltzmann equation (LBE),

$$f_i(\boldsymbol{x} + c_i\Delta t, t + \Delta t) = f_i(\boldsymbol{x}, t) + \Omega_i(\boldsymbol{x}, t) \qquad 2\text{–}11$$

where t is the time and Ω_i represents the collision operator, which redistributes particles amongst the populations, relaxing them towards an equilibrium state. The local equilibrium distribution function is,

$$f_i^{eq}(\boldsymbol{x}, t) = w_i\rho\left(1 + \frac{\boldsymbol{u}\cdot c_i}{c_s^2} + \frac{(\boldsymbol{u}\cdot c_i)^2}{2c_s^4} - \frac{\boldsymbol{u}\cdot\boldsymbol{u}}{2c_s^2}\right) \qquad 2\text{–}12$$

where w_i are the weights specific to the lattice implemented and c_s is the isothermal lattice speed of sound which provides the relationship between pressure and density $p = c_s\rho$. The macroscopic fluid density ρ and velocity $\boldsymbol{u}$ can be found from,

$$\begin{aligned} \rho &= \sum_i f_i^{eq} = \sum_i f_i \\ \rho\boldsymbol{u} &= \sum_i c_i f_i^{eq} = \sum_i c_i f_i \end{aligned} \qquad 2\text{–}13$$

It is conventional to name the velocity set (model) with respect to the number of special dimensions *d* and discrete velocities *q*, i.e., D*d*Q*q*. The most common models are D2Q9 and D3Q19, which describe a 2D lattice with 9 discrete velocities and a 3D lattice with 19 discrete velocities, respectively.

It is necessary for a model to adhere to a general set of requirements which include mass and momentum conservation, whilst providing sufficient isotropy to properly describe the underlying physics. To satisfy the N-S equations, all moments of the weight w_i up to fifth order must be isotropic and non-negative, which specifies the following conditions [104],

$$\begin{aligned}
&\sum_i w_i = 1,\\
&\sum_i w_i c_{i\alpha} = 0,\\
&\sum_i w_i c_{i\alpha} c_{i\beta} = c_s^2 \delta_{\alpha\beta},\\
&\sum_i w_i c_{i\alpha} c_{i\beta} c_{i\gamma} = 0,\\
&\sum_i w_i c_{i\alpha} c_{i\beta} c_{i\gamma} c_{i\mu} = c_s^4 \left(\delta_{\alpha\beta}\delta_{\gamma\mu} + \delta_{\alpha\gamma}\delta_{\beta\mu} + \delta_{\alpha\mu}\delta_{\beta\gamma}\right),\\
&\sum_i w_i c_{i\alpha} c_{i\beta} c_{i\gamma} c_{i\mu} c_{i\nu} = 0
\end{aligned} \qquad 2\text{–}14$$

It has been noted, that for advection-diffusion problems a lower level of isotropy may be sufficient such that only the first four of Eq. 2–14 are necessary [104]. LB simulations involving the energy equation often require large velocity sets, i.e., D3Q27, since higher order moments are required to be solved.

As previously mentioned, the most common lattice structures are the D2Q9 and D3Q19 models. Apart from the above, there exist many alternatives however symmetrical lattices are most widely used. In 2D popular models are D2Q7 and D2Q9, while in 3D the D3Q15, D3Q19 and D3Q27 are most favoured. The D2Q9 velocity set is described as

$$\begin{aligned}
&[c_0, c_1, c_2, c_3, c_4, c_5, c_6, c_7, c_8]\\
&= \begin{bmatrix} 0 & 1 & 0 & -1 & 0 & 1 & -1 & -1 & 1 \\ 0 & 0 & 1 & 0 & -1 & 1 & 1 & -1 & -1 \end{bmatrix}
\end{aligned} \qquad 2\text{–}15$$

where the lattice weights are

$$w_i = \begin{cases} 4/9, & i = 0 \\ 1/9, & i = 1,2,3,4 \\ 1/36, & i = 5,6,7,8 \end{cases} \qquad 2\text{–}16$$

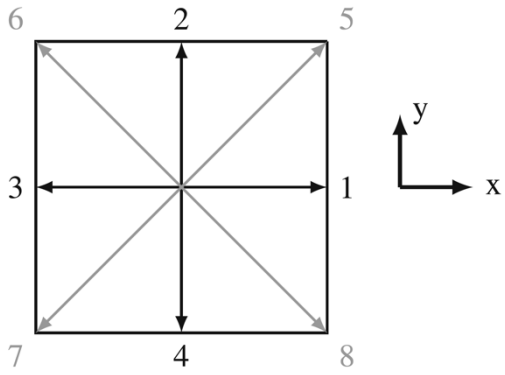

Figure 2-15. Scematic of D2Q9 velocity set. Note, rest velocity ($c_0 = 0$) is not shown [104]

After studying the LBE it is not immediately obvious how it relates to solving hydrodynamics problems. Through a perturbation and expansion process, it can be shown that the macroscopic N-S equations can be resolved. Chapman-Enskog [105] analysis is one such technique in which the distribution function f_i is expanded around the equilibrium distribution function f_i^{eq} through utilising the Knudsen number Kn as an expansion parameter. Through this process, terms are able to be grouped more easily according to their Kn, such that [104]

$$f_i = f_i^{eq} + \epsilon f_i^{(1)} + \epsilon^2 f_i^{(2)} + \cdots \qquad 2\text{–}17$$

where the parameter ϵ provides an indication of the order of Kn. Terms above ϵ^1 are often neglected under the assumption that only the two lowest orders are required to recover the N-S equations.

2.5.1 From Lattice Gas Automata to Lattice Boltzmann Equation

The LBE is an evolution of the Lattice Gas Automata (LGA), first proposed by McNamara and Zanetti [106]. To overcome the statistical noise associated with the Boolean nature of the LGA, distribution functions were introduced. In its early formulation, the LBE had inherent complexity as a result of non-linearity. This was quickly amended with the introduction of a quasi-linear collision operator. Assuming f_i is close to equilibrium f_i^{eq} ($f_i = f_i^{eq} + f_i^{neq}$) then the collision operator can be described as,

$$\Delta_i f_i = A_{ij}\left(f_i - f_i^{eq}\right) \qquad 2\text{–}18$$

where A_{ij} is the collision matrix governed by underlying LGA dynamics. The collision matrix, simplified by Chen et al. [107] and others, gave rise to a similar formulation as the Bhatnagar-Gross-Krook (BGK) [108] method in kinetic theory. The BGK collision operator, owing to intrinsic simplicity, improves the computational efficiency of the LBE. Consequently, the LBGK method is conceivably the most prevalent in the LB community.

2.5.2 From Boltzmann Equation to Lattice Boltzmann Equation

It has been demonstrated recently that the LBE can be directly derived from the continuous Boltzmann equation by special discretisation of time and space [109]. This implies, at least theoretically, that the LBE is independent of the LGA.

The continuous Boltzmann equation, with BGK collision operator, takes the following form [109],

$$\frac{\partial f}{\partial t} + \xi \cdot \nabla f = -\frac{f - g}{\tau} \qquad 2\text{–}19$$

where $f \equiv f(\boldsymbol{x}, \xi, t)$ is the single-particle distribution function, ξ is the microscopic velocity, τ is the relaxation rate and g is the Boltzmann-Maxwell distribution function given by [109],

$$g \equiv \frac{\rho}{(2\pi RT)^{D/2}} e^{\left(-\frac{(\xi - \boldsymbol{u})^2}{2RT}\right)} \qquad 2\text{–}20$$

where R is the ideal gas constant, D is the number of spatial dimensions and $\rho, \boldsymbol{u}$, and T are the macroscopic density, velocity and temperature. The macroscopic variables can be found through moments of the distribution function,

$$\begin{aligned} \rho &= \int f \, d\xi \\ \rho \boldsymbol{u} &= \int \xi f \, d\xi \\ \rho \varepsilon &= \frac{1}{2} \int (\xi - \boldsymbol{u})^2 f \, d\xi \end{aligned} \qquad 2\text{–}21$$

Discretisation of the moments, in momentum space, is approximated by quadrature [109]

$$\int \psi(\xi) f(\boldsymbol{x}, \xi, t)\, d\xi = \sum_i W_i \psi(\xi_i) f(\boldsymbol{x}, \xi_i, t) \qquad 2\text{–}22$$

where $\psi(\xi)$ is a polynomial of ξ, W_i is the weight coefficient, and ξ_i is the discrete velocity set. Therefore, the hydrodynamic moments (Eq. 2–21) can be expressed in a similar form to,

$$\rho = \int f\, d\xi = \sum_i f_i \qquad 2\text{–}23$$

and hence the macroscopic quantities (Eq. 2–13) are derived. An interesting quantity surrounding the Boltzmann equation is the notion of *entropy* or the so-called H function [104].

$$H = \int f \ln f\ d^3\xi \qquad 2\text{–}24$$

It was demonstrated by Boltzmann that the H function is not a conserved property, in fact it is monotonically decreasing over time, $dH/dt \leq 0$ [110], analogous with the thermodynamic quantity of entropy. The concept of entropy and H-Theorem is still a much-debated topic. Some have commented that a system which merely demonstrates these qualities does not necessarily mean that it is equivalent to the 2nd Law of Thermodynamics [111]. Nonetheless, this quality has been shown to assist in the stability of Boltzmann models.

2.5.3 Lattice Bhatnagar-Gross-Krook Method

While there are many different collision operators Ω_i available, the most popular model is based on the simple collision operator suggested by Bhatnagar, Gross and Krook (BGK) [108]

$$\Omega_i(\boldsymbol{x}, t) = -\frac{\Delta t}{\tau}\left(f_i(\boldsymbol{x}, t) - f_i^{eq}(\boldsymbol{x}, t)\right) \qquad 2\text{–}25$$

It is evident that the BGK collision model only utilises a single relaxation rate, τ, for all corresponding hydrodynamic moments, related to the kinematic viscosity through,

$$\nu = c_s^2 \left(\frac{1}{\tau} - \frac{1}{2}\right) \qquad 2\text{–}26$$

Physical properties, such as bulk and shear viscosity, are therefore unfortunately not able to be set independently of one another.

Additionally, the accuracy of single-relaxation-time (SRT) models is inescapably linked to the relaxation rate. Despite this, the method is able to reproduce the continuity and N-S equations, providing the catalyst for broadening the interest in LBM.

2.5.4 Multiple-Relaxation-Time Schemes

Developed by d'Humieres [112] around the same time as the LBGK model, the multiple-relaxation-time (MRT) scheme overcomes some of the limitations of the original mode, such as fixed Prandtl number [113], by using multiple relaxations. The basic premise of MRT is to modify the collision operator to allow moments, instead of populations, to be relaxed with individual rates. The transformation between velocity space and moment space can be accomplished by [104],

$$m_k = \sum_{i=0}^{q-1} M_{ki} f_i \quad \text{for } k = 0, \dots, q-1 \qquad 2\text{–}27$$

where M is the transformation matrix. The LBE can therefore be expressed in a modified form,

$$f_i(x + c_i \Delta t, t + \Delta t) - f_i(x,t) = -M^{-1} S[m(x,t) - m^{eq}(x,t)]\Delta t \qquad 2\text{–}28$$

where $m(x,t)$ and $m^{eq}(x,t)$ are vectors of moments, and S is the relaxation matrix, usually diagonal $S = \text{diag}\left(s_0, s_1, \dots, s_{q-1}\right)$. These individual relaxation rates can be regulated to enhance model stability and accuracy. Although there is no prescribed manner in which the rates should be set, it has been mentioned that conserved moments, i.e., mass and momentum, should be set to a non-zero value in order to retain trapezoidal integration [114]. Transformation back to velocity space is attained by [104],

$$f_i = \sum_k M_{ik}^{-1} m_k \qquad 2\text{–}29$$

Similar to the LBGK model, the streaming (propagation) step is carried out in velocity space. It is only the collision operation which is performed in moment space. The conversion process can be achieved using Hermite polynomials or Gram-Schmidt procedure, with the latter being widely favoured due to its orthogonality [104]. The Gram-Schmidt procedure consists of constructing a set of orthogonal vectors to occupy the transformation matrix, based on underlying physical properties. The outcome is a set of equilibrium moments which are a function of density and velocity. For a D2Q9 velocity set, the moments are [113,115],

$$\begin{gathered}
\rho^{eq} = \rho \\
e^{eq} = -2\rho + 3\rho\left(u_x^2 + u_y^2\right) \\
\epsilon^{eq} = \rho - 3\rho\left(u_x^2 + u_y^2\right) \\
j_x^{eq} = \rho u_x \\
q_x^{eq} = -\rho u_x \\
j_y^{eq} = \rho u_y \\
q_y^{eq} = -\rho u_y \\
p_{xx}^{eq} = \rho\left(u_x^2 - u_y^2\right) \\
p_{xy}^{eq} = \rho u_x u_y
\end{gathered} \qquad 2\text{–}30$$

The dependence of kinematic viscosity on relaxation-time can be removed due to the introduction of multiple relaxations to control the fluid. The low viscosity limit, inherent in LBGK models, can be lifted since there are additional relaxation parameters in control of the viscosity. Additionally, kinematic ν and bulk ζ viscosities to be chosen independent of each other.

$$\nu = c_s^2\left(\frac{1}{s_\nu} - \frac{1}{2}\right), \qquad \zeta = c_s^2\left(\frac{1}{s_e} - \frac{1}{2}\right) \qquad 2\text{–}31$$

It goes without saying, with the additional steps required for MRT, the computational overhead is increased compared to the original model. D'Humieres et al. [116] demonstrated that the MRT scheme is around 20% slower than the LBGK for tests carried

out on a D3Q15 model. This computational overhead can be offset by reducing the domain size (coarser mesh) and setting the viscosity to a small value, thus a reduction in perceivable timescale. With that being said, MRT has been comprehensively developed and extensively applied to a range of flow regimes. The additional stability has allowed for the simulation of high Reynolds number flows [117,118], droplet collision and breakup [119,120] and porous media [121–123]. It is particularly suitable to multiphase flow simulations involving large density and viscosity differences due to viscosity independence and reduced spurious artifacts.

2.5.5 Two-Relaxation-Time Schemes

The two-relaxation-time (TRT) Lattice Boltzmann model is a simplified version of the MRT model capable of reproducing solutions of the Navier-Stokes equations [104]. It benefits from the simplicity of the original LBGK but also numerical stability and accuracy of MRT. Unlike MRT, where there can be numerous tuneable free parameters, TRT only has two hence the name two-relaxation-time. The first relaxation is associated with the shear viscosity, leaving the other as a free parameter.

Proposed by Ginzburg et al. [124], the TRT collision model reduces the complexity of MRT by only having two relaxation rates. Having only two relaxation rates can help improve the accuracy of the LBGK model by reducing the numerical error associated with relaxation τ dependence, whilst remaining simple enough to mathematically analyse. The basic concept of the TRT collision operator is to decompose the populations into its symmetric and asymmetric components. A so-called magic parameter Λ is shown to control the accuracy and stability through,

$$\Lambda = \left(\frac{1}{\omega^{+}\Delta t} - \frac{1}{2}\right)\left(\frac{1}{\omega^{-}\Delta t} - \frac{1}{2}\right) \qquad 2\text{–}32$$

where ω^{-} is a free parameter and ω^{+} modifies the kinematic viscosity through,

$$\nu = c_s^2\left(\frac{1}{\omega^{+}\Delta t} - \frac{1}{2}\right) \qquad 2\text{–}33$$

The choice of magic parameter Λ can lead to the emergence of distinguishing features. It has been demonstrated that certain selections can result in more stable simulations,

cancellation of third and fourth-order spatial errors, and enhanced boundary implementation [125].

2.5.6 Multiphase/multicomponent LB models

Multiphase fluid flows appear in a multitude of science and engineering fields. These can manifest as single component multiphase fluids, e.g. liquid water and its vapour, and multicomponent multiphase fluids, e.g. oil and water.

Over the past few decades, many multiphase LB models have been suggested. The majority of these models fall into one of the following categories: colour-gradient method, free energy method, phase-field method and pseudopotential method.

Rothman and Keller [126] were the first to extend the FHP model to multiphase flows. Coloured particles were introduced to differentiate between phases and a nearest-neighbour interaction used to enable interfacial dynamics such as surface tension to transpire.

Gunstensen et al. [127] proposed an improved multiphase scheme by combining the work by Rothman and Keller, and the newly formed LBE. The scheme involves two particle distributions, often represented by the colours Red and Blue, to describe two immiscible fluids. The model describes two phases occupying the same space, however it is the collision rule which enforces preferential grouping of like phases. During the collision, there is no distinction between the two colours. The major innovation comes in the form of a perturbation step. The step is applied to the nodes containing mixed densities in such a way as to recuperate a surface tension. Mass is depleted on lattice nodes parallel to the interface and redistributed to the nodes perpendicular to the interface, thus conserving mass and momentum at the site. The recolouring step enforces the segregation of the two fluids, where particles move preferentially towards similar coloured particles and repel opposing colours.

Although the model was used for many applications, it suffers from some unfavourable qualities. The model does not solve the exact governing equations of two-phase flow, even though Galilean invariance is still recovered by correct assignment of rest particles. Also, the model can be computationally inefficient due to the fact that the fully linearised collision operator involves complex matrix multiplication at each position and time step. This adds computational expense to the simulations, especially in three dimensions.

Finally, the model lacks the capability of incorporating variable densities and viscosities, thus restricting simulations to fluids with the same densities and viscosities.

Grunau et al. [128] proposed an extension of the model to allow for fluids with variable density and viscosity. This was achieved through a combination of a space-dependent relaxation process and the freedom of the rest particle equilibrium distribution. Latva-Kokko and Rothman [129] identified a problem with the recolouring step in the original Gunstensen model. At the interface between fluids, if there is insufficient velocity to move particles from one site to another, the interface cannot move thus it is pinned to the lattice. To overcome the problem of lattice pinning they suggested an alternative algorithm for the recolouring step, allowing fluids to mix slightly at the tangent of the interface. This alteration has been shown to alleviate this unwanted side-affect whilst also providing a reduction in spurious velocities. Reis and Phillips [130] recommend an improvement to the collision operator to help restore correct surface tension in the macroscopic limit.

In an attempt to establish thermodynamic consistency in LBM, Swift et al. [131] developed a method using a free-energy approach. A non-ideal pressure tensor is implemented directly into the collision operator resulting in phase transition which is pressure driven. Thermodynamic consistency is established through correct choice of EOS which coincides with proper selection of the bulk term. Although the free-energy model satisfies local conservation of mass and momentum, it was shown to suffer from a lack of Galilean invariance in multiphase fluid flows due to the addition of some non-Navier-Stokes terms. In [132], the authors offered some improvement by including additional terms in the pressure tensor however they found that the lack of Galilean invariance could not be completely removed.

To restore Galilean invariance Inamuro et al. [133] applied asymptotic theory to the free-energy method. Droplet deformation and breakup were used to show Galilean invariance had been reinstated. In an effort to extend the applicability of free-energy-based models to flows analogous with nature, Inamuro et al. [134] suggests a model with large density differences. The approximate pressure Poisson equation must be solved which is used to obtain the pressure. It was noted that although density ratios of up to 1000 can be achieved, solving the Poisson equation iteratively requires more computational time as the density ratio increases [135].

Similarly, Zheng et al. [95] proposed a Galilean invariant free-energy-based model capable of replicating multiphase flows with large density ratios. Fakhari and Rahimian [136] analysed the model and concluded that it is only valid for density-matched fluids. The authors hence proposed an improved model, based on phase-field theory, with the aim of overcoming the apparent shortcomings of multiphase flows with large density differences. The method involves solving two distribution functions, one for capturing interfacial dynamics and another to predict hydrodynamics, to describe immiscible fluid interactions. Interface capturing equations such as Cahn-Hilliard [137] or Allen-Cahn [138] are often favoured in phase-field models, with the latter receiving more interest in recently [139,140].

Moreover, the pseudopotential model, developed by Shan and Chen (SC) [141], introduces the notion of non-local interactions between particles at neighbouring sites. The concept, based in kinetic theory, describes the interaction forces required to simulate non-ideal gases and mixtures. As a result, phase separation emerges naturally averting the need for interface tracking or capturing, which is mandatory for many other models. The original definition came associated with some unwanted artifacts such as lack of thermodynamic consistency, large spurious velocities and small density ratios.

The pseudopotential model can be incorporated into both single and multiple component flows, utilising multiphase or single-phase scenarios. Single component, multiphase (SCMP) models are more stable than their multiple components, multiphase (MCMP) counterpart, hence have attained much more attention in the LB community. Nonetheless, MCMP models have been employed in the study of realistic fluid interactions involving porous media [142,143], and fuel cell applications [144–146]. MCMP models aim to solve a set of populations $f_{i,\sigma}$ for each component σ,

$$f_{i,\sigma}(\boldsymbol{x} + c_i\Delta t, t + \Delta t) = f_{i,\sigma}(\boldsymbol{x}, t) + \Omega_{i,\sigma}(\boldsymbol{x}, t) \qquad 2\text{–}34$$

where $\Omega_{i,\sigma}$ is the collision operator of each component. The key difference comes in the definition of the equilibrium distributions $f_{i,\sigma}^{eq}$, where density ρ_σ is the component density and velocity u_σ^{eq} is the velocity of the fluid mixture [104]. The description of u_σ^{eq} generally follows two methods; SC and Guo, however only the latter will be discussed here. For more in depth analysis see [104]. The Guo method involves the use of a

barycentric velocity, which is second order accurate in time and space, to define not only the equilibrium velocity but also the physical velocity of the fluid mixture [104].

$$u_b = \frac{1}{\rho}\sum_{\sigma}\left(\sum_{i} f_{i,\sigma}c_i + \frac{\boldsymbol{F}_\sigma \Delta t}{2}\right), \quad \rho = \sum_{\sigma}\rho_\sigma, \quad u_b = u_\sigma^{eq} \qquad 2\text{–}35$$

2.6 Scope for progress

The application of SAW-based devices in microfluidics has demonstrated to have tremendous consequences for chemical and biological sciences. Extensive research, described in this chapter, has already been done to try and better understand the effects of device parameters (IDT type, substrate material, frequency and RF power range) whilst investigating the underlying physical mechanisms responsible for the complex fluid behaviours due to acoustic excitation. Although much has been studied, there still remains room for progress, especially in numerical modelling of SAW-fluid interactions to further enhance understanding of the coupling mechanisms. Modelling fluid flows at the continuum scale using N-S based equations have been widely developed, providing researchers with a more complete idea of the SAW-based interactions of liquids, especially in low power applications where droplet deformation can be neglected. However, since interfacial dynamics are represented at the microscale, it only seems appropriate that numerical models should reflect this. Hence, the development of meso or microscale computational models could provide more realistic interfacial deformation and thus more accurate fluid transport of sessile droplets due to SAW excitation.

Chapter 3 – Pseudopotential LB Multiphase Models

3.1 Introduction

As previously described, the pseudopotential model [141], introduces the notion of non-local interactions between particles at neighbouring sites. To introduce the effects from inter-particle forces an additional momentum forcing term is added to the velocity field at each time step. It is assumed that a momentum force changes the momentum of the fluid after each collision, resulting in a new equilibrium state. Hence, the new equilibrium velocity is found from [147],

$$u^{eq} = u + \frac{F\tau}{\rho} \tag{3–1}$$

where the term F is the total force on the system ($F = F_{int} + F_{ads} + F_b$) which includes the inter-particle force F_{int}, interactions between the fluid and solid F_{ads} and any external body forces F_b such as gravity for example. The inter-particle force is defined as,

$$F_{int}(x) = -G\psi(\boldsymbol{x}) \sum_{i=1}^{N} w_i(|\boldsymbol{c}_i|^2)\psi(\boldsymbol{x} + \boldsymbol{c}_i\delta t)c_i \tag{3–2}$$

where ψ is the pseudopotential, $w(|\boldsymbol{c_i}|^2)$ are the weights and G controls the strength of the interaction, whilst the sign determines whether it is attractive or repulsive. The equation of state (EOS) of the SC multiphase model is [104],

$$p(\rho) = c_s^2\rho + \frac{c_s^2\Delta t^2 G}{2}\psi^2(\rho) \tag{3–3}$$

Despite the success of the model, it has been the object of widespread criticism. In the original model, the effective mass is represented by,

$$\psi(\rho) = \rho_0[1 - exp(-\rho/\rho_0)] \tag{3–4}$$

where ρ_0 is a reference density. This was later demonstrated by He and Doolen [148] to be thermodynamic inconsistent. They pointed out that any choice of ψ other than $\psi \propto \rho$ will result in a violation of the thermodynamic consistency condition for the SC LBM. In

an attempt to re-establish consistency in a binary fluid, Shan and Chen offered an alternative form of the pseudopotential [149]. Once again, He and Doolen revealed that since $\psi \propto exp(-\rho_0/\rho)$ instead of $\psi \propto \rho$, the correct pressure tensor would not be recovered resulting in thermodynamic inconsistency. Another problem with the original SC model was the lack of flexibility in the adjustment of the surface tension independent of EOS. This can cause complications in applications which require an adjustable surface tension. Also, similar to other LBM multiphase models, the dynamics at the interface near curved interfaces is plagued by spurious velocities. These unphysical currents are understood to be caused by insufficient isotropy in the gradient operator [150]. An imbalance of the discretised forces provides some additional momentum to the fluid, resulting in unphysical velocity fields being generated near curved interfaces. From the forcing mechanism, it can be identified that the magnitude of spurious velocities is proportional to the surface tension, which is modelled by the forcing scheme, and inversely proportional to the viscosity [151].

Sbragaglia et al. [152] demonstrated that these deficits could be overcome by extending the spatial range of the interactions from nearest-neighbours to next-nearest. Huang et al. [147] did some comprehensive analysis on several forcing schemes proposed for the SC LBM. They found that thermodynamic consistency could be restored by adjusting the strength of the surface tension to match the Maxwell construction curve. Li et al. [153] also carried out a broad study regarding the forcing scheme in the pseudopotential model, however they also suggest improvements. They propose a modification to the velocity in the Guo et al. [154] forcing scheme to include additional terms which can adjust the mechanical stability condition. The amended forcing model demonstrates better agreement with the Maxwell construction curve for both flat interface and circular droplet tests.

An aspect of the original SC model which has restricted its applicability is its inability to simulate large density ratio problems. This is partly due to the simple EOS employed and also the effect from spurious velocities. Increasing the density ratio inevitably results in an increase in spurious velocity which can lead to an unstable simulation. Yuan and Schaefer (YS) [155] successfully incorporated several different EOS's into the pseudopotential model. In their study, they reveal the density ratio can be significantly extended, to a more favourable region to allow for realistic fluids to be studied, by simply choosing an appropriate EOS. The Exact Difference Method (EDM) developed by

Kupershtokh et al. [156] similarly can achieve high density ratios by incorporating arbitrary EOS's.

A modification to the pseudopotential model has been recently proposed by Khajepor and co-workers [157,158] to allow for the EOS of real fluids to be implemented without compromising thermodynamic consistency. The authors recognised that the only thermodynamically consistent SC model, capable of reproducing a free-energy model, is limited due to the fact that the EOS is unique. Unlike other SC models, the scheme involves multiple-pseudopotential interactions (MPI) to help capture the complex properties of two-phase fluid flow.

$$F^{MPI} = F_1 + F_2 + \cdots + F_n \tag{3–5}$$

$$F^{MPI} = \sum_{j=1}^{n} -G_j \psi_j(x) \sum_{i=1}^{N_j} w_i(|\boldsymbol{c}_i|^2)\, \psi(\boldsymbol{x} + \boldsymbol{c}_i \delta t) c_i \tag{3–6}$$

Each potential must satisfy the thermodynamic requirement in order to preserve consistency. Matching the mechanical stability to the Maxwell equal area rule, the pseudopotential is established by,

$$\frac{d\psi}{\psi^{1+\varepsilon}} = \lambda \frac{d\rho}{\rho^2} \tag{3–7}$$

where λ is an arbitrary parameter. The consistent pseudopotential in general form is shown to be,

$$\psi_j(\rho) = \left(\frac{\rho}{\lambda_j \varepsilon_j + C_j \rho} \right)^{1/\varepsilon_j} \tag{3–8}$$

where C_j is a constant and ε_j is a flexible parameter used to release the constraint of the MPI.

The MPI scheme, although only utilising a single relaxation-time, has been shown to be capable of significantly reducing spurious velocities as well as improving accuracy in liquid/vapour coexistence curves over the original SC. Recently, the MPI scheme has been combined with the MRT collision operator which provides an additional level of

flexibility in the model [159]. At low reduced temperature, the coexistence densities obtained by the MPI deviate from the Maxwell curve. To overcome this shortcoming, it has been shown that by splitting the free parameter ε_j in Eq. 3–8 into two parts; one for the EOS and the other for forcing scheme, the thermodynamic consistency can be vastly improved over a large range of density ratios.

3.2 Analysis of Pseudopotential models

In the following a range of pseudopotential models are investigated, highlighting their advantages and disadvantages in respect to application to the study of surface acoustic wave research.

There have been many adaptations of the original SC model to help overcome the aforementioned limitations such as large spurious velocities, restricted density ratio and thermodynamic consistency. To allow for the study of more realistic fluids Yuan and Schaefer [155] proposed a methodology to incorporate various EOS's through modifying the definition of the pseudopotential to a square-root formulation,

$$\psi(\boldsymbol{x}) = \sqrt{2(p_{EOS} - \rho c_s^2)/Gc^2} \qquad 3\text{–}9$$

where p_{EOS} is the pressure form of non-ideal EOS ($p_{EOS} = p(\rho)$). Unlike the original SC method where G controls the strength of interactions, in the YS formulation, the only requirement for G is to ensure the term inside the square root remains positive, hence it is usually set to $G = -1$. As a consequence, the terms of the EOS control the interactions, with several choices being available, i.e., cubic, viral-like, etc. In the LB community, there are two EOS's which have been most widely preferred, namely Carnahan-Starling (CS) [160] and Peng-Robinson (PR) [161]. The CS EOS can be expressed as [155],

$$p_{EOS,CS} = \rho RT \frac{1 + b\rho/4 + (b\rho/4)^2 - (b\rho/4)^3}{(1 - b\rho/4)^3} - a\rho^2 \qquad 3\text{–}10$$

while the PR EOS is given as [155],

$$p_{EOS,PR} = \frac{\rho RT}{1 - b\rho} - \frac{a\alpha(T)\rho^2}{1 + 2b\rho - b^2\rho^2} \qquad 3\text{–}11$$

$$\alpha(T) = \left[1 + (0.37464 + 1.54226\omega - 0.26992\omega^2) \times \left(1 - \sqrt{T/T_c}\right)\right]^2$$

Variables a and b represent the attraction and repulsion forces in a cubic EOS [155]. They can be carefully set to control the interface thickness and hence the impact from spurious velocities [162]. The additional parameter ω in Eq. 3–11, known as the acentric factor, allows for different fluids to be modelled. The notion of reduced properties was also introduced to relate the physical properties to lattice units [155]. Properties such as density, pressure and temperature can all be expressed as $\rho_R = \rho/\rho_c$, $p_R = p/p_c$ and $T_R = T/T_c$, where subscripts R and c denote reduced and critical values, respectively.

This new formulation provides a framework for large density ratios to be simulated (>1000), thus realistic fluid models could be studied. Similarly, the EDM suggested a scheme to incorporate various EOS's however to ensure correct thermodynamic consistency, with the Maxwell construction, modification to the forcing implementation was proposed. Also, EDM alleviates the density dependence on non-dimensional relaxation time which is intrinsic with the velocity shifted method used in the original SC method. Guo et al. [154] developed a discrete forcing scheme which can also release this unphysical dependence on relaxation time. The incorporation of forces is implemented through a source term in the LBE. Finally, the newly proposed MPI scheme was developed to overcome the thermodynamic consistency of the original SC. By introducing multiple potentials, it was proposed that it will provide a more accurate description of realistic fluid flows.

To analyse the above methodologies, conventional benchmark problems are investigated to provide an overall picture of how each suppresses spurious velocities, enhances stability and ensures thermodynamic consistency. All tests are conducted using the CS EOS unless stated otherwise.

3.2.1 Thermodynamic consistency and density dependence

Firstly, to analyse the thermodynamic consistency of the models, the coexistence densities of a two dimensional (2D) flat interface is considered. Numerical simulations were carried out on a domain N_x x N_y = 200 x 200 lu (lu represents lattice length units) with interfaces at x = 50 and x = 150, and periodic boundary conditions on all four

directions. The computation is initiated with the liquid and vapour densities close to their respective coexistence values, and hence evaluated once the simulation has commenced.

To ensure thermodynamic consistency a model must be able to replicate the liquid-vapour-equilibria expressed from the Maxwell equal-area construction. The Maxwell construction is given as,

$$\int_{\rho_g}^{\rho_l} [p_0 - p(\rho, T)] \frac{1}{\rho^2} \, d\rho = 0 \qquad 3\text{–}12$$

where $p(\rho, T)$ is the EOS of the system. Any EOS which can fulfil the above relation is said to be thermodynamically consistent. The problem exists in the deviation of the vapour branch densities, from the Maxwell, as the reduced temperature is decreased. In order to maintain consistency both densities must satisfy the mechanical stability condition expressed by [163],

$$\int_{\rho_g}^{\rho_l} \left[p_0 - \rho c_s^2 - \frac{G}{2} \psi^2 \right] \frac{\psi'}{\psi^{1+\varepsilon}} \, d\rho = 0 \qquad 3\text{–}13$$

Violation of the above requirement is often the cause of thermodynamic inconsistency. Li et al. [153] explored the possibility of improving the thermodynamic consistency through modification of ε, in the mechanical stability condition, by using the relation $\varepsilon = -2(\alpha + 24\delta_t G\sigma)/\beta$. Using nearest neighbours ($\alpha = 0$ and $\beta = 3$), the relation reduces to $\varepsilon = -2(24\delta_t G\sigma)/3$ for a D2Q9 lattice. Through careful tuning of σ Li demonstrated compliance with the analytical thermodynamic consistency [153].

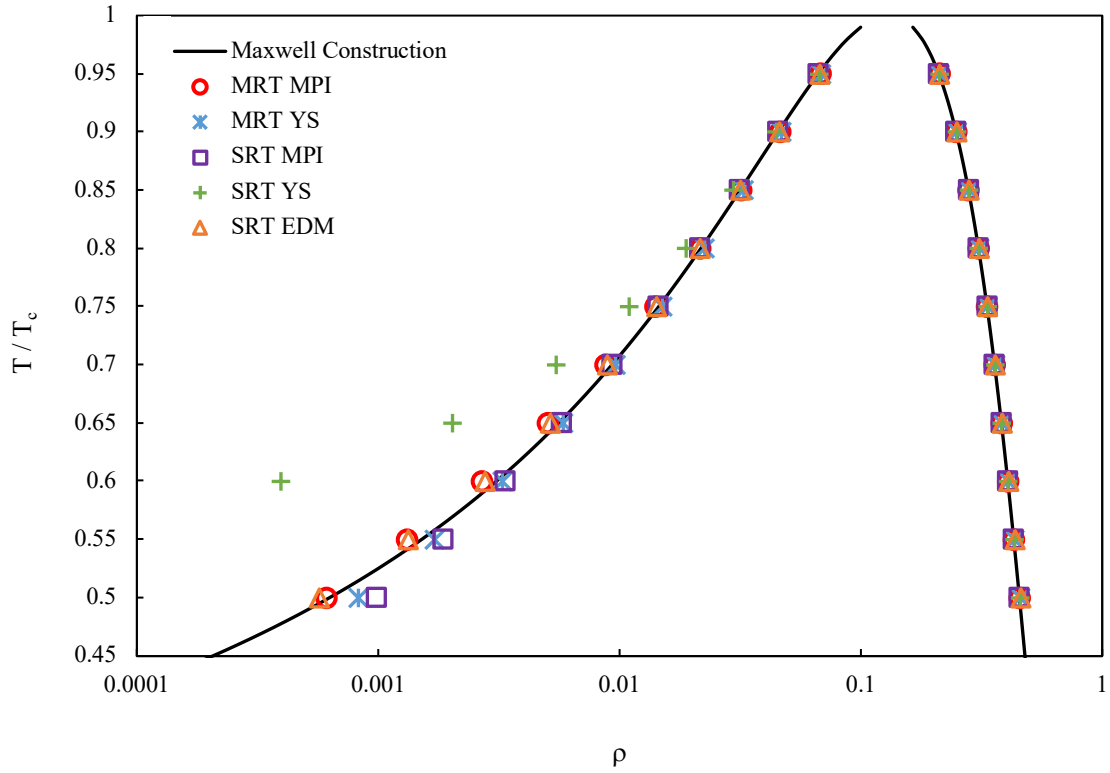

Figure 3-1. Maxwell construction for CS EOS

As shown in Figure 3-1, the thermodynamic consistency can be vastly altered between each scheme. Focusing on the SRT models; EDM and MPI models provide good agreement with the Maxwell construction, however the YS model quickly deviates as the reduced temperature decreases or density ratio increases. Beyond $T_R \sim 0.8$, the vapour branch loses consistency with the Maxwell as the coexistence density increases into the superheated region of the phase diagram. On the contrary, the liquid branch remains steady throughout the range of simulations. The major cause of this deviation can be attributed to the use of the velocity-shifted method which can cause large fluctuations in the densities. Guo's discrete forcing term was further improved by Li et al. [153] where the velocity is modified hence there are no longer unwanted additional terms in the macroscopic equations. The MPI scheme incorporates the modified Guo forcing into the model, which can explain why it matches so well with the Maxwell construction. Again, the EDM scheme used is based on suggestions by Kupershtokh et al. [156], where the interaction is modified to decrease thermodynamic consistency, thus it provides excellent agreement with the Maxwell.

To improve on thermodynamic consistency, the introduction of MRT allows for minor adjustment of the forcing, where an additional parameter σ can be adjusted.

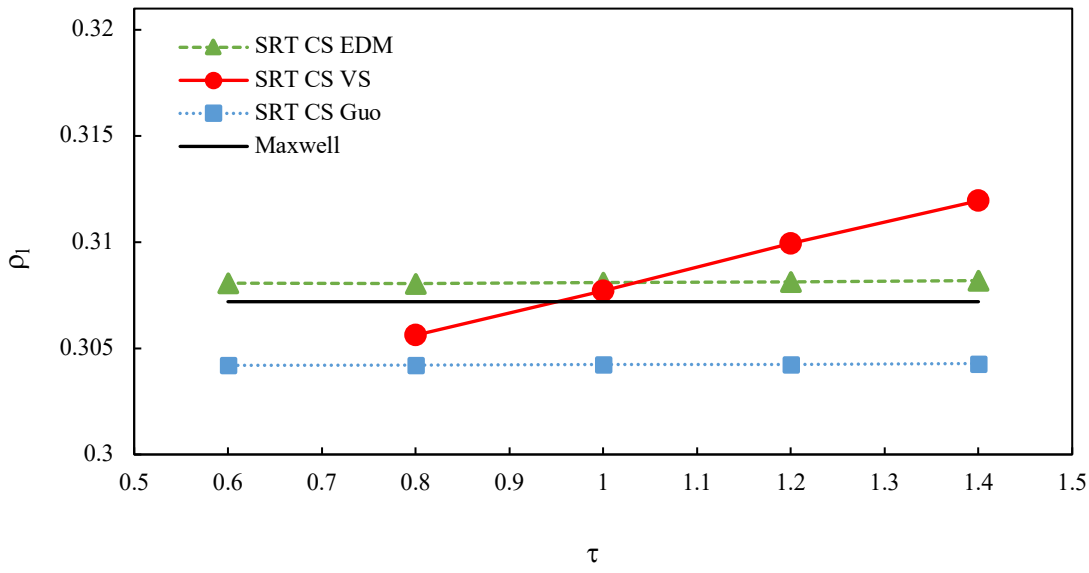

Figure 3-2. Density dependence on relaxation-time

Moreover, there has been much detailed on the dependence of density on the non-dimensional relaxation time in the original SC model. The velocity-shifted (VS) method intrinsically links them both together, hence adjustment of one leads to the modification of the other. To help demonstrate this effect the liquid branch will be investigated using three common forcing techniques, namely VS, EDM and Guo. Numerical simulations were carried out on a domain N_x x N_y = 200 x 200 lu with droplet of radius, R = 40 centred at (x,y) = (N_x/2, N_y/2), periodic boundary conditions on all four directions and a reduced temperature T_R = 0.8.

It is clear from Figure 3-2 that only the VS method alters the density when the relaxation is adjusted. The other two methods maintain an almost unchanged density over the range of relaxations investigated.

Before continuing with the analysis, it is worthy of noting the convergence criteria which has been used in the tests. Dependent on the aspect being considered (density, spurious velocities, etc), the criteria for evaluation will follow a similar approach. To evaluate the convergence of the liquid density during the simulation, the maximum is obtained at each timestep and compared to the previous, to determine the fluctuation with time, represented by

$$max\ |\rho^{n+1} - \rho^{n}| \leq \varsigma \qquad 3\text{–}14$$

where n and $n+1$ represent the parameter value at the previous and new timesteps, respectively. The value of ς determines the acceptable convergence criteria, set to 10^{-6} in this study to provide adequate convergence without incurring additional computational overhead. This strategy has been adopted for all static testing, with a steady state or equilibrium state denoted once this criteria has been fulfilled.

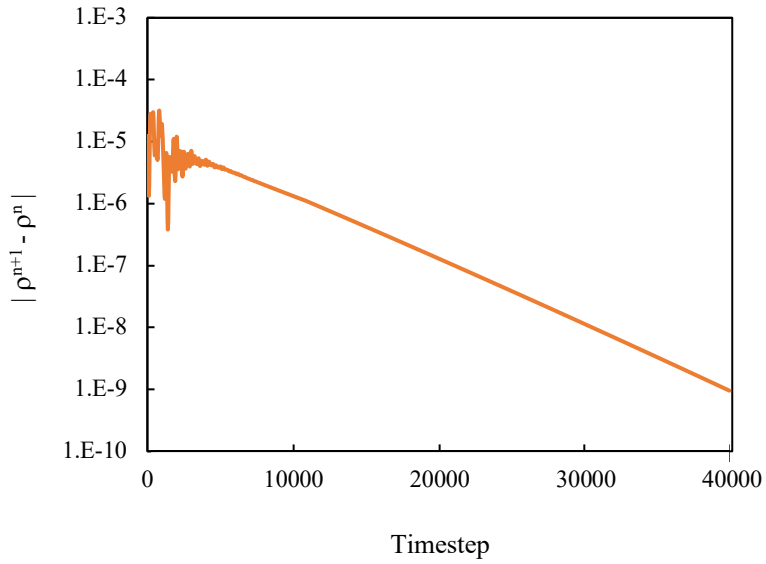

Figure 3-3. Convergence of liquid density during thermodynamic consistency test

An example of convergence has been provided for illustration, shown in Figure 3-3. Within approximately 10000 timesteps the criteria has been met, with the fluctuations in density being less than 10^{-6}. In the remaining tests, once the criteria is met the simulation is terminated however, for illustrative purposes, the full runtime has been included.

3.2.2 Spurious velocities and model stability

Finally, to ensure suitable stability in pseudopotential models it is essential to reduce numerical artifacts emerging from the forcing between phases. Spurious velocities at the liquid-vapour interface can have a dramatic effect on the stability of simulations. High spurious velocities can introduce areas of numerical uncertainty in the domain. To examine how implementation of EOS strategy in the pseudopotential model, three techniques are scrutinised, namely Piecewise, MPI and YS. To ensure fairness in the cross examination, densities and interface thickness is maintained constant throughout the tests. Numerical simulations were carried out on a domain similar to Section 3.2.1 with a free droplet, however the reduced temperature is set as $T_R = 0.5$.

Briefly, the piecewise linear EOS method is introduced [164]. To compensate for numerical errors caused by the discretisation in phase space, the spinodal region is self-tuning during computation, resulting in a dynamically optimised EOS. The piecewise linear EOS is defined as [164],

$$p(\rho) = \begin{cases} \rho\theta_v & \text{if } \rho \leq \rho_1 \\ \rho_1\theta_v + (\rho - \rho_1)\theta_M & \text{if } \rho_1 < \rho \leq \rho_2 \\ \rho_1\theta_v + (\rho_2 - \rho_1)\theta_M + (\rho - \rho_2)\theta_L & \text{if } \rho > \rho_2 \end{cases} \qquad 3\text{–}15$$

Similar to other EOS's, the piecewise linear EOS is inserted into Eq. 3–9 via the p_{EOS} term in the YS method. A set of five free parameters ($\theta_v, \theta_M, \theta_L, \rho_1$ and ρ_2) exclusively determine the EOS, where θ_v is the slope of pressure of the vapour branch, θ_L is the slope of pressure of the liquid branch and θ_M is the slope of pressure of the unstable region [164]. Once these variables have been chosen then the spinodal points (ρ_1 and ρ_2) can be acquired by solving two sets of equations, one for determining the mechanical equilibrium and another for chemical equilibrium [164],

$$\int_{\rho_V}^{\rho_L} dp = (\rho_1 - \rho_v)\theta_v + (\rho_2 - \rho_1)\theta_M + (\rho_L - \rho_2)\theta_L = 0 \qquad 3\text{–}16$$

$$\int_{\rho_V}^{\rho_L} \frac{1}{\rho} dp = \log(\rho_1/\rho_v)\theta_v + \log(\rho_2/\rho_1)\theta_M + \log(\rho_L/\rho_2)\theta_L = 0 \qquad 3\text{–}17$$

Looking firstly at the trend of both sets of data, the largest magnitude of spurious velocity occurs at the lowest relaxation-time, which is to be expected. As τ approaches 0.5 the stability is vastly impacted as the viscosity of the fluid is reduced.

Focusing on Figure 3-4 (a), it is interesting to see that there appears to be an optimum relaxation-time, for each methodology, which results in a minimum spurious velocity. This is generally in the range of τ = 0.7-0.75 for all implementations studied. For the whole domain, it appears as the piecewise EOS generates slightly higher spurious velocities over the range of τ, with MPI and then YS methods performing more favourably. However, at low relaxations, i.e., >0.6, all methods demonstrate similar spurious velocity outcomes.

Looking at Figure 3-4 (b) a different trend is observed, with the lowest velocities inside the drop being observed when the relaxation-time is equal to 1. Also, in the liquid region there is a larger difference between the sets of data being examined. It is clearly shown that the YS method generates the largest currents inside the drop, approximately 1.7 times and 4 times larger than MPI and Piecewise, respectively, over the range of τ.

3.3 Investigation of Fluid-Solid Interactions

When a solid wall is encountered, an adhesive force between the fluid and solid should be considered. Incorporating wetting behaviour into pseudopotential models can be achieved in a few different ways. In the literature, the most common techniques proposed to mimic the adhesive force in the pseudopotential method are; density-based interactions [165,166] and pseudopotential-based interactions [167,168].

The density-based method, proposed by Martys and Chen [165], takes the following form,

$$F_{ads} = -G_w \rho(x) \sum_i w_i s(x + c_i) c_i \qquad 3\text{–}18$$

where G_w controls the strength of the adhesion and $s(x + c_i)$ is a switch function, with s = 1 at the solid boundary and s = 0 in the fluid phase. In addition, Kang et al. [166] proposed a density-based interaction model based on the assumption of a constant number density (n_w) at the wall, where $n_w(x + c_i)$ is equal to zero elsewhere.

$$F_{ads} = -G_w n(x) \sum_i n_w(x + c_i) c_i \qquad 3\text{–}19$$

It was pointed out in [169] that $n_w(x + c_i) = n_w s(x + c_i)$ hence the two methods provide a similar fluid-solid interaction.

The major difference between the former and the pseudopotential-based models is the introduction of the pseudopotential as the presum factor instead of the density. Sukop and Thorne [167] reformulated the work by Raiskinmäki et al. [168] to give,

$$F_{ads} = -G_w \psi(x) \sum_i w_i s(x + c_i) c_i \qquad 3\text{–}20$$

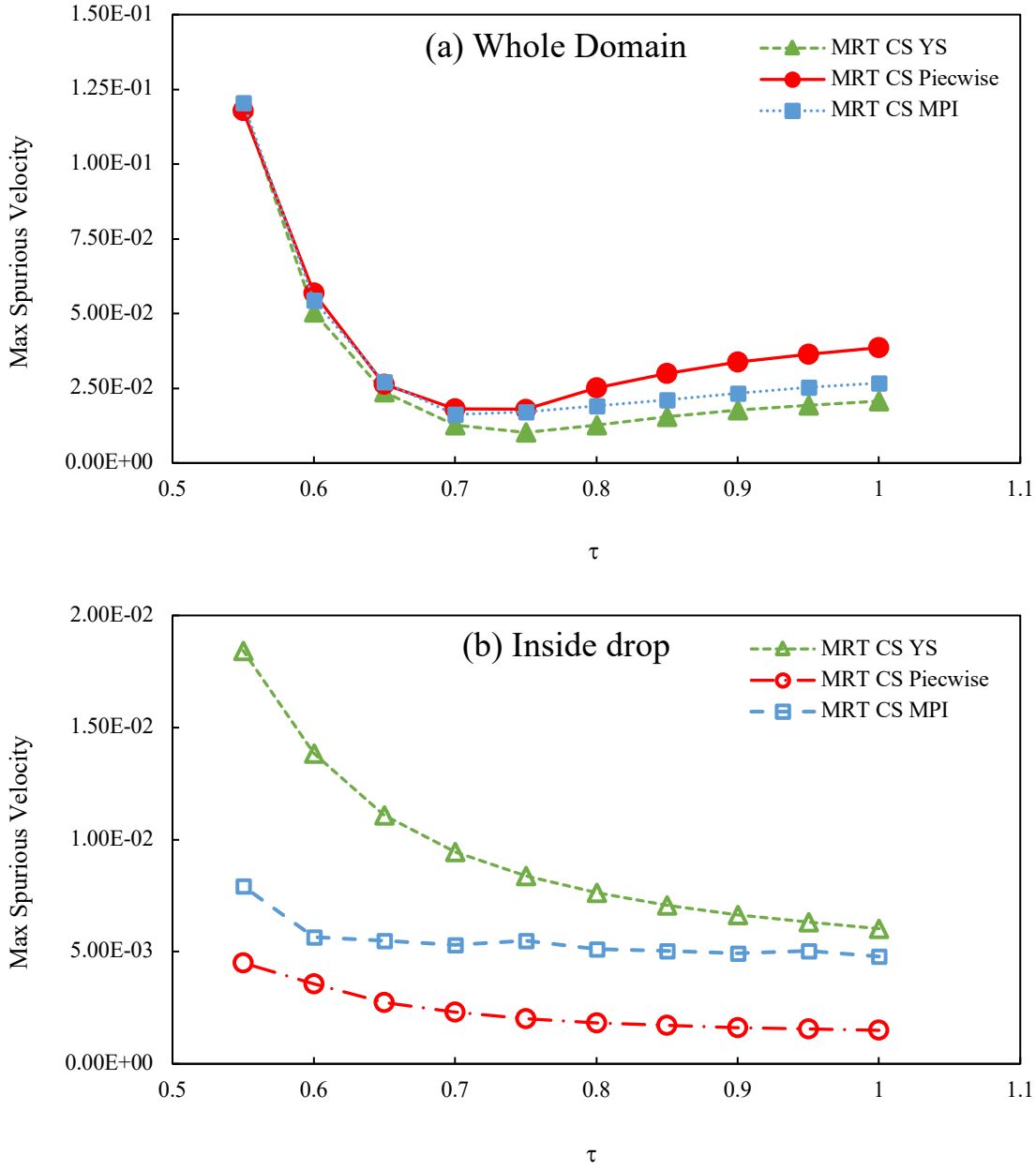

Figure 3-4. Maximum spurious velocities as a function of relaxation-time. (a) whole domain, (b) inside droplet

Alternatively, Benzi et al. [170] introduce a parameter $\psi(\rho_w)$ to fix the pseudopotential at the wall, leading to the following

$$F_{ads} = -G\psi(x)\sum_i w_i\psi(\rho_w)s(x+c_i)c_i \qquad 3\text{–}21$$

The density constraint at the solid nodes (ρ_w) can be adjusted to vary the wettability, whereas in Eq. 3–20, G_w controls the adhesion. Again, it was made clear in [169] that

these two methods provide a similar outcome since ρ_w is a constant hence it can be absorbed into G. Additionally, Li et al. [169] suggested a modification to the pseudopotential-based interaction,

$$F_{ads} = -G_w \psi(x) \sum_i w_i S(x + c_i) c_i \qquad 3\text{–}22$$

where $S(x + c_i) = \phi(x) s(x + c_i)$. Unlike in Eq. 3–21, the choice of $\phi(x)$ is not static at the solid boundary, hence when $\phi(x) = \psi(x)$ the solid-fluid interactions appear to mimic the fluid-fluid interactions in the bulk fluid.

More recently, the geometric formulation [171] of wetting boundary has been adopted into pseudopotential models [172,173]. Unlike an adhesive force from solid-fluid interactions, the geometric formulation is based on the geometric properties of the model, allowing for desired contact angles to be inputted resulting in the desired wettability conditions. The density-based geometric formulation, in two-dimensional space, is given as [171],

$$\rho_{i,0} = \rho_{i,2} + \tan\left(\frac{\pi}{2} - \theta\right) \left|\rho_{i+1,1} - \rho_{i-1,1}\right| \qquad 3\text{–}23$$

where $\rho_{i,0}$ represents a layer of ghost cells adjacent to the solid boundary and θ is the prescribed static contact angle. The first and second subscripts denote coordinates along and normal to the solid wall.

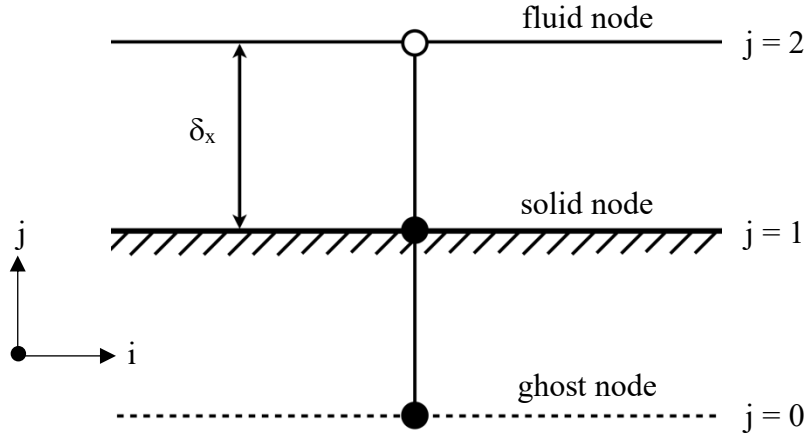

Figure 3-5. 2D schematic of geometric formulation

The scheme requires a layer of ghost nodes adjacent to the solid boundary in order to calculate the value of density. Figure 3-5 provides a simplistic schematic of the system, providing details of the coordinate system and layout of each node (fluid, solid or ghost). The fluid layers are located at j = 2 and the solid boundary at j = 1, with the ghost layer located at the bottom of the domain j = 0. Unlike the fluid-solid methods detailed previously, the only requirement for this scheme is the definition of desired contact angle, hence no additional forcing is implemented. Calculation of the density in the ghost, solid and adjacent fluid nodes is added to the rest the of the computational domain, resulting in a more accurate wettability condition.

It has been noted in the literature [174,175] that density-based fluid-solid interactions can lead to unphysical mass transfer along the wall boundary, especially at contact angles close to 0º and 180º.

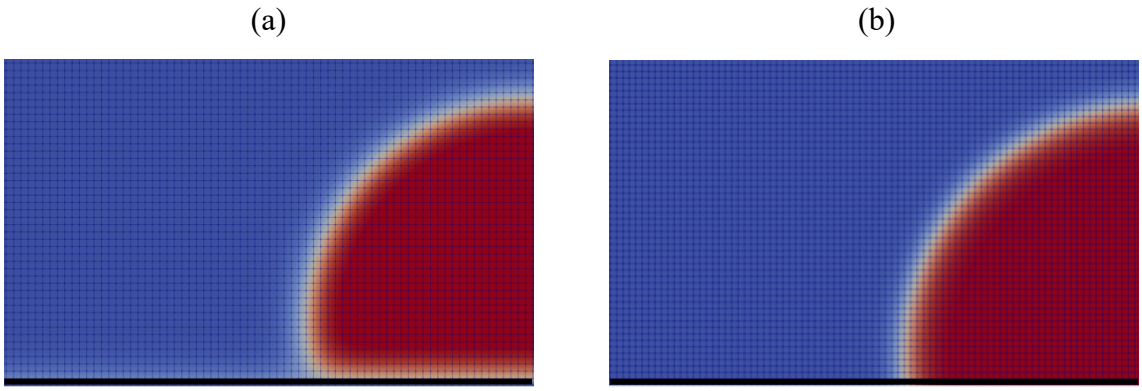

Figure 3-6. Comparison of wetting boundary conditions (a) density-based interaction (b) geomtric formulation

As shown in Figure 3-6, the density-based interaction scheme leads to some unphysical mass transfer near the solid boundary (solid boundary shown as black area at bottom of domain). In contrast, when the geometric formulation is employed, no such anomaly is observed. Looking closer at the density profiles through the centre of the domain for each wetting condition (Figure 3-7), it is evident that there is unphysical mass transfer at the wall. For the density-based scheme, within approximately 6 lattices of the solid boundary, the density deviates drastically.

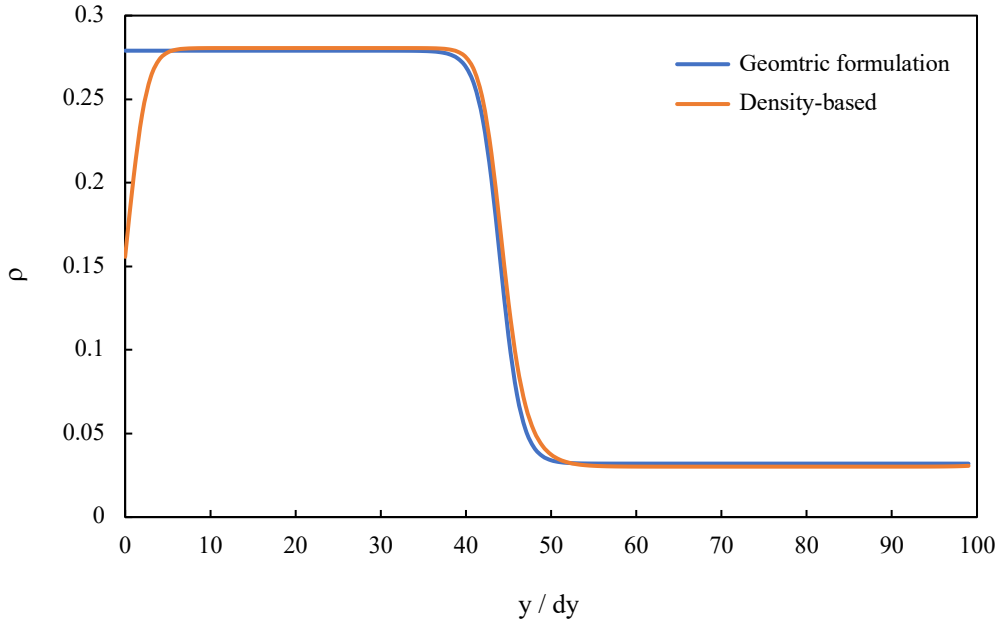

Figure 3-7. Comparison of density profiles, through centre of domain in vertical direction, for different wetting boundary conditions. Reduced temperature of $T_R = 0.8$.

As for the geometric formulation, the density profile is exact regardless of the wall. Khajepor et al. [176] also researched the influence of wall boundary conditions on domain characteristics. They report that the pseudopotential-based interaction, coupled with standard bounce-back, results in the largest density fluctuation near the solid wall, as compared to the other schemes investigated.

There are two main techniques of calculating the contact angle of a liquid on a solid boundary; the first involves utilising the geometry of the droplet whilst the other focuses on the interface region to distinguish between phases. The first method, often referred to as the spherical cap method, calculates the apparent contact angle θ from the base L and height H of the droplet. If the radius is found from $R = (4H^2 + L^2)/8H$ then the contact angle can be estimated by $\tan\theta = L/2(R - H)$. This method is quick and convenient since determining the base and height is relatively straightforward, hence this method is conventionally used in benchmark tests where gravity is neglected.

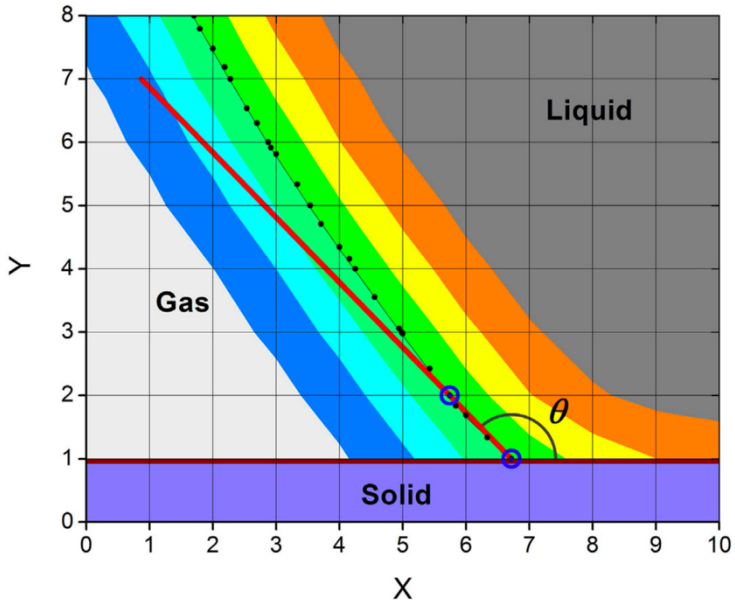

Figure 3-8. Illustration of the measurement of contact angle on mesoscopic scale. Black spots are the intersections of droplet surface and gas-liquid links. Blue circles indicate first and second points, and the red line represents the tangential line of the droplet at the triple-phase contact point [177]

Alternatively, employing the location of the triple-phase contact point can allow for a local contact angle to be measured irrespective of droplet deformation due to external forcing. As shown in Figure 3-8, it is necessary to capture points inside the interface, between liquid and gas, to establish a tangential line which connects the region to the triple-point on the surface. Firstly, a point on the surface is found to represent the triple-phase contact point (y = 1) then a set of discrete points are employed to allow for the angle to be calculated. From [177], the most accurate estimation of contact angle is found when the second point is set at (y = 2) or one lattice above the solid boundary. To establish the precise location of the points, a linear interpolation formula is employed [177],

$$x = x_g + \frac{\rho_{av} - \rho(x_g)}{\rho(x_l) - \rho(x_g)} d \qquad 3\text{–}24$$

where x_l and x_g are the liquid and gas nodes in the interface region, ρ_{av} is the average of the liquid and gas density, and d represents the direction from gas to liquid. This scheme provides a more flexible approach to contact angle measurement since it is not dictated only from basic droplet geometry, allowing for asymmetry to be captured in the presence

of external forcing. Owing to its flexibility, the method will be employed in this study to ensure irregularity can be observed.

Adopting the geometric formulation, the measured contact angles in the domain agree well with the analytical solution, seen in Figure 3-9. Departure can be witnessed at contact angles above approximately 120º, however over the range of angles studied the deviation is within 2%. A further validation of the schemes ability to correctly implement static contact angles is through scrutinising the equilibrium shape of the drop. In the absence of gravity, Dupont and Legendre [178] demonstrate that by conservation of volume, it is possible to geometrically calculate the equilibrium quantities of the droplet; radius R, spreading length L and height e, through,

$$R = R_0\sqrt{\frac{\pi}{2(\theta_s - \sin\theta_s\cos\theta_s)}}, \quad L = 2R\sin\theta_s\,, \quad e = R(1-\cos\theta_s) \qquad 3\text{–}25$$

with R_0 representing the initial droplet radius. Figure 3-10 reports the numerical values for dimensionless wet length (L/R_0) and height (e/R_0) against the static contact angle θ_s. The values correspond well to the analytical solution for the range of angles investigated. This is comparable with the findings in [178] where contact angles between 30º and 120º follow the analytical trend, whereas above or below sees a departure.

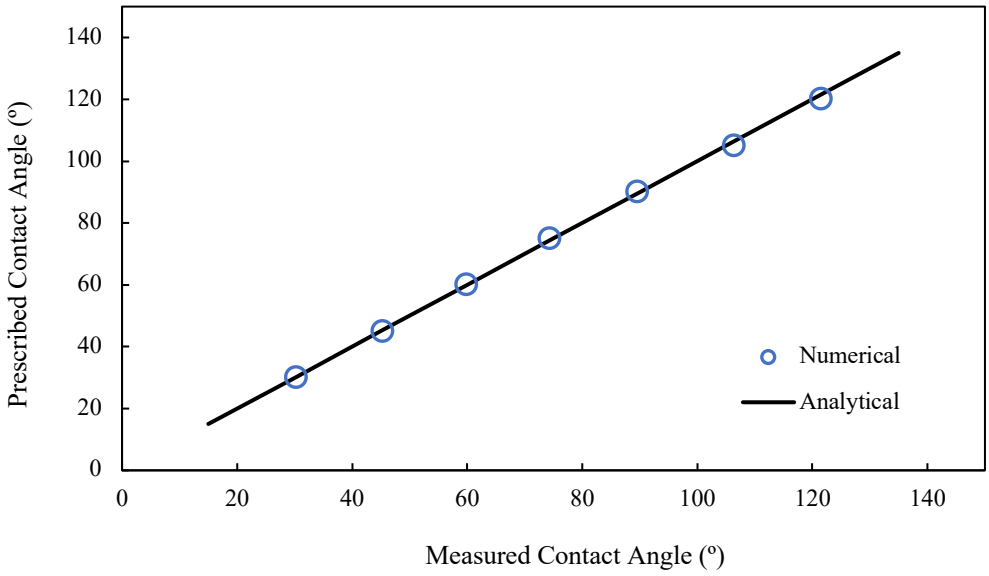

Figure 3-9. Measured contact angles for geometric formulation at high density ratio (T_R = 0.5)

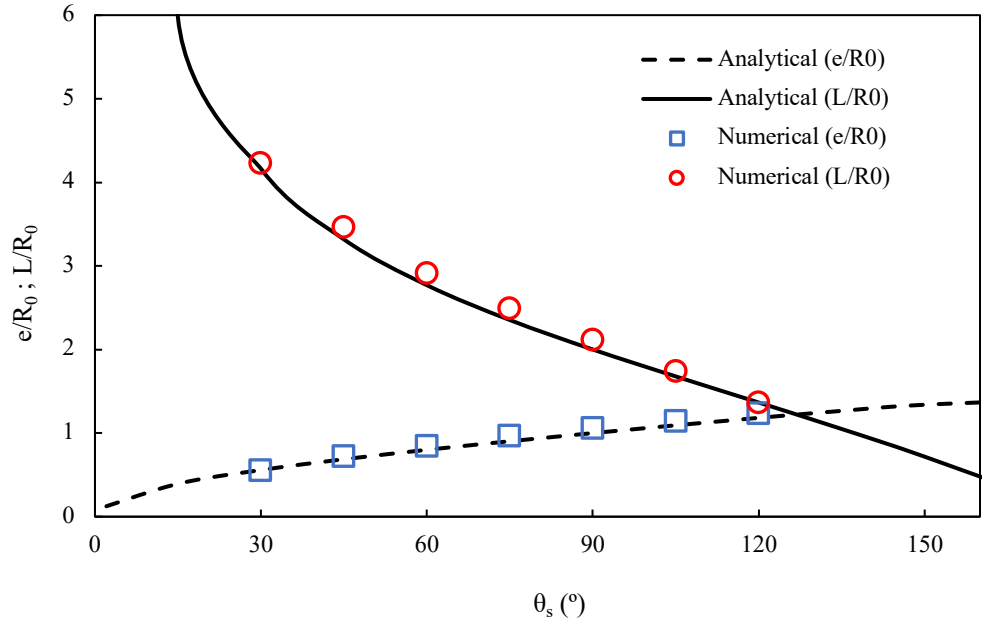

Figure 3-10. Dimensionless wet length L/R_0 and height e/R_0 of a droplet at equilibrium as a function of static contact angle θ_s

Additionally, the magnitude of spurious velocities is investigated to see if the surface wettability plays a key role. As can be seen in Figure 3-11 (a), there appears to be no tangible effect of contact angle on spurious velocities in the whole domain. For all methodologies examined there is no distinct change in the size of spurious velocities when

the surface wetness is altered. Likewise, when looking at the maximum spurious velocities inside the droplet (Figure 3-11 (b)), there is not a substantial change across the range of contact angles investigated.

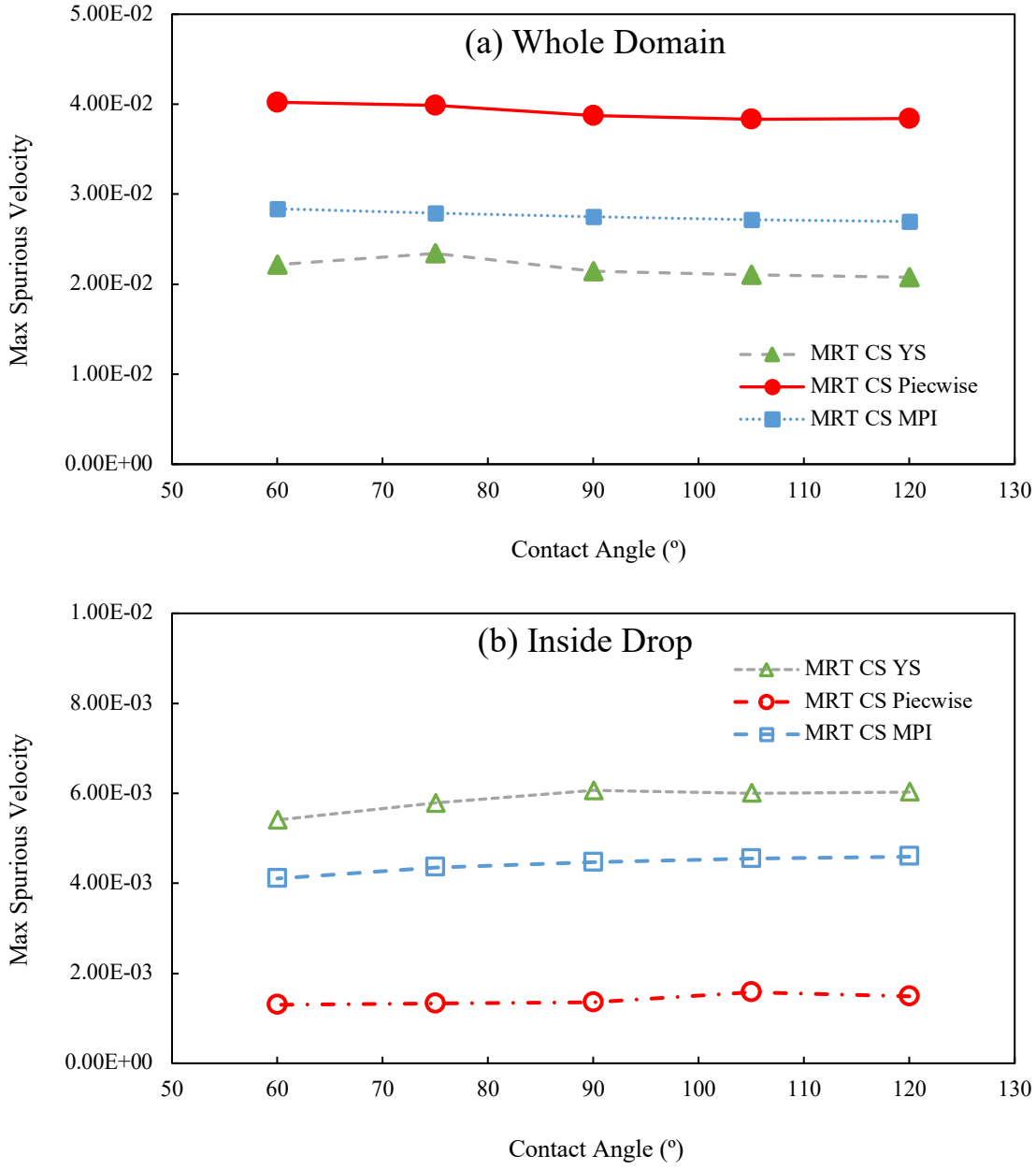

Figure 3-11. Maximum spurious velocities as a function of contact angle; (a) whole domain (b) inside droplet

Finally, the size of the droplet radius is scrutinised to determine its effect on the magnitude of spurious velocities in the whole domain as well as inside the droplet. The droplet radius is increased from 30 to 45 whilst keeping the domain size constant. Again, as can be seen in Figure 3-12 there is no significant effect from altering the radius of the

drop, with the magnitude of spurious velocities remaining fairly constant over the range of cases.

From these findings it can be concluded that surface wettability and size of droplet radius do not play an important role in the generation of spurious velocities, when the geometric formulation method is adopted.

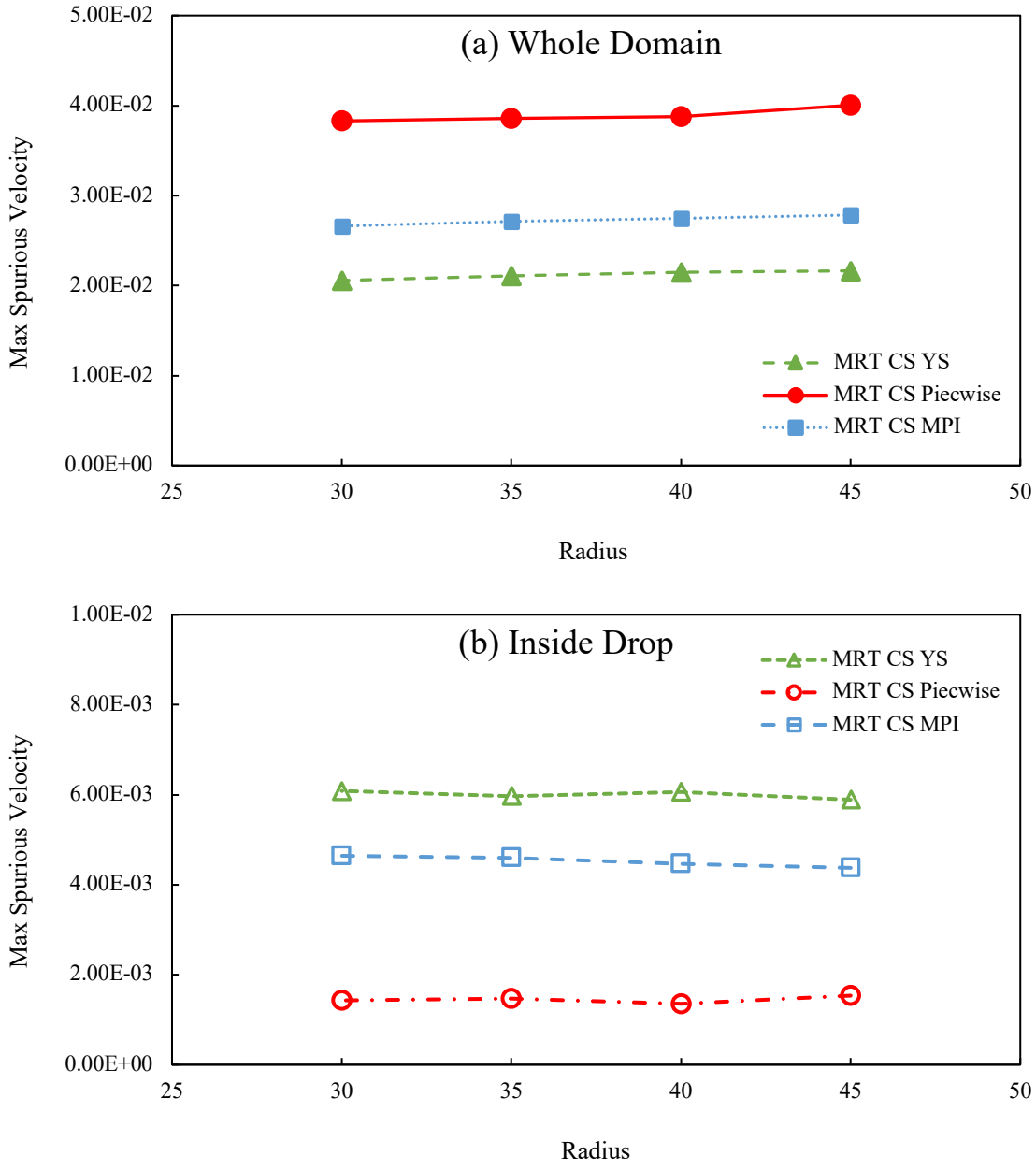

Figure 3-12. Maximum spurious velocities as a function of drop radius; (a) whole domain (b) inside droplet

3.4 Droplet on an Inclined Slope

Droplet adhesion and motion on inclined solid walls is another interesting area which has many applications in engineering. Droplets can be intentionally or unintentionally restricted from moving along sloping surfaces as a result of the type of coating added to the solid wall. It has been demonstrated that by increasing the hysteresis window, the droplet can be pinned in place, in the presence of external forces such as gravity.

Wang et al. [179] investigated the effects of ideal and non-ideal walls on droplet slipping under gravity. They conclude that for an ideal wall, the droplet will slip along the surface however when a hysteresis window is introduced, the droplet will deform and remain in place. Contact angle hysteresis (CAH) is defined as the difference between advancing and receding contact angles [180], with $CAH\ (\Delta\theta) = \theta_A - \theta_R$. A force balance between the gravitational component tangential to the wall and the surface tension allows the droplet to stick to the surface [179], as presented in Figure 3-13. When the gravitational force exceeds the surface tension, the droplet will begin to slip. To overcome this, a larger hysteresis window can be implemented, by increasing θ_A or decreasing θ_R.

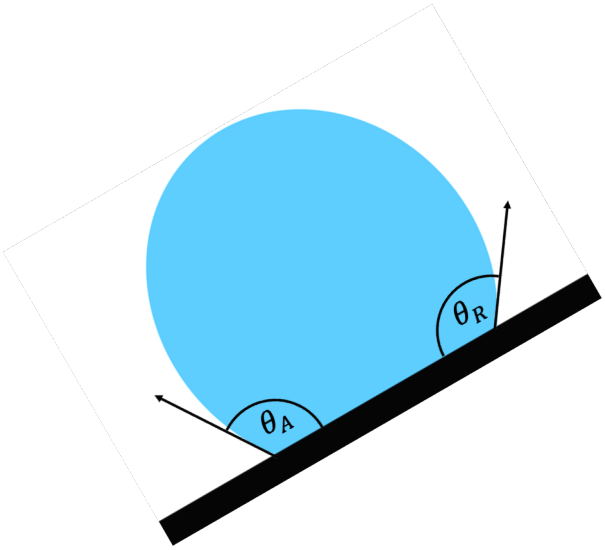

Figure 3-13. Sketch of droplet on an inclined slope, illuminating advancing and receding contact angles

Implementation of CAH in the model is relatively straightforward. When the contact angle θ is within a hysteresis window, it is defined as,

$$\theta_R \leq \theta \leq \theta_A \qquad 3\text{–}26$$

To realise the hysteresis effect, at each timestep the local contact angle is obtained and compared to the receding and advancing angles. The computational procedure is as follows [171]:

- If $\theta \leq \theta_R$ the contact angle in Eq. 3–23 is replaced with θ_R
- If $\theta \geq \theta_A$ the contact angle in Eq. 3–23 is replaced with θ_A
- Else θ in Eq. 3–23 is unchanged

In the SC fluid-solid forcing methods mentioned previously, there is no immediate way of implementing a hysteresis window into the model since it only relies on the interaction strength to control the wettability of the solid. Some may see this as an advantage since the contact angles do not have be known a priori to the start of the simulation, hence the droplet shape is a consequence of only the surface tension against external forces. Conversely, the geometric formulation provides limitations on size of the hysteresis window but does not restrict a moving contact line. This can allow simulated droplets to be pinned to a slope in the presence of a gravitational force, based on experimental data to set the appropriate CAH.

To test the opposing approaches, the density-based method and the geometric formulation will be examined for a droplet on a 90º inclined slope in the presence of a gravitational force. All tests were carried out using the MRT CS YS method, described previously, on a domain N_x x N_y = 100 x 300 lu with a droplet of radius R = 40 centred at (x,y) = (5, N_y/2). Periodic boundary conditions were applied in the y direction whilst the side walls are treated as solid boundaries with no-slip condition.

Initially, the contact angle is set to ~100º and the droplet is allowed to reach equilibrium before the gravitational force is applied. The gravity force is added to the model through [96],

$$F_g = g(\rho - \rho_g) \qquad 3\text{–}27$$

where g is the gravitational acceleration and ρ_g is the density of the gas. Similar to [179], the Eotvos number, defined as $Eo = \frac{\rho_l g R^2}{\sigma}$, is used to characterise the magnitude of gravity in the simulations. In all cases $Eo = 0.5$, with a hysteresis window of $(\theta_R, \theta_A) = (60,120)$ implemented for the geometric formulation.

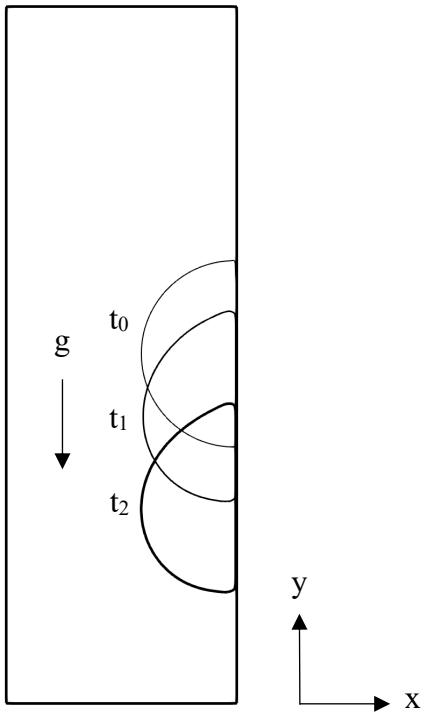

Figure 3-14. Numerical droplet behaviour on an ideal wall for Eo = 0.5. Droplet movement over time is depicted, with the black outline representing the latter timestep.

As can be seen in Figure 3-14, when an ideal wall is assumed, the droplet is unable to remain in place as the gravity force overcomes the surface tension between the fluid and the solid. Once the droplet starts to move downwards (t_1) it is unable to counteract which results in the droplet slipping further down the surface (t_2). In an attempt to remedy this, an artificial friction force is proposed and added to the bottom of the droplet to counteract the gravitational force, helping to fix the droplet in place on the inclined wall.

The basic premise behind the scheme is to specify a reference point x_{ref}, here the right contact point is defined at the interface between the droplet and the solid surface, to monitor throughout the simulation. As the point deviates from the reference point, a force is applied to correct the abnormality, either positive or negative, depending on the direction of the drop. The formulation takes the form,

$$F_f = -a\left(x_{ref} - i\right) \begin{cases} if\ F_f > F_{f,max} \rightarrow F_f = F_{f,max} \\ if\ F_f < -F_{f,max} \rightarrow F_f = -F_{f,max} \end{cases} \quad 3\text{–}28$$

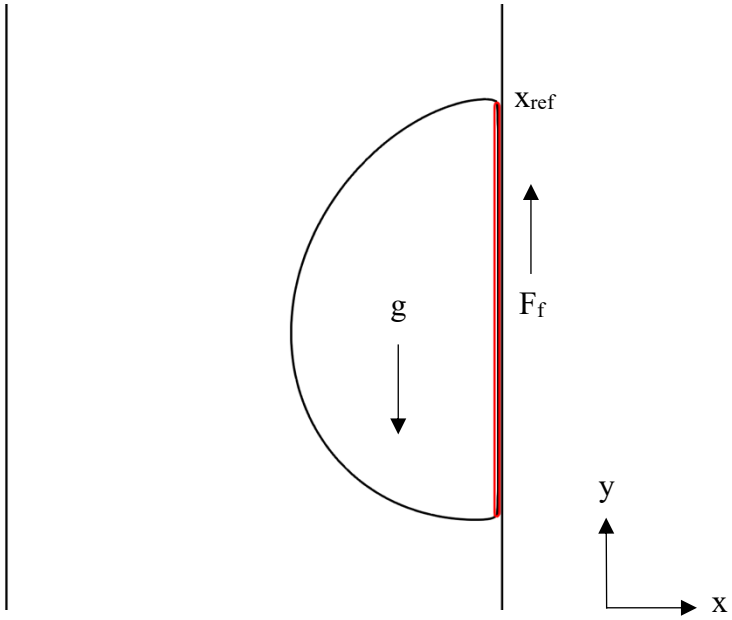

Figure 3-15. Illustration of artificial friction force acting on droplet on inclined slope. Red zone shows area where artificial friction force is implemented.

where a is an arbitrary constant and $F_{f,max}$ is a maximum allowable force. By imposing the above relation, the contact point fluctuates around the reference point until it once again reaches a steady state. The force only acts on the fluid nodes inside the droplet which are adjacent to the solid boundary, ensuring the forcing is only functional at the interface, as shown in Figure 3-15.

Although the two opposing techniques result in the droplet being pinned on the inclined surface, the deformation due to gravity is vastly different. In the artificial friction forcing case there is minimal deformation from the equilibrium shape, with a slight elongation in the direction of the gravity force (Figure 3-16 (a)). Comparing the shape to the geometric formulation (Figure 3-16 (b)), the droplet is much more deformed in the downward direction, as the advancing and receding angles adjust to prevent any slippage.

Looking more closely at the evolution of the front (θ_A) and rear (θ_R) contact angles for both cases, again there are vast differences. From Figure 3-17, it is clear that for the geometric formulation the contact angles evolve towards their respective limits, i.e., the hysteresis window, to counteract the gravitational force. After approximately 2500 timesteps, the advancing angle has reached its limit whilst the receding eventually reaches an equilibrium value of slightly higher than its minimum at around 4000 timesteps. In contrast, the contact angles for the artificial friction force, implemented into the fluid-solid interaction, do not vary much from the static contact angle. Since the hysteresis

window is not responsible for ensuring droplet pinning, the contact angles are not required to dynamically adjust, hence the minor departure from static angle is purely a consequence of the fluid momentum inside the droplet due to gravity and the newly defined friction force. Similarly, an equilibrium state is reached after approximately 4000 timesteps where both contact angles remain almost constant.

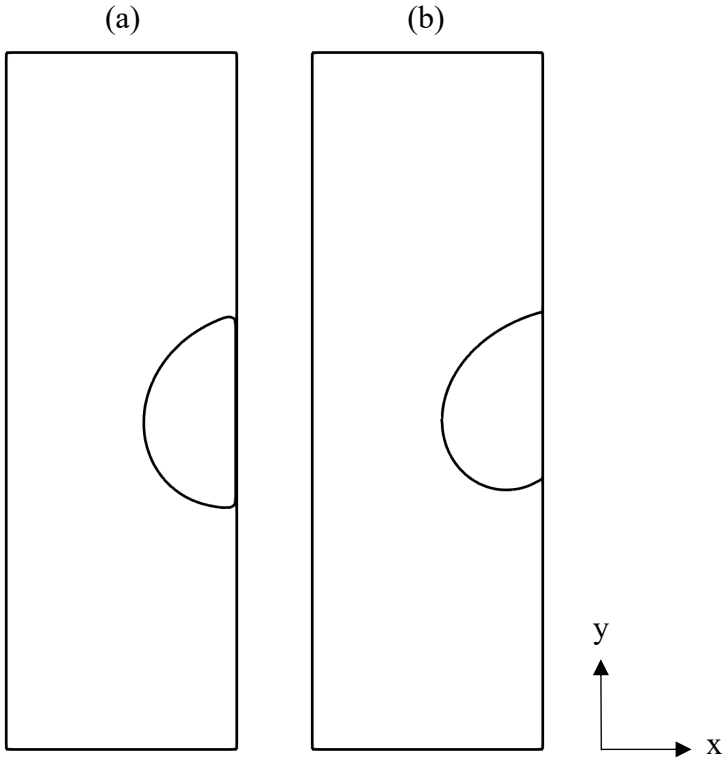

Figure 3-16. Droplet behaviour on non-ideal wall for Eo = 0.5; (a) droplet pinned due to artificial friction force (b) droplet deforms and remains stationary due to hysteresis $(\theta_R,\theta_A) = (60,120)$

While the artificial friction force can achieve droplet pinning behaviour, the large discrepancy between deformation and contact angles to those witnessed in nature remedy it unsuitable to simulations which involve a direct comparison to experimental or physical data. If the only objective of the model is to immobilise a droplet on an inclined slope, then this could be a potential alternative approach, however for the purposes of this study, droplet deformation and CAH can play an important role in the transport of the droplet across the solid surface, especially when excited by an external source such as a SAW.

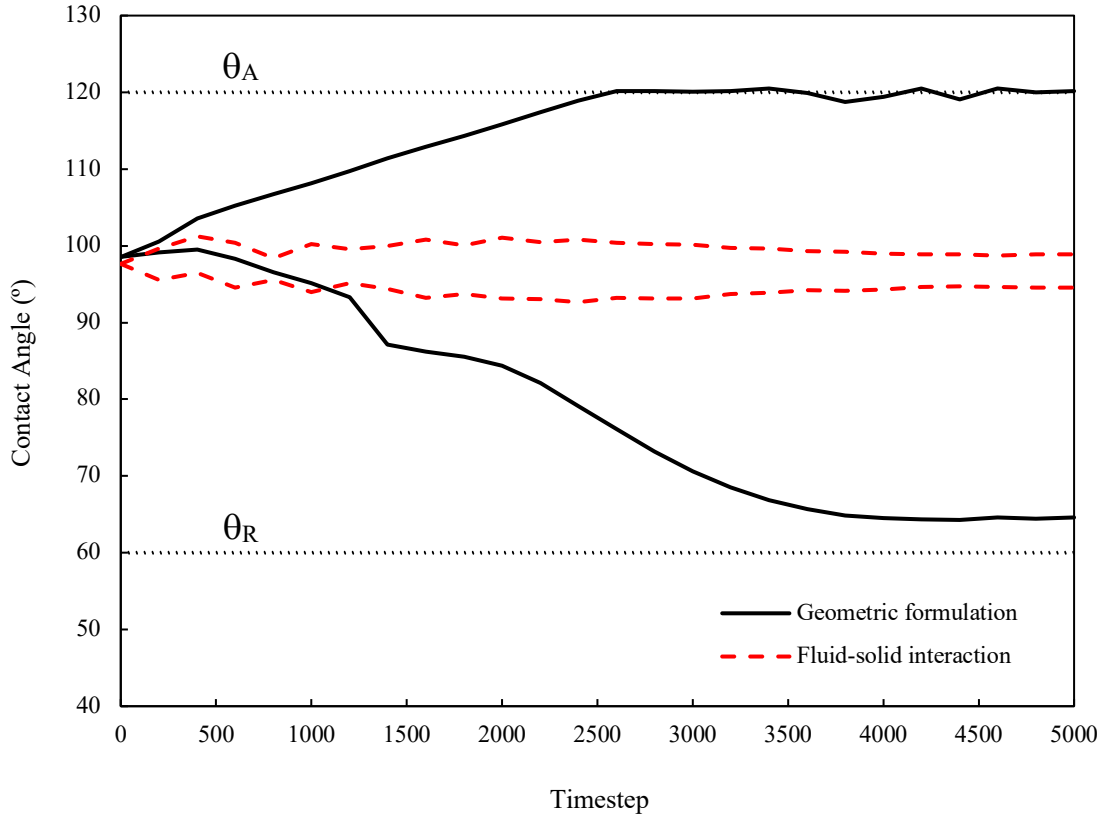

Figure 3-17. Comparison of advancing and receding contact angles over time for geometric formulation and fluid-solid interaction with artificial friction force. Eo = 0.5 and $(\theta_R,\theta_A) = (60,120)$

3.5 Summary

In this chapter the pseudopotential method has been briefly investigated to determine the most suitable approaches for investigation of SAW-droplet interactions. Initially, several methods were studied to reveal their ability to capture thermodynamic consistency, especially at high density ratios. It was revealed that most models, except SRT YS, were consistent with the Maxwell construction for the majority of the range of reduced temperatures examined, hence all are suitable. Additionally, the dependence of density on non-dimensional relaxation-time was considered for SRT models. Only the VS method exhibits dependence whereas the Guo and EDM methods are independent. MRT models have intrinsic independence of relaxation parameters and density.

Moreover, the stability of various EOS implementation techniques was examined to determine their disparities with respect to spurious velocities both inside and outside of a free droplet. The overall stability of pseudopotential models is inescapably linked to the magnitude of spurious velocities in the model. Large parasitic currents at the

liquid/vapour interfaces pose a potential problem for dynamic simulations involving high density ratios. It is therefore one of the most important aspects of the model to inspect. Of the three techniques tested, the YS method performed the best for spurious velocities in the whole computational domain. Interestingly, at low relaxation-time all methods converge around a similar value. However, when only the inside of the droplet is considered, the piecewise linear method exhibits the lowest spurious velocities.

Additionally, the implementation of solid wettability into the pseudopotential model was investigated. Considering the fluid-solid interactions, the density-based method was demonstrated to have undesirable mass transfer near the solid boundary, with large density fluctuations. In comparison, the geometric formulation maintains an exact density profile even near to the solid boundary, demonstrating superior compliance. Moreover, the measured static contact angle is compared to the prescribed angle, with only a deviation of 2% observed over the range of angle tested. Further, agreement with analytical solutions for dimensionless wet length and height reveal the geometric formulation to be an excellent candidate for solid wettability implementation. Finally, the effect of contact angle and droplet size on spurious velocities was investigated for several EOS implementations. The outcome suggests that contact angle and droplet size do not play an important role in creation of spurious velocities, with little deviation being witnessed over the ranges tested.

Lastly, droplet pinning on an inclined slope, due to gravity, was considered. When the fluid-solid interaction scheme is employed, an ideal solid boundary is assumed hence when a droplet is subject to external gravitational forcing, it will slide and continue to do so for the duration of the computation. However, as indicated in the literature, when a non-ideal surface is implemented, the droplet can be pinned in place similar to what is witnessed in nature. This pinning is attributed to the contact angle hysteresis window, the size of which can dictate the magnitude and tilt angle of the slope allowable for the droplet to remain stationary. In opposition to the CAH method, an artificial friction forcing has been presented which can be easily integrated into the fluid-solid interaction scheme to counteract against the gravitational force, rendering the droplet static. The two techniques were scrutinised and the outcomes were quite different. Both methods successfully pinned the droplet on an inclined slope for $Eo = 0.5$ similar to those detailed in the literature, however that is where the similarity ends. For the artificial friction force method, the contact angles (advancing and receding) do not evolve much away from the static contact

angle, whereas for the geometric formulation they tend towards the limits of the CAH window as the simulation advances. The intrinsic nature of the geometric formulation allows the momentum inside the droplet to dynamically alter the contact angles in order to balance against external forces, providing a much more realistic interface deformation, more suited to validation against experimental datasets.

Therefore, considering the above, MRT will be applied in this study due to its enhanced accuracy and compliance with the Maxwell construction. Furthermore, the geometric formulation will be employed to introduce solid boundary wetting conditions as it has been demonstrated to have excellent agreement with all analytical tests completed. Additionally, for cases involving droplets on inclined slopes, the CAH model will be implemented into the geometric formulation due to its dynamically moving contact angles.

Chapter 4 – Development of lattice Boltzmann model for surface acoustic wave interactions in sessile droplets

4.1 Introduction

Based on the discussions of the pseudopotential LB models in the previous chapter, the application of such methodology, in the context of surface acoustic waves, will be explored. The aim of this Chapter is to introduce a novel numerical scheme which can be used in the research and innovation of SAW-droplet devices.

The three-dimensional two-phase lattice Boltzmann model presented in this work is constructed and applied to simulate the kinetic impact from a SAW on a microscale sessile drop. SAW parameters (amplitude and frequency) are investigated and their influences on mixing, pumping, and jetting are analysed. It is the objective of this study, in additional the model development, to provide a comprehensive understanding of the roles that each parameter plays on SAW induced streaming and deformation.

4.2 Surface Acoustic Wave (SAW) droplet interaction and model assumptions

Before moving to the developed model, a brief outline of the physics of SAW-droplet interactions is introduced which will aid in the discussion of the model setup and the results obtained. In general, it can be summarised as, SAW propagates along the substrate in the direction of the liquid droplet. Upon entering the droplet, the acoustic wave is dampened exponentially, causing longitudinal pressure waves to be emitted through the liquid (See Figure 4-1) at a Rayleigh angle , $\theta_R = \sin^{-1}\frac{C_f}{C_R}$, where C_f and C_R are the sound velocity in the liquid and the Rayleigh SAW velocity on the SAW substrate, respectively [181,182]. This initiates complex streaming patterns to emerge which can cause mixing, translation or jetting of the droplet. It is assumed that the dynamics shown in Figure 4-1 are decoupled into the dynamics of SAW transportation in solid and the dynamics of droplet impacts of leaked SAW acting on the liquid droplet. The one-way coupling interaction, from the SAW on the solid surface to the fluids, is modelled by the body force, described by Eq. 2–9. No thermal impacts are considered, and the fluids are considered as incompressible fluids.

Due to the limitations of the experimental setup, these processes can be difficult to thoroughly study empirically, therefore it is necessary that computational methods are developed which can capture the two-phase flow pattern within the droplet, the

deformation, and jetting. Due to the microscopic nature of these flow patterns, it only seems fitting that the chosen numerical model should be also. Consequently, the LB methodology has been specifically chosen for this work. The LBM is a kind of mesoscopic model, lying between macroscopic and microscopic regimes, providing relatively high physical insight without the computational overhead of particle-based models, Molecular Dynamics (MD) for example [183]. Additional benefits of the LBM are its ability to model complex boundary conditions, predict interfacial dynamics, and implement external forces with ease. This could be particularly beneficial in the exploration of SAW-based microfluidics involving curved or complex shaped devices.

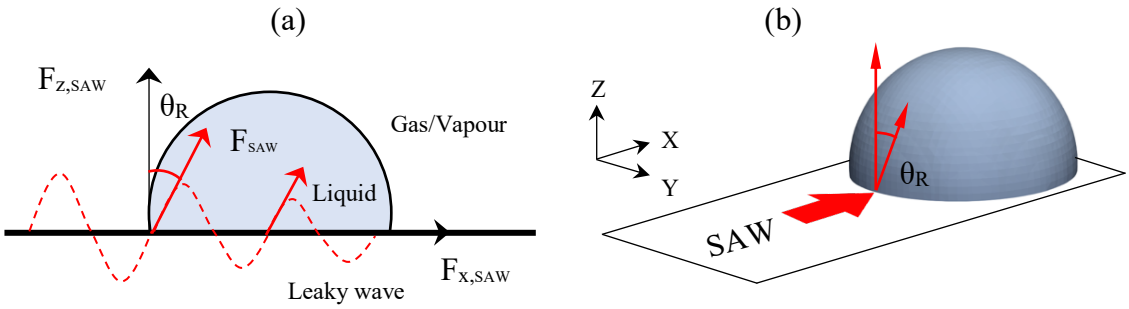

Figure 4-1. (a) 2D illustration of SAW propagation along substrate (b) 3D schematic of wave orientation and propagation

In the following sections, the numerical model will be outlined and validated before SAW interactions are introduced. Numerical results will then be compared with experimental observations, validating the constructed model, and culminating in a study of various LB parameters to determine their impact on droplet shape and motion.

4.3 Model description

Based on the discussion in Section 4.2, the liquid droplet is considered as an incompressible fluid, for which the LBM, derived from incompressible Navies-Stocks equations, can be applied.

4.3.1 Three dimensional multiple-relaxation-time two-phase LB model

In the present study, the multiple-relaxation-time scheme is employed in the pseudopotential lattice Boltzmann framework to simulate multiphase fluid flows. In the

LB community, the evolution equation with MRT collision operator can be written as [115],

$$f_i(\boldsymbol{x}+\boldsymbol{c}_i\delta_t, t+\delta_t) = f_i(\boldsymbol{x},t) - \bar{\mathrm{S}}_{ij}\left(f_j(\boldsymbol{x},t) - f_j^{eq}(\boldsymbol{x},t)\right) + \left(1-\frac{\bar{S}_{ij}}{2}\right)F_i\delta_t \qquad 4\text{–}1$$

where f_i is the density distribution function, $\boldsymbol{x}$ is the spatial position, $\boldsymbol{c}_i$ is the discrete particle velocity along the *i*th direction, δ_t is the time step, F_i is the forcing term in discrete velocity space and $\bar{S}_{ij}$ is the collision matrix, expressed by [184]

$$\overline{\boldsymbol{S}} = \boldsymbol{M}^{-1}\boldsymbol{S}\boldsymbol{M} \qquad 4\text{–}2$$

where $\boldsymbol{M}$ is the orthogonal transformation matrix (given in Appendix A) and $\boldsymbol{S}$ is the relaxation matrix, $\boldsymbol{S} = \mathrm{diag}\left(s_\rho, s_e, s_\varepsilon, s_j, s_q, s_j, s_q, s_j, s_q, s_\nu, s_\nu, s_\nu, s_\nu, s_{xyz}\right)$. For the D3Q15 lattice, the lattice velocities ($\boldsymbol{c}_i$) are given by,

$$[\boldsymbol{c}_0, \boldsymbol{c}_1, \boldsymbol{c}_2, \boldsymbol{c}_3, \boldsymbol{c}_4, \boldsymbol{c}_5, \boldsymbol{c}_6, \boldsymbol{c}_7, \boldsymbol{c}_8, \boldsymbol{c}_9, \boldsymbol{c}_{10}, \boldsymbol{c}_{11}, \boldsymbol{c}_{12}, \boldsymbol{c}_{13}, \boldsymbol{c}_{14}]$$

$$= c\begin{bmatrix} 0 & 1 & -1 & 0 & 0 & 0 & 0 & 1 & -1 & 1 & -1 & 1 & -1 & 1 & -1 \\ 0 & 0 & 0 & 1 & -1 & 0 & 0 & 1 & 1 & -1 & -1 & 1 & 1 & -1 & -1 \\ 0 & 0 & 0 & 0 & 0 & 1 & -1 & 1 & 1 & 1 & 1 & -1 & -1 & -1 & -1 \end{bmatrix} \qquad 4\text{–}3$$

where $c = \delta_x/\delta_t = 1$ is the lattice constant.

The density distribution function f_i and equivalent equilibrium distribution f_i^{eq} can be found through projecting the distributions onto moment space via $\boldsymbol{m} = \boldsymbol{M}\boldsymbol{f}$, where $\boldsymbol{m} = \boldsymbol{m}^{\boldsymbol{eq}}$. Therefore, the right-hand-side of Eq. 4–1 can be re-written as,

$$\boldsymbol{m}^* = \boldsymbol{m} - \boldsymbol{S}(\boldsymbol{m}-\boldsymbol{m}^{eq}) + \delta_t\left(\boldsymbol{I}-\frac{\boldsymbol{S}}{2}\right)\boldsymbol{M}\widetilde{\boldsymbol{F}} \qquad 4\text{–}4$$

where $\boldsymbol{I}$ is the unit tensor, $\boldsymbol{M}\widetilde{\boldsymbol{F}}$ is the forcing term in moment space with $(\boldsymbol{I}-\boldsymbol{S}/2)\boldsymbol{M}\widetilde{\boldsymbol{F}} = \boldsymbol{M}\boldsymbol{F}'$, and the equilibrium moments $\boldsymbol{m}^{eq}$ are given by,

$$\boldsymbol{m}^{eq} = \rho\Big(1, -1 + |\boldsymbol{u}|^2, 1 - 5|\boldsymbol{u}|^2, u_x, -\frac{7}{3}u_x, u_y, -\frac{7}{3}u_y, u_z, -\frac{7}{3}u_z, 2u_x^2 - u_y^2 - u_z^2, u_y^2 - u_z^2, u_x u_y, u_y u_z, u_x u_z, 0\Big)^T \quad 4\text{–}5$$

where u_x, u_y and u_z are the velocity components of the fluid in the x, y, and z directions, respectively. The magnitude of velocity is calculated through $|\boldsymbol{u}|^2 = u_x^2 + u_y^2 + u_z^2$. The streaming process of the MRT LB equation is implemented in velocity space as [184]

$$f_i(\boldsymbol{x} + \boldsymbol{e}_i\delta_t, t + \delta_t) = f_i^*(\boldsymbol{x}, t) \quad 4\text{–}6$$

where $\boldsymbol{f}^* = \boldsymbol{M}^{-1}\boldsymbol{m}^*$. The macroscopic density ρ and velocity $\boldsymbol{u}$ are acquired through,

$$\rho = \sum_i f_i \quad , \quad \rho\boldsymbol{u} = \sum_i \boldsymbol{c}_i f_i + \frac{\delta t}{2}\boldsymbol{F} \quad 4\text{–}7$$

where $\boldsymbol{F}$ is the total force exerted on the system which includes, in this study, the interparticle force $\boldsymbol{F}_{int}$, adhesive force from solid boundaries, which can be treated through boundary conditions, and any external forces, e.g. the SAW force acting to the droplet, $\boldsymbol{F}_{saw}$, with $\boldsymbol{F} = F_{int} + \boldsymbol{F}_{saw} = (F_x, F_y, F_z)$.

4.3.2 Fluid-fluid interactions

In the pseudopotential model [141,149], multiphase flow phenomena is established via an interaction force which aims to mimic molecular interactions. For a single component, the interaction force is given by Eq. 3–2 with the weights $w(|\boldsymbol{c_i}|^2)$, given by $w(1) = 1/3$ and $w(2) = 1/24$ with $N = 14$ for nearest-neighbour interactions on a D3Q15 lattice. The thermodynamic pressure, p, related to the pseudopotential in the pseudopotential model, is given by $p = \rho c_s^2 + \frac{Gc^2}{2}\psi^2$ with the lattice sound speed $c_s = c/\sqrt{3}$.

To introduce adjustable interfacial tension into MRT models, Li et al. [184] suggest the addition of a source term $\boldsymbol{C}$ into the MRT LB equation,

$$\boldsymbol{m}^{*} = \boldsymbol{m} - \boldsymbol{S}(\boldsymbol{m} - \boldsymbol{m}^{eq}) + \delta_t \left(\boldsymbol{I} - \frac{\boldsymbol{S}}{2}\right)\boldsymbol{M}\widetilde{\boldsymbol{F}} + \boldsymbol{C} \tag{4–8}$$

where the forcing term in moment space $\boldsymbol{M}\widetilde{\boldsymbol{F}}$ is defined as [185],

$$\begin{aligned}\boldsymbol{M}\widetilde{\boldsymbol{F}} = \Bigg(0, 2\boldsymbol{u}\cdot\boldsymbol{F} + \frac{6\sigma|\boldsymbol{F}|^2}{\psi^2\delta_t(s_e^{-1} - 0.5)}, -10\boldsymbol{u} \\ \cdot\boldsymbol{F}, F_x, -\frac{7}{3}F_x, F_y, -\frac{7}{3}F_y, F_z, -\frac{7}{3}F_z, 4u_xF_x - 2u_yF_y \\ - 2u_zF_z, 2u_yF_y - 2u_zF_z, u_xF_y + u_yF_x, u_yF_z + u_zF_y, u_xF_z \\ + u_zF_x, 0\Bigg)^T\end{aligned} \tag{4–9}$$

with the parameter σ used to alter the mechanical stability of the model [162], ensuring thermodynamic consistency. Additionally, the source term $\boldsymbol{C}$ is defined to adjust the interfacial tenson [185],

$$\begin{aligned}\boldsymbol{C} = \Big(0, \frac{4}{5}s_e\big(Q_{xx} + Q_{yy} + Q_{zz}\big), 0, 0, 0, 0, 0, 0, 0, -s_v\big(2Q_{xx} - Q_{yy} - Q_{zz}\big), \\ -s_v\big(Q_{yy} - Q_{zz}\big), -s_vQ_{xy}, -s_vQ_{yz}, -s_vQ_{xz}, 0\Big)^T\end{aligned} \tag{4–10}$$

with variables Q_{xx}, Q_{yy}, Q_{zz}, Q_{xy}, Q_{yz} and Q_{xz} obtained from [185],

$$\boldsymbol{Q} = \kappa\frac{G}{2}\psi(\boldsymbol{x})\sum_{i=1}^{14} w(|\boldsymbol{c_i}|^2)[\psi(\boldsymbol{x} + \boldsymbol{c}_i) - \psi(\boldsymbol{x})]c_ic_i \tag{4–11}$$

where κ is used to adjust the interfacial tension γ. According to [184], the addition of $(1 - \kappa)$ in the discrete form pressure tensor is intended to allow the interfacial tension to decrease and approach zero as κ increases from 0 to 1. The above methodology provides flexibility and stability in the model to simulate fluid flows at high density ratio and low viscosity, whilst allowing for adjustable interfacial tension.

4.3.3 Fluid-solid interactions

As mentioned previously, incorporating adhesive effects between solids and fluids in the pseudopotential LB scheme has been widely studied. Generally, there have been two main methodologies developed to mimic fluid-solid interactions, namely the density-based interaction [165,166] and the pseudopotential-based interaction [169,170]. For the density-based interaction models a fictious wall density is introduced at the solid nodes, whereas for pseudopotential-based interactions schemes, a pseudopotential is adopted at the solid nodes. Recently, the geometric wetting condition [171], originating in the phase-field LB method, has been adopted to incorporate wetting phenomena in multiphase pseudopotential LB method. In three-dimensions $(x, y, z) = (i, j, k)$, the scheme takes the following form,

$$\rho_{i,j,0} = \rho_{i,j,2} + \tan\left(\frac{\pi}{2} - \theta\right)\zeta \qquad 4\text{–}12$$

where,

$$\zeta = \sqrt{\left(\rho_{i+1,j,1} - \rho_{i-1,j,1}\right)^2 + \left(\rho_{i,j+1,1} - \rho_{i,j-1,1}\right)^2} \qquad 4\text{–}13$$

The first and second subscripts denote directions along the solid boundary, whereas the third gives coordinates normal to the solid, and θ is the prescribed contact angle for adjustment of the wetting condition. The scheme requires a layer of ghost nodes adjacent to the solid boundary in order to calculate the value of density. The fluid layers are located at k = 2 and the solid boundary at k = 1, with the ghost layer located at the bottom of the domain k = 0. Unlike the fluid-solid methods detailed previously, the only requirement for this scheme is the definition of desired contact angle, hence no additional forcing is implemented. Calculation of the density in the ghost, solid and adjacent fluid nodes is added to the rest the of the computational domain, resulting in an accurate wettability condition. This scheme will be applied in this study.

4.3.4 Fluid-SAW interactions

As discussed in Section 2.2 the emitted pressure waves generated from the SAW devices induce a body force in the liquid medium, instigating a circulatory motion within the fluid. The magnitude of SAW force F_{SAW} can be expressed by Eq. 2–9, with horizontal and vertical components being specified from Eq's 2–8.

The SAW force is implemented in the numerical scheme as an external force in the pseudopotential method through $\boldsymbol{F}$. In physics, as discussed in Section 2.2, the surface acoustic wave enters the liquid droplet upon reaching the interface, where the difference in sound speeds between the liquid and substrate causes it to radiate momentum into liquid along the Rayleigh angle. To introduce these effects into the model, a set of conditions are imposed to allow the forcing to only be active in the liquid phase. This is achieved via the average density of the domain which allows the model to distinguish between liquid and gas/vapour. By doing so a sharp cut-off is achieved through the interface and into the droplet, preventing any SAW forcing from being active in the gas/vapour phase. Additionally, the contact points of the droplet are continuously monitored to ensure the droplet is still in contact with the SAW substrate. Once the droplet leaves the surface, the forcing (SAW) is inactive as that in the physical experiments.

4.4 LB model validation

In the following, the model is validated using conventional benchmark tests to demonstrate its capability and applicability to the current study. Note, the Yuan and Schaefer [155] method, described previously in Section 3.2, is chosen with CS EOS for all cases unless stated otherwise. The parameters a, b and R are set to $a = 0.25$, $b = 4$ and $R = 1$, respectively.

4.4.1 Evaluation of thermodynamic consistency

To evaluate the thermodynamic consistency of the model, the numerically obtained coexistence curves are compared against the analytical Maxwell construction through simulating flat interfaces.

A domain size of $N_x \times N_y \times N_z = 100 \times 100 \times 100$ is implemented, with periodic boundary conditions applied in all directions. The density field is initialised as,

$$\rho(x, y, z) = \rho_g + \frac{\rho_l - \rho_g}{2}[\tanh(z_1) - \tanh(z_2)] \qquad 4\text{–}14$$

where $z_1 = 2(z - 25)/W$ and $z_2 = 2(z - 75)/W$, with $W = 5$ as the initial interface thickness. The value of σ in Eq. 4–9 is set to 0.12 in all simulations unless stated otherwise.

The coexistence curves shown in Figure 4-2 agree with the Maxwell construction, demonstrating the schemes capability of capturing the saturate phase behaviour of the fluid, even at large density ratios.

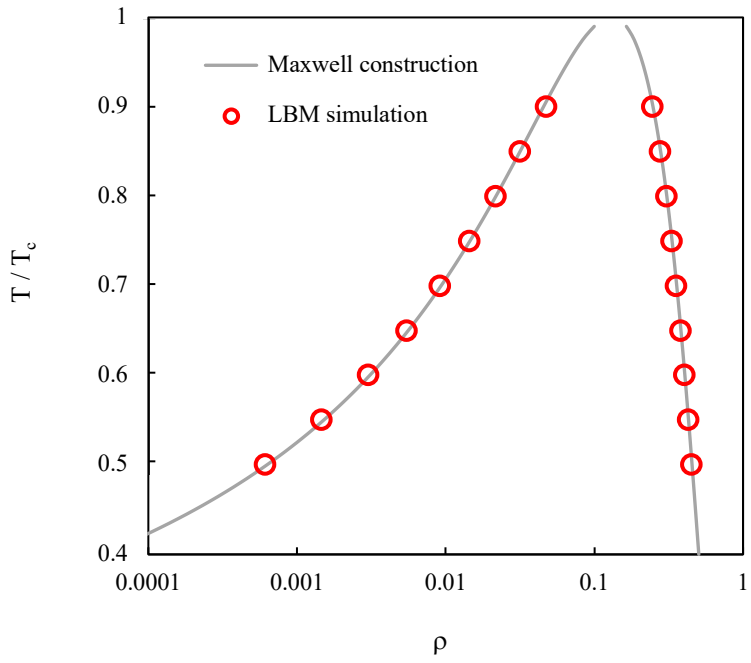

Figure 4-2. Comparison of numerical coexistence curve with the analytical curve predicted by Maxwell construction

4.4.2 Evaluation of spurious velocities

In this study, spurious velocities are evaluated to determine the performance of the current MRT model compared to the SRT model. Following [185], the parameters in the relaxation matrix $\boldsymbol{S} = \mathrm{diag}(s_\rho, s_e, s_\varepsilon, s_j, s_q, s_j, s_q, s_j, s_q, s_\nu, s_\nu, s_\nu, s_\nu, s_\nu, s_{xyz})$ are selected as $s_\rho = s_j = 1.0,\ s_e = s_\varepsilon = s_q = 1.1,$ and $s_{xyz} = 1.2$ for the MRT model, while the relaxation rates in the SRT model are equal to each other $s_\rho = s_j = s_e = s_\varepsilon = s_q = s_{xyz} = s_\nu$. A lattice size of $N_x \times N_y \times N_z = 120 \times 120 \times 120$ is adopted in the simulations, with a spherical droplet of radius $R_0 = 30$ initially positioned in the centre of the domain. Periodic boundary conditions are applied in all three directions and the density field is initialised as follows,

$$\rho(x,y,z) = \frac{\rho_l + \rho_g}{2} - \frac{\rho_l - \rho_g}{2}\tanh\left[\frac{2(R - R_0)}{W}\right] \qquad 4\text{–}15$$

where $R = \sqrt{(x-x_0)^2 + (y-y_0)^2 + (z-z_0)^2}$, with (x_0, y_0, z_0) being the centre of the computational domain, and $W = 5$ is the initial interface width. The reduced temperature is set to $T_R = 0.5$ which corresponds to a density ratio of $\rho_l/\rho_g \approx 750$.

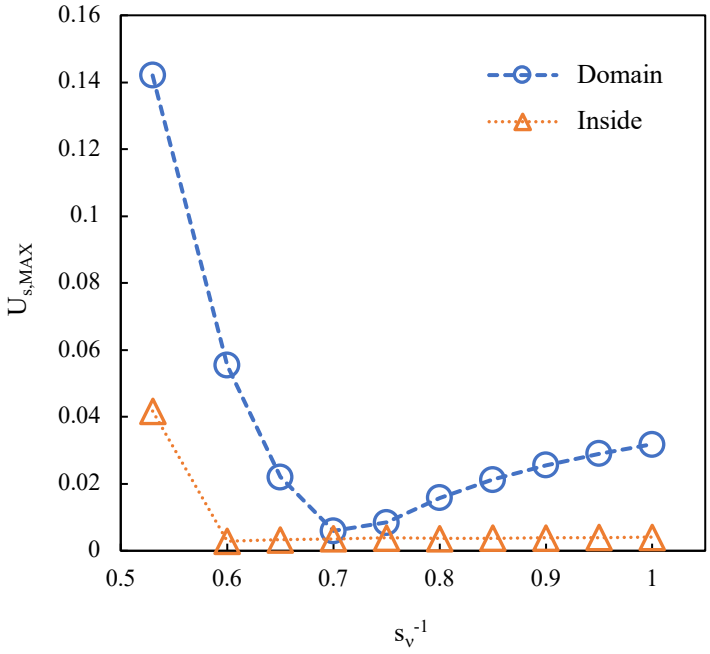

Figure 4-3. Maximum spurious velocities for whole domain and inside droplet at T_R = 0.5

The maximum spurious velocities for the whole domain, as well as those inside the droplet, at $T_R = 0.5$ are plotted against ${s_v}^{-1}$, shown in Figure 4-3. It is found that the maximum spurious velocity in the whole domain is smaller than 0.04 for ${s_v}^{-1} \geq 0.65$, however as ${s_v}^{-1} < 0.65$ this increases to around 0.06 then finally to approximately 0.14 for ${s_v}^{-1} = 0.53$. Conversely, the magnitude inside the droplet is small and remains fairly constant over the range of ${s_v}^{-1}$ only increasing once ${s_v}^{-1} < 0.6$. The spurious velocities inside the droplet and the effects on simulation SAW-droplet interactions will be discussed in Section 4.5.1.

Table 4-1. Maximum spurious velocities for SRT and MRT methods (T_R=0.5)

		$\kappa = 0$	$\kappa = 0.5$	$\kappa = 0.95$
${s_v}^{-1} = 0.6$	SRT	-	-	-
	MRT	0.055411	0.056327	0.067002
${s_v}^{-1} = 1.0$	SRT	0.040350	0.034532	0.027726
	MRT	0.031796	0.026633	0.021215

It is found from the simulations that the maximum spurious velocities are all materialised outside of the droplet. From Table 4-1 it shows that MRT provides a reduction of spurious currents, whilst also enhancing the numerical stability of simulations over SRT models. Interestingly at $s_v{}^{-1} = 1.0$ spurious currents are reduced with an increase in parameter κ (decrease in interfacial tension), however when $s_v{}^{-1} = 0.6$ the opposite it witnessed.

4.4.3 Evaluation of spatial accuracy

To assess the spatial accuracy of the model, the equilibrium densities of a spherical droplet, of various radius and mesh sizes, is analysed. The mesh sizes simulated were $N_x \times N_y \times N_z = 44 \times 44 \times 44,\ 88 \times 88 \times 88,\ 132 \times 132 \times 132$ and $176 \times 176 \times 176$, with the droplet radius equal to $R = N_x/4$. Periodic boundary conditions are applied in all three directions and the density field is initialised according to Eq. 4–15. To estimate the error of the mesh size, the following formula is employed [185]; $\mathrm{Error}(N_x) = |\rho(N_x) - \rho(176)|$, where $\rho(N_x)$ is the obtained liquid or gas density at each mesh size, which will be compared to those obtained for the largest mesh size (N_x=176).

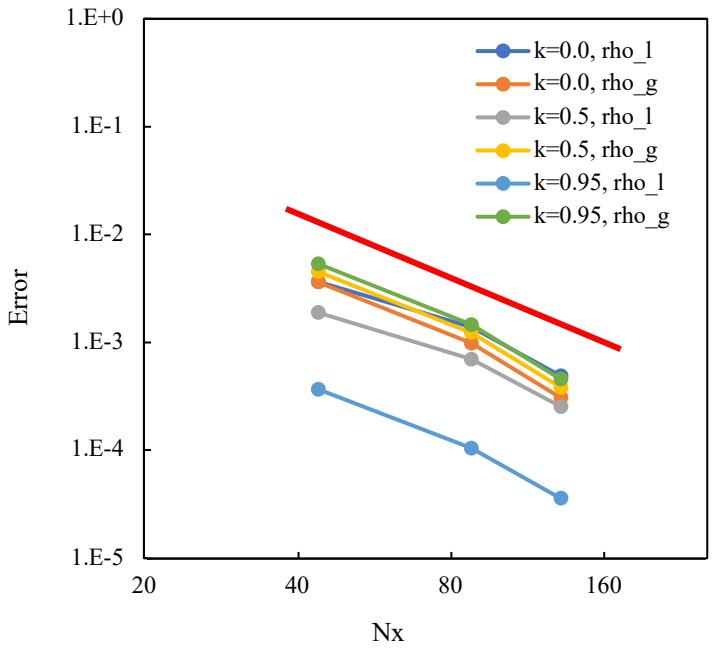

Figure 4-4. Numerical errors of density as a function of mesh size. Solid red line represents exact second-order accuracy.

The change in relative error in steady state densities, with mesh size, are shown in Figure 4-4. Three test cases were simulated with varying κ in Eq. 4–11, with the results compared

to exact second-order accuracy depicted as the solid red line in Figure 4-4. It is shown that the model has approximate second-order accuracy in space.

4.4.4 Evaluation of Laplace's law

Laplace's law is employed to validate the simulation of droplets of different radii. According to Laplace's law, the pressure difference across the interface of a spherical drop is related to the interfacial tension and the radius of the drop. In three-dimensions, the law is given by $\delta p = p_{in} - p_{out} = 2\gamma/R$, where p_{in} and p_{out} are the fluid pressures inside and outside of the drop, respectively, and R is the droplet radius. Once the interfacial tension is given, the pressure difference will be proportional to $1/R$.

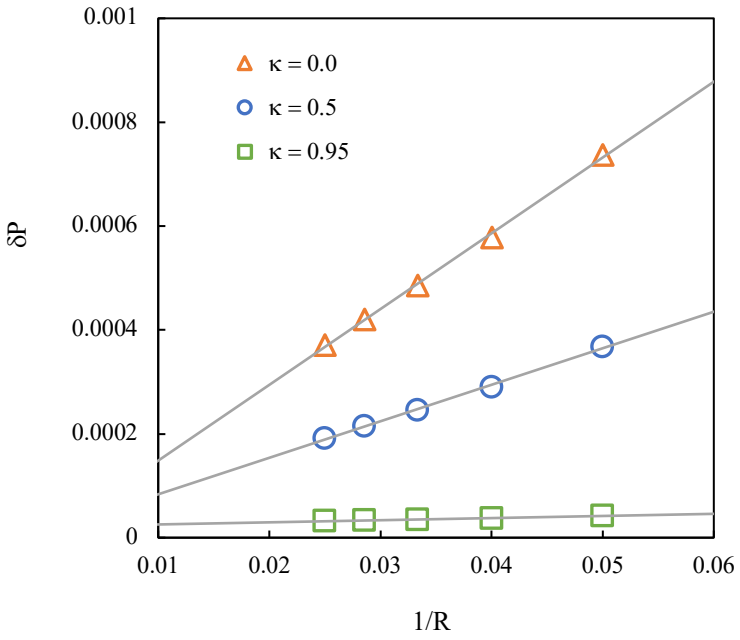

Figure 4-5. Numerical validation of Laplace's law

Simulations are carried out under the same cases set in Section 4.4.2. To test the relationship numerically, the radius of the droplet is varied within $20 < R < 40$, and the pressure difference obtained. Additionally, the adjustment of the interfacial tension via Eq. 4–11 is validated for $\kappa = 0$, $\kappa = 0.5$ and $\kappa = 0.95$. As shown in Figure 4-5, a linear relationship is confirmed for all cases with the coefficients of determination being 0.9986, 0.9976 and 0.9860, respectively. The model demonstrates a proportional relationship between the pressure difference inside and outside of the drop, and the inverse of drop radius thus Laplace's law is substantiated.

4.4.5 Evaluation of static contact angle

A liquid droplet placed on a flat solid surface will exhibit an equilibrium state of either partial or complete wetting [186]. During partial wetting, the free energy of each phase (solid, liquid, and gas/vapour) is in equilibrium, with the interfacial tension balance at the three-phase contact line being represented by Young's equation,

$$\gamma_{SV} - \gamma_{SL} - \gamma_{LV} \cos\theta_{\gamma} = 0 \qquad 4\text{–}16$$

where γ_{SV}, γ_{SL} and γ_{LV} represent the interfacial tensions of solid-gas/vapour, solid-liquid and liquid-gas/vapour interfaces, respectively, with the macroscopic contact angle being equal to the microscopic contact angle θ_{γ} [187]. Considering the above, the simulated static contact angle is evaluated against the analytical solution using the geometric formulation. In the simulations, a stationary semi-spherical droplet of radius $R = 25$ is initially placed on a flat surface with no body force applied. A lattice size of $N_x \times N_y \times N_z = 120 \times 120 \times 80$ is adopted, with periodic boundary conditions applied in the x and y directions, while a no-slip condition is added to the upper and lower boundaries. As previous, the reduced temperature is set to $T_R = 0.5$.

The results in Figure 4-6 show good agreement with the analytical solution demonstrating the capability of the model to simulate static contact angles accurately. Additionally, as seen in Table 4-2, the discrepancy between the prescribed and measured contact angle is relatively low, with a maximum error of ~3.7%. Interestingly, over the range of angles studied, the method seems to underestimate the contact angle as compared to the analytical solution.

Table 4-2. Error in measured equilibrium contact angle

Prescribed Contact Angle	Measured Contact Angle	% Error
120	118.0308657	1.6409452
105	102.6914144	2.198653
90	88.2815703	1.9093663
75	74.05764681	1.2564709
60	58.04907659	3.251539
45	43.90244078	2.4390205
30	28.88460754	3.7179749

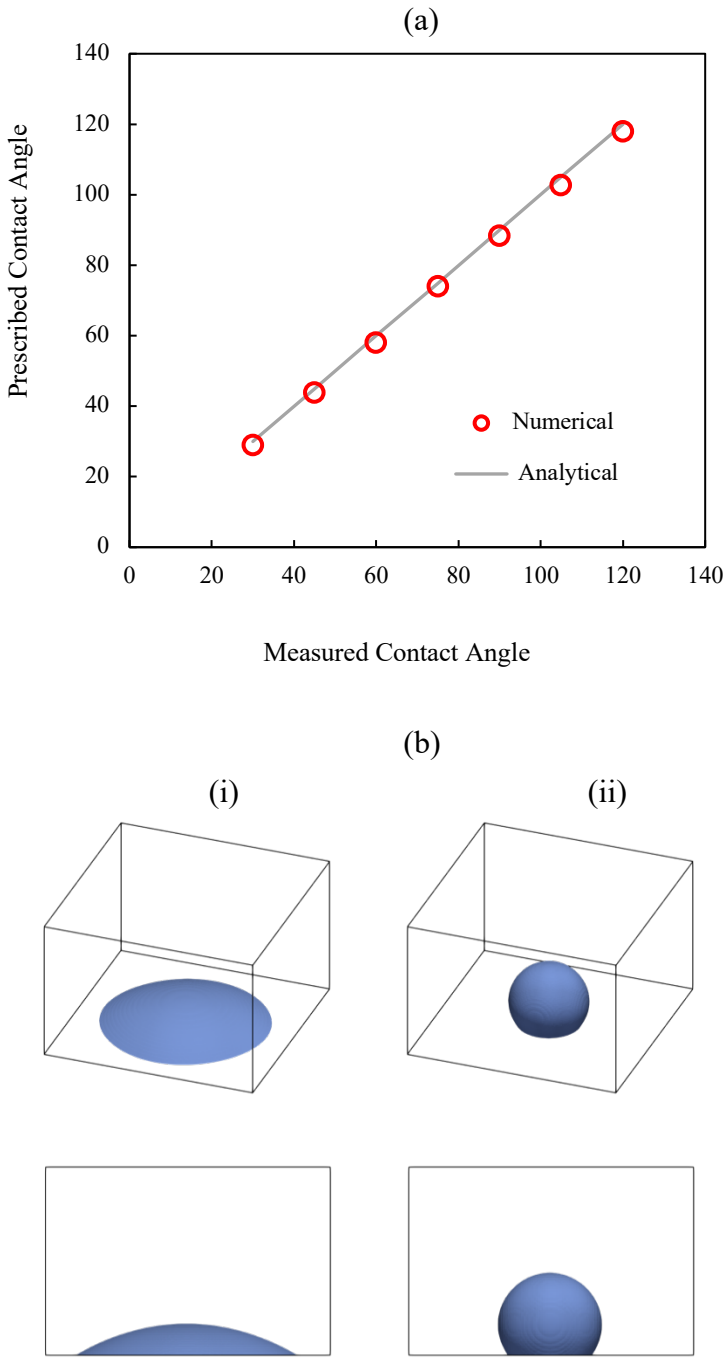

Figure 4-6. Simulated contact angles using geometric formulation; (a) validation against analytical solution (b) images for (i) θ ≈30° (ii) θ ≈120°

4.4.6 Evaluation of droplet oscillation

Since the nature of the study requires evaluation of droplet dynamics, a dynamic validation case is presented. Here an oscillating droplet is simulated, which is initially placed at the centre of the domain and deformed to an ellipsoidal shape by,

$$\frac{(x-x_0)^2}{R_0^2}+\frac{(y-y_0)^2}{R_0^2}+\frac{(z-z_0)^2}{(0.8R_0)^2}=1 \qquad 4\text{–}17$$

where (x_0, y_0, z_0) is the centre of the domain and R_0 is the initial radius of the drop, set to $R_0 = 30$. The frequency of the nth mode oscillation is given by Miller and Scriven [188]

$$\omega_n = \omega_n^* - \frac{1}{2}\alpha\omega_n^{*\frac{1}{2}} + \frac{1}{4}\alpha^2 \qquad 4\text{–}18$$

where ω_n is the angular response frequency and ω_n^* is Lamb's natural resonance frequency [189]

$$(\omega_n^*)^2 = \frac{n(n+1)(n-1)(n+2)}{R_e^3\left[n\rho_g + (n+1)\rho_l\right]}\gamma \qquad 4\text{–}19$$

where R_e is the radius of the drop at equilibrium. Parameter α, in Eq. 4–18, is given by [188]

$$\alpha = \frac{(2n+1)^2\left(\mu_l\mu_g\rho_l\rho_g\right)^{1/2}}{\sqrt{2}R_e\left[n\rho_g + (n+1)\rho_l\right]\left[(\mu_l\rho_l)^{1/2} + \left(\mu_g\rho_g\right)^{1/2}\right]} \qquad 4\text{–}20$$

where μ_l and μ_g are the dynamic viscosities of the liquid and gas/vapour phases, respectively, with $\mu = \rho\nu$. Due to the effect of interfacial tension and viscous dampening, the ellipsoidal droplet oscillates until a spherical shape is reached, with the amplitude of the oscillations decreasing over time. Figure 4-7 illustrates the evolution of the normalised droplet radius in both the horizontal and vertical directions. At the intersection of the solid and dashed lines, the droplet is spherical in shape.

The analytical solution of the time period $T = 2\pi/\omega_n$ for the second mode (n = 2) obtained from Eq. 4–18 is compared to the simulation result. The analytical oscillatory period is found as $T_a = 2601$, while the numerical oscillation period is $T_{LBM} = 2748$,

giving a relative error of 5.7%. Additionally, the influence of interfacial tension on the droplet oscillations is studied by varying the parameter κ, in Eq. 4–11, $0 < \kappa < 0.5$. The numerical and analytical oscillation periods for $\kappa = 0.25$ are $T_a = 3016$ and $T_{LBM} = 3211$, respectively, while for $\kappa = 0.5$, $T_a = 3748$ and $T_{LBM} = 3950$. The relative errors being 6.5% and 5.4% are consistent with those reported in the literature [190].

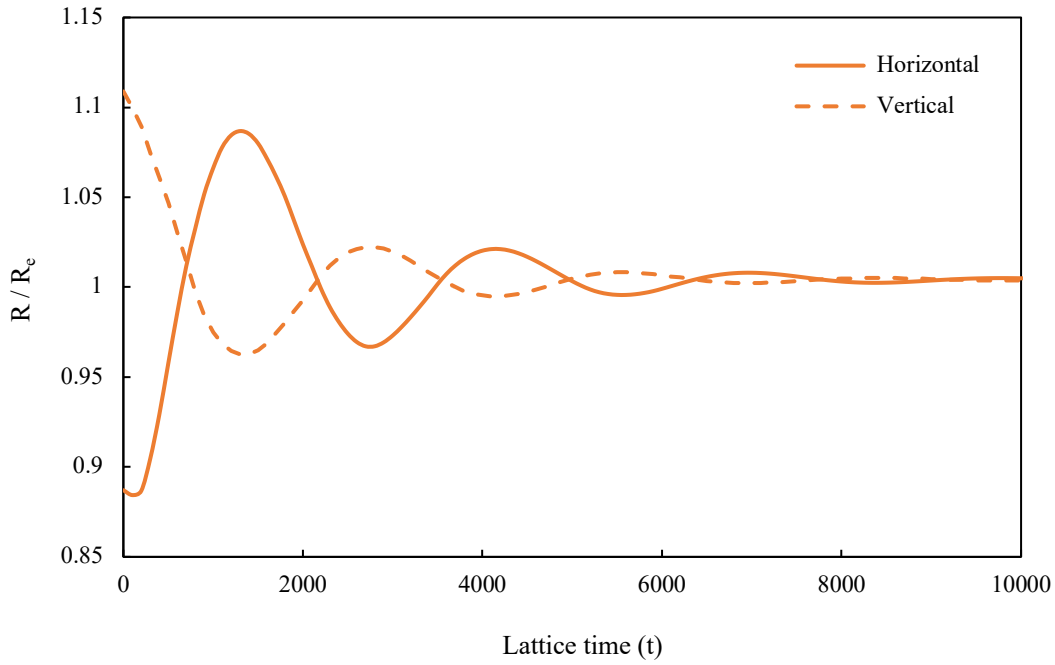

Figure 4-7. Normalised radius of oscillatory droplet as a function of time for $\kappa = 0$

4.5 Numerical analysis of SAW interaction on a drop

In the subsequent section, the constructed SAW-LB model is applied to study the effects of SAW interactions on a droplet to demonstrate how the constructed model can simulate and predict the internal physics and dynamics before further applications. Following the computational setup, the model is firstly validated then the effects of parameters such as wave amplitude, frequency, surface wettability, viscosity ratio and interfacial tension on droplet are examined. Thermal and aperture effects are not considered in this study. The mesh independent and grid resolution tests identify a mesh of $N_x \times N_y \times N_z = 5R \times 3R \times 4R$, with a drop radius of $R = 40$, to capture the flow dynamics with optimised computational cost.

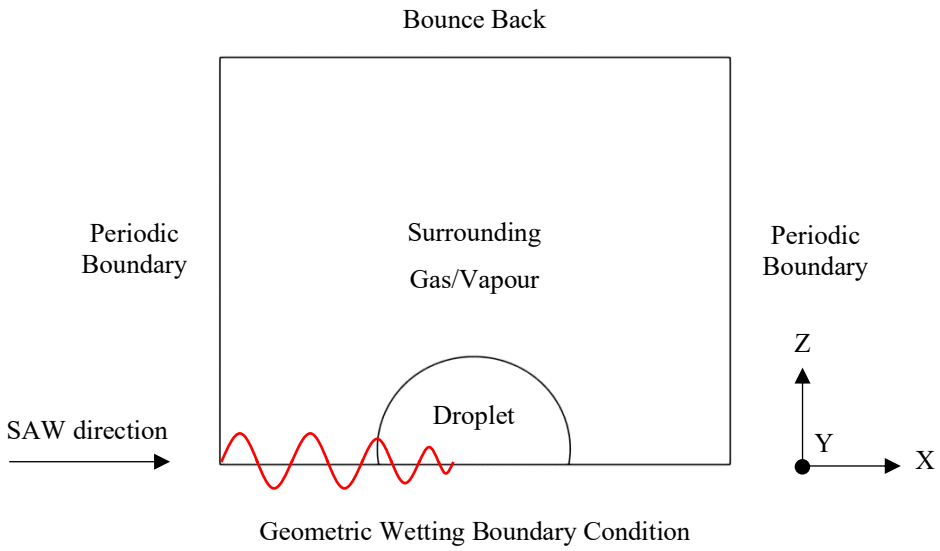

Figure 4-8. Schematic of SAW-drop setup and boundary conditions

In the simulations, a semi-spherical droplet of radius $R = 40$ initially placed on the bottom surface with initial contact angle ~100° and its centre at (100,60,5), unless stated otherwise. The setup of the simulation can be referred to in Figure 4-8, including the boundary conditions. The reduced temperature is again set to $T_R = 0.5$, equivalent to a density ratio of $\rho_l/\rho_g \approx 750$ $(\rho_l = 0.454, \rho_g = 0.0006)$ with $\nu_g/\nu_l \approx 15$ and $s_\nu{}^{-1} = 0.5077$ set for the liquid phase to provide appropriate conversion parameters to match the interfacial tension between physical and LB. Periodic boundary conditions are applied in the x and y directions, while a no-slip condition is added to the upper and lower boundaries. The droplet is first allowed to reach an equilibrium state on the SAW substrate, after which the SAW interactions are introduced.

To validate the SAW interactions in the LB model, the simulation results are quantitatively compared with experimental data, which are taken from the selected records of previous experiments described in [34]. Three different modes are considered; *mixing*, *pumping,* and *jetting*, which will demonstrate the applicability of the proposed methodology to SAW based microfluidics applications. A set of non-dimensional groups have been chosen to allow for comparison between numerical and experimental data, which are Reynolds number, Weber number and capillary number, defined as, $Re = \frac{\rho_l u D}{\mu_l} = \frac{uD}{\nu_l}$, $We = \frac{\rho_l u^2 D}{\gamma}$, and $Ca = \frac{\mu_l u}{\gamma}$ with D the droplet diameter, u the droplet velocity and γ the interfacial tension. Note, the velocity definition for pumping is the mean velocity, summarised as the movement of the droplet along the surface, whereas for

jetting it is along the length of the droplet from initial state until the drop is ejected from the surface.

Physical parameters are related to lattice units through unit conversion. To properly convert between the LB and physical domains, three independent primary conversion factors are required. In this work, a droplet of water with volume 5 µl and initial radius of 1.34 mm is studied, which corresponds to a Length scale conversion $C_l = 33.4$ µm. Physical properties of water at 20°C are taken as [191]; $\rho_w = 998.2\ \mathrm{kg\,m^{-3}}$, $\nu_w = 1.004 \times 10^{-6}\ \mathrm{m^2 s^{-1}}$, and $\gamma_w = 0.07273\ \mathrm{N\,m^{-1}}$. The consequent Time conversion factor is $C_t = 2.85 \times 10^{-6}\ \mathrm{s}$, with a velocity scale conversion calculated as $C_u = C_l/C_t = 11.72\ \mathrm{m s^{-1}}$. A full derivation can be found in Appendix B. $LiNbO_3$ based SAW devices were used, with designed wavelengths of 64, 32, 20 and 12 microns, corresponding to the measured frequencies of 61.7, 110.8, 199.4 and 250.1 MHz, which were reported in detail in [34]. SAW parameters applied in the simulations are representative of $LiNbO_3$ substrate, where $\alpha_1 = 2.47$ and $k_i = -1370\ \mathrm{m^{-1}}$ [29] in Eq. 2–9.

4.5.1 The role of spurious velocities

A major concern of implementing the pseudopotential model in the study of SAW streaming and its effect on droplet dynamics, is the presence of spurious (parasitic) velocities. In its current formulation, when comparing the magnitude of velocities inside the drop it is not possible to readily distinguish between spurious currents and acoustic streaming. As can be seen from a droplet on a surface (Figure 4-9 (a)), without external forcing, displays a symmetrical pattern which is purely a consequence of the numerical scheme. Comparing it to a droplet subjected to low SAW forcing (Figure 4-9 (b)), a more asymmetric pattern is witnessed, where a streaming state has been induced.

For a droplet without any SAW interaction there is a large velocity near the top centre and the majority of velocities are located near the interface where interfacial tension effects are highest. On the contrary, when SAW is introduced, the largest velocities are found at the left-hand-side where the interaction point resides. The direction of the flow field has been altered, as the momentum of the liquid has been pushed upwards along the Rayleigh angle, with a primary vortex established at the right-hand-side of the droplet. Although the order of magnitude between the two sets of data is similar, the composition is distinctly different. When SAW is acting, a mixing field is noticeably produced.

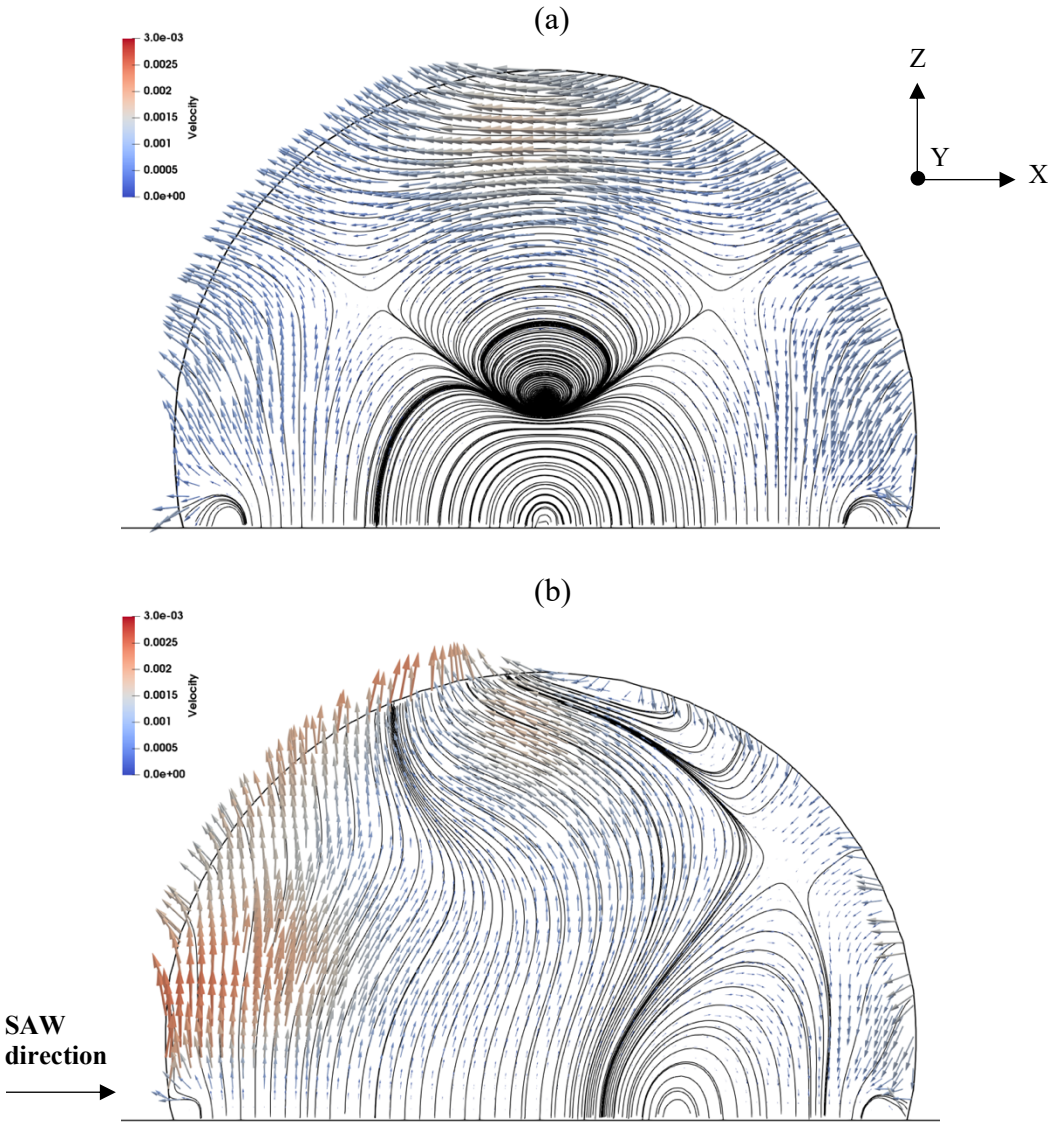

Figure 4-9. Velocity streamlines and vectors for droplet with; (a) no SAW interaction and (b) SAW interaction at 61.7 MHz [Note: Flow field in lattice units]. View is slice through centre of droplet at 17 ms.

Further indication that a streaming state is initiated is confirmed by a velocity profile across the centre of the droplet. In Alghane et al. [79] they provide extensive details on the velocity profiles expected when a low power SAW is interacting with a 30 µl liquid droplet. They demonstrate a high velocity near the interaction area (Fig. 10 (a) of [79]), diminishing along the width of the droplet with two lower peaks at the middle and far side. Now, if the velocity profile across the droplet in the present study is examined (Figure 4-10), at a height of 400 µm from the droplet bottom, a similar outcome it perceived. Although it has already been noted that spurious velocities and streaming velocities cannot be distinguished readily, there can be no doubt that the forcing scheme

employed stimulates streaming inside the drop which can cause mixing, pumping and jetting with increase in wave amplitude (power).

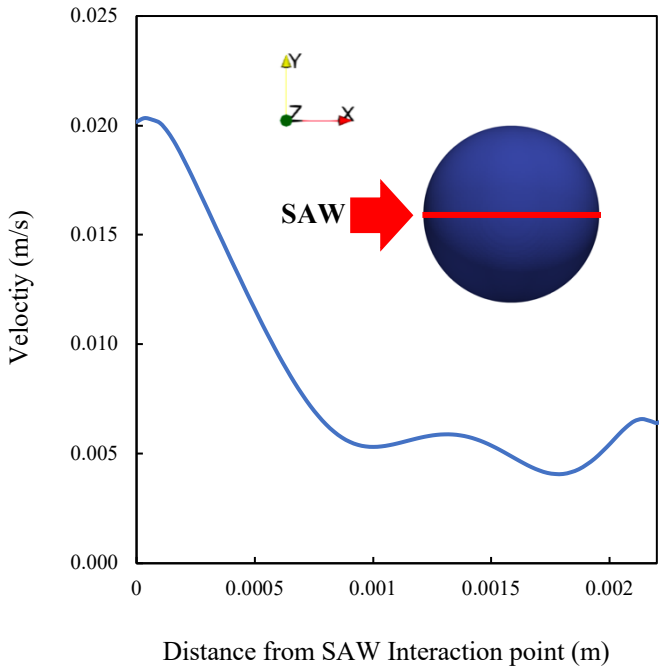

Figure 4-10. Velocity profile through centre of droplet. (5 µl drop at 0.4 mm above surface at 61.7 MHz)

In the following, these effects are investigated with the aim to clarify at which range of wave amplitude are spurious velocities no longer dominant and streaming can be predicted. In this part, a resonant frequency of 61.7 MHz is selected and the interfacial tension is altered from 0.055 N/m to 0.092 N/m. A range of wave amplitudes are studied and compared to a droplet at rest, on a SAW substrate, without any SAW interaction. The flow field and velocity profiles, across the width of the drop, are analysed. The culmination of the data reveals a threshold amplitude at which streaming/mixing can be achieved for each value of interfacial tension (Figure 4-11). The areas above and below this threshold have been termed as ***Streaming Dominant*** and ***Spurious Dominant***, respectively, to reflect the flow field attained. In this analysis Streaming Dominant has been defined as being an internal flow structure and velocity profile which resembles the research in [79] whilst Spurious Dominant is outlined as a symmetrical velocity field, comparable to that of a droplet on a solid surface without any SAW interactions.

As shown in Figure 4-12, the magnitude of wave amplitude plays an important role in the formation of streaming inside the droplet. Comparing low amplitude and hence low

power (Figure 4-12 (c) - (d)) to the droplet without SAW interaction (Figure 4-12 (a) - (b)), there are similarities. Firstly, the flow field and velocity vectors are comparable with central vortices dominating. Also, taking a profile across the droplet the largest velocity magnitude is realised at the edges, close to the interface, yielding a parabola distribution. The main differences between the two sets of data are; the velocity has been increased with SAW forcing and the flow field no longer has exact symmetry. This type (Figure 4-12 (c) – (d)) can be categorised as a Spurious Dominant flow. As the amplitude is further increased, the velocity distribution starts to depart from symmetry to that which resembles a mixing scenario. Looking at the Figure 4-12 (e) - (f), there are large velocities on the left-hand-side of the droplet, above the interaction area, and a vortex located at the right side. Additionally, the velocity profile reflects this with a large magnitude close to the interaction point, diminishing along the length with smaller peaks near the centre and far side of the droplet. The velocity distribution in Figure 4-12 (f) is the same as those found in Fig. 10 (a) of [79] by experiments and computational fluid dynamics (CFD) modelling, hence it is classified as a Streaming Dominant flow.

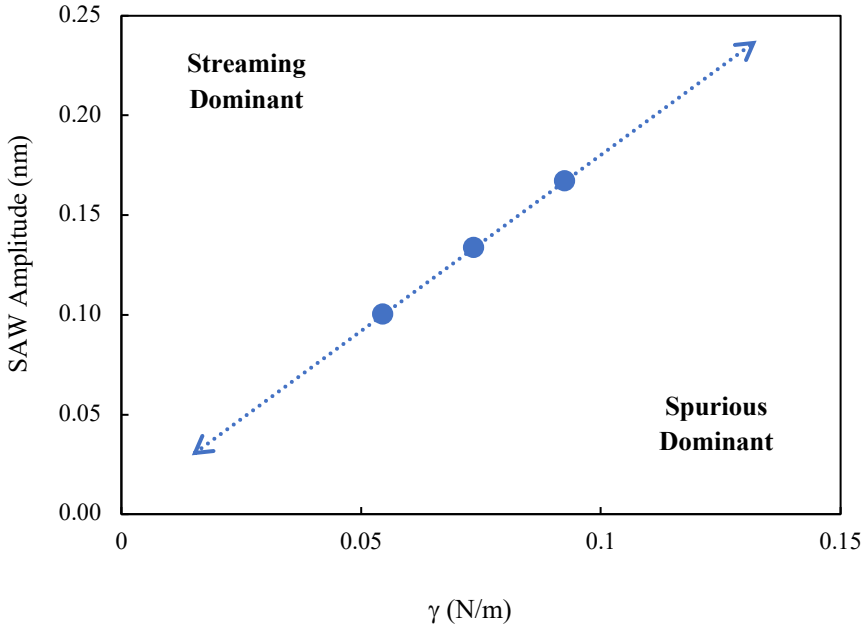

Figure 4-11. SAW amplitude for different interfacial tensions at which streaming/mixing is induced for 61.7 MHz. Above dotted line is streaming dominant and below is spurious current dominant.

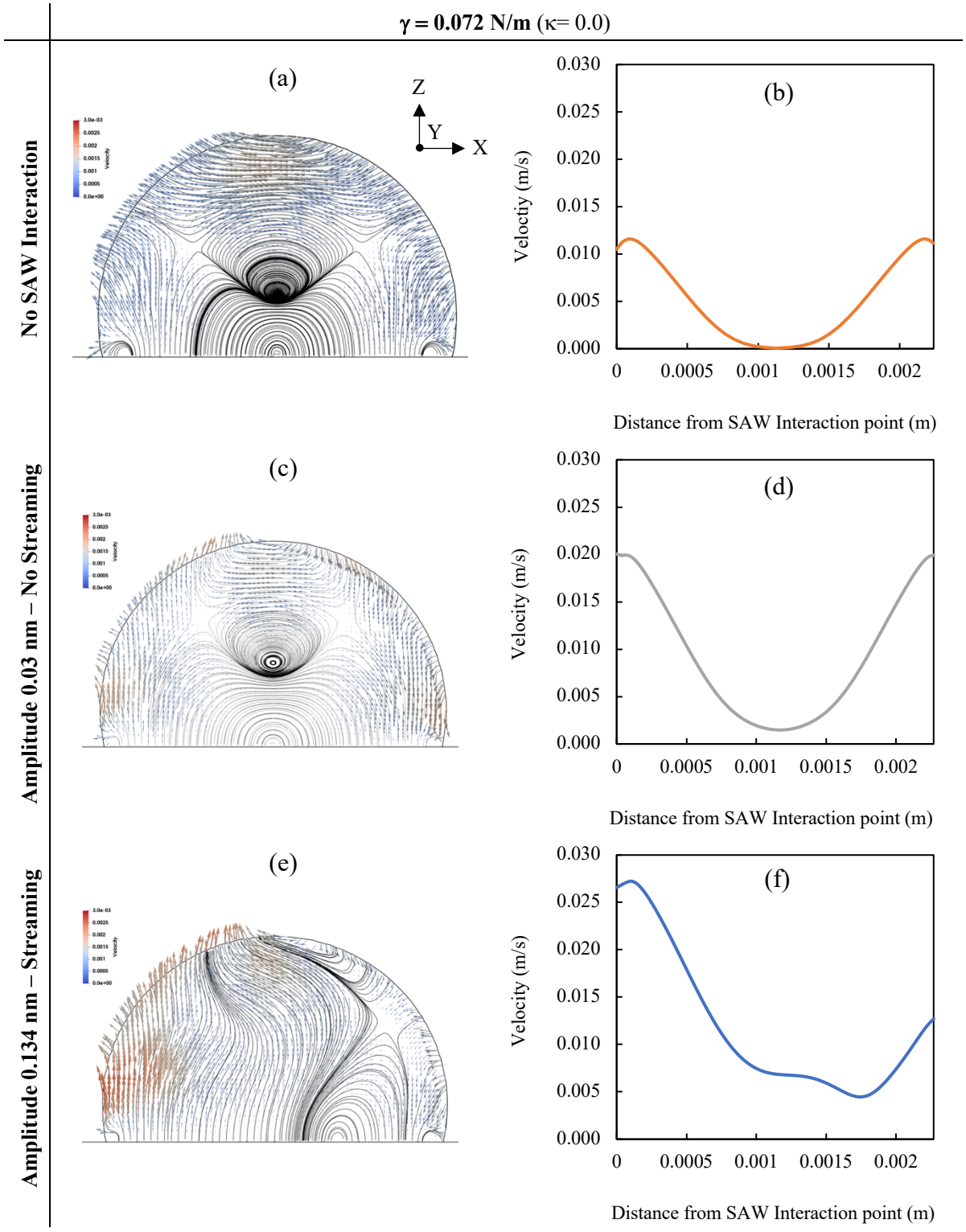

Figure 4-12. Flow field and velocity profiles inside droplet at κ = 0 and 61.7 MHz. Droplet without SAW interaction (a,b), and with SAW interaction; 0.03 nm wave amplitude (c,d) and 0.134 nm wave amplitude (e,f) [Note: Flow field in lattice units] View is slice through centre of droplet at 17 ms.

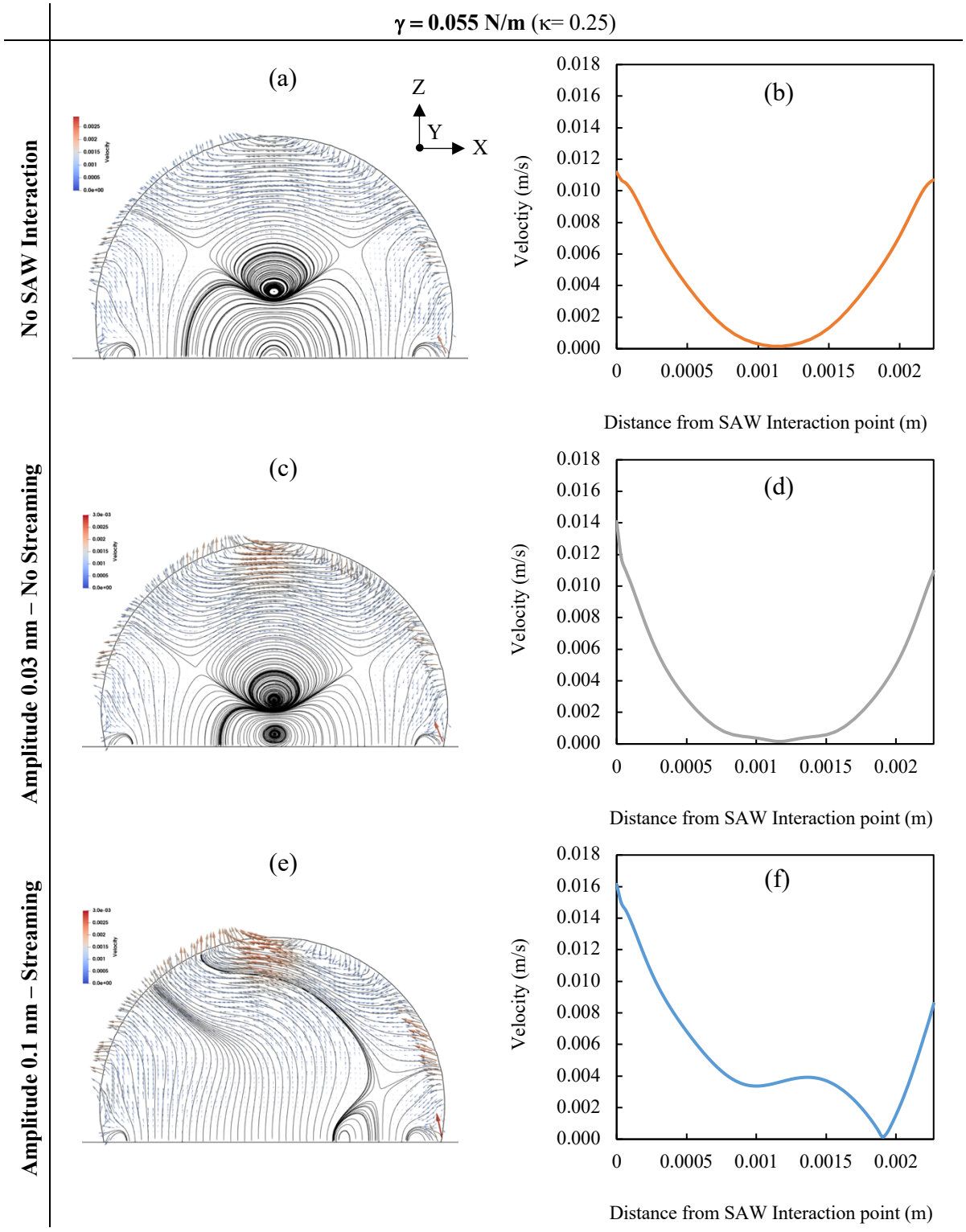

Figure 4-13. Flow field and velocity profiles inside droplet at κ = 0.25 and 61.7 MHz. Droplet without SAW interaction (a,b), and with SAW interaction; 0.03 nm wave amplitude (c,d) and 0.1 nm wave amplitude (e,f) [Note: Flow field in lattice units]. View is slice through centre of droplet at 17 ms.

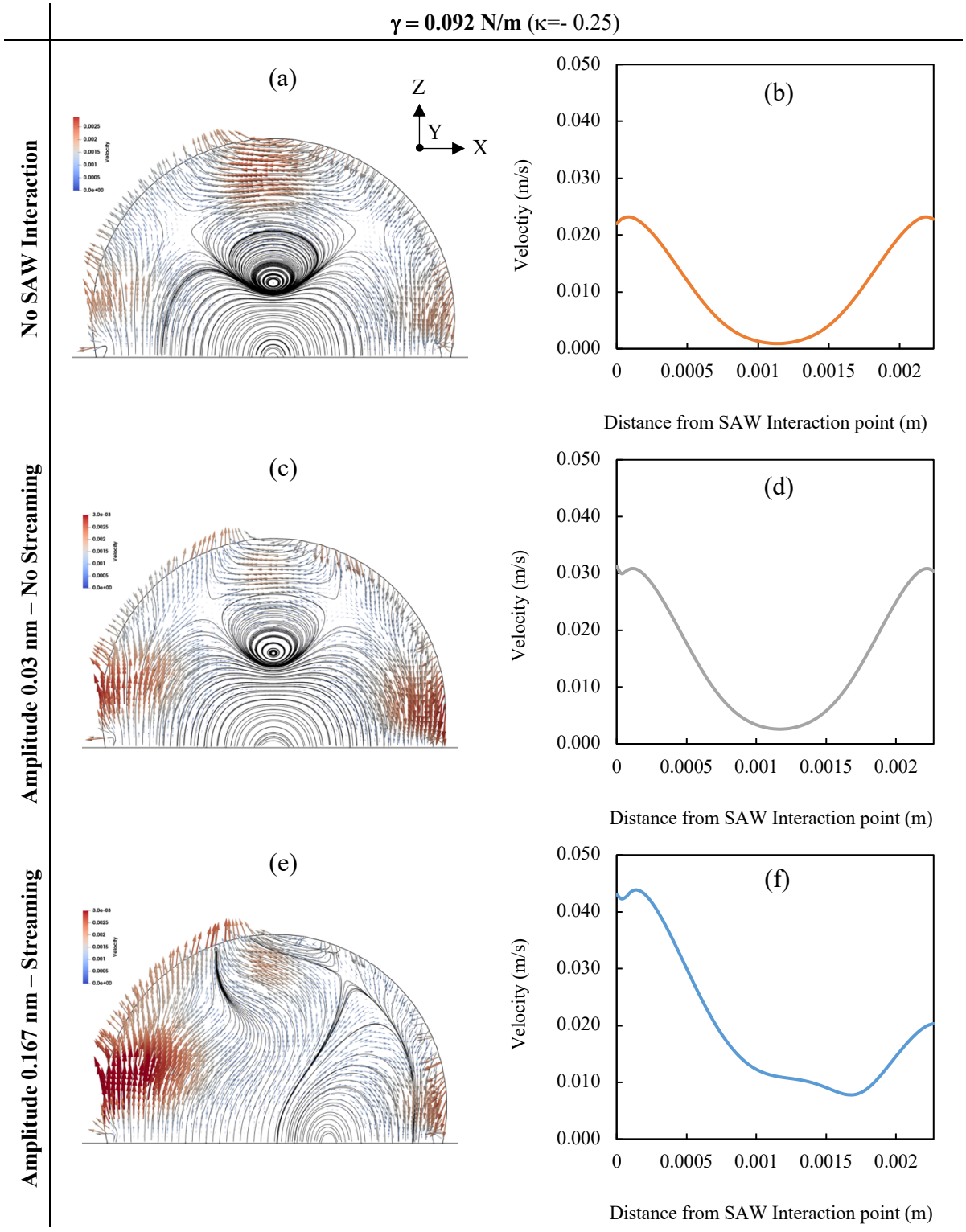

Figure 4-14. Flow field and velocity profiles inside droplet at κ = -0.25 and 61.7 MHz. Droplet without SAW interaction (a,b), and with SAW interaction; 0.03 nm wave amplitude (c,d) and 0.167 nm wave amplitude (e,f) [Note: Flow field in lattice units]. View is slice through centre of droplet at 17 ms.

Similar tests, for a further two interfacial tension variations, are conducted. The spurious currents inside the droplet can be rearranged and reorientated by the SAW forcing, as illustrated in Figure 4-13 and Figure 4-14, if the wave amplitude is sufficiently large. At small amplitudes it has been shown that the forcing does not add enough momentum to the fluid to alter the flow structure already imposed by the numerical scheme, hence a velocity field similar to that of a droplet without SAW interaction is achieved. This flow field is maintained with further increase in wave amplitude until it reaches a threshold, at which point the forcing is able to reorder the flow resulting in a streaming/mixing state.

From this study it has been discovered that an increase in interfacial tension requires an increase in wave amplitude to elicit a streaming mode within the droplet. This can be partly attributed to the increased spurious velocities inside the droplet which are a consequence of the interfacial tension at the intermolecular level. The increased interaction force between phases causes a higher magnitude of currents to be established at the interface. To overcome these currents, a stronger SAW force is required to manipulate and rearrange into a streaming pattern, as shown in Figure 4-11.

In this study, results obtained for mixing/streaming are all from simulations in the streaming dominate regime, which are in good agreement with those from experiments.

4.5.2 SAW streaming/mixing

The first mode, mixing or streaming, is primarily analysed against experimental data. At low magnitude of SAW power, the droplet is able to stay in its original place and undergoes minimal deformation. This is due to the interfacial tension effect being high enough to withstand the SAW interaction. From experiments [34] they investigated the effect of increasing frequency to determine the threshold power to achieve streaming inside the droplet, revealing that an increase in SAW power is required, i.e., 0.2 W at 61.7 MHz to 0.47 W at 250.1 MHz.

Consequently, in the LB simulations a similar outcome is achieved. As shown in Figure 4-15, the droplet is slightly elongated in the z-direction however it remains pinned to the surface even after a few milliseconds. For the range of resonant frequencies, a minimum amplitude is required to initiate mixing inside the droplet. Below this threshold amplitude SAW based streaming does not occur. Instead, unphysical spurious currents dominate, showcasing symmetrical flow patterns inside the drop which can be mistaken for

streaming, ranging in order of magnitude from 10^{-2} to 10^{-5} (in lattice units) dependent on area of droplet being examined. In this study, four different resonant frequencies, as introduced previously, are studied. It is demonstrated that only a small change in SAW amplitude is required between frequencies to achieve mixing phenomena inside the drop.

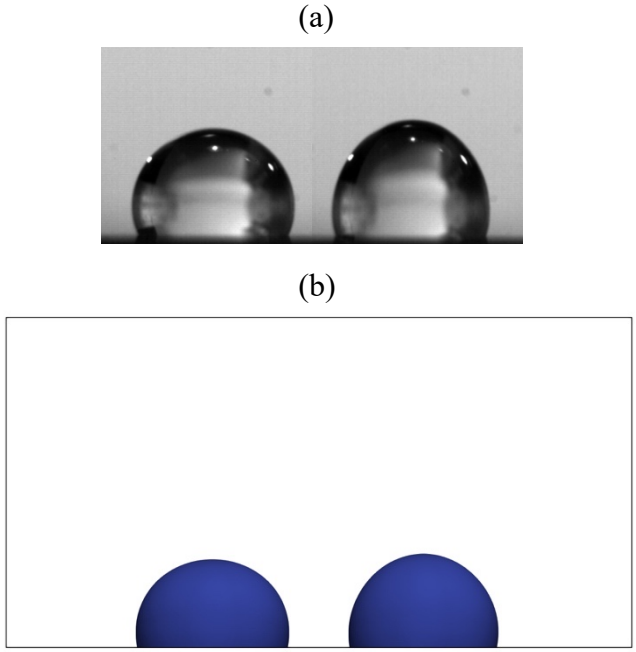

Figure 4-15. (a) Experimental images of deformation phenomena due to streaming for 5 µl droplet operated at 61.7 MHz and low power of 0.2 W and (b) LB simulation results.

4.5.3 SAW pumping and jetting

Moreover, further increase in SAW power provides additional momentum to the fluid along the Rayleigh angle. Increased circulatory motion within the droplet causes a wobbling effect in the initial few milliseconds, where the droplet is held in place although the interface moves upwards from left to right (Figure 4-16). After this period, the droplet moves downwards which causes the rear contact area to begin to creep forward, hence a pumping state is initiated. As reported in [34], a larger disparity between SAW power is required to initiate pumping at lower frequency to high frequency than in the previous streaming mode.

From the research it is found that the non-dimensional SAW amplitude (A/λ) is increased linearly with an increase in SAW frequency, until at high frequencies where the trend is downward (Figure 4-18). Overall, the simulation data are approximately half of those

from the experiments for the range of frequencies. Unlike the mixing/steaming mode, during the pumping the droplet moves along the substrate. The interfacial tension between the fluid and the SAW substrate is not enough to withstand the body force applied during the SAW interaction. Comparing the shape obtained from the experiment to that in the simulation there are some differences. In the experiment the droplet is slightly more elongated to the right, with a tip being formed at the top. However, in the simulation there is no such feature. This could be a consequence of interfacial tension being dissimilar. Overall, the simulations are in agreement as there is some upward movement and slight asymmetry however not as pronounced as in the physical experiment. Additionally, when velocity comparison to the experimental data is examined (Figure 4-17) it is shown that the predictions are in good agreement. In each of the simulated cases, the model slightly over predicts the velocity at the onset of the pumping mode. In our research, a pumping mode is initiated at; $60 < Re < 140$, $0.02 < We < 0.1$, and $3\text{x}10^{-4} < Ca < 7\text{x}10^{-4}$, hence interfacial tension effects are dominant in this region.

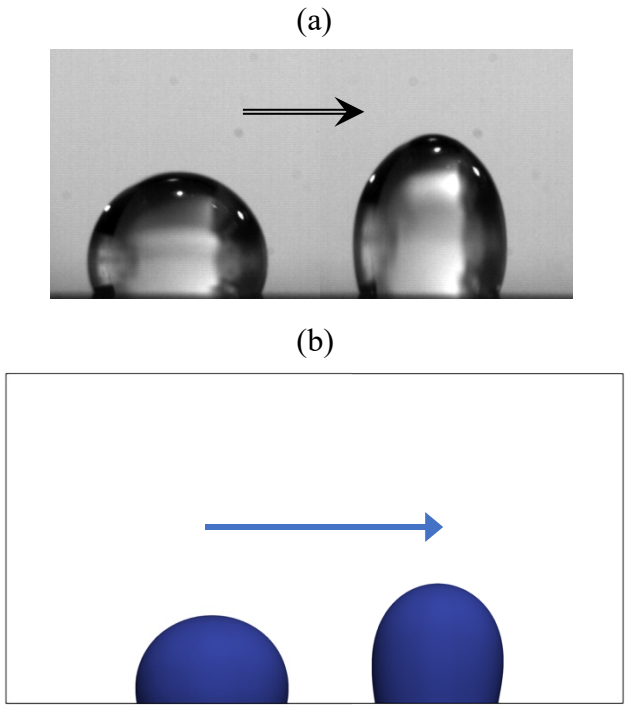

Figure 4-16. (a) Experimental images of pumping phenomena for 5 µl droplet agitated by SAW device with a frequency of 110.8 MHz and applied power of 1.2 W, (b) LB simulation results. Arrows show movement of droplet.

When the SAW power is increased to such a point where the droplet is ejected from the surface, it is termed a jetting mode. Depending on the type of substrate being used,

$LiNbO_3$ or zinc oxide film coated on silicon (ZnO/Si), the shape and overall motion of the jet can be different. The shape can vary from a thin beam [34] to full ejection of the droplet from the surface (Figure 4-17). For ZnO/Si SAW devices [34], although able to achieve jetting effects, they require significantly more power for similar frequency with those for $LiNbO_3$. This is an area which is planned for future research. For $LiNbO_3$ devices the droplet is ejected from the surface as the SAW energy transferred into the liquid is large enough to overcome the those from interfacial tension and gravitational forces. A comparison between experimental and simulation results is presented in Figure 4-17. The results are in good agreement with the shape and general motion of the LB simulations being comparable to those of the experiments.

(a)

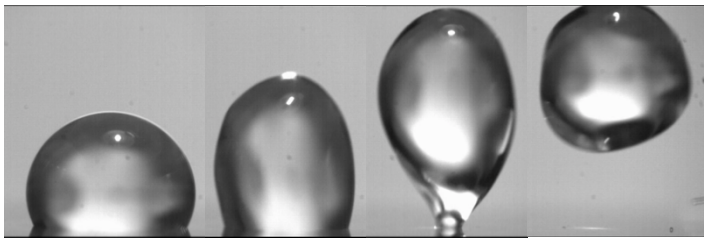

(b)

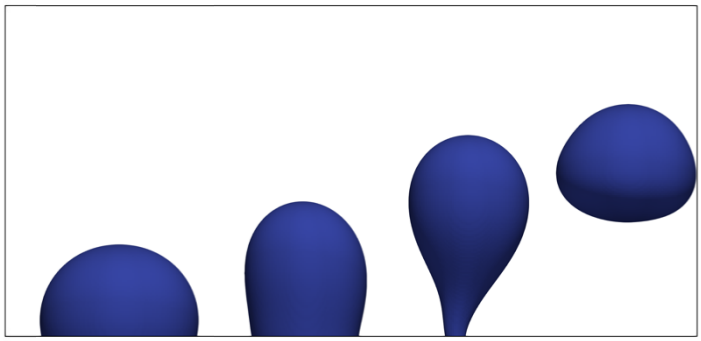

Figure 4-17. (a) Experimental images of jetting mode for 5 μl droplet agitated by SAW device with a frequency of 199.4 MHz and applied power 4.2 W, (b) LB simulation results

From the data it can be shown that the ratio of SAW amplitude to SAW wavelength is almost linear with an increase in SAW frequency (Figure 4-18). Up to frequencies of around 110.8 MHz, the simulation results are in close agreement with the experimental data. Above this frequency, the association starts to diminish. In the initial period the droplet is pushed upwards, elongating vertically and shrinking horizontally whilst the interface is deformed. As the SAW forcing is large, the left contact area is moved in the

x-direction toward the right contact area, causing a balloon shape to emerge. Once the contact area is small enough that the SAW forcing can overcome the interfacial tension, the droplet leaves the surface along the Rayleigh angle.

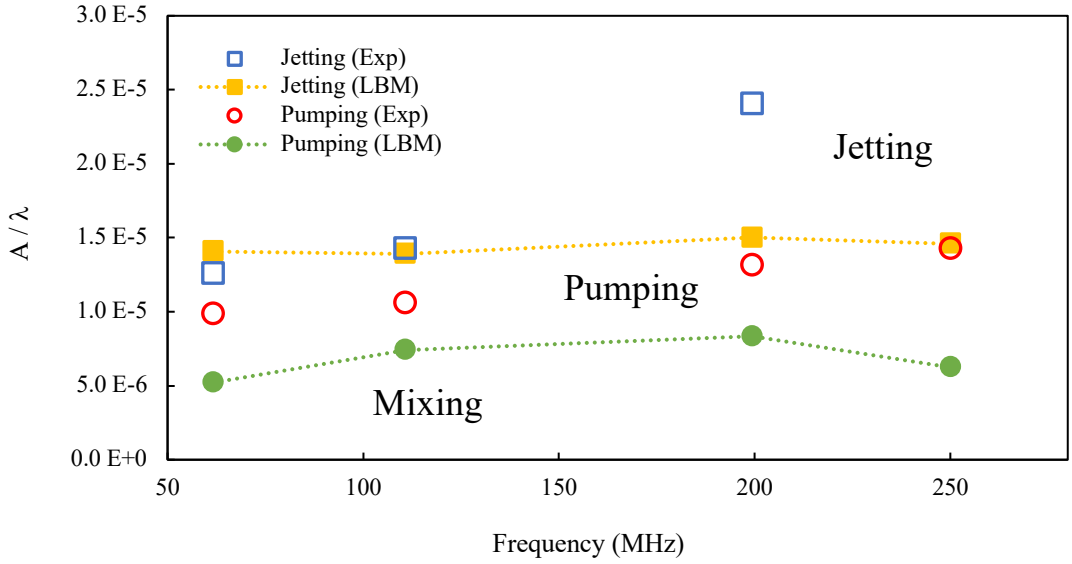

Figure 4-18. Relationship between A/λ and frequency for transitioning between; Mixing, Pumping and Jetting. *(Experimental data extracted from* [34])

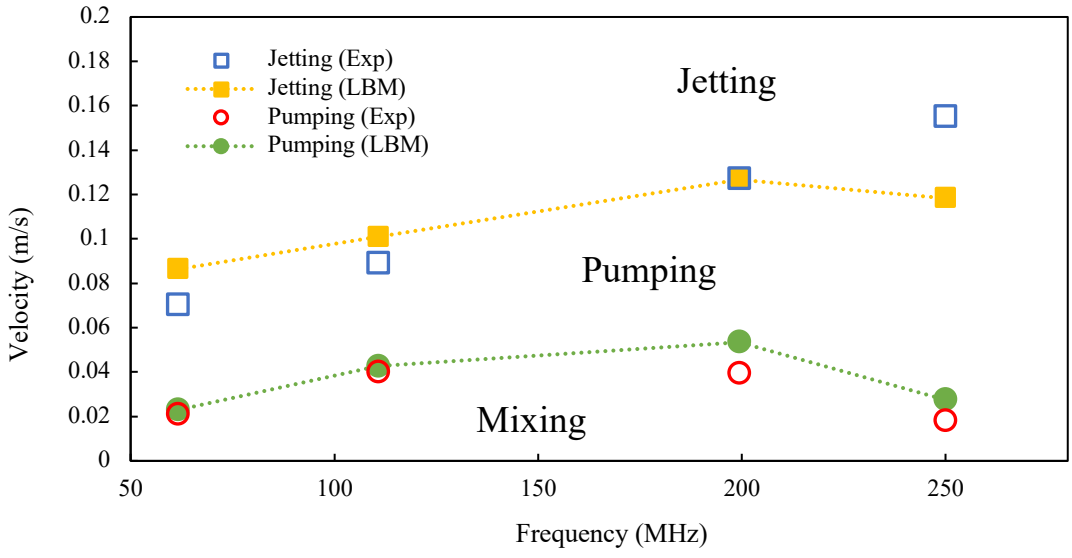

Figure 4-19. Velocity of droplet as a function of resonant frequency at the transition from Mixing to Pumping (pumping data points), and Pumping to Jetting (jetting data points). *(Experimental data extracted from* [34])

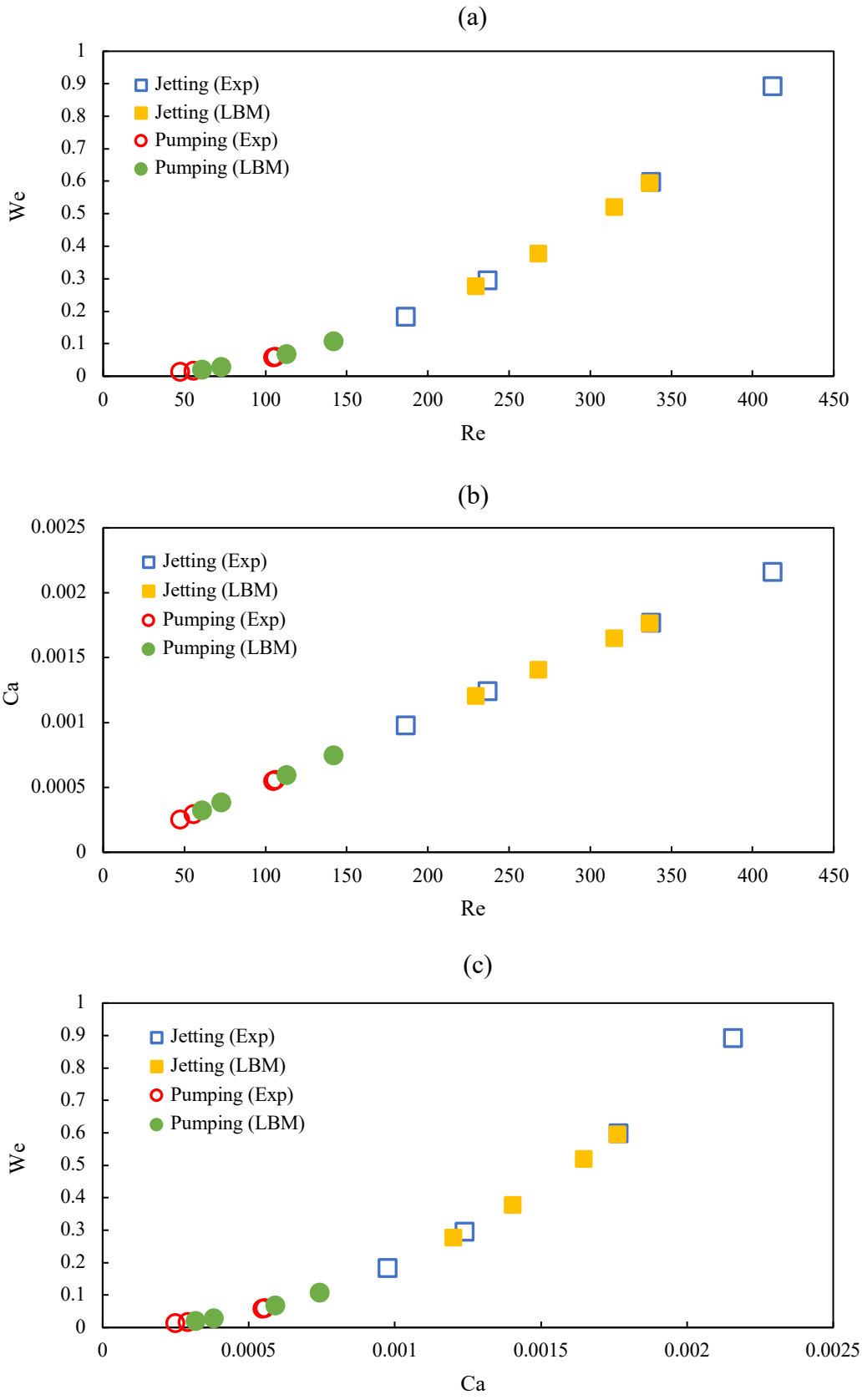

Figure 4-20. Comparison between experimental [34] and simulated data (a) Weber number vs Reynolds number, (b) Capillary number vs Reynolds number, and (c) Weber number vs Capillary number

As shown in Figure 4-19, the velocity data of the simulations alongside the experiment agrees well. For SAW device with frequencies of 61.7 MHz, 110.8 MHz, and 199.4 MHz the numerical velocity is overpredicted slightly, however with 250.1 MHz it is underpredicted quite considerably. In our analysis, jetting mode is commenced at; $230 < Re < 340$, $0.28 < We < 0.6$, and $1.2\text{x}10^{-3} < Ca < 1.8\text{x}10^{-3}$. In the study by Tan et al [26] they witness the onset of single and multiple droplet ejection at Weber numbers of 0.1 and 0.4, respectively. In the study, similar behaviour is observed since at $We < 0.1$ the droplet remains on the surface and undergoes a pumping action, as described previously.

In summary, the above comparison between experimental and LB simulation results demonstrates the ability of the proposed methodology for capturing the intricate dynamics of SAW interactions on a microscale sessile droplet. The validation of mixing, pumping and jetting has been presented and analysed. It is observed that there is a threshold wave amplitude at each frequency, at which the aformentioned modes can be achieved. Analysis of the data reveals that the amplitude present in the model is not consistent with the experimental trend. In spite of this, the results from the study are in good agreement with experimental findings, being within 4% relative error in velocity for pumping and jetting. In the following section, the effects of surface wettability on droplet dynamics are examined when surface acoustic wave interactions are introduced.

4.6 Effect of droplet volume

To further analyse the constructed SAW-LB model, additional tests were carried out with various droplet volumes ranging 1 µl to 10 µl. Similar to the previous section, pumping and jetting modes will be scrutinised for resonant frequencies of 61.7 MHz to 250.1 MHz. Computational setup parameters were kept constant from Section 4.5 with the experimental droplet size changing between cases and hence the conversion factors. Thus, LB parameters ${s_v}^{-1}$ for liquid and vapor alongside SAW variables A, k_i and ω are updated to reflect any changes in droplet volume.

Again, the non-dimensional SAW amplitude is compared for each droplet volume over the range of resonant frequencies studied. As shown in Figure 4-21, it is clear that the largest SAW amplitudes are confined to mostly the 1 µl droplet volume for jetting mode over all frequencies. The overall trend, for each frequency, seems to follow in order of droplet volume size, with the largest A/λ at 1 µl and the lowest at 10 µl. At 61.7 MHz, the dataset is in close proximity of each other whilst as the frequency is increased the

difference between each volume starts to become greater. Most droplet volumes don't require much of an increase in SAW amplitude, between frequencies, to transition from pumping to jetting. Only the 1 µl displays a steep upward trend from 110.8 MHz to 199.4 MHz and even further to 250.1 MHz.

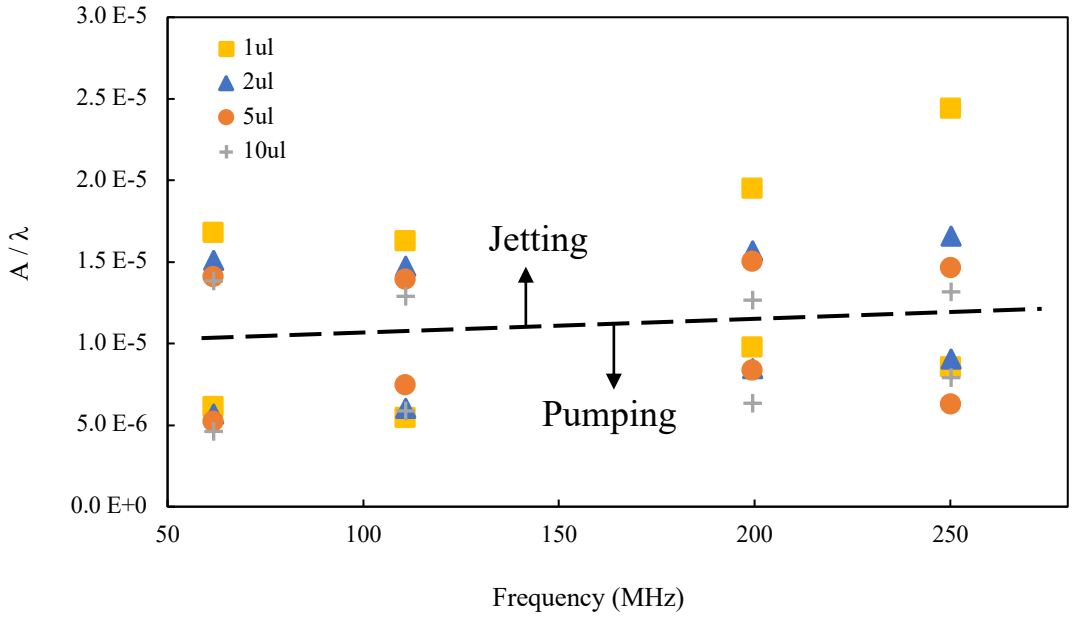

Figure 4-21. Relationship between A/λ and frequency for various droplet volumes. Black dashed line illustrates transition zone between pumping and jetting. Note, streaming zone has been omitted for clarity.

Additionally, for the pumping region the data suggests a much more chaotic trend. Initially, for low resonant frequency of 61.7 MHz, the data points are closely bunched together suggesting the applied SAW amplitude is similar for all volumes. However, this trend is not visible over the range of frequencies with a wide variety and organisation of points being observed. Unlike the jetting regime, there is no clear order to each set of frequencies, where the largest and smallest A/λ fluctuates between each of the volumes, hence no real conclusions can be made based on the data.

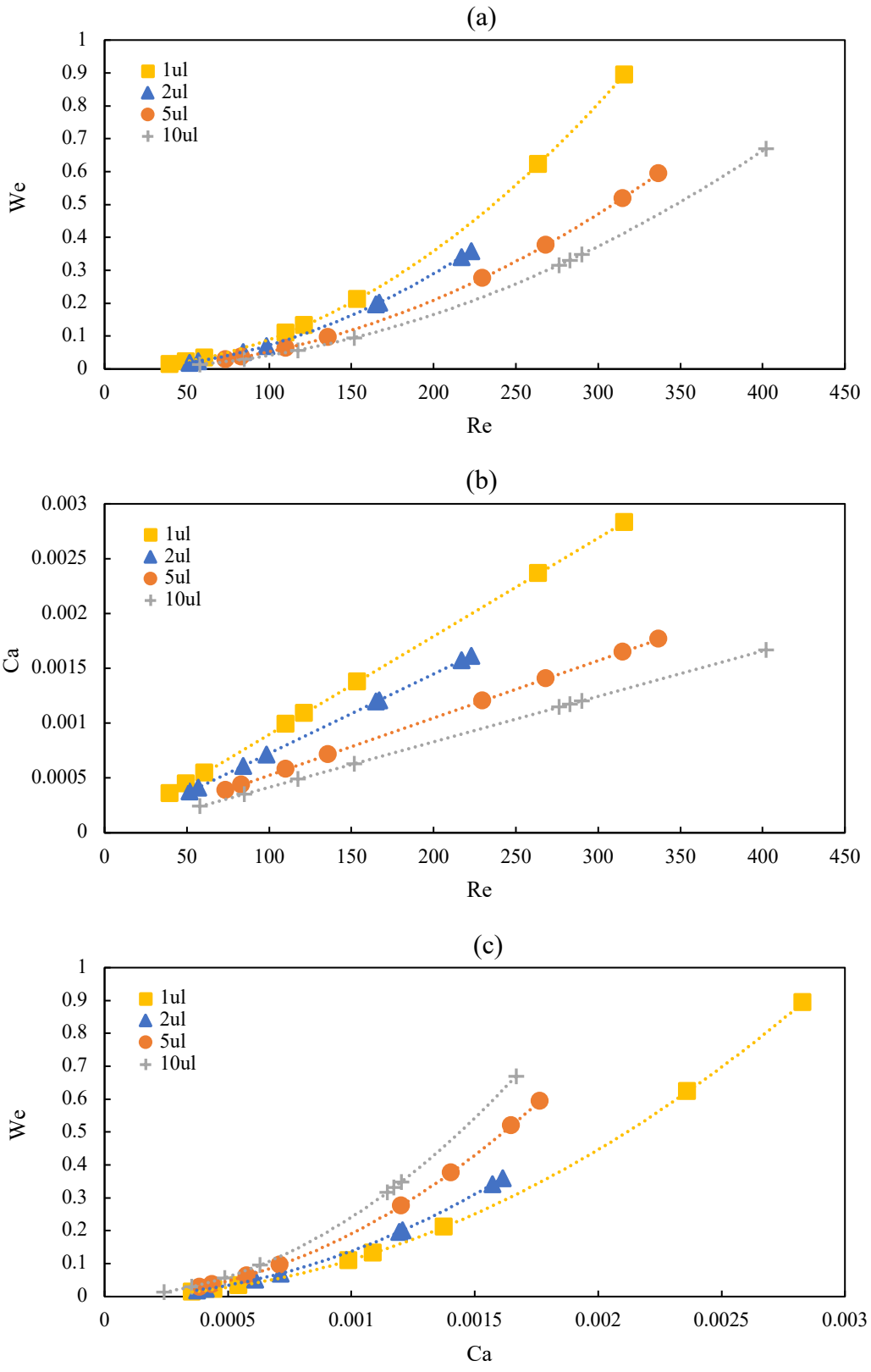

Figure 4-22. Comparison of droplet volume for simulated data (a) Weber number vs Reynolds number, (b) Capillary number vs Reynolds number, and (c) Weber number vs Capillary number

Looking more closely at the droplet movement for each volume tested, again a series of non-dimensional numbers, namely Weber, Reynolds and capillary number are adopted. The results are detailed in Figure 4-22. At lower Reynolds numbers ($Re < 100$) there is not much distinction between all volumes, however as it is increased further a clear division is perceived, as shown in Figure 4-22 (a). Interestingly, a clear trend is observed with the highest Weber numbers resulting from the smallest droplet volume. An increase in inertia, in the smaller volumes, allows for the droplet to be translated and ejected from the substrate much more easily. Looking closer at Figure 4-22 (b) for the same value of Reynolds number, a higher capillary number is achieved by the smaller droplet volumes. The increased velocity in small droplets causes a higher viscous drag which overcomes the surface tension; thus, the droplet is ejected more easily. Lastly, when comparing Weber number to capillary number in Figure 4-22 (c) there is a visible trend in the data. At capillary numbers ($Ca < 0.0005$) the data is almost indistinguishable with no perceivable differences, whereas above this value the trends start to emerge. For an equivalent value of capillary number, a higher Weber number is generated for larger droplet volumes. Conversely, for an equivalent value of Weber number, a higher capillary number is achieved for smaller volume droplets.

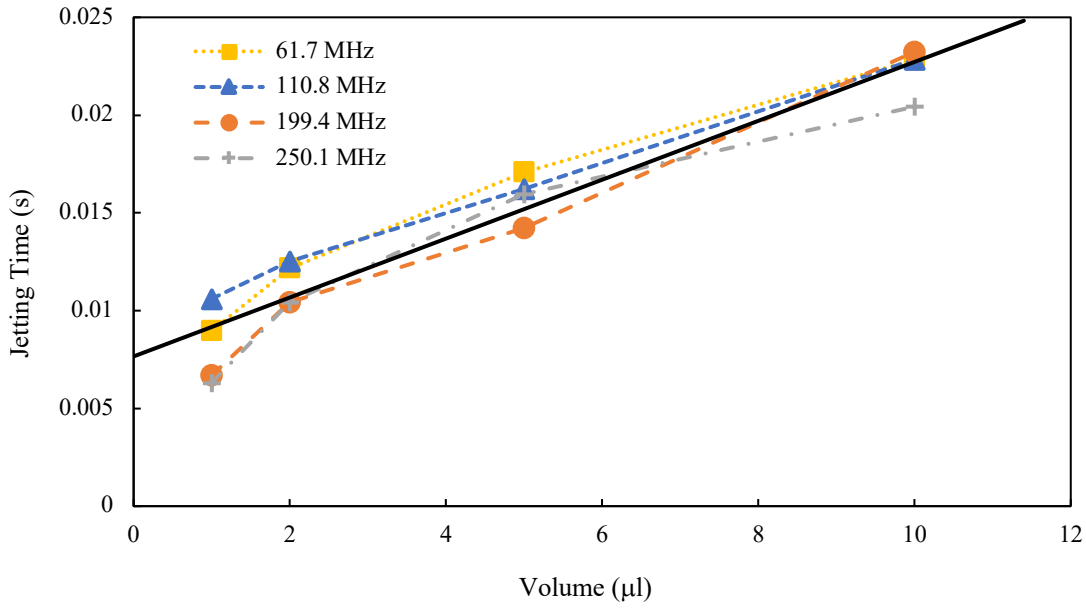

Figure 4-23. Numerical results for jetting time against droplet volume for various resonant frequency. Black line indicates linear trend of jetting time and droplet volume

Taking a closer look at the jetting regime (Figure 4-23), when the jetting time is considered there appears to be a clear upward trend, with lower times being experienced for the smaller droplet volume, increasing steadily as the volume is increased. This linear trend can be expressed as $\text{Time (s)} = 0.0015\text{V}(\mu\text{l}) + 0.007$, hence approximate predictions of jetting time can be easily calculated for various droplet volumes, negating the need for experimental observation which could save time and resources.

The findings reveal that smaller droplet volumes can be manipulated more easily than larger droplets due to higher inertia overcoming viscous and adhesive forces. This allows for increased droplet velocity on the substrate and a reduction in jetting time, leading to faster ejection from the surface. The variation in time across the droplet volumes examined indicates a linear relationship which can be implemented for quick and approximate jetting time calculations.

4.7 Evaluation of LB parameters on dynamic behaviour

In the subsequent sections, the effects of LB parameters such as surface wettability, viscosity ratio and interfacial tension are studied, on droplet dynamics excited by SAW, to determine the role each plays in interface deformation, effectiveness of acoustic wave coupling and mode outcome.

4.7.1 Effect of surface wettability

In this part, the effect of surface wettability on droplet dynamics is analytically investigated for the specific case of resonant frequency 199.4 MHz. All SAW parameters are kept constant with only the surface wettability being modified. Three wettability's are chosen to be investigated: with initial static contact angles (θ_s) of 60º, 90º and 120º. The shape and subsequent modes are analysed to determine the effect droplet contact angle has on SAW energy transfer into the droplet.

As shown in Figure 4-24, a change in surface wettability can vastly alter the amount of SAW energy transferred into the droplet, resulting in different dynamics. For the hydrophilic surface (e.g. θ_s of 60º) the SAW interaction results in spreading with slight droplet movement. The increased interfacial tension, due to lower contact angle, is strong enough to overcome the SAW force. Moving to the surface with a static contact angle of 90º, no spreading on the SAW surface is observed, while, only a pumping state is achieved as the acoustic forcing is not sufficient to cause ejection from the surface. Again, this can

be explained by an increased contact area being able to withstand the forcing for longer as compared to the hydrophobic surface. An increase in SAW power would be required to cause a transition from pumping to jetting at this wettability condition, as shown in Figure 4-24.

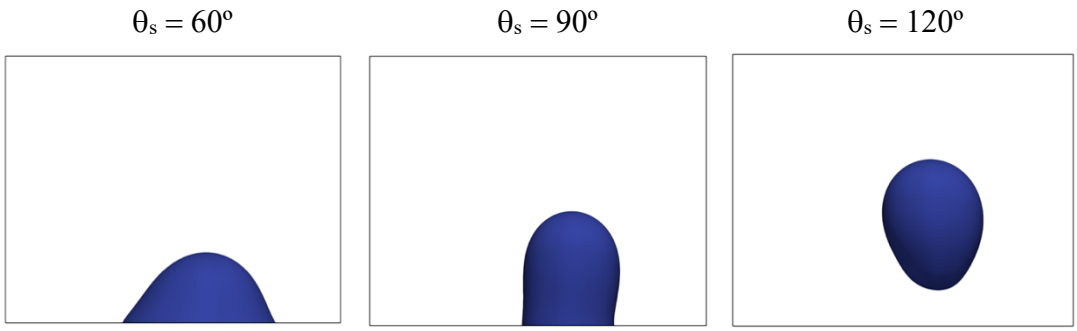

Figure 4-24. Simulation results at 10ms for resonant frequency 199.4MHz at different surface wettability

The findings from the study reveal the importance of surface wettability to effectiveness of SAW energy transfer into the drop. At the same wave amplitude and frequency, through altering the wettability of the substrate, different modes can be achieved, intentionally or unintentionally. Careful design of the SAW device can allow for more efficient energy transfer, resulting in less power requirements. This can be particularly useful for applications involving DNA where cells are susceptible to damage [42].

4.7.2 Effect of viscosity ratio

In this portion, an investigation into the effect of viscosity difference on droplet dynamics, in the presence of surface acoustic wave interactions, is conducted. Similar to previous, all computational parameters are kept constant with the exception of kinematic viscosity. In order to introduce a viscosity difference between the liquid and gas/vapour phase the conventional methodology is adopted, where $\nu(\rho) = \nu_l$ for $\rho > \rho_c$ and $\nu(\rho) = \nu_g$ for $\rho \leq \rho_c$ [162].

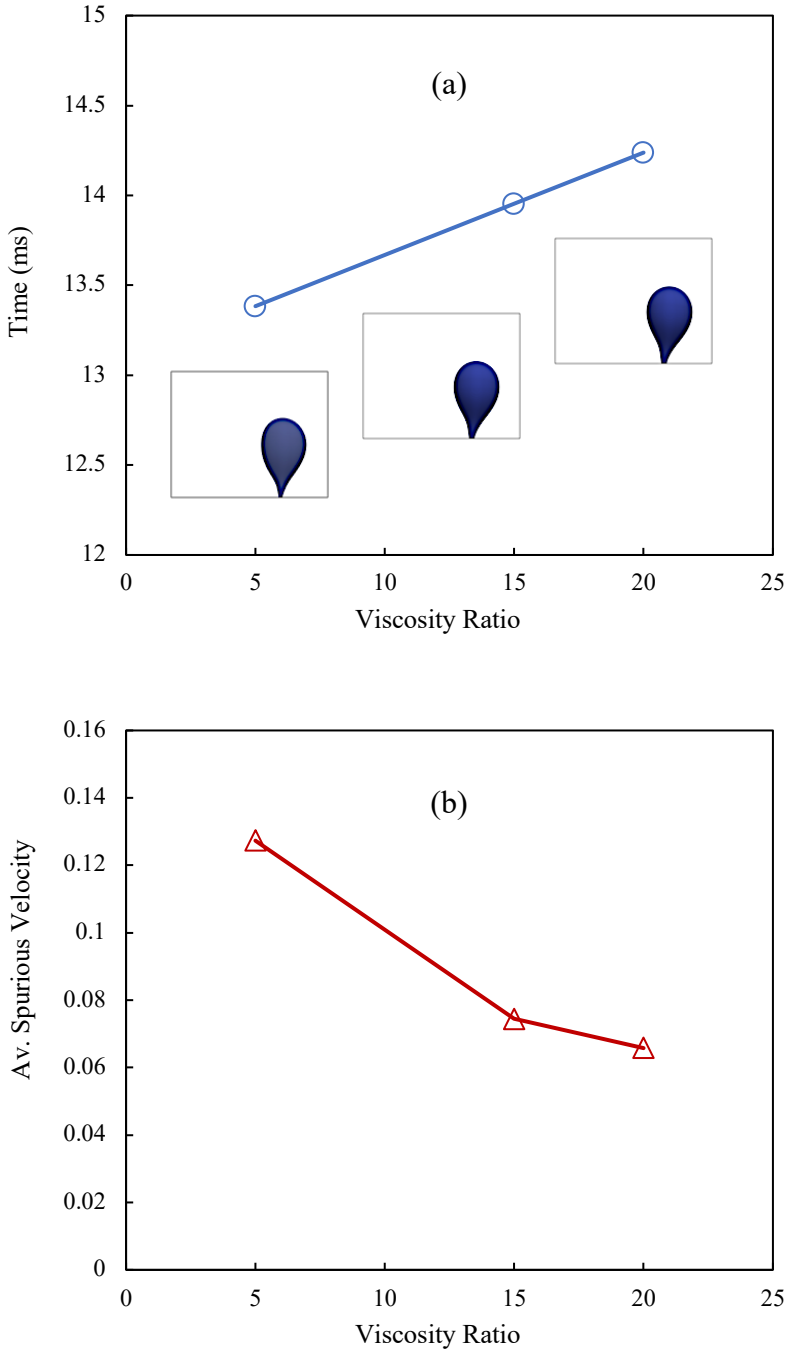

Figure 4-25. Numerical results for jetting at resonant frequency 199.4 MHz (a) Time for droplet to be ejected from surface against viscosity ratio (b) Average spurious velocities, in the simulation domain, before SAW interaction against viscosity ratio

Considering the above treatments, three different cases are investigated for the present test; $\nu_g/\nu_l = 5$, $\nu_g/\nu_l = 15$ and $\nu_g/\nu_l = 20$. As before, a resonant frequency of 199.4 MHz has been assumed, with droplet shape and motion being compared when a jetting mode is witnessed.

As can be seen in Figure 4-25 (a), the effect of viscosity ratio on droplet dynamics is apparent. An increase in viscosity ratio has been shown to linearly increase the time taken for the droplet to be ejected from the surface of the substrate. This delay in jetting can be explained due to the increased viscosity of the gas phase slowing the energy transfer as the droplet interface is moved along the Rayleigh angle. Another interesting aspect to note is the reduction in spurious velocities as a consequence of viscosity ratio (Figure 4-25 (b)). The unphysical parasitic velocities which plague most multiphase LB models are those which can cause major instabilities in models, especially dynamic simulations. A reduction can be useful in both helping to stabilise the computational domain and when analysing results.

4.7.3 Effect of interfacial tension

To analyse the effect of interfacial tension between the liquid and gas/vapour, the Xu et al method [185] is employed, described in Eq. 4–11, which is an extension of the already widely used methodology proposed by Li-Luo [184] to 3D space. It has been commented in the literature [159] that this approach is more effective for reducing interfacial tension whereas the scheme by Huang-Wu [192] is more suited to increasing interfacial tension. It is assumed that currently this strategy for interfacial tension adjustment has not yet been extended to 3D hence why the aforementioned has been selected for this work.

To study the effect of interfacial tension on droplet behaviour, a resonant frequency of 199.4 MHz and a jetting regime is once again chosen. As before, the same computational setup is maintained with only the interfacial tension adjustment parameter, κ, being altered. A range of κ, from -0.25 to 0.25, is investigated which will provide some insight into how increasing or decreasing interfacial tension effects the transfer of surface acoustic wave energy into the microdroplet.

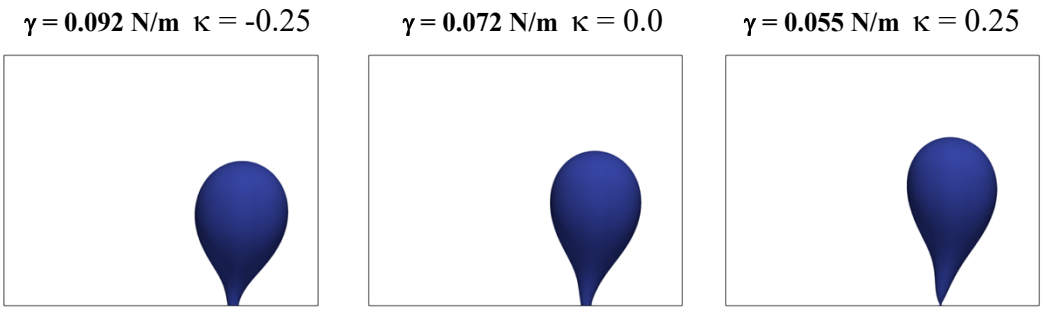

Figure 4-26. Simulation results at 14 ms for resonant frequency 199.4MHz at different interfacial tension

The results illustrate the effect of modifying the interfacial tension between the droplet and the surrounding gas/vapour. At the moment just before the droplet is ejected from the surface, the shape and dynamics are scrutinised. Looking at Figure 4-26, going from left to right, there are some differences in the droplet dynamics. At an increased interfacial tension (κ = -0.25) the droplet is slightly more balloon shaped and has more of a curvature, leaning further to the right, whereas with a reduced interfacial tension (κ = 0.25), the droplet is elongated further along the Rayleigh angle, with less curvature and balloon shape. This demonstrates that the interfacial tension has a strong influence on droplet shape however has less impact on droplet dynamics since, in all scenarios, the droplet is ejected from the substrate at approximately the same amount of time. Interestingly, the maximum velocity inside the droplet at the moment before ejection is altered as a result of interfacial tension adjustment. An increase in interfacial tension results in a rise in velocity of approximately 4.5% compared to the unmodified droplet. Similarly, when the interfacial tension is reduced, there is a lesser increase in maximum internal velocity of $\approx$1.6%.

4.8 Summary

In summary, a three-dimensional numerical model for acoustic interactions with microscale sessile droplets under SAW excitation is developed, using a two-phase multiple relaxation-time pseudopotential lattice Boltzmann method. The proposed model is initially validated against numerical benchmark tests. The results are in excellent agreement with the analytical solutions.

The developed model is then used in the study of SAW interactions with a microscale sessile droplet on a $LiNbO_3$ substrate. Simulation results are validated against

experimental data, evaluating mixing, pumping and jetting modes. A good agreement between simualtions and experiments is achieved. The results demonstrate the applicability of the proposed methodology in the prediction of droplet dynamics subjected to SAW agitations. It is observed that there is a threshold wave amplitude at each frequency, at which the aformentioned modes can be achieved. Analysis of the data reveals that the amplitude in the model is not consistent with the experimental trend. Despite this, the results from the study agree with experimental findings, being within 4% relative error in velocity for pumping and jetting. The transition of mixing to pumping state is observed at $We > 0.02$, $Ca > 3\text{x}10^{-4}$ and $Re > 60$, with the onset of jetting mode at $We > 0.1$, $Ca > 1.2\text{x}10^{-3}$ and $Re > 230$.

Additionally, the effect of droplet volume has been examined. The results uncover that smaller droplet volumes can be manipulated more easily than larger droplets due to higher inertia overcoming viscous and adhesive forces. This allows for increased droplet velocity on the substrate and a reduction in jetting time, leading to faster ejection from the surface. The variation in time across the droplet volumes examined indicates a linear relationship which can be implemented for quick and approximate jetting time calculations.

Furthermore, the effect of surface wettability on droplet dynamics is investigated. It is found that on hydrophilic surfaces, the energy transfer from the SAW to the droplet is impeded by the large interfacial tension force. This is in opposition to hydrophobic surfaces where the droplet is moved and ejected from the substrate more easily. These results can be useful in the development of more efficient SAW devices.

Moreover, the effect of viscosity ratio and interfacial tension has been investigated when the droplet is subjected to SAW interactions. The findings reveal that viscosity ratio can play a role in delaying the ejection of the droplet from the surface. Movement of the liquid-gas/vapour interface is slowed resulting in a longer jetting time. Modification of the interfacial tension can lead to different droplet dynamics being witnessed. At larger interfacial tension, the droplet resists the deformation from the acoustic wave propogation, maintaining its spherical balloon shape. Alternatively, a reduction in interfacial tension allows the droplet to deform more along the Rayleigh angle, resulting in a longer jet to be seen. Focusing on the maximum internal jetting velocity, it is interesting to note that modifying the interfacial tension alters the velocity magnitude, nevertheless this has inconsequential impact of the ejection time from the SAW substrate surface.

Chapter 5– Influence of configuration parameters on SAW-droplet interactions

This chapter reports the influence of numerical simulation configuration parameters on SAW-droplet interactions. The effect of contact angle hysteresis (CAH) is investigated and its consequence compared to experimental data and results in the previous chapter (Chapter 4), with focus on A/λ ratio, droplet velocity and non-dimensional numbers. Additionally, spurious velocities are further examined in relation to choice of MRT free parameters and EOS to provide further understanding on their influence on SAW-droplet interactions.

5.1 Introduction

Considering the previous study, the influence of spurious velocities has been shown to have an adverse impact on the numerical stability due to large magnitudes forming near the liquid-vapour interface, causing large velocity gradients. Additionally, determining the impacts of external forcing can often be complex as the magnitude of spurious velocities is similar to streaming flow inside the droplet. Thus far, it has been shown how this can be circumvented somewhat by demonstrating precise zones where the flow field can be assumed to be appropriately rearranged as a consequence of the forcing, hence the data can be suitably examined and compared. In the subsequent sections, spurious velocities reduction will be investigated through choice of MRT free parameters and EOS implementation. The role of spurious velocities in SAW-droplet interactions will then be examined to provide a better understanding of cause and effect.

5.2 Investigation of MRT free parameters on spurious velocities

The relaxation matrix in the D3Q15 model $\boldsymbol{S} = \mathrm{diag}(s_\rho, s_e, s_\varepsilon, s_j, s_q, s_j, s_q, s_j, s_q, s_\nu, s_\nu, s_\nu, s_\nu, s_\nu, s_{xyz})$ has 15 relaxation rates. Variables s_ρ and s_j correspond to collision invariants (ρ, j_x, j_y, j_z) which are conserved during the collision process, hence the choice of relaxation rate is unimportant. It has been noted in the literature that these variables should be set to a non-zero value to obtain the correct hydrodynamic equations in the continuum limit [193]. By setting the relaxation rates to unity ($s_\rho = s_j = 1$) second-order discretisation of source terms is preserved. Moreover, s_e and s_υ are related to the bulk and kinematic viscosities, respectively. Additional parameters s_ε, s_q and s_{xyz} are related to the kinetic energy square, energy flux and

antisymmetric third-order moment, respectively. These parameters are considered free to modify and tune in the model.

Due to the impact of spurious velocities in the model, in this section an investigation into the effect of modifying the relaxation rates in the diagonal matrix is carried out to determine the most optimum configuration for the current study. The intended outcome from modification of the relaxation matrix would be low spurious velocities in the liquid and gas phase whilst unaffecting variables such as density ratio. Low spurious velocities inside the droplet (liquid phase) provide a much clearer insight into how the SAW interactions affect the flow patterns, whilst a reduction in the surrounding gas phase enhances stability of the model.

Initially, the sensitivity of each parameter is determined through a Taguchi method, where an orthogonal L_{16} array is adopted, with three factors and four levels. The Taguchi method allows factors in experiments to be independently evaluated by means of a small number of trials [194]. As part of the study, the three factors (A, B and C) represent the relaxation parameters $(s_\varepsilon, s_q \text{ and } s_{xyz})$ with the four levels of optimisation (1, 2, 3 and 4) signifying $(1, 0.7, 1.1, \text{and } 0.3333)$, given in Table 5-1.

Table 5-1. L_{16} orthogonal array and results of maximum spurious velocities

Test	Factor			Velocity [Vapour]	Velocity [Liquid]
	A	B	C	(lu/ts)	(lu/ts)
1	1	1	1	2.30E-03	1.73E-03
2	1	2	2	9.22E-03	4.35E-03
3	1	3	3	3.96E-03	1.51E-03
4	1	4	4	4.26E-02	2.35E-02
5	2	1	2	1.84E-03	1.78E-03
6	2	2	1	8.58E-03	4.17E-03
7	2	3	4	2.38E-03	1.92E-03
8	2	4	3	3.51E-02	2.13E-02
9	3	1	3	2.39E-03	1.72E-03
10	3	2	4	1.13E-02	4.85E-03
11	3	3	1	3.90E-03	1.52E-03
12	3	4	2	3.89E-02	2.38E-02
13	4	1	4	2.20E-03	2.19E-03
14	4	2	3	7.99E-03	3.89E-03
15	4	3	2	3.13E-03	1.58E-03
16	4	4	1	3.03E-02	1.63E-02

The average spurious velocity for each factor is collected at each level in the vapour phase, and the outcome presented in Table 5-2 and Figure 5-1. Analysing the figure, both factors A and C appear to be relatively unaffected by changes in level value. From this initial evaluation it has been shown that the magnitude of spurious velocity for factor B can be adjusted by up to 95% through choice of level value.

Table 5-2. Average spurious velocity values for each factor and factor level in the vapour phase

Factor	Average spurious velocity in vapour phase			
	Level 1	Level 2	Level 3	Level 4
A	1.45E-02	1.20E-02	1.41E-02	1.09E-02
B	2.18E-03	9.28E-03	3.34E-03	3.67E-02
C	1.13E-02	1.33E-02	1.24E-02	1.46E-02

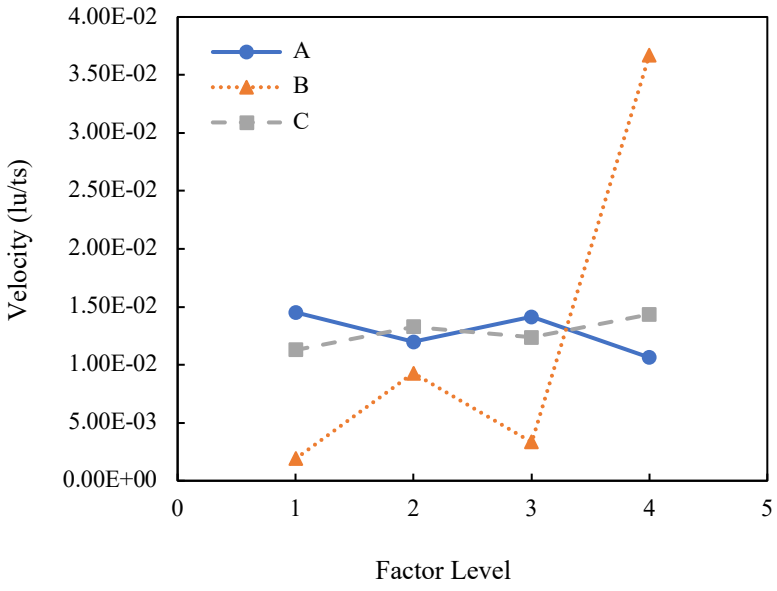

Figure 5-1. Average spurious velocity response of each factor for vapour phase

Moreover, the average spurious velocity for each factor is gathered at each level in the liquid phase. Examining Table 5-3 and Figure 5-2, again both factors A and C appear to be relatively unaltered by changes in level value. On the other hand, it has been shown that, for factor B, the magnitude of spurious velocity inside the droplet can be adjusted by up to 92% through choice of level value.

Table 5-3. Average spurious velocity values for each factor and factor level in the liquid phase

Factor	Average spurious velocity in liquid phase			
	Level 1	Level 2	Level 3	Level 4
A	7.77E-03	7.30E-03	7.98E-03	5.99E-03
B	1.85E-03	4.31E-03	1.64E-03	2.12E-02
C	5.93E-03	7.88E-03	7.12E-03	8.11E-03

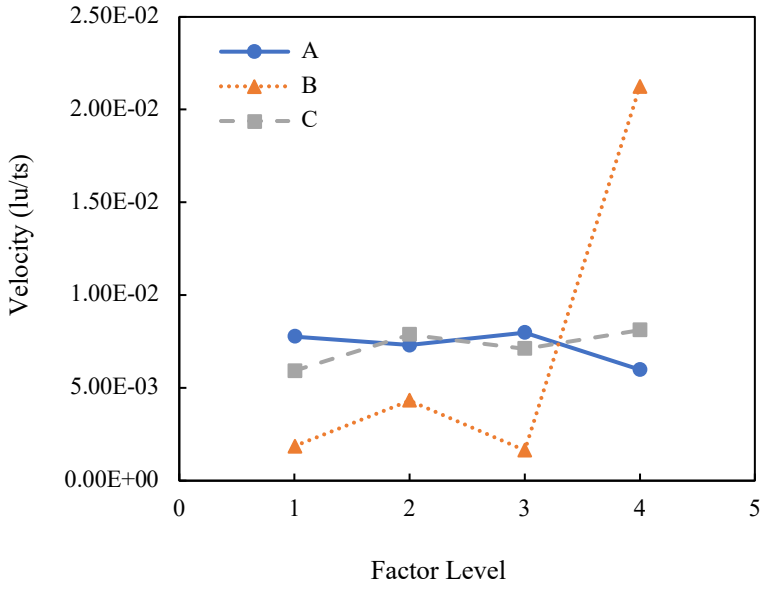

Figure 5-2. Average spurious velocity response of each factor for liquid phase

To find the optimum configuration of relaxation parameters, the data is further examined. The pre-set relaxation rates used so far in the study (see Section 4.4.2), will be used as a reference from which the cases will be initially compared to. Factor levels (1-4) are reviewed in relation to factor B to evaluate its impact on spurious velocities. Note, test variations will be referred to according to their number shown in Table 5-1 for simplicity.

As presented in Figure 5-3, the tests have been organised according to the factor level for factor B, allowing for a visual comparison of the data. It is evident that levels 2 (Figure 5-3 (b)) and 4 (Figure 5-3 (d)) result in unfavourable spurious velocities with a large rise over the reference case. All tests produce greater magnitude velocities inside the liquid droplet and in the surrounding vapour phase, hence this configuration is not particularly suitable for the study of fluid dynamics at high density ratio. Moreover, level 3 (Figure 5-3 (c)) configurations are shown to have a minimal response to the variation in parameter

value, exhibiting values close to the reference case. Thus, level 1 (Figure 5-3 (a)) provides the most optimal outcome with a large reduction in spurious velocities throughout the domain (vapour phase). Looking closer at the data (tests 1, 5, 9 and 13), the largest reduction of spurious velocities in the vapour phase is achieved when s_ε and s_{xyz} are set to 0.3333. Interestingly, increasing these values results in an inferior reduction as compared to the reference case. Additionally, alteration in the configuration values has only a slight consequence to the magnitude of spurious velocities inside the liquid drop. Over the tests conducted in level 1, the variation in results range from 10% to 29%, with the lowest achieved when s_ε and s_{xyz} are set to either 1.0 or 1.1.

(a) Level 1

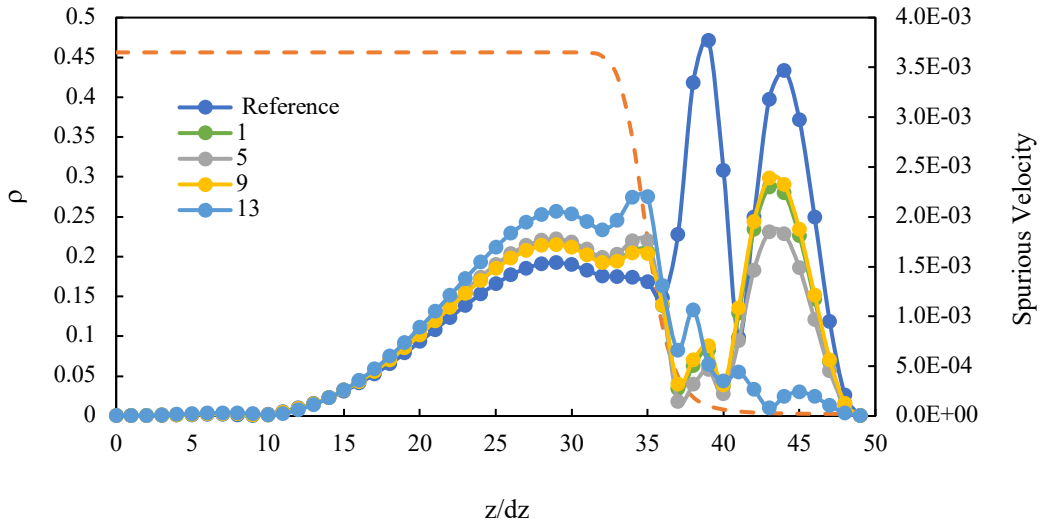

(b) Level 2

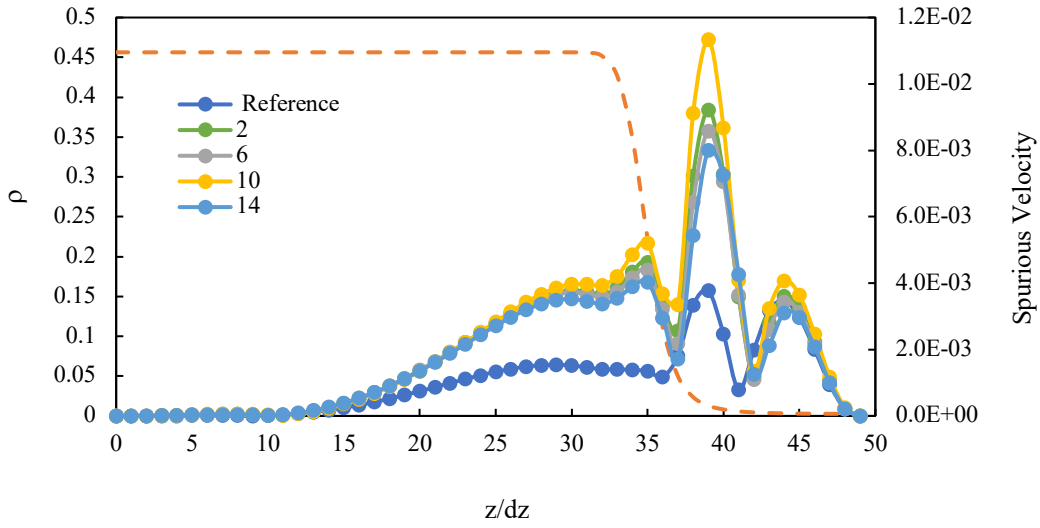

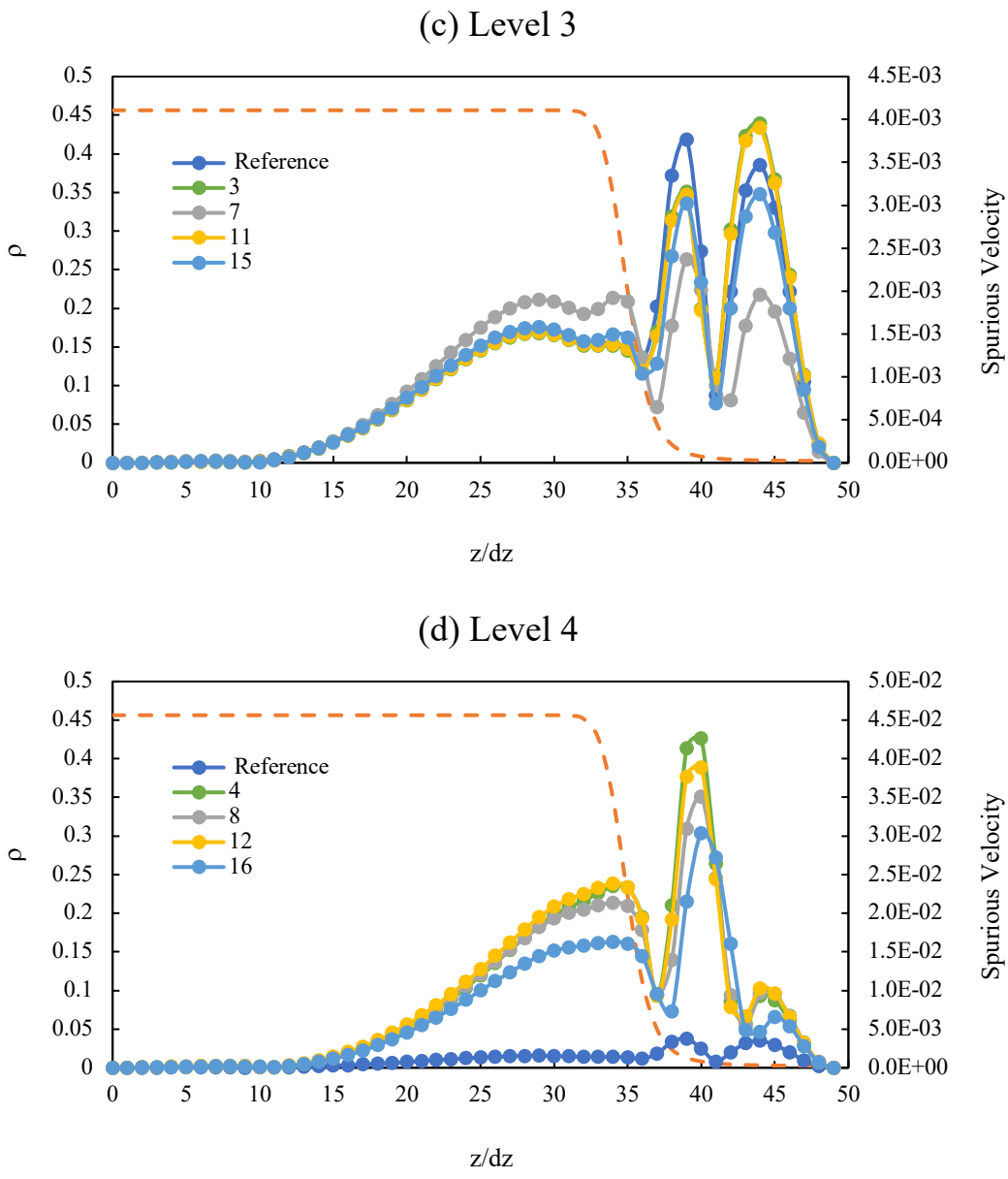

Figure 5-3. Comparison of spurious velocities with factor level in Taguchi method, organised for factor B. Dashed orange line represents density profile.

The results in Figure 5-3 indicate that:

- Reducing the value of s_q below 1.0 leads to a large increase in spurious velocities in the vapour and liquid phases
- Setting the value of s_ε and s_{xyz} to 0.3333 leads to a significant decrease in spurious velocities in the vapour phase when $s_q = 1.0$
- Setting the value of s_ε and s_{xyz} to 1.0 or above provides the most optimum magnitude of spurious velocities in the liquid phase when $s_q = 1.0$

Considering all the above, there are some clear indicators which can help in the reduction of spurious velocities and hence provide a more stable computational simulation. Most alterations provide an unfavourable change in the magnitude inside the droplet, as compared to the reference values. The foremost advantage of optimising the relaxation parameters appears primarily in the vapour phase (outside the droplet), where large reductions can be made.

According to the Table 5-2, an optimum configuration of relaxation parameters for reduced spurious velocities, in the vapour phase, is s_ε = 0.3333, and s_q = s_{xyz} = 1.0. Similarly, inspecting Table 5-3, optimal relaxation values for reduced spurious velocities, in the liquid phase, are s_ε = 0.3333, s_q = 1.1 and s_{xyz} = 1.0. These arrangements are analysed and compared to the reference values.

Table 5-4. Maximum spurious velocities, in liquid and vapour phase, for optimal relaxation parameters compared to reference values

	Vapour		Liquid	
	Velocity (lu/ts)	Change from Reference value	Velocity (lu/ts)	Change from Reference value
Reference	3.77E-03		1.54E-03	
Optimal (vapour)	1.94E-03	-94.70%	1.72E-03	10.58%
Optimal (liquid)	3.50E-03	-7.63%	1.52E-03	-1.23%

As expected, when the optimal values are adopted, the maximum spurious velocities in the vapour phase are reduced considerably with an increase in the liquid phase, as depicted in Table 5-4. Interestingly, this configuration does not result in the largest reduction as test 13 provides a decrease of approximately 255% over the reference data. Likewise, the configuration chosen for the liquid phase results in a small reduction in spurious velocities inside the droplet (Table 5-4). Again, these values do not provide the biggest decrease, with test 3 resulting in a decline of around 1.7% as compared to the reference data.

Considering the reasoning behind modifying the relaxation matrix, there appears to be only one logical case which fulfil the criteria. Test cases presented in factor level 1 of Figure 5-3 demonstrate the best outcomes, although they are all slightly different.

Contemplating the dynamic nature of the simulations being carried out and tested in this instance, it makes sense to have a much more stable computational domain at the expense of a slight rise in spurious velocities inside, hence moving forward the free relaxation parameters will be set to unity ($s_\varepsilon = s_q = s_{xyz} = 1.0$) in the remaining chapters of this thesis.

5.3 Effect of contact angle hysteresis (CAH) on droplet dynamics

As demonstrated in the previous section, the developed pseudopotential LB model can capture the intricate interactions between SAW's and a microscale sessile drop. The qualitative and quantitative results show good agreement with the experimental data, establishing the numerical model is capable. The model has been shown to provide excellent agreement at lower resonant frequencies (i.e., <150 MHz) in the jetting regime, however for the pumping mode there are some clear differences. One reason postulated for this discrepancy has been the interfacial tension or more precisely the adhesive interaction between the liquid droplet and the substrate. In the physical experiments, once the SAW interacts with the droplet, to overcome the momentum the contact line dynamically adjusts, resulting in a stronger adhesive force. Once the SAW power reaches a certain value, the inertia inside the drop is large enough to overcome the liquid-solid interaction, resulting in droplet movement across the substrate. The fluid momentum is still low enough to allow the front and rear contact areas to move reasonably hence a pumping or translation mode is initiated. Further increase in SAW power causes a more instantaneous increase in flow velocity inside the droplet hence the liquid is manipulated more distinctly along the Rayleigh angle, deforming, and stretching the interface until the elongated droplet separates from the surface, as a single droplet or multiple droplets depending on power ranges.

In the previous numerical study, the contact angle is restricted to a local equilibrium contact angle for the duration of the computation, hence it is prevented from dynamically evolving during the simulation. By adopting a moving contact line, the liquid adhesion to the substrate can be increased (as contact angle is altered) preventing droplet slippage at low powers thus the amount of SAW forcing required to instigate pumping and then jetting modes is expected to increase, bridging the gap between numerical and experimental results. Thus far, it is understood that the rapid increase in velocity, for jetting regime, prevents the movement of the contact line from having quite as much

influence on droplet behaviour hence the results, shown in Figure 4-18, more closely match the experimental data.

In the following sub-section, the effect of contact angle hysteresis (CAH) on droplet behaviour will be examined and compared to the previous datasets. Initially, a specific case will be scrutinised before further corroboration is studied.

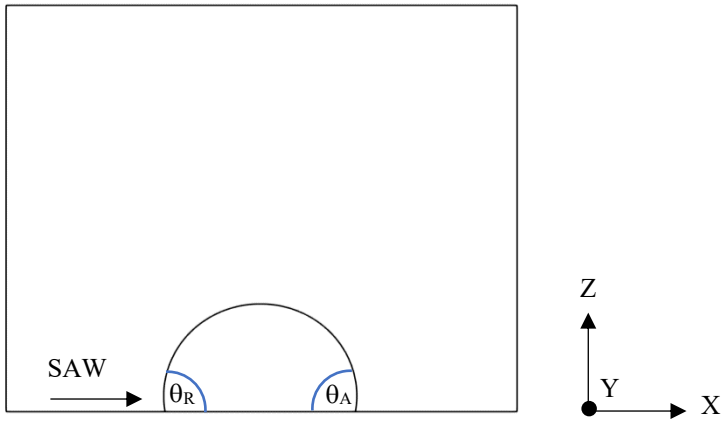

Figure 5-4. Illustration of receding and advancing contact angles as part of initial setup

To study the effects of CAH, the definition, outlined in Section 3.4, is implemented into the model, however without the need for an inclined slope. A set of advancing and receding contact angles are imposed to establish varying CAH cases. To initially test the model, a specific case is chosen (0.9 W RF power at 110.8 MHz resonant frequency) from which to gauge the effectiveness of the given CAH cases. Similar to the previous study, the setup remains constant to allow for direct comparison although the CAH conditions are imposed. Three CAH cases are chosen as part of the study: 1 - $(\theta_R, \theta_A) = (75,105)$, 2 - $(\theta_R, \theta_A) = (85,105)$ and 3 - $(\theta_R, \theta_A) = (95,105)$.

As illustrated in Figure 5-4, the contact area on the LHS of the droplet which interacts with the SAW signifies the receding contact angle whilst the leading edge of the droplet on the RHS denotes the advancing contact angle. From the experimental data presented in [34] it is estimated that the total distance the droplet is moved along the substrate, over the 62 ms pumping time, is approximately 6 mm (Fig 2 in [34]). Taking this measurement as a reference, the numerical results are compared. Analysing the results in Figure 5-5, there appears a clear trend between pumping distance and size of CAH window. With a larger window (Case 1) the droplet is moved along the substrate much less distance as compared to a lesser CAH (Case 3). This can be attributed to a lower receding contact

angle providing a larger contact area between the liquid and solid, offering more adhesive force. The SAW force has much less initial impact on droplet deformation at this lower contact angle where the internal flow momentum is less freely available to circulate due to a reduced droplet height. By implementing a CAH of $(\theta_R, \theta_A) = (95,105)$, the pumping distance provides a reasonable match to the experimental data, with an approximate error of 5%.

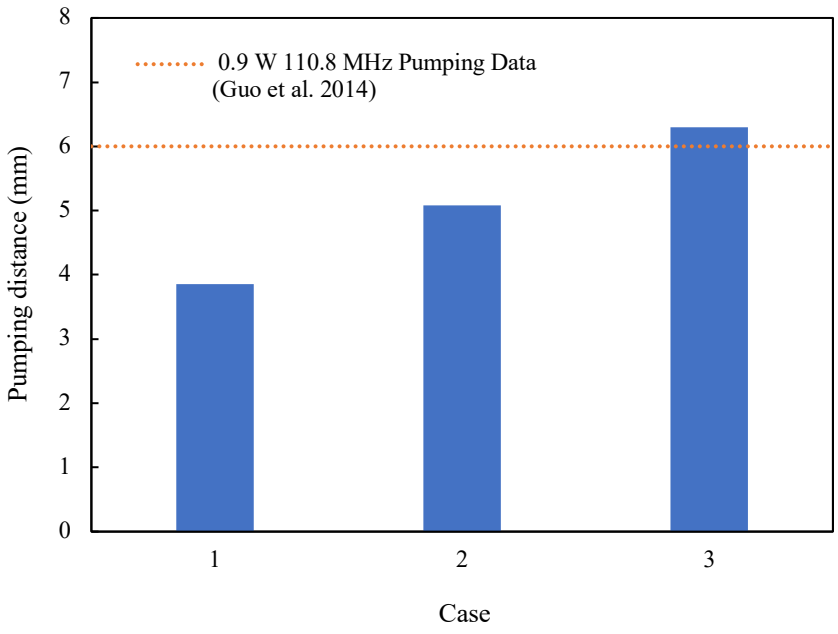

Figure 5-5. Simulated pumping distance of 5µl droplet at 0.9 W RF power for 110.8 MHz frequency with different CAH

Noori et al. [195] conducted a similar study for 2D SAW-droplet interactions using a colour gradient method LB model. They found that employing a CAH model can help improve the simulation results by approximately 20% when comparing to experimental data. The research suggests a CAH of $(\theta_R, \theta_A) = (95,105)$ yields the most favourable outcome over the range of test cases. Additionally, the study investigated the effects of CAH on droplet displacement along the substrate. The conclusion reveals that an increase in surface roughness (large CAH window) results in a reduction in droplet movement for the pumping mode, and an increase in droplet instability for the jetting mode.

With this outcome, the proposed CAH window $(\theta_R, \theta_A) = (95,105)$ is further assessed against a range of experimental data to determine its effectiveness and capability. Again, turning to the work in [34], the estimated droplet velocity at various powers and frequencies (Fig 3 (d) in [34]) is taken as a benchmark from which to compare the

numerical results. In the tests, a frequency of 61.7 MHz, with a RF power range of approximately 0.3 W to 1.1 W, is adopted. Similar to the previous study, the power is converted into non-dimensional amplitude to provide comparison via the correlation described in Eq. 2–10.

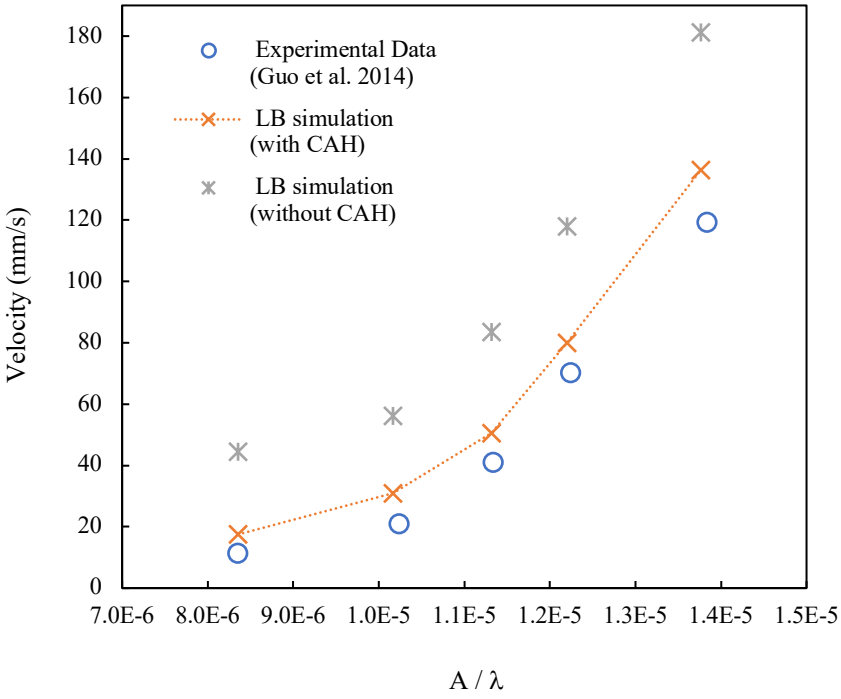

Figure 5-6. Comparison of droplet velocity against A/λ at frequency 61.7 MHz

The numerical results presented in Figure 5-6 demonstrate a good agreement with the experimental data when CAH is employed. Similar to before, the LB simulations somewhat overestimate the droplet movement at each datapoint, however the overall trend is comparable. The outcome from this initial analysis indicates the significance of CAH in SAW-droplet interactions. In the physical experiments, although the substrate surface is treated such that a hydrophobic equilibrium contact angle is achieved, throughout the SAW interaction the droplet contact areas are able to dynamically evolve to counteract the change in internal momentum, resulting in interface deformation. However, if this evolution is not specified in the computational model explicitly then the contact angles will be constrained to the initial contact angle throughout the duration of the simulation. By employing a moving contact line model [179], the droplet deformation, especially at the interface between liquid and solid, is a consequence of the SAW forcing inside.

Finally, the range of frequencies studied in the previous chapter is executed once more, with the newly described CAH conditions implemented. The boundary between modes is highlighted and compared to the previous experimental reference data. As can be seen in Figure 5-7, through applying a CAH model the results more closely match the lab experiments, with an average reduction in error of approximately 20%.

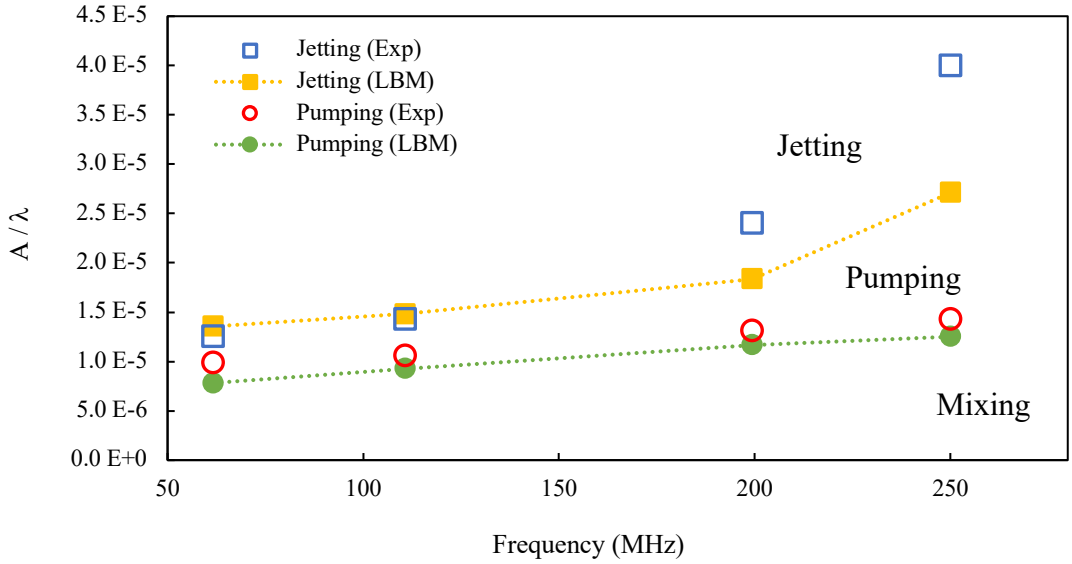

Figure 5-7. Relationship between A/λ and frequency for 5 µl droplet. LBM simulations with CAH (θ_R,θ_A) = (95,105). Experimental data extracted from [34]

By allowing the advancing and receding contact angles to evolve towards their prospective limits during the simulation, the droplet is able to withstand a higher SAW forcing before transitioning between regimes, hence the relationship is improved compared to the previous study (Section 4.5). Interestingly, in the initial SAW interaction period for the pumping mode, the rear contact area is fixed in place as the contact angle dynamically adjusts however the front droplet interface is moved forward due to the SAW forcing. After a few milliseconds, the internal liquid momentum increases which in turn causes the rear interface to start to move, overcoming the adhesive force provided by the advancing contact angle.

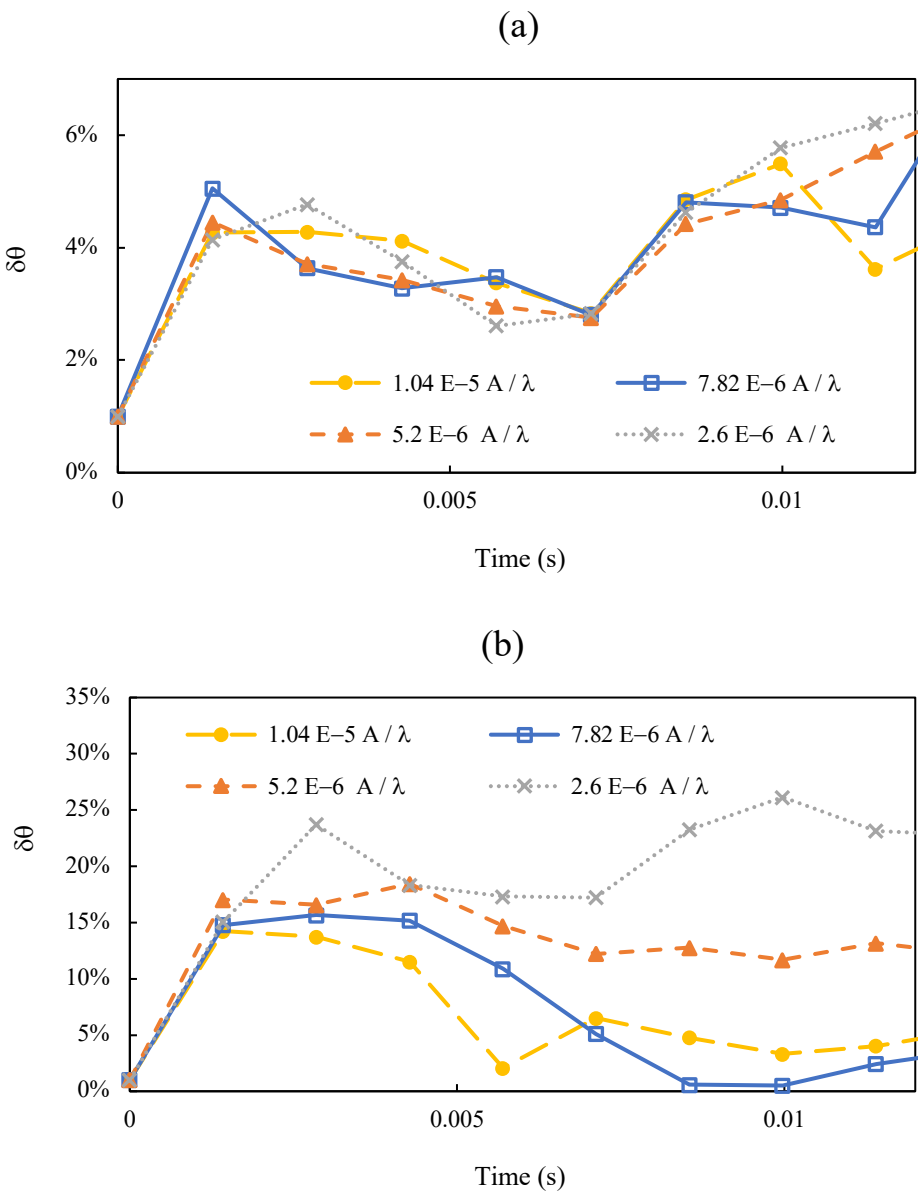

Figure 5-8. Percentage change in contact angle compared to reference value for varying SAW amplitudes, (a) left contact angle (b) right contact angle

Looking at the evolution of contact angle, as compared to a non CAH model, during the simulation for low to medium power applications, the influence is quite apparent. In Figure 5-8, the percentage change in contact angle (absolute), from the reference value, is described for various SAW powers by

$$\delta\theta = \frac{|\theta_{CAH} - \theta_{REF}|}{\theta_{CAH}} \qquad 5\text{–}1$$

where θ_{CAH} represents the contact angle with CAH employed and θ_{REF} is the reference contact angle when no CAH is implemented. As presented in Figure 5-8 (a), the left contact angle evolves, initially from the static contact angle, towards the CAH window where it remains for the duration of the simulation. Comparing the different power data, the trends are analogous, thus within this power range, the SAW doesn't have much influence on the development of contact angle. However, looking at Figure 5-8 (b), the rear contact angle exhibits more response to the SAW parameter input. Interestingly, in the initial few milliseconds, all data follows a similar trend, with a large departure from the static contact angle. As the computation progresses, the lower powers tend to stabilise, whereas the higher powers fluctuate drastically. The higher SAW power produces more internal liquid momentum which instigates a forward motion of the droplet on the substrate, of which the advancing angle is constantly altering to combat against.

The effect of CAH on jetting has been shown to have a lesser impact since the high velocity flow inside the droplet is directed along the Rayleigh angle, elongating the interface more vertically than horizontally along the substrate. Looking at Figure 5-7, for lower resonant frequencies (i.e., <150 MHz), there appears to be very minor alteration of the relationship when CAH is introduced. For high frequencies the adjustment is much more pronounced, with simulated A/λ approaching the experimental data. As the SAW forcing in this range is large, the instantaneous velocity change is much more abrupt triggering the contact angles to adjust towards their limits hence the influence of CAH is much more pronounced.

The impact of CAH has been shown to have a positive effect on simulated results, reducing the error against experimental data. Interestingly, although the SAW forcing (A/λ) is increased as compared to the previous study (Section 4.5), the droplet velocity is nevertheless analogous. This is due to the CAH window opposing the horizontal momentum, maintaining droplet position on the substrate until the forcing is large enough to initiate a pumping mode and further a jetting mode. Before, the droplet velocity is measured from a lower SAW forcing, for each frequency, as compared to the experimental results. Not to be misunderstood, these results were compared to lab experiments at the boundary between each regime (mixing, pumping, and jetting) to provide an insight into model performance and applicability. With the CAH implemented, the actual power ranges being studied are more closely matched hence the results can be

useful in revealing the underlying physical mechanisms which dictate SAW-droplet interactions.

5.4 Analysis of EOS implementation in SAW-droplet interactions

As previously shown in Chapter 3, the choice of EOS implementation (YS, piecewise linear and MPI) can have an impact on the magnitude of spurious velocities inside the liquid droplet as well as the surrounding gas phase. So far it has been demonstrated that the YS method performed the best for spurious velocities in the whole computational domain, whilst the piecewise linear method exhibits the lowest spurious velocities in the liquid droplet. In this section these methods will be further examined to analyse their effect on SAW-droplet interactions, scrutinising aspects such as density ratio, internal flow velocities and droplet behaviours.

As formerly introduced, the piecewise linear EOS requires a set of free parameters to be exclusively determined hence the spinodal points can be acquired by solving a set of equations, one for determining the mechanical equilibrium and another for chemical equilibrium. Li and Luo [196] investigated the effects of modifying the slope of EOS in the vapour-phase region, unstable region and liquid-phase region. The findings reveal that influence of droplet size can be reduced by increasing the slope in the vapour phase (θ_V). Additionally, setting the vapour phase sound speed ($\sqrt{\theta_V}$) to the same order of magnitude as the lattice sound speed (c_s^2) helps to maintain a constant vapour density [196].

To provide fair comparison between all implementations the numerical setup is kept constant with initial densities, droplet size, wettability conditions, and SAW forcing being conserved. Computational setup remains unchanged from those described in Section 4.3. Both pumping and jetting modes are studied, with a frequency of 61.7 MHz selected. Considering a 5 μl droplet, for the pumping mode, a A/λ ratio of 7.8 x 10^{-6} is chosen as this has already been demonstrated to be boundary for initiating droplet translation along the substrate (Figure 5-7). Additionally, for jetting mode, a A/λ ratio of 1.4 x 10^{-5} is adopted for similar motivations.

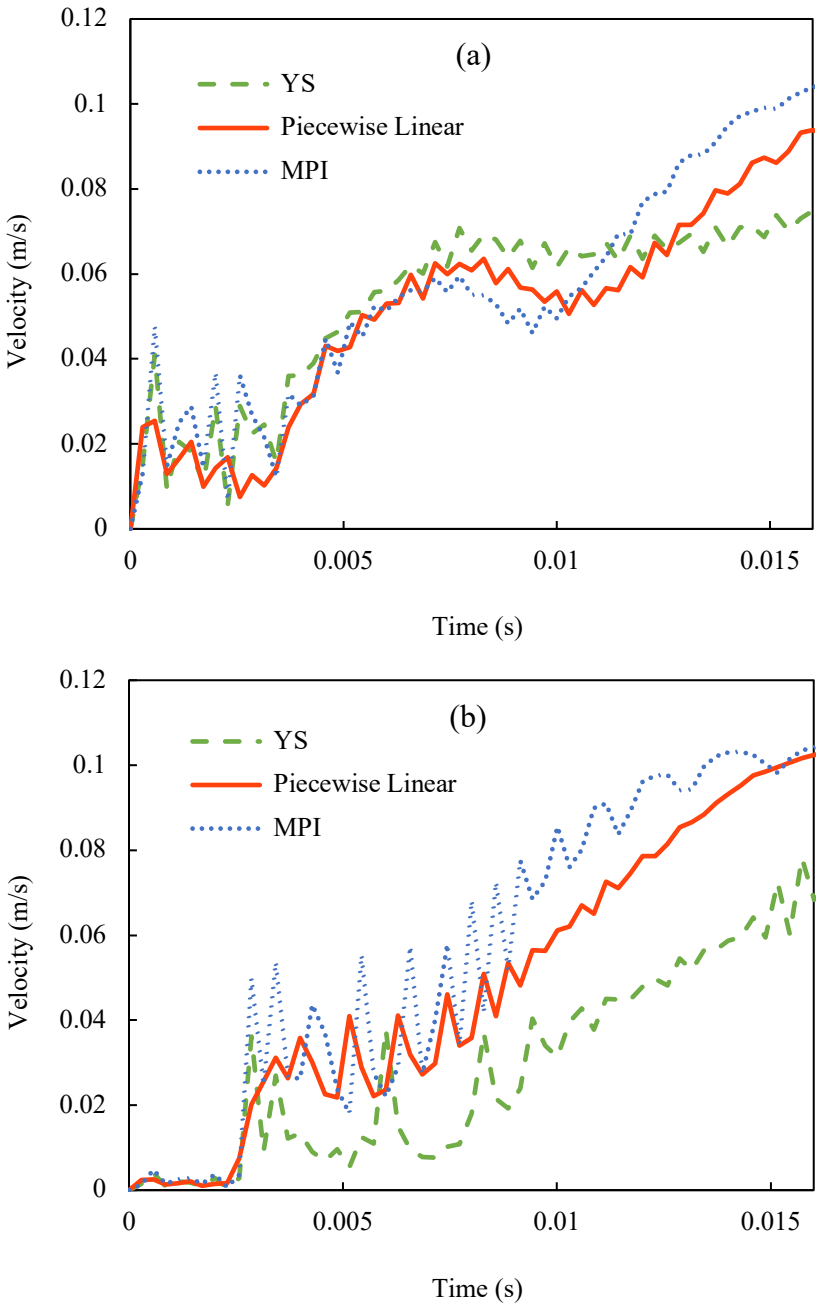

Figure 5-9. Evolution of droplet transport velocity, (a) front point (b) rear point

In the simulations, a large density ratio is considered, similar to the previous study (T_R = 0.5, CS EOS) with $\rho_l = 0.44$ and $\rho_v = 0.0006$. For the YS method, parameters are left unchanged from those defined in Section 4.3. Moreover, according to [197], for the piecewise linear method, the free parameters should be set to $\theta_V = 0.64c_s^2$, $\theta_L = c_s^2$ and $\theta_M = -0.04c_s^2$. However, in this study $\theta_M = -0.033c_s^2$ to ensure a relatively thin interface whilst maintaining model stability. Considering the above, according to Eq. 3–16 and Eq. 3–17, variables ρ_1 and ρ_2 are given as $\rho_1 = 0.000709$ and $\rho_2 = 0.43154$ [197]. Lastly, in the MPI method, the thermodynamic consistency is corrected through splitting the free

parameter ε_j in Eq. 3–8 into two parts [159], with $\varepsilon_{forcing,j} = 0.98\ \varepsilon_{EOS,j}$ providing good agreement with the Maxwell construction (see Appendix B).

Focusing on the pumping mode, it is evident that for the same initial SAW amplitude and frequency, the droplet behaviour is quite different. Figure 5-9 provides an insight into the front and rear contact point transport velocities for each EOS implementation. Here transport velocity is defined as the horizontal movement (x-direction) of the droplet along the substrate. Viewing the data there is a similar overall trend observed between the sets of results, particularly Figure 5-9 (a). In the initial few milliseconds there is increased velocity at the front of the droplet where the SAW interacts, however the rear remains almost at rest. At approximately 2 ms, the rear experiences a rapid velocity increase as the internal momentum overcomes the surface adhesion. Interestingly, at this juncture, the velocity at the front of the droplet decreases as a result. After 10 ms the droplet is mobile, hence it moves with relative ease over the substrate.

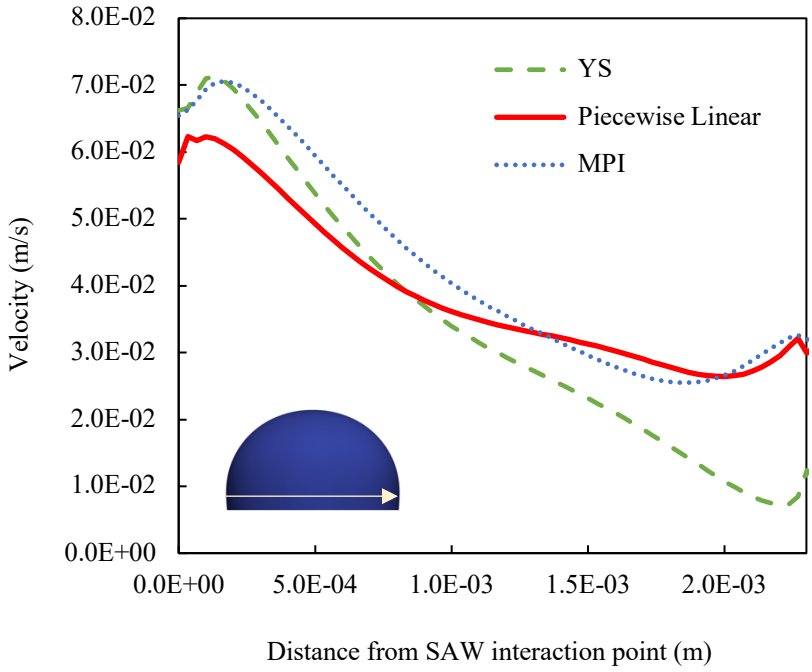

Figure 5-10. Velocity profiles through centre of droplet, in x-direction, for pumping mode at approximately 3 ms and 0.4 mm above the substrate (61.7 MHz with A/λ = 7.8 x 10^{-6}). Image inset depicts profile position and direction.

Looking at the velocity profile through the centre of the droplet (Figure 5-10), there appears to be a higher internal velocity for both the YS and MPI, near to the SAW interaction area, compared to the piecewise linear method. This phenomenon could be a

potential reason why the transport velocity at frontal area of the droplet is marginally lower in comparison to the others (Figure 5-9 (a)) if the piecewise linear EOS is applied. The internal momentum has less impact on the contact line movement hence it moves slower. Conversely, at the rear of the droplet, the YS method has a low internal flow velocity which again could be the cause of the lesser transport droplet velocity at the rear point (Figure 5-9 (b)).

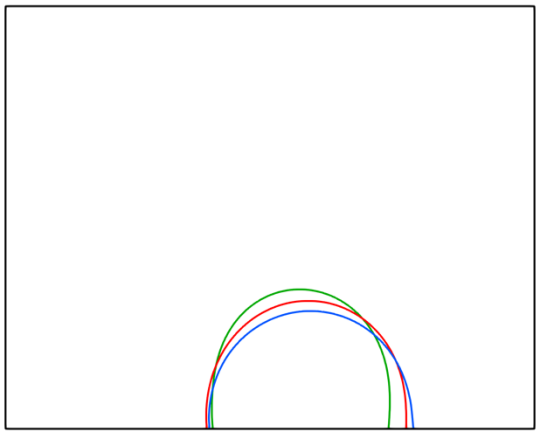

Figure 5-11. Droplet shape comparison between YS, piecewise linear and MPI for pumping mode with frequency 61.7 MHz at approximately 10 ms. Green line depicts YS, Red line illustrates piecewise linear and Blue line shows MPI.

Overall, the pumping distance achieved over the numerical simulation is shorter with the YS method as compared to the MPI and piecewise linear method. The shape of the droplet is also distinctive for the YS method, with it being more elongated in the vertical direction (Figure 5-11). This is a consequence of the internal and external velocities being dissimilar during the computation, causing subtle differences in the value of the contact angle at the rear of the droplet. As illustrated in Figure 5-11, the YS method experiences the largest contact angle which helps to fix the droplet in place whilst the SAW forcing influences the internal fluid momentum. The MPI method demonstrates a reduced contact angle at the rear which produces a shallower droplet height and more horizontal movement along the substrate.

Additionally, when scrutinising the velocities near the interface area at the rear of the droplet there are again some differences. Figure 5-12 provides some understanding of the link between droplet movement and velocities. Over the bulk of the droplet, the velocity profiles are comparable however at the interface region there is a large increase for the

piecewise linear and MPI methods over the YS. All models experience large velocity magnitudes outside the droplet interface, with the peak of the YS method being about 40% lower than the other methods.

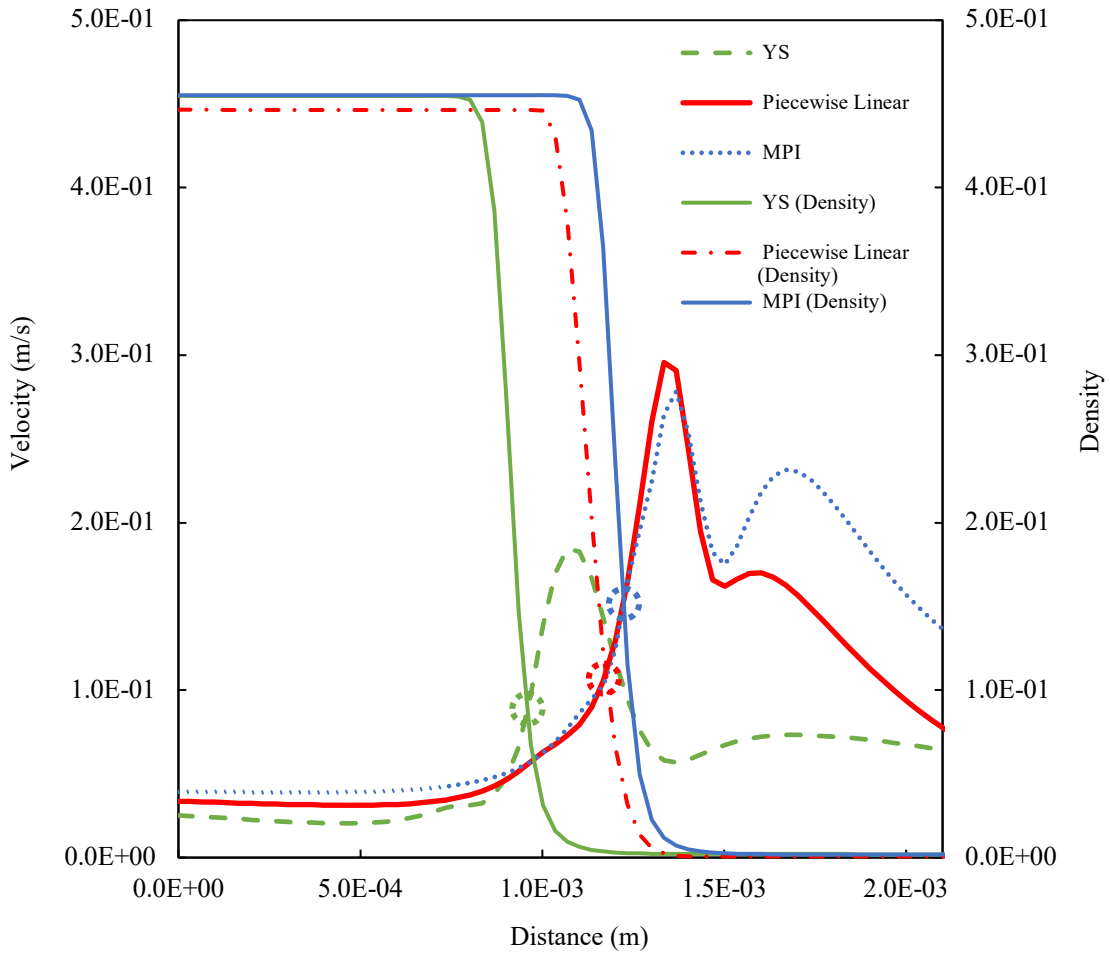

Figure 5-12. Velocity and density profiles from centre of droplet in x-direction at 0.4 mm above substrate, approximately 10 ms. Intersection between velocity and density has been highlighted for each method.

Upon closer inspection of the intermolecular forces for each EOS implementation, there are some variations. As illustrated in Figure 5-13, the distribution of intermolecular forces, in the x-direction (F_x) at the beginning of SAW interactions, is quite different between the piecewise linear EOS and the other methods (YS and MPI). At this timestep, the droplet shape is largely unaffected by the SAW which provides an ideal evaluation. Although the localised maximum values are diverse, it was demonstrated that the total value of the intermolecular force is closely matched, within 0.3% variation [197]. It is not surprising that the distributions for YS and MPI are equivalent since it was shown that

the behaviour of each is very similar when the same parameters are adopted, resulting in comparable densities, pseudopotentials, and spurious velocities in the 2D free droplet tests conducted in [197]. Evaluation of the SAW forcing, for each EOS, reveals indistinguishable distributions therefore it is not included here.

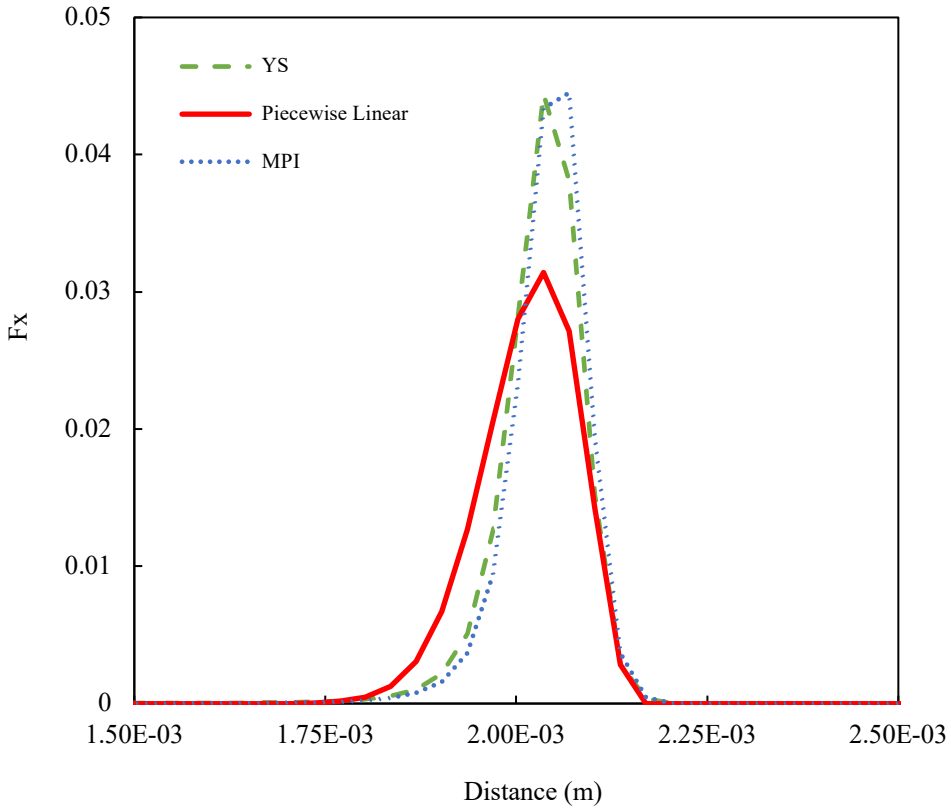

Figure 5-13. Intermolecular force distribution, in x-direction, for YS, piecewise linear method and MPI. Data is from intial timestep of SAW-droplet interactions, at the left-hand-side interface of droplet.

Looking at the jetting mode, again it is apparent that there are some minor differences in droplet shape between the methods. As presented in Figure 5-14, at approximately 10 ms, the droplet has become more elongated in the z-direction as the strong SAW forcing pushes the liquid inside upwards along the Rayleigh angle. Consequently, the piecewise linear method experiences the most upward movement with a slightly larger droplet height over the others. This can be attributed to high internal velocities in the x and z-directions (Figure 5-15 (a) and (c)), causing the liquid-vapour interface to deform more as the fluid momentum increases due to the SAW. Intriguingly, the droplet jetting time is increased marginally when the YS method is adopted, ejected the droplet from the substrate around 1 ms later than the other two methods tested.

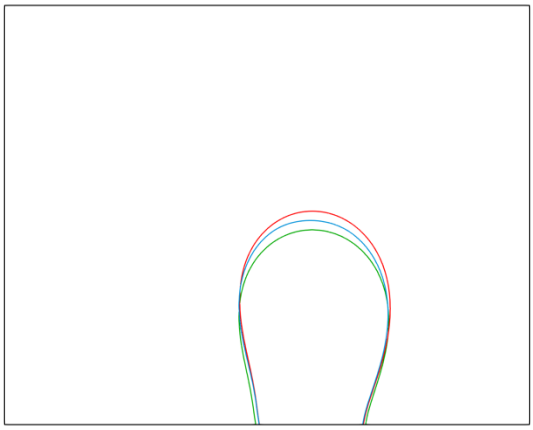

Figure 5-14. Droplet shape comparison between YS, piecewise linear and MPI for jetting mode with frequency 61.7 MHz at approximately 10 ms. Green line depicts YS, Red line illustrates piecewise linear and Blue line shows MPI.

Furthermore, the density ratio fluctuation throughout the computation is evaluated for the pumping and jetting modes. According to Figure 5-16, the piecewise linear method is far superior to the other methods, with a density ratio close to initialisation being achieved throughout the simulations. After a few milliseconds, the YS and MPI experience a large increase in density ratio which then drastically reduces to a value far below the coexistence densities expected at this reduced temperature. Again, as pointed out in [197], the MPI behaves similar to the YS method hence it is not unforeseen that the results follow a comparable trend. It appears though while able to predict static saturation densities with reasonable accuracy for free droplets and fixed on a surface, when the SAW interaction is introduced, the vapour phase density rapidly changes causing disparity in the density ratio during the simulation. The data from Figure 5-16 indicates that the fluctuation of density ratio is largely insensitive of input SAW power, with Figure 5-16 (a) and (b) displaying similar results.

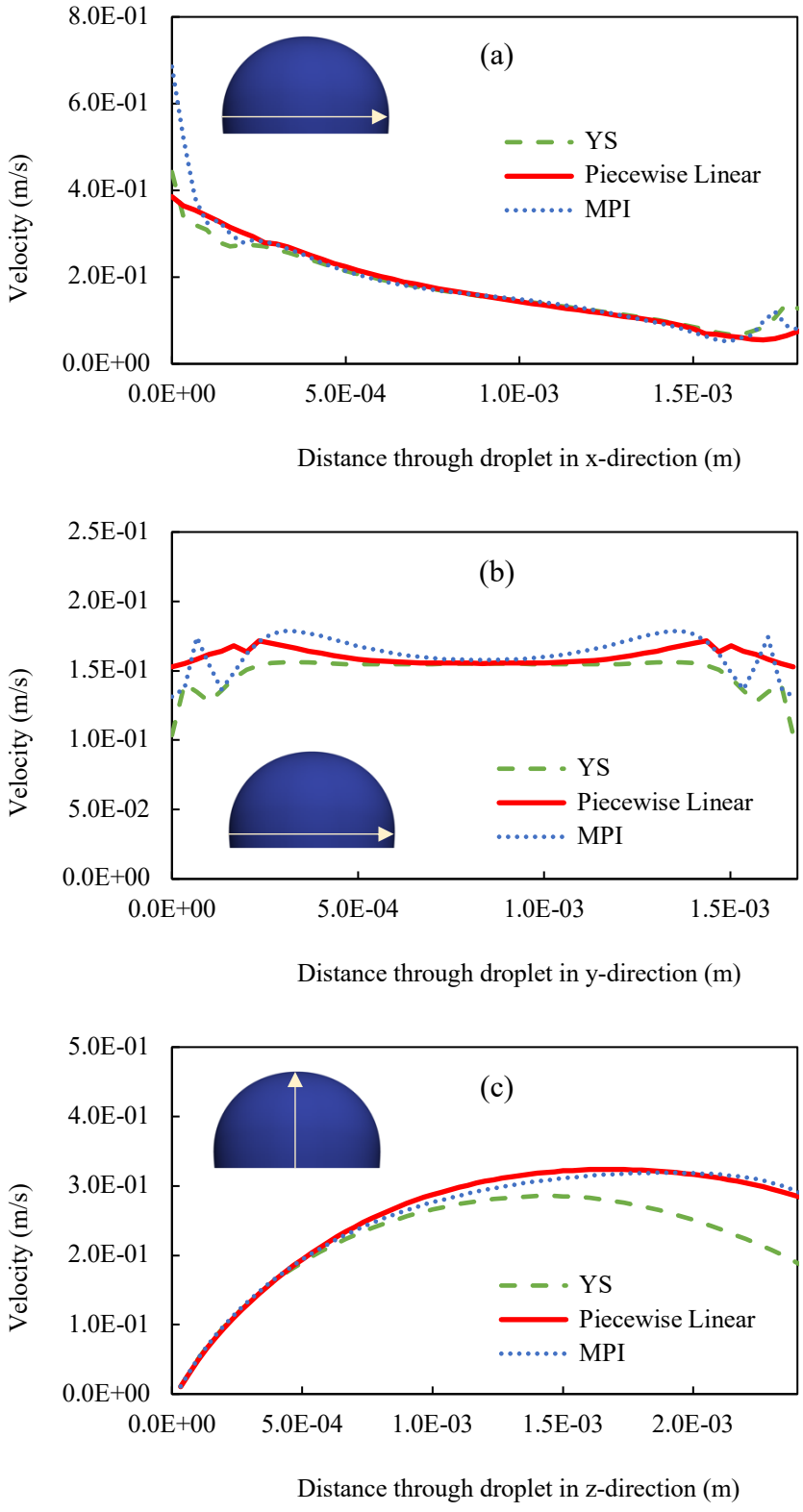

Figure 5-15. Velocity profiles through centre of droplet for jetting mode at approximately 10 ms (61.7 MHz with $A/\lambda = 1.4 \times 10^{-5}$), (a) x-direction, (b) y-direction and (c) z-direction. x and y measurements taken from 0.4 mm above substrate. Image inset depicts profile position and direction.

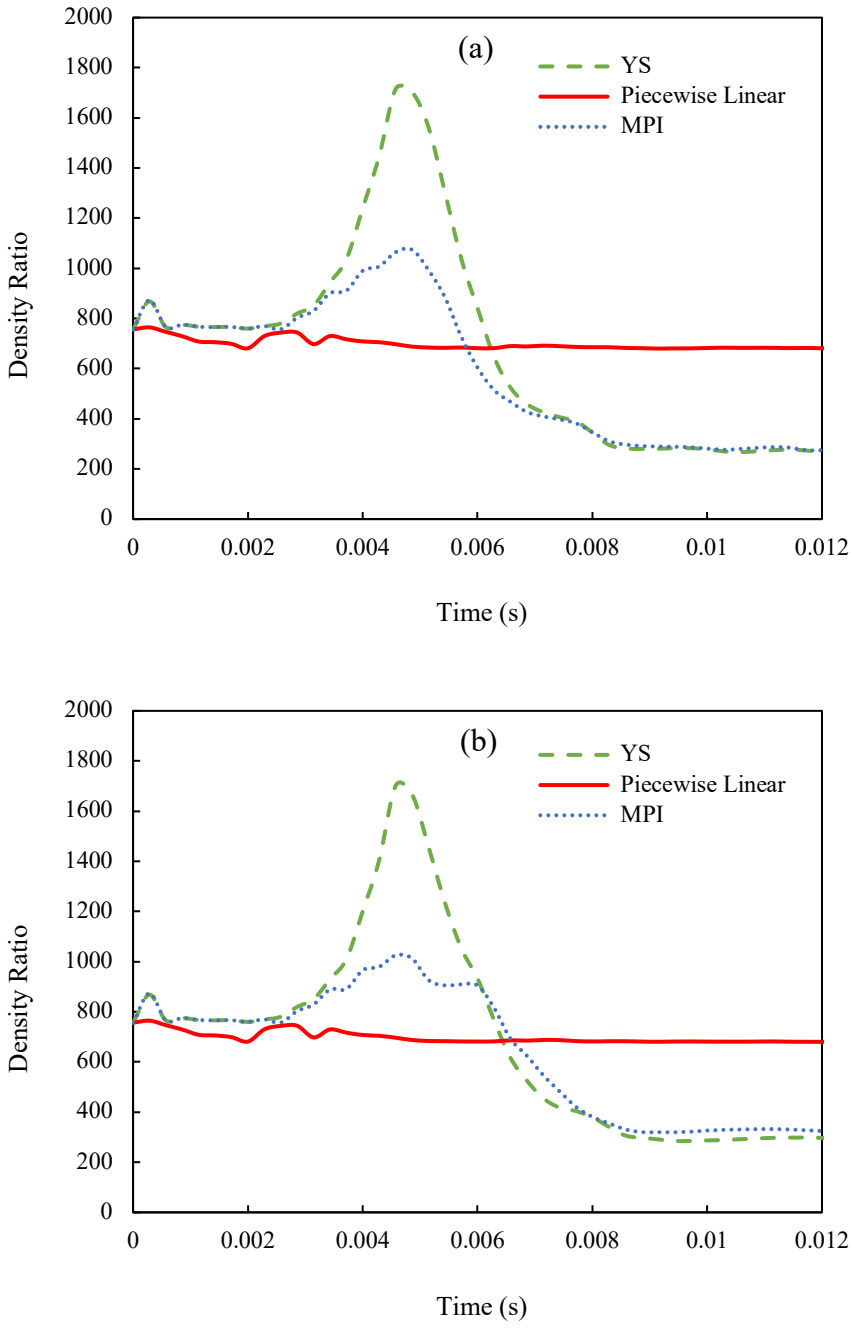

Figure 5-16. Evolution of density ratio, (a) pumping mode, (b) jetting mode

Lastly, the computational overhead associated with each method is analysed. The YS and piecewise linear method are executed in a comparable timeframe however the MPI, with its additional potentials, takes on average 52% more time to complete.

5.5 Summary

In summary, as a consequence of large spurious velocities in the pseudopotential method, the effect of adjusting the free relaxation parameters in the MRT model is investigated.

The outcome demonstrates the importance of correct choice of these parameters since a slight modification can lead to a rise in spurious velocity magnitude throughout the domain as well as inside the droplet. It is recommended that if the objective is to reduce spurious velociites, solely in the vapour phase, then setting parameters s_ε and s_{xyz} to 0.3333 with s_q = 1.0 provides an optimum outcome at the expense of a rise in the liquid phase. Conversely, setting parameters s_q and s_{xyz} to 1.1 with s_ε = 1.0 provides a small reduction of spurious velocities in the liquid phase at the expense of a rise in the vapour phase. From the tests carried out, there are some indicators which point out that setting all free parameters to unity can provide a substantial reduction in spurious velocities in gas phase which can be beneficial for model stability.

Moreover, the impact of CAH on droplet dynamics and behaviours has been studied. The outcome reveals that a CAH window of $(\theta_R, \theta_A) = (95{,}105)$ has been shown to have a positive effect on simulated results, reducing the error against experimental data. The influence of CAH on jetting has been demonstrated to have a lesser impact, compared to mixing and pumping, due to a higher velocity flow inside the droplet elongating the interface along the Rayleigh angle. With CAH implemented, the power ranges being studied more closely match the lab data hence the results can be useful in revealing the underlying physical mechanisms which dictate SAW-droplet interactions.

Lastly, the influence of EOS implementation on SAW-droplet interactions has been examined, focusing on droplet behaviour for pumping and jetting modes. For the pumping mode, the impact of EOS is quite prevalant with shorter pumping distances and more droplet deformation being produced for the YS method. Also, for the jetting mode a similar outcome is perceived with longer jetting times being reported for the YS method, as compared to the others tested. Interestingly, the only method to provide a consistent density ratio over the duration of the simulation is the piecewise linear method, with the others fluctuating immensely during the tests.

Chapter 6– Investigation of the dynamics of surface acoustic wave interactions in sessile droplets

6.1 Introduction

This chapter investigates the dynamics of SAW-droplet interactions on an inclined substrate, concentrating on pumping/translation and jetting regimes. A variety of droplet volumes, SAW amplitudes and slope angles are examined, with particular attention being drawn to droplet velocity across the substrate. Additionally, droplet impact on an inclined substrate is studied, at various impact velocities, with and without SAW interactions to determine the droplet behaviours as a consequence of the acoustic interaction. Initially, the model is validated for a droplet with free impact on the substrate, before SAW interactions are introduced. Specific focus is made on droplet-substrate contact time, maximum spreading of droplet and rebound angle.

Moreover, the kinetic impact of dual SAW interactions on sessile droplets is examined. A variety of SAW configurations and powers are examined, with consideration on internal flow, deformation and droplet dynamics.

6.2 Investigation of SAW in sessile droplets on inclined slope

In recent years, there has been a growth in demand for novel SAW devices which are compact and efficient. Conventionally acoustofluidics has been restricted to the manipulation of fluid mediums on flat (horizontal) surfaces, only taking advantage of the lateral and longitudinal directions. However, by introducing a sloped surface, devices can benefit vertically by including multiple layers resulting in a more compact system.

So far, this unique device design is in its infancy with only a few studies being published [198,199]. The main research avenues conducted have been mainly focused on thin film piezoelectric devices due to their low production cost, flexible electrode design and ease of deposition on different substrate materials. Conventional devices are mostly composed of bulk $LiNbO_3$ substrates which have a high electromechanical coupling coefficient and low input power requirements.

In the present study, the 3D pseudopotential MRT model recently developed, validated, and optimized as introduced in the previous chapters, is employed in the investigation of SAW-droplet interactions on an inclined substrate. In this instance, the piecewise linear

method is employed due to its enhanced ability to maintain density ratio and reduced spurious velocities in the liquid phase.

Initially the model is validated for droplet pinned on an inclined slope, in the presence of gravity, before SAW interactions are introduced. As part of this study, a $LiNbO_3$ substrate is utilised for all numerical simulations.

6.2.1 Evaluation of contact angle hysteresis

An important aspect of the model which should be highlighted is the ability to pin a drop on a surface in the presence of external forcing or slope inclination. When the solid-fluid model is chosen based on the density or pseudopotential interaction described previously, the drop is unable to remain in place. It has been shown that a static contact line is not appropriate for this scenario, instead a dynamic model is required. The CAH model, described in Section 3.4, is implemented into the constructed model and evaluated against published studies [178,179].

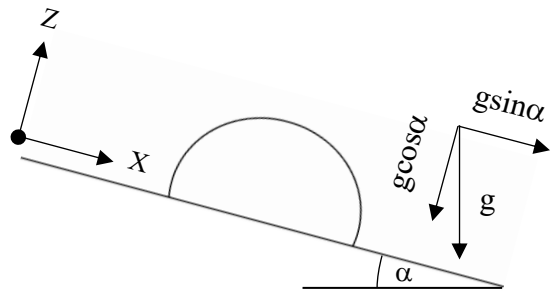

Figure 6-1. Schematic of droplet on an inclined surface

To validate the above scheme, a droplet is simulated on an inclined slope subjected to a gravitational force. In the evaluation, four incline angles (15°, 30°, 60° and 90°) are chosen to be analysed. A lattice size of $N_x \times N_y \times N_z = 100 \times 100 \times 50$ is selected and a stationary semi-spherical droplet of radius $R = 20$ is initially placed on the solid surface with a gravitational force $\boldsymbol{F}_g$ applied and initial contact angle ~100°. Periodic boundary conditions applied in the x and y directions, while a no-slip condition is added to the upper and lower boundaries.

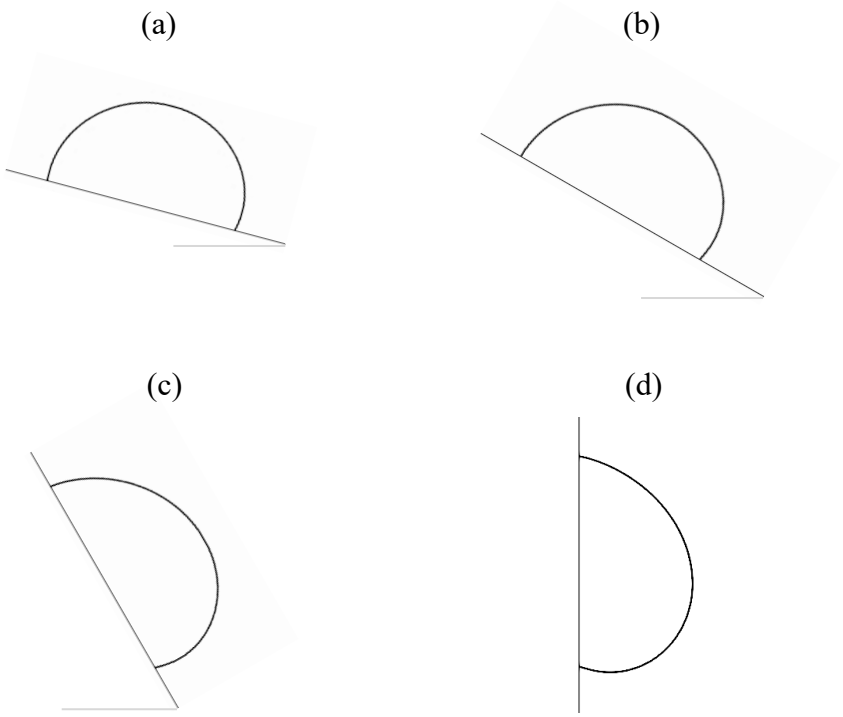

Figure 6-2. Interface profiles when droplets reach steady state at different inclined angles. The hysteresis window is set as (θ_R,θ_A) = (60°,120°) with Eo = 0.5. Inclined angles are (a) α = 15°, (b) α = 30°, (c) α = 60°, (d) α = 90°, respectively.

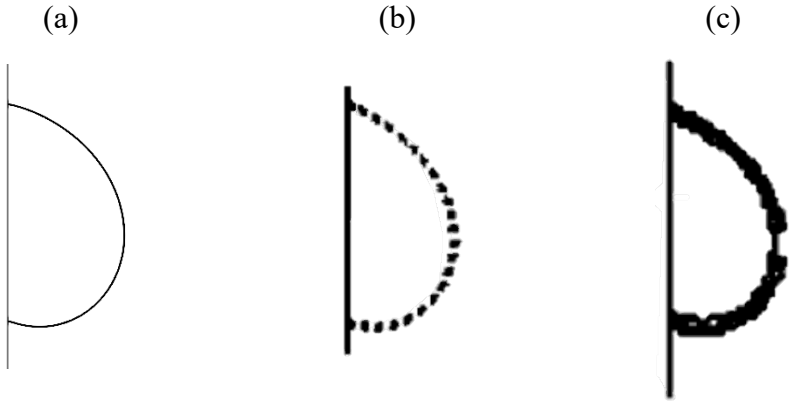

Figure 6-3. Comparison of interface profiles at inclined angle of 90°; (a) present study, (b) Wang et al. [179] and (c) Dupont et al. [178].

As demonstrated in Figure 6-2, the droplet can remain static on the inclined surfaces when a hysteresis window of $(\theta_R, \theta_A) = (60,120)$ is used for $Eo = 0.5$. This result is comparable to those published in the literature [178,179]. Additionally, the interface deformation for a drop on a 90° incline is compared to [178,179]. The shape is in good

agreement (Figure 6-3) with the published images thus demonstrating the validity of the current implementation in the constructed model.

6.2.2 SAW-droplet interactions on inclined slope

Theoretical analysis of a droplet on an inclined sloping surface has been well documented. In the absence of SAW agitation, the force balance of the droplet is governed by; a resistance force, determined by CAH, which aims to counteract motion, a reaction force normal to the surface and gravity which elicits droplet deformation [200]. For inclination angles less than the critical value, the droplet will remain static on the surface however once this value is exceeded, the droplet will start to move.

The addition of acoustic wave interactions on the droplet introduces extra forces into the liquid. With a SAW propagating from the left (see Figure 6-4), the direction of movement of the droplet is to the right, which is in opposition to the resistance force generated from the CAH. Additionally, the gravitation components are also in opposition to the SAW which deforms the liquid against the direction of travel. Lastly, after the droplet starts to move along the substrate, a shearing force is generated due to the strain at the contact line between the liquid and the surface [198].

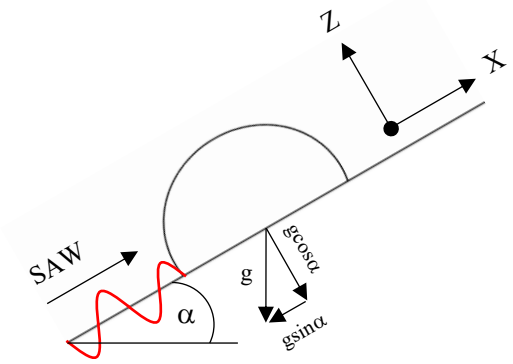

Figure 6-4. Schematic of droplet on an inclined surface with SAW interaction

The interaction between SAW and sessile droplets on an inclined slope is investigated to determine the influence of amplitude, inclination angle and volume on droplet pumping/translation velocity along the substrate. The results are qualitatively compared to research in the literature, with specific inferences highlighted in the summary.

In the simulations, a lattice size of $N_x \times N_y \times N_z = 200 \times 120 \times 120$ is adopted and a stationary semi-spherical droplet of radius $R = 40$ is initially placed on the substrate with

a gravitational force $\boldsymbol{F}_g$ applied and initial contact angle ~100°. Periodic boundary conditions applied in the x and y directions, while a no-slip condition is added to the upper and lower boundaries. The resonant frequency is set to 61.7 MHz with an initial SAW amplitude established based on the findings in Figure 5-7. In the initial evaluation, a 1 µl droplet is selected with a variety of inclination angles ranging 0° to 180° to be analysed. As before, the droplet is allowed to reach static equilibrium on the surface before SAW interactions are introduced.

Figure 6-5 illustrates the average transportation/pumping velocity for a 1 µl droplet with varying inclination angle and SAW amplitude. Here, average pumping velocity is calculated using the velocity data from three points; front, centre, and rear of droplet, to provide an average of the values.

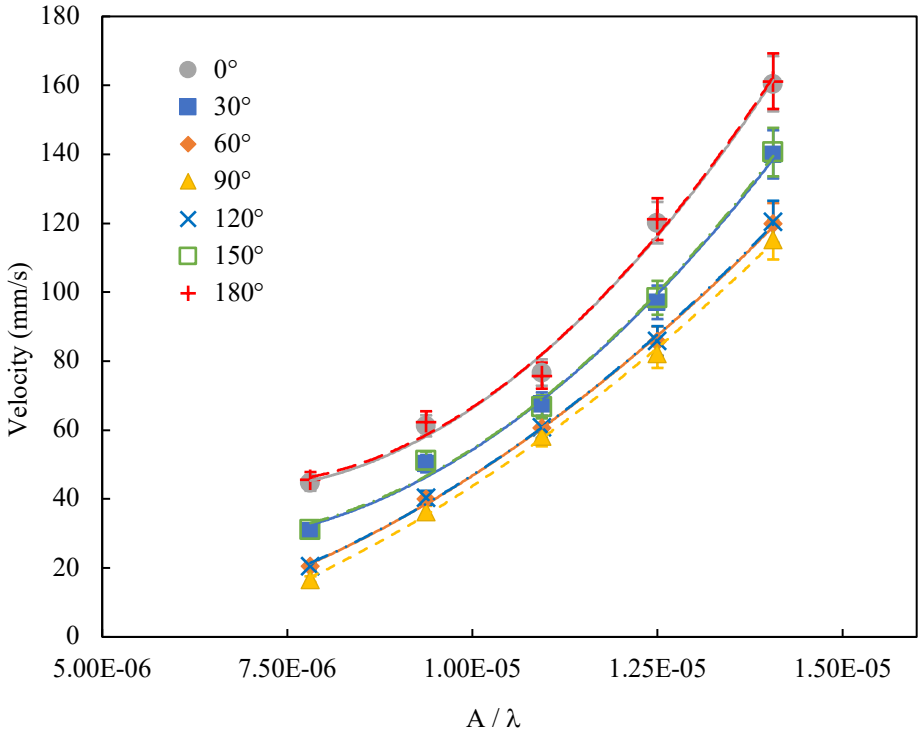

Figure 6-5. Average pumping velocity for 1 µl droplet along various inclination angles under different A/λ. Lines represent best fit to each set of data.

The results indicate that an increase in SAW amplitude (power) corresponds to an increase in pumping velocity, for each slope angle. At a fixed amplitude, the average droplet velocity is decreased as the incline angle is increased until it reaches a minimum at 90°. Increasing the slope angle further, the opposite it seen as the pumping velocity increases with slope inclination. These findings are consistent with those found in [198].

It is evident that the sets of data for 0° and 180°, 30° and 150°, and 60° and 120° are analogous with one another. Numerically obtained pumping images, for a 1 µl droplet, are provided in Figure 6-6.

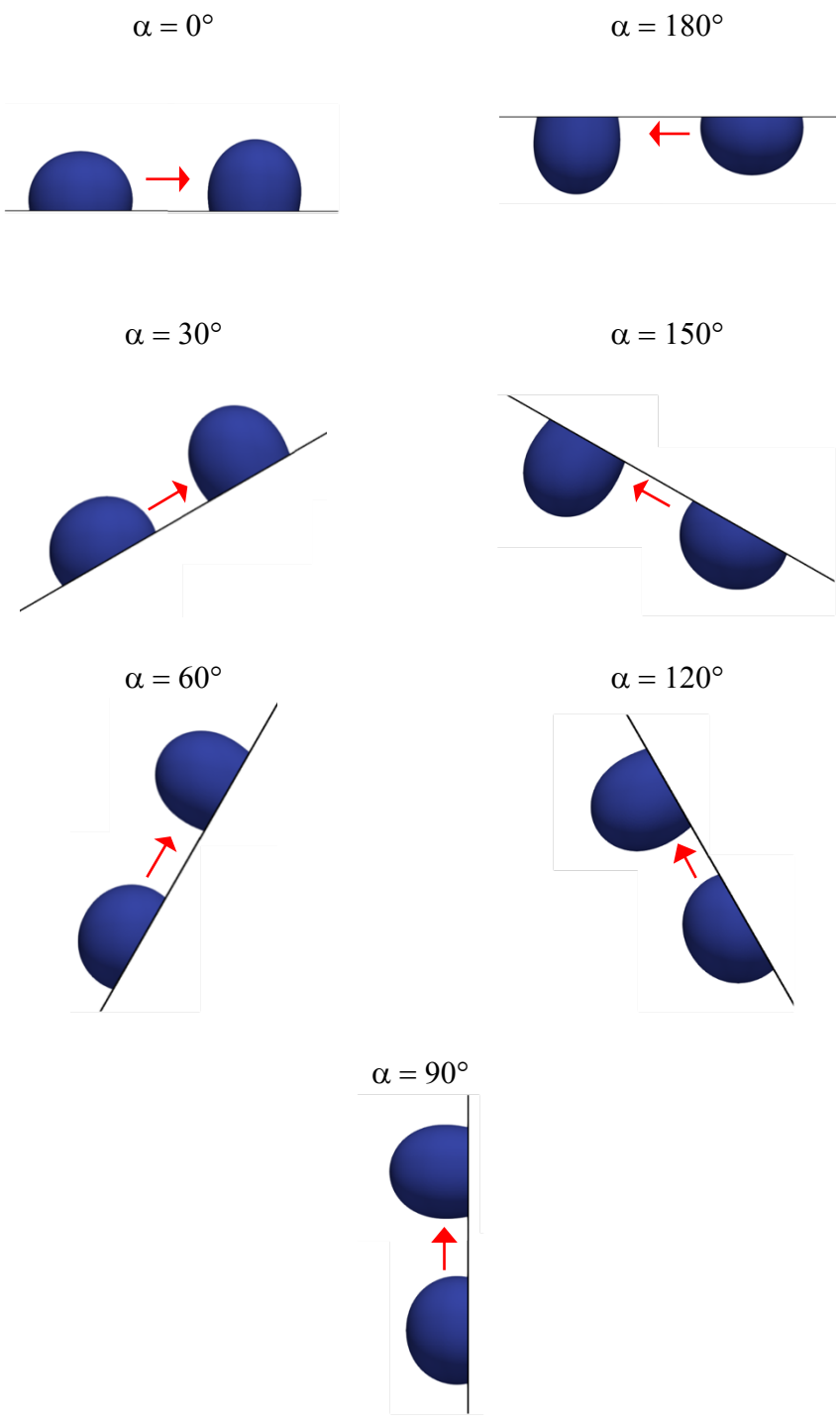

Figure 6-6. Numerical pumping images of 1 µl droplet along inclined surfaces for SAW input 9.38 x 10^{-6} A/λ. Arrow shows direction of travel.

To evaluate the effect of droplet volume on the pumping velocity, the volume is varied from 1 µl to 10 µl, with an inclination angle of 30° being examined for comparison. Figure 6-7 indicates that as SAW amplitude is enlarged, the increase in velocity is lesser in larger droplets as compared to the small droplets, demonstrated by a less steep trend. Furthermore, for the same amplitude, a smaller droplet will have a larger average pumping velocity due to its lower contact area preventing droplet motion along the substrate. Similarly, this outcome is comparable with those found in lab experiments [198].

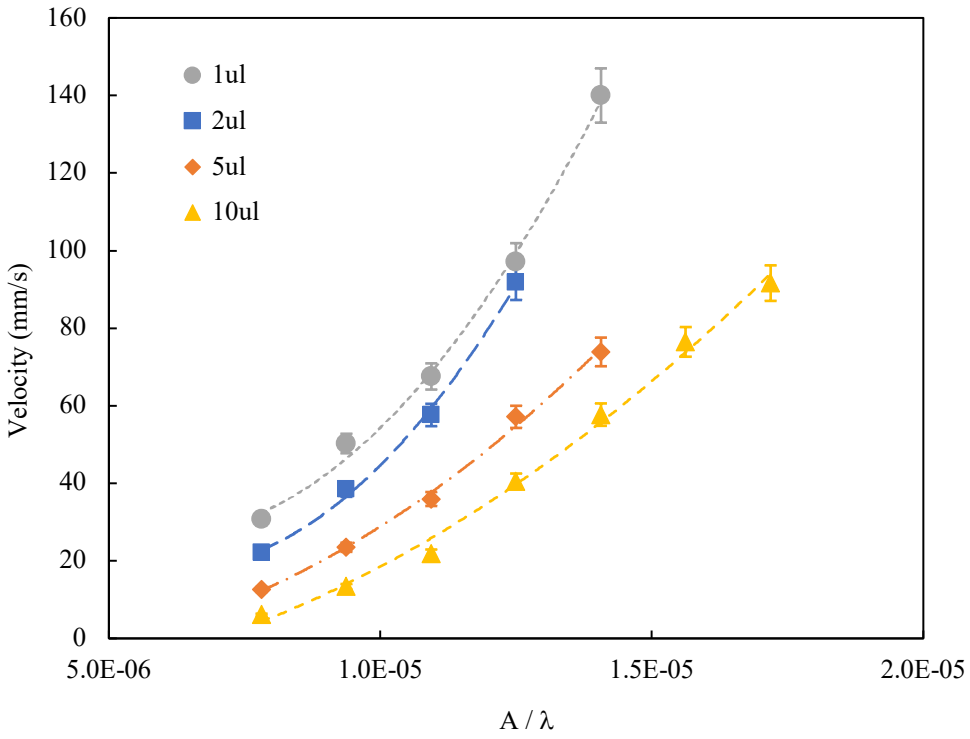

Figure 6-7. Average pumping velocity of droplets with different volumes at 30° inclined surface under different A/λ. Lines represent best fit to each set of data.

Further increase in SAW amplitude leads to jetting where the droplet is ejected from the surface. The power ranges (A/λ) and velocities demonstrated in Figure 6-7 are consistent with those found in Chapter 4 for a 5 µl droplet on a flat surface.

6.2.3 Analysis of droplet impact on inclined slope with and without SAW

Over the past decades, liquid droplet impact on solid inclined surfaces has been comprehensively studied due to increased interest in science and industrial applications [201–203]. Upon droplet impact on the dry solid surface, the liquid deforms

and spreads to a maximum spreading diameter, and then, conditional on the surface treatment and impact velocity, there can be a variety of outcomes including partial or full rebound, splashing, or deposition on the surface permanently [201]. Recently, research has revealed that the intricate interplay between droplet and surface can be controlled or manipulated with the introduction of SAW's [83]. This is of particular interest in applications where liquid adhesion on surfaces is unfavourable such as self-cleaning [204–206].

Initially as part of this study, the model against is compared against published experimental data for droplet impact on a flat horizontal surface without any SAW interactions. The works by Bayer and Megaridis [207] offers a comprehensive understanding of contact angle dynamics during free droplet impact and the effect of surface wetting on droplet spreading. It is found that the wettability of the surface has an insignificant consequence on the maximum spreading of asymmetric inertia dominated droplet impacts [207].

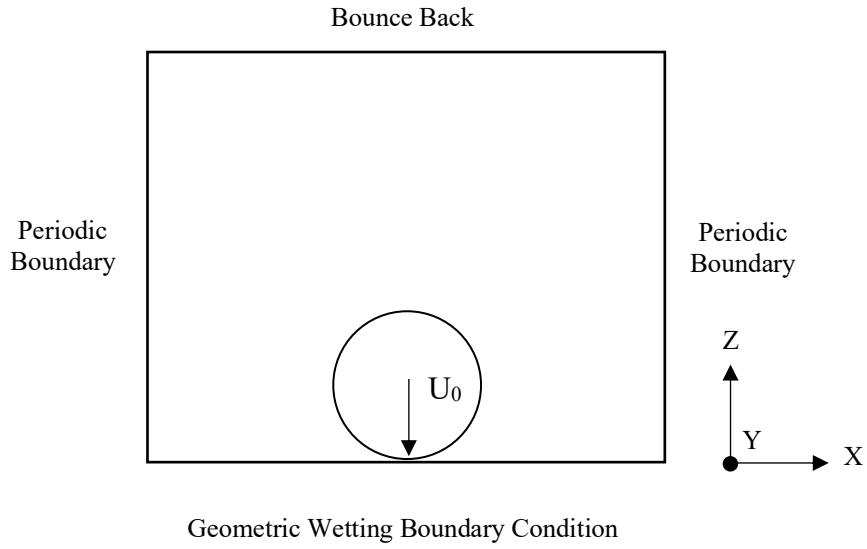

Figure 6-8. Numerical setup of droplet impact on solid surface

To substantiate the model, a comparative study is carried out, employing the published experimental data for reference. A 1.4 mm diameter droplet is numerically impacted on horizontal surfaces of varying wettability (wetting, partial and non-wetting) at different impact velocities. The evolution of maximum droplet spreading is qualitatively and quantitively compared to the data in [207]. In the simulations, a spherical droplet of radius $R = 30$ initially placed at a height of $2R$ above the bottom surface with its centre at

(125,125,30). The setup of the simulation can be referred to in Figure 6-11, including boundary conditions. In this instance, the Reynolds number and Weber number are defined as, $Re = \frac{U_0 D_0}{\nu_l}$ and $We = \frac{\rho_l {U_0}^2 D_0}{\gamma}$, with U_0 and D_0 as the initial impact velocity and droplet diameter, respectively.

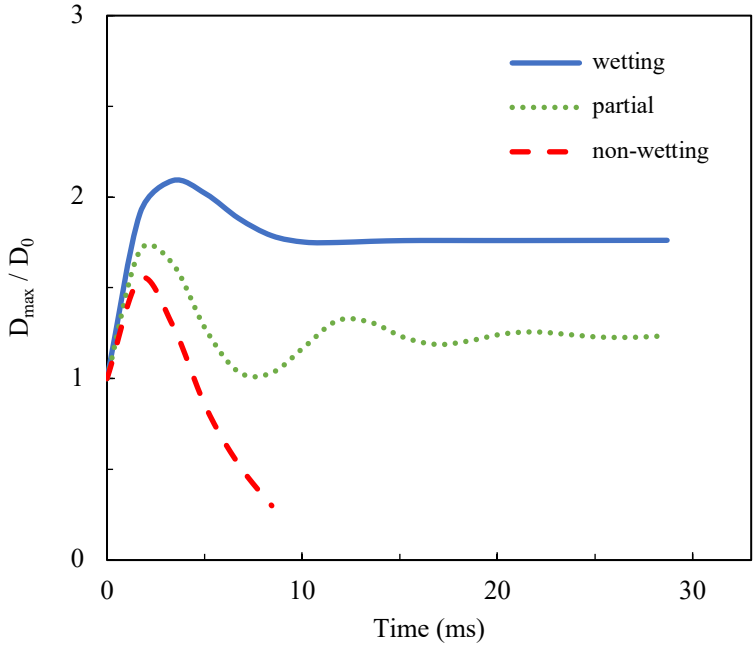

Figure 6-9. Maximum spreading diameter of droplets impacting on surfaces with different wetting characteristics at We = 11.5

As shown in Figure 6-9, the droplet behaviour can be altered considerably with the choice of surface wettability. When a wet surface is adopted (hydrophilic), for We = 11.5, the droplet reaches a maximum spreading diameter then retracts and ultimately adheres to the surface, without any rebound. Moving to a partially wet surface, a similar outcome is observed, with the droplet attaching to the surface after impact. There is an additional spreading phase however the energy is not enough to overcome the solid-liquid bond. Lastly, when the surface is non-wetting (hydrophobic) the droplet experiences minimal spreading before being separated from the surface after ~ 10 ms. The numerical results presented here are comparable to the experimental work published in Fig. 5 of [207].

The influence of surface wettability on maximum droplet spreading diameter is examined for a range of impact velocities. Again, three surface treatments are considered (wetting, partial and non-wetting) with impact velocities ranging 0.42 – 1.4 ms^{-1} ($4.6 < We < 50.2$). Figure 6-10 provides an insight into the maximum spreading diameter as a function of

$ReWe^{1/2}$ for different surface treatments. For the scenarios tested, the data collapses into a single regression line represented by

$$\frac{D_{max}}{D_0} = 0.56\left(Re\sqrt{We}\right)^{0.15} \qquad 6\text{–}1$$

This outcome is similar to that found in [207], where $D_m / D_0 = 0.72\ (ReWe^{1/2})^{0.14}$, signifying that maximum droplet spreading is largely insensitive to surface treatment and demonstrating the capability of the constructed model to capture the dynamics of droplet impact on solid surfaces.

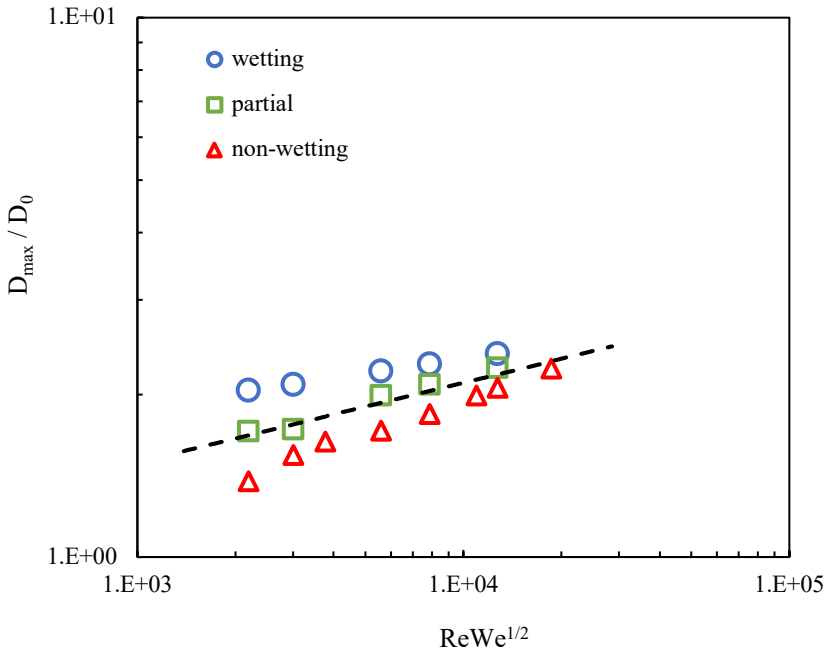

Figure 6-10. Influence of surface wettability on maximum spreading diameter. Dashed line represents regression fit to the data ($D_{max} / D_0 = 0.56\ (ReWe^{1/2})^{0.15}$)

In the following, droplet impact on inclined surface will be studied with and without SAW interactions. A 3.5 µl droplet is numerically impacted on surfaces of varying slope inclination at different impact velocities. To study the effect of travelling SAW on droplet impact on inclined surfaces, parameters such as contact time, maximum spreading diameter and rebound direction are examined. A description of the parameters is provided here: 'contact time' is defined as the duration of time the droplet is in contact with the surface, 'maximum spreading diameter' is the distance between the two extremities of the droplet, when is contact with the surface, along the x-direction, and 'rebound angle'

is the direction at which the droplet is displaced from the surface, in relation to the surface normal direction. An illustration is shown in Figure 6-11. The droplet dynamics for a free impact drop (FID) are contrasted with the SAW interaction drop (SID) to establish a relationship between input power and droplet behaviour. The evolution of normalised droplet height and spreading diameter is qualitatively compared to the data in [83].

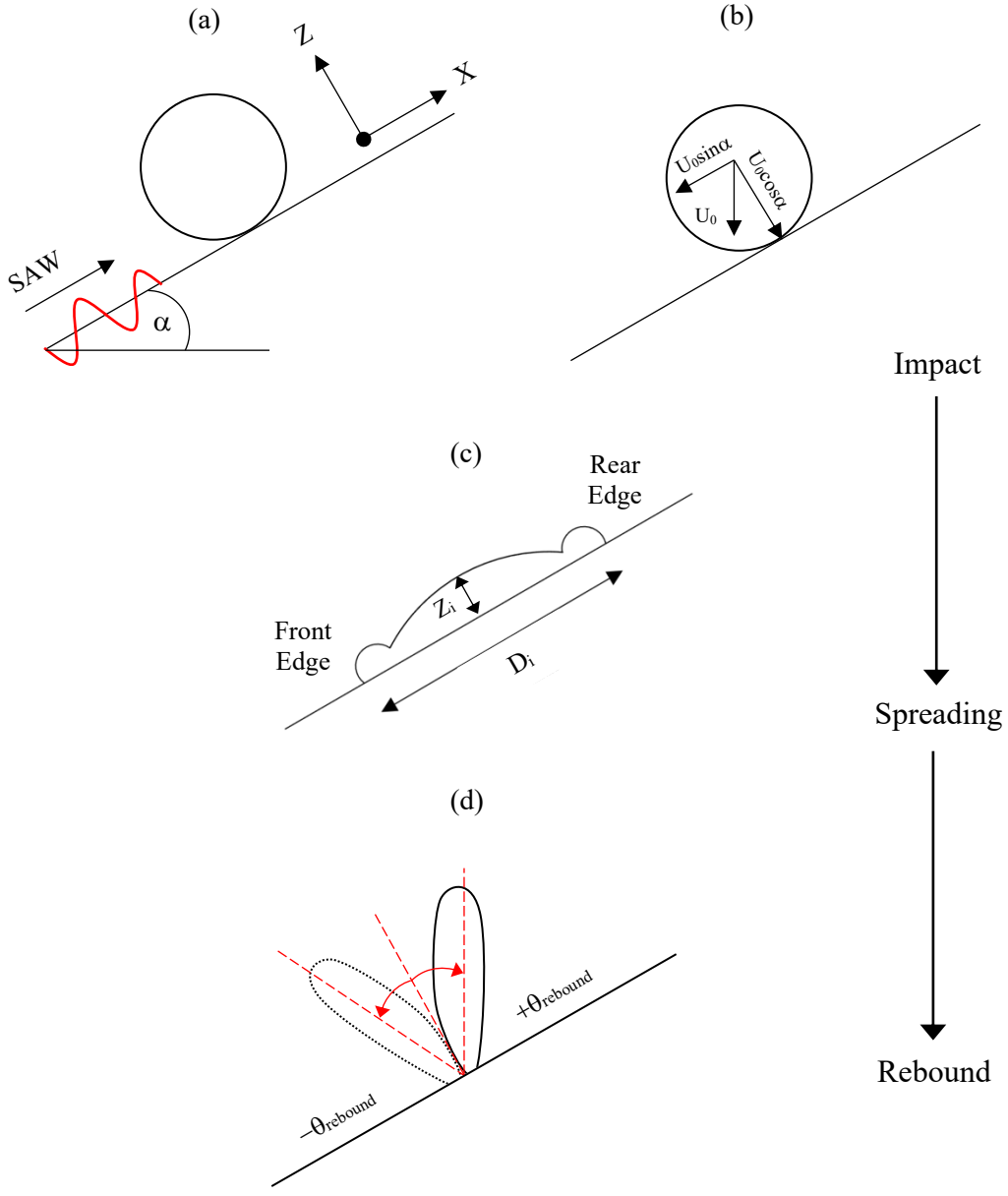

Figure 6-11. Illustration of droplet impact on an inclined surface; (a) with upward travelling SAW interaction (SID) and (b) free impact (FID). Schematic view of; (c) droplet height and spreading diameter, and (d) rebound angle

The impact velocity, U_0 = 1.4 ms^{-1} corresponding to a We = 50, and droplet volume are kept constant throughout the initial simulations. The slope inclination is set to 30° to provide a qualitative comparison to the results presented in [83]. As demonstrated in Figure 6-12 (a), upon impact on the surface the droplet experiences a spreading phase (~ 3 ms) where the liquid is spread to a maximum diameter without any splashing. Then the droplet starts to retract as the rim is moved towards the centre of the liquid. For both scenarios, the spreading phase is similar with the maximum droplet spreading diameter and time being analogous. However, for the SID case (2 W applied power), as the SAW interacts with the droplet it speeds up the retraction phase which reduces the contact width of the droplet compared to the FID case. Consequently, the droplet is separated from the surface at ~16.4 ms for SID and ~17.1 ms for the FID case.

Furthermore, the normalised droplet height is examined for free impact and SAW interaction scenarios. Figure 6-12 (b) illustrates the ratio of droplet height, Z_i, to the initial value, Z_0. As the droplet spreads to its maximum diameter, the normalised height (Z_i / Z_0) is reduced to a minimum, with both scenarios exhibiting a similar evolution. As the SAW interaction begins to influence the droplet (> 5 ms), the Z_i / Z_0 is enlarged more rapidly, leading to an increased tip height at the point of droplet separation from the surface. The above results from the initial LB simulations agree with the observations presented in [83], with SAW interactions reducing droplet contact time and increasing the normalised droplet height over a free impact scenario. The droplet behaviour, for the initial test case, is analogous with those provided in the literature, hence further investigation into the effect of SAW power, inclination angle and We number is conducted.

In the simulations, a range of SAW powers (0 W to 8 W) will be examined for an inclined substrate of different angles (0° - 60°) and droplet impact Weber numbers (We = 10 – We = 50). The droplet contact time and rebound angle will be scrutinised to determine the influence of the above factors.

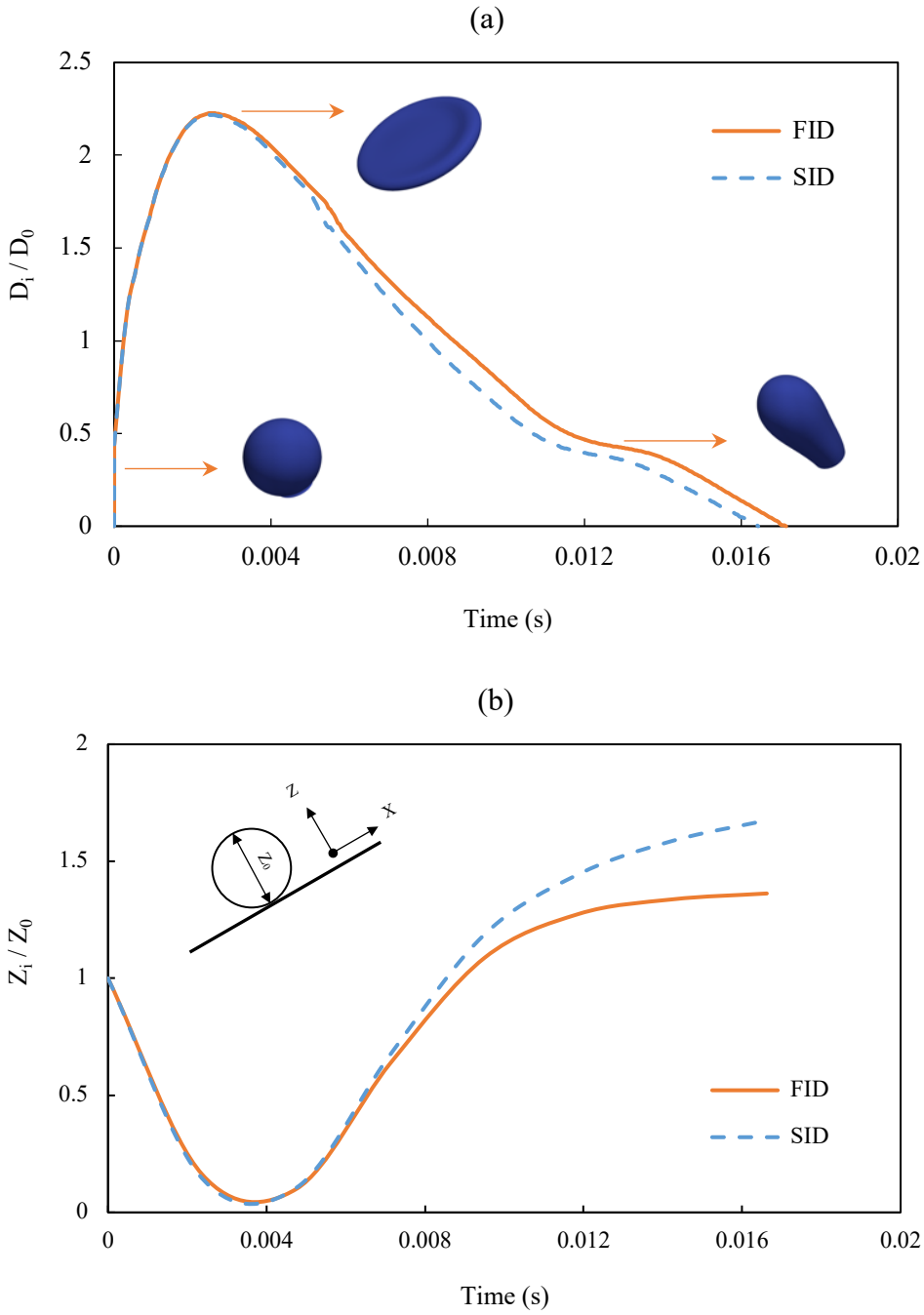

Figure 6-12. Comparison of results for free impact drop (FID) and SAW interaction drop (SID) with power 2 W at 30° inclined surface and We = 50 (a) Evolution of normalised droplet spreading diameter (b) Evolution of normalised droplet height

Figure 6-13 provides a snapshot of a droplet impacting a 15° inclined surface at Weber number of 50 for both free drop and travelling SAW interaction. For FID case (Figure 6-13 (a)), the droplet spreads to a maximum diameter after about 2 ms, then the rim starts to retract towards to centre of the liquid, pushing the droplet upwards. After ~17.7 ms the droplet is separated from the surface, at an angle approximately coincident to the slope,

as the kinetic energy is large enough at this Weber number. Looking at the SID scenario (Figure 6-13 (b)), the initial spreading phase (~2 ms) is disturbed as the SAW deforms the front edge of the droplet, forcing the rim up the slope. As a result, at ~5 ms, the contact area of the droplet is reduced as the liquid is driven upwards. At this SAW power, the forcing is large enough to produce a liquid jet directed approximately along the Rayleigh angle, which is ultimately ejected from the substrate at ~12.4 ms, a substantial reduction in droplet contact time over the FID case.

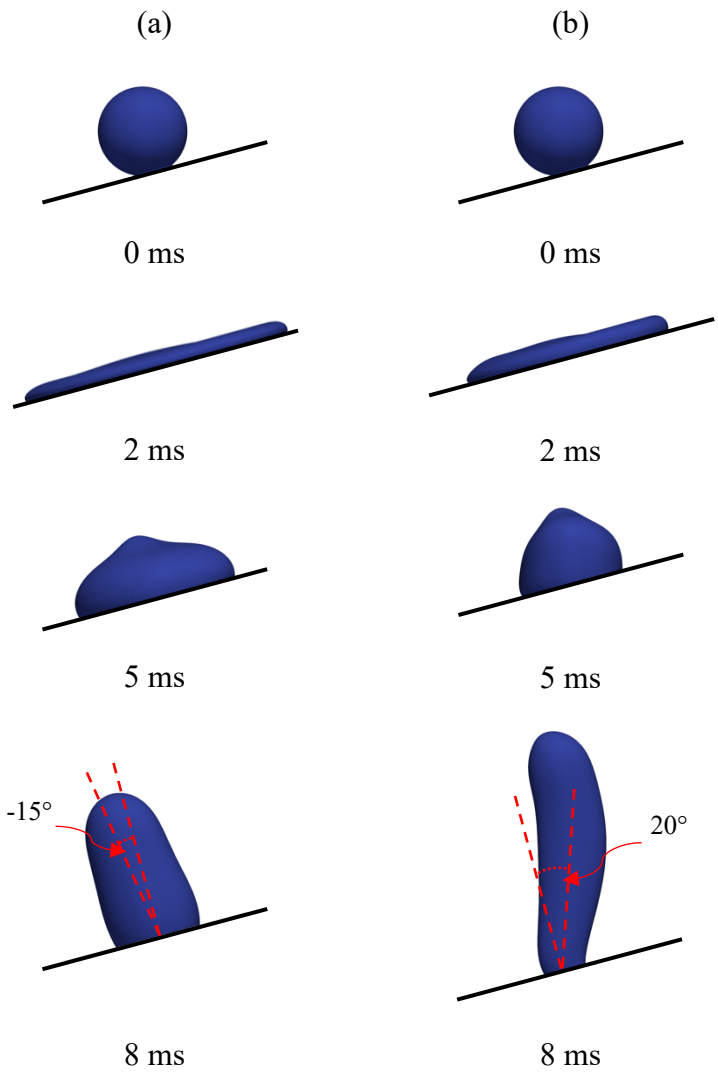

Figure 6-13. Sequential snapshots of droplet impacting on solid surface at 15° inclination angle and Weber number of 50 for (a) free impact drop (FID) and (b) SAW interaction drop (SID) with power of 8 W. Highlighted angles correspond to droplet rebound angle.

Taking a closer look at the internal flow of both cases, presented in Figure 6-14, it is evident that the structures are considerably different. For the FID case, a circulatory flow is generated, orientated around the centre of the droplet. This maintains an almost symmetrical droplet shape on the surface with a tip forming at the top. In contrast, for the SID scenario, the velocity vectors demonstrate a strong flow guiding the liquid vertically against the angle of the slope. High flow is perceived at the left-hand-side of the droplet causing a tip to form, with a velocity gradient realised towards the front of the droplet.

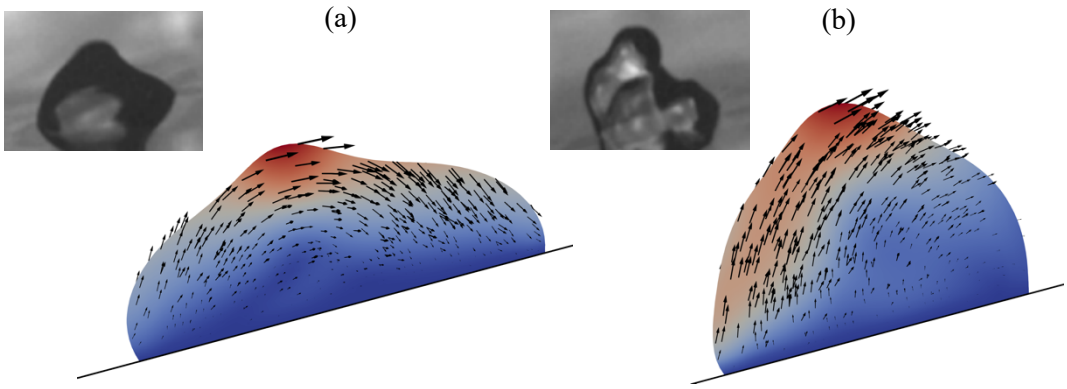

Figure 6-14. Internal flow structure with velocity vectors overlaid at 5 ms for; (a) FID and (b) SID case with applied power of 8 W. Inclination angle is 15° and Weber number of 50. Experimental images representative of droplet impact on ZnO substrate at We ~ 30, extract from Biroun et al [83]

In the subsequent timesteps, the flow inside is intensified as the SAW dominates the fluid orientation and deformation. At the point of ejection from the substrate, the flow is predominantly directed approximately along the Rayleigh angle. On the other hand, for the free impact drop the internal flow of liquid is orientated roughly normal to the slope angle at the point of separation from the surface.

As shown in Figure 6-15, the inclusion of SAW interaction on droplet impact has a positive effect on contact time on the substrate. Taking a surface inclination angle of 0° for example, increasing the applied SAW power from 2 W to 8 W can reduce the contact time by 16%, from 16.9 ms to 14.1 ms, respectively. This reduction is even more apparent on surfaces with large inclination angle (>45°) as the droplet it separated from the surface up to 40% faster than the lower power counterpart.

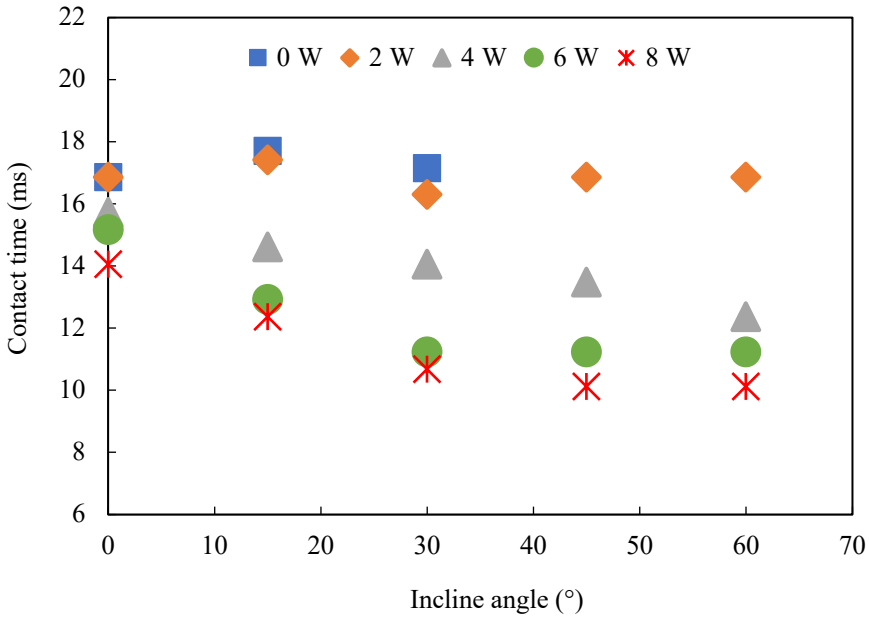

Figure 6-15. Droplet contact time against substrate inclination angle for different SAW powers at We = 50

Additionally, applying SAW to droplet impact on inclined substrate can alter the angle at which it rebounds, dependent on the power. Looking at Figure 6-16, when no SAW interaction is present, the droplet will rebound at an angle approximately coincident to the slope. However, when SAW is introduced, the rebound angle is adjusted until, at sufficient powers, it corresponds to the Rayleigh angle. From the cases studied here, only at SAW power 8 W and greater will the droplet be deformed in a direction close to the Rayleigh angle, irrespective of surface inclination. To reiterate, in this study rebound angle has been defined as being positive for clockwise direction (up slope) and negative for anti-clockwise direction (down slope).

Looking at the effect of applied SAW power on maximum spreading diameter (Figure 6-17), there appears to be a distinct linear trend. For each slope inclination, by increasing the SAW power, the maximum spreading diameter of the droplet is decreased. This can be attributed to the SAW interaction, at the front edge, restricting the droplet spreading and forcing the liquid back towards the centre, reducing the contact area. From the data there is no clear correlation between maximum spreading diameter and slope inclination, for each applied SAW power, hence no conclusion can be made.

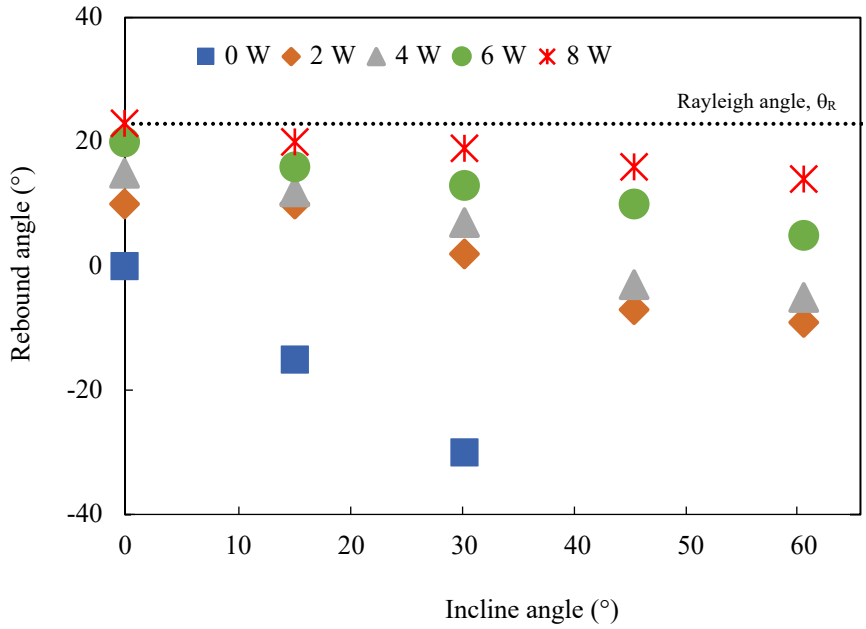

Figure 6-16. Effect of surface inclination on rebound angle for various applied SAW powers at We = 50

In the following, a comparison of results for different Weber numbers (10, 30 and 50) will be examined, once again, in relation to contact time, rebound angle and maximum spreading diameter. SAW power of 6 W has been selected with a 3.5 µl droplet kept constant.

Figure 6-18 (a) provides insight into the effect Weber number has on droplet contact time for various slope angles. For horizontal surfaces (0°), the change in Weber number has insignificant influence on the contact time, with all cases separating the droplet from the substrate after a similar timeframe. Interestingly, as the slope is increased, the differences in contact time become more apparent. At 15° inclination, an increase in Weber number results in a longer contact time, approximately ~1.7 ms or 13% increase from We = 10 to We = 50. A similar trend can be observed for most angles, with an increase in initial impact velocity leading to a longer droplet contact time with the substrate.

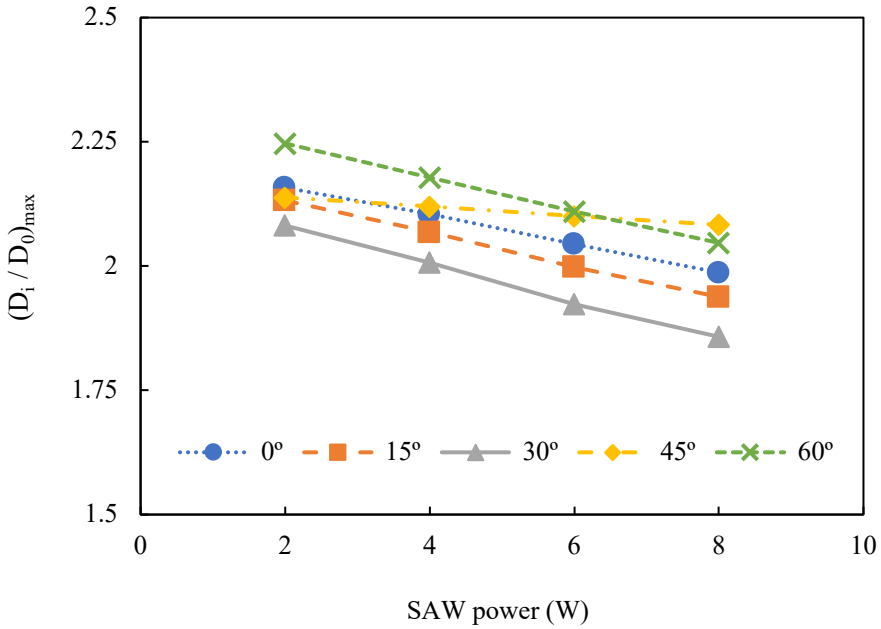

Figure 6-17. Maximum normalised spreading diameter at different applied SAW powers for varying slope inclination angles. For all cases,Weber number of 50

Furthermore, the influence of Weber number on rebound angle is examined. As shown in Figure 6-18 (b), the droplet rebound angle is not significantly affected with a change of We, especially in lower slope inclinations (<45°). The standard deviation (SD) for these sample measurements can be calculated from [208]

$$SD = \sqrt{\frac{1}{N-1}\sum_{i=1}^{N}(E_i - \bar{E})^2} \qquad 6\text{–}2$$

where N is the number of samples, E_i is the value of each sample and $\bar{E}$ is the mean value for the dataset. From Eq. 6–2, the maximum SD for the lower slope inclinations (<45°) is 2° indicating the rebound angle remains almost constant as the impact velocity is increased. As the slope angle is increased, the deviation between Weber numbers is enlarged, with a ~4° difference between the data. Intriguingly, there is no obvious trend in the data, as an increase in Weber number does not guarantee a larger or smaller rebound angle, over the slope angles tested. It is clear though that for each set of data, the largest rebound angle is perceived on a horizontal flat surface (0°) and as the inclination angle is increased, the droplet rebound angle is lessened.

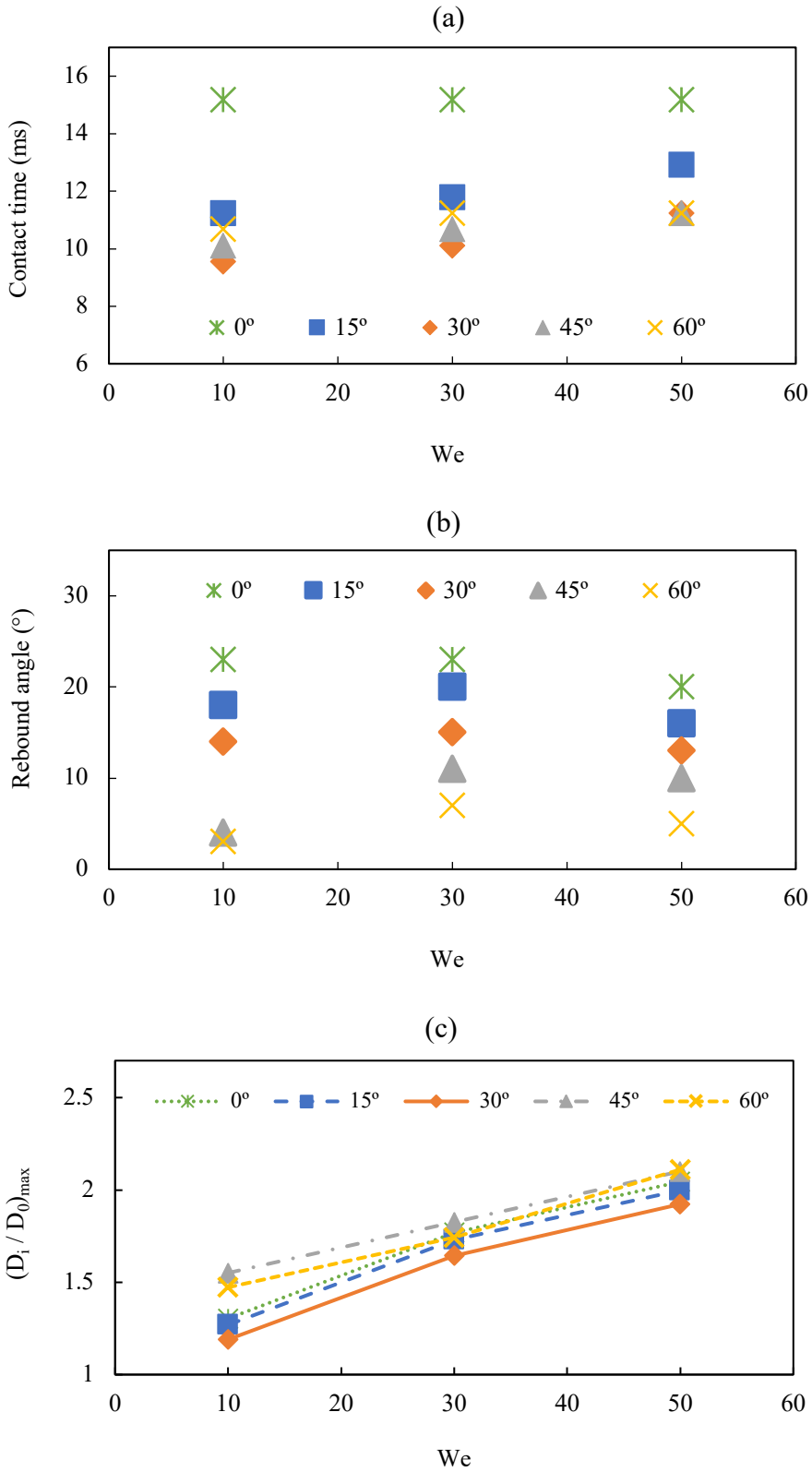

Figure 6-18. Effect of Weber number and surface inclination angle on; (a) contact time, (b) rebound angle and (c) maximum normalised spreading diameter. For all cases, applied SAW power of 6 W

Lastly, the maximum droplet spreading diameter is analysed for the different Weber numbers tested. It is found from the data that the magnitude of impact velocity has a large effect on the maximum spreading diameter of the droplet. As demonstrated in Figure 6-18 (c), there is a clear linear trend between maximum spreading and We, which is to be expected. An increase in impact velocity (Weber number) provides the droplet with more kinetic energy as it collides with the surface. In the absence of splashing, the energy must be dissipated hence the droplet will experience more spreading as a result. Again, there is no observable correlation between maximum normalised spreading diameter and slope inclination, for each Weber number, therefore no deductions can be presented.

6.3 Investigation of dual SAW interactions in sessile droplets

The use of opposing SAWs has been shown to have positive repercussions in science and engineering applications such as ink jet printing, cell sorting, etc. The travelling SAWs, from contrasting directions, interact with each other in the liquid to form a standing surface acoustic wave (SSAW) [209]. The longitudinal waves radiate into the droplet along the Rayleigh angle, causing strong internal streaming near the top of the droplet.

In this section, two aligned SAWs are propagated towards the droplet, from opposite directions, to determine the influence of variables such as applied SAW power and configuration on droplet dynamics and internal flow arrangement. Firstly, the model is corroborated against published experimental data. A 10 µl droplet is initially placed at the centre of the bottom surface with SAW interactions from opposing sides (see Figure 6-19). The aperture of each SAW is greater than the width of the droplet hence forcing is active over the whole droplet width and is perfectly aligned. In the study, a range of SAW powers are examined (1-10 W), and the droplet deformation and dynamics recorded.

According to [26], the transition between vibration and single droplet ejection can be expressed in terms of jet Weber number,

$$We_j = \frac{\rho U_j^2 R_j}{\gamma} \qquad 6\text{–}3$$

where U_j represents the velocity of the jet and R_j is the radius of the jet. Additionally, the length of the jet, L_j, is normalised by the initial droplet radius, R_d, to provide more insight into the effect SAW forcing has on the droplet deformation.

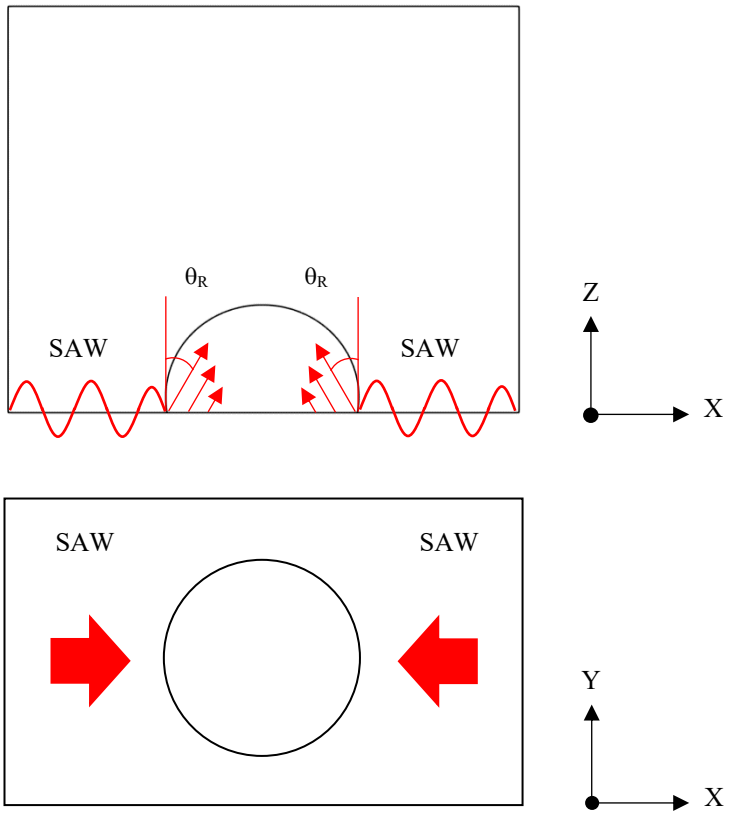

Figure 6-19. Schematic illustration of dual SAW-droplet interactions from opposing aligned IDT's; (a) side view (b) top view

As demonstrated in Figure 6-20, for $We_j < 0.07$ the droplet experiences vibration when the SAWs are interacting, as the liquid is pushed symmetrically upwards. As the power is not enough to overcome the interfacial tension and surface adhesion, the droplet reaches a peak height then retracts downwards as the momentum is dissipated (see Figure 6-21 (a)). After approximately 16 ms the droplet has almost returned to its original spherical shape. For $We_j > 0.07$, single droplet ejection is achieved as the driving force inside the liquid is strong enough to overcome the surface energies. Comparing the images in Figure 6-21 (a) and (b), the contact angle is drastically altered when the SAW power is increased. No longer is the liquid able to spread and reduce its angle on the surface, with the higher power, the contact areas are pushed towards the centre of the drop which forces the liquid inside upwards. After approximately 14 ms, the contact area is diminished such that the droplet is ejected from the surface. In study by Tan et al. [26], they witness the transition between drop vibration and of single droplet ejection at $We_j \approx 0.1$. Unlike the simulated images, in the experiments only a portion of the liquid is expelled from the surface, with

the rest of the droplet able to remain fixed on the surface until the jet Weber number reaches $We_j \approx 0.4$ where breakup is achieved, and multiple droplets are formed.

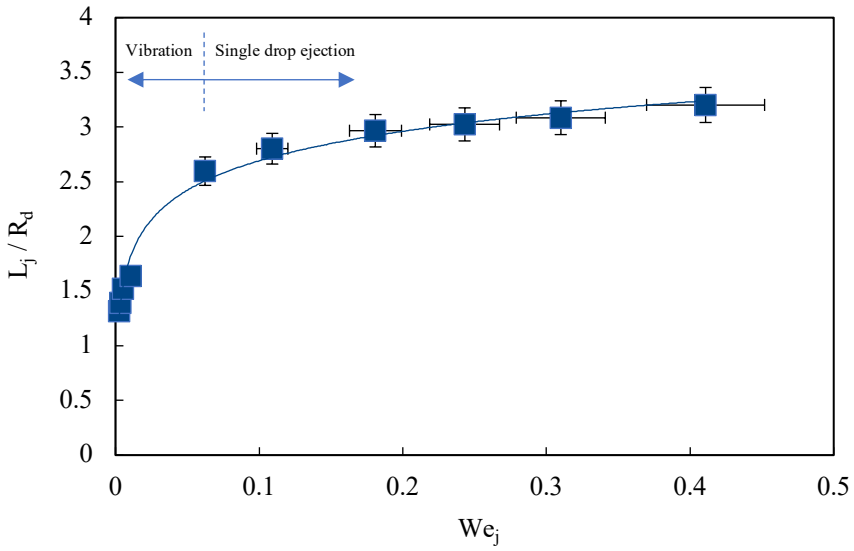

Figure 6-20. Dimensionless jet length as a function of jet Weber number. Line represents best fit of data

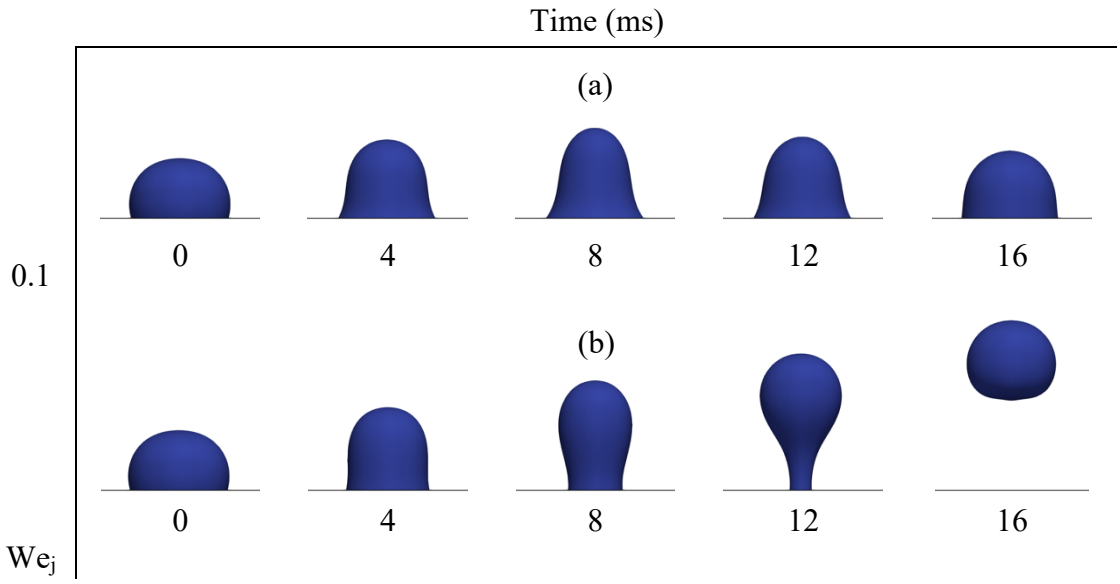

Figure 6-21. Numerical images demonstrating transition from (a) droplet vibration to (b) jetting with increase of jet Weber number We_j

Looking at the flow behaviour inside the droplet during vibration, as demonstrated in Figure 6-22 (a), it is evident that the equal SAW interactions generate a symmetrical flow pattern which pushes the interface upwards as the velocity is intensified. There appears a higher velocity zone near the top of the droplet which, as already depicted in Figure 6-21,

is not enough to cause a transition from vibration to jetting. In contrast, when the applied power is increased, the magnitude of internal flow velocities is strengthened which has more energy to manipulate the droplet causing deformation of the interface. Again, a symmetrical pattern is observed, shown in Figure 6-22 (b), with high internal flow focused towards the top and central region within the droplet.

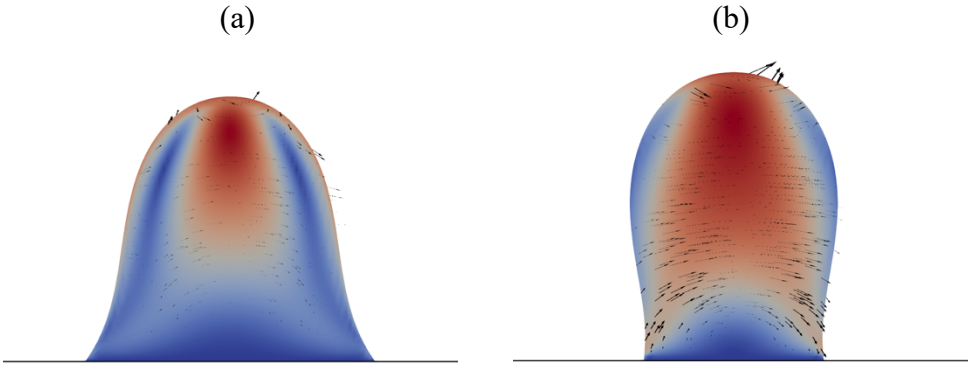

Figure 6-22. Internal velocity structure during dual SAW interactions at 8 ms for; (a) 4W and (b) 6W applied powers. Red colour depicts highest velocity regions.

The influence of SAW power on jet velocity is scrutinised for the single droplet ejection regime. As presented in Figure 6-23, there are appears to be a linear relationship between average jet velocity and applied SAW power for the cases studied. At the onset of jetting, an increase in power has a direct impact on the velocity of the jet, which can be estimated by,

$$\overline{U_J} = 0.0322 P_D \qquad 6\text{–}4$$

where $\overline{U_J}$ symbolises the average jet velocity in m s^{-1} and P_D is the applied SAW power in Watts.

As part of the study, a further two droplet volumes are considered (1 µl and 5 µl) with the results presented in Figure 6-24. It is observed that the transition from drop vibration to droplet jetting is achieved at $We_j > 0.07$ for all volumes tested. Again, these findings are in reasonable agreement with the experimental study by Tan et al. [26].

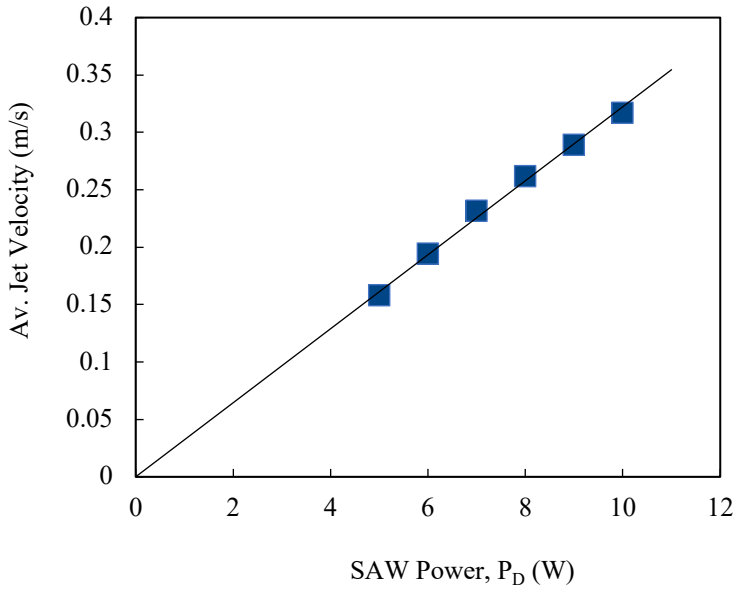

Figure 6-23. Average jet velocity as a function of applied SAW power for single droplet ejection ($We_j > 0.07$)

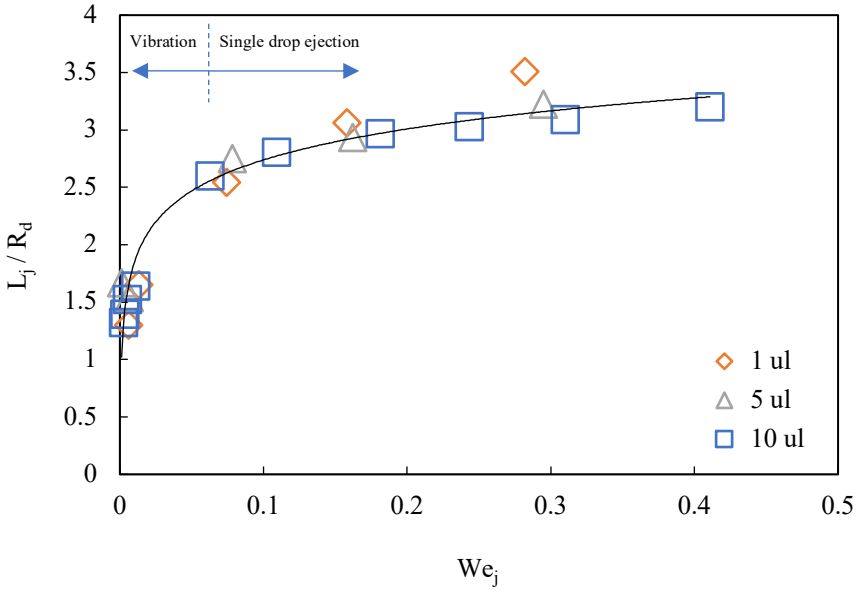

Figure 6-24. Dimensionless jet length as a function of jet Weber number for various droplet volumes. Line represents best fit of data

6.3.1 SAW configurations influence on droplet dynamics and internal flow

In the following, the effect of SAW configuration on droplet deformation and behaviour is examined. In the previous section two perfectly aligned travelling SAWs, from opposite sides, interacts with the droplet causing a symmetrical response. The alignment of the

SAWs will be adjusted, and the results analysed with particular focus on droplet shape, movement, and orientation. In the study, a semi-spherical droplet of volume 2 µl is located at the centre of the bottom surface, with SAW interactions from opposing sides. In the test cases, the ratio of the offset between the SAWs to droplet diameter (L/D) will increase from 0 (perfectly aligned SAWs) to 1.5 (offset). An illustration can be found in Figure 6-25.

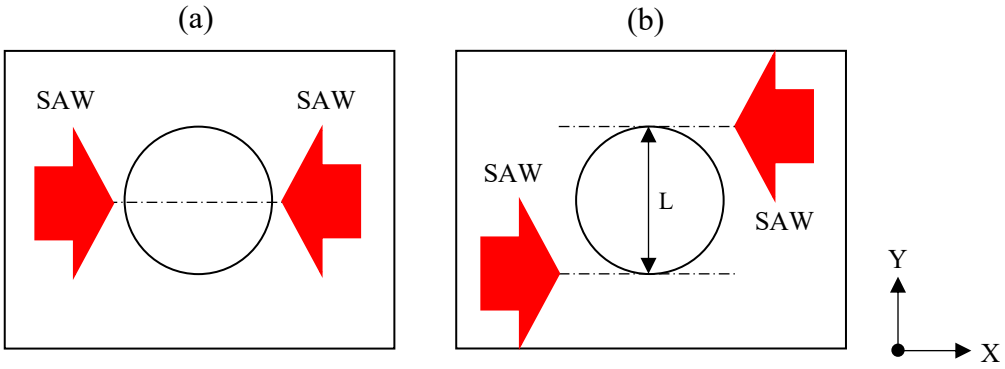

Figure 6-25. Schematic illustration of dual SAW configurations (a) aligned (b) offset

By offsetting the opposing SAWs, it is expected that it will instigate a circulatory motion inside the droplet, rotating around the Z axis. As presented in Figure 6-26 (a), when the SAWs are perfectly aligned, the flow structure is orientated such that four zones are created. These zones are not perfectly described by the current model due to the presence of spurious velocities inside the droplet however with the magnitude of SAW forcing, they are reconfigured in the general direction.

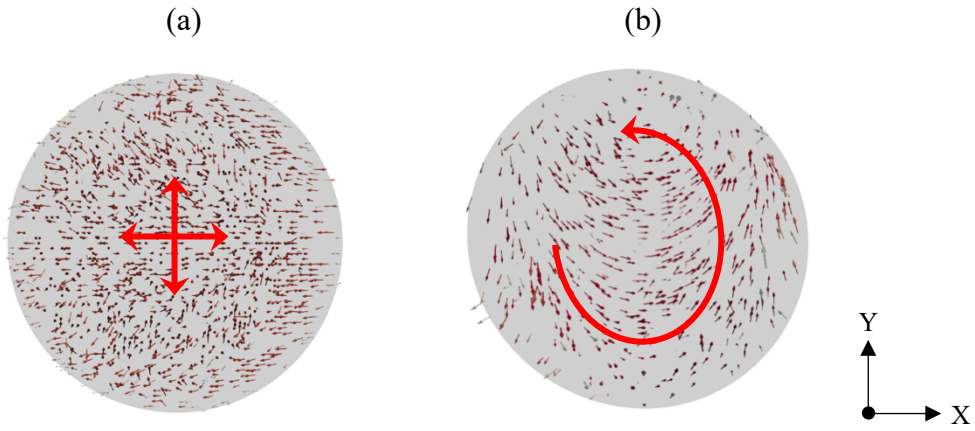

Figure 6-26. Internal flow orientation for SAW configurations (a) aligned (L/D = 0) (b) offset (L/D = 1). Red arrows added as a guide to flow orientation

Contrastingly, when the SAWs are offset there is an obvious circulatory motion, around the Z axis, demonstrated inside the liquid (Figure 6-26 (b)). The shape of the droplet is deformed due to the offset, warping in the direction of the internal flow to an elliptical shape. Looking at the XZ and YZ axis views (Figure 6-27), a swirl-like flow is generated when the SAWs are offset, with the liquid inside the droplet is rotated around the Z axis.

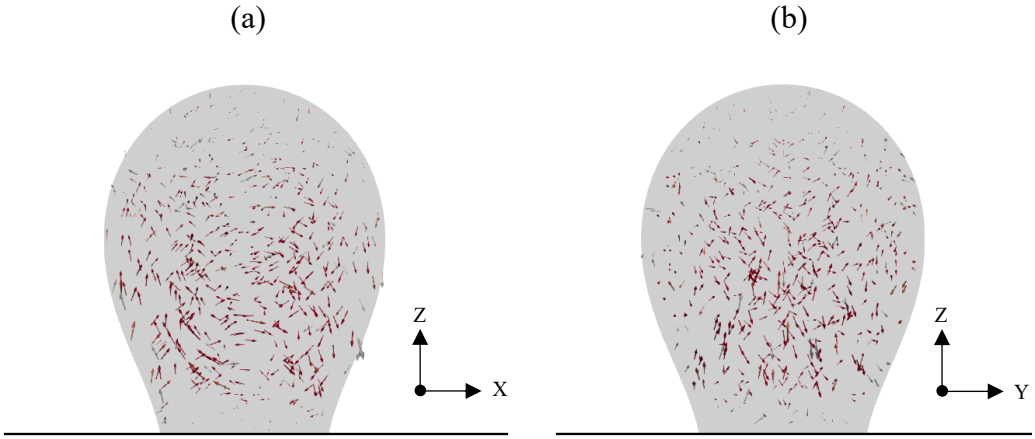

Figure 6-27. Internal flow patterns during jetting for dual offset SAWs (L/D = 1). (a) XZ view (b) YZ view

To further explore the effect of SAW configuration, the offset between opposing SAWs (L/D) is altered from 0 to 1.5 and the results analysed with respect to tip velocity and jetting time. The droplet volume and applied power is kept constant throughout the examination. As shown in Figure 6-28, when the offset between the opposing SAWs is increased the tip velocity is decreased. This is due to the offset SAWs generating more circulatory internal flow motion which is in contrast with the upward (vertical) direction experienced when the SAWs are in alignment. The decrease in upward flow inside the liquid also results in an increased jetting time, with the droplet remaining on the substrate for longer. It has been shown that perfectly aligned SAWs (IDTs) produce faster jetting droplets whilst increasing the offset between IDT's can significantly reduce the upward movement of the droplet as a circulatory flow becomes more dominant. At L/D = 1, the circulatory flow is at its most optimum, providing the peak flow velocities to the liquid. Further increase of the offset results in a weakening of the flow structure as less of the droplet is visible to the acoustic waves, therefore less interaction. The findings from this analysis agree well with the experimental and numerical study by Biroun et al. [85].

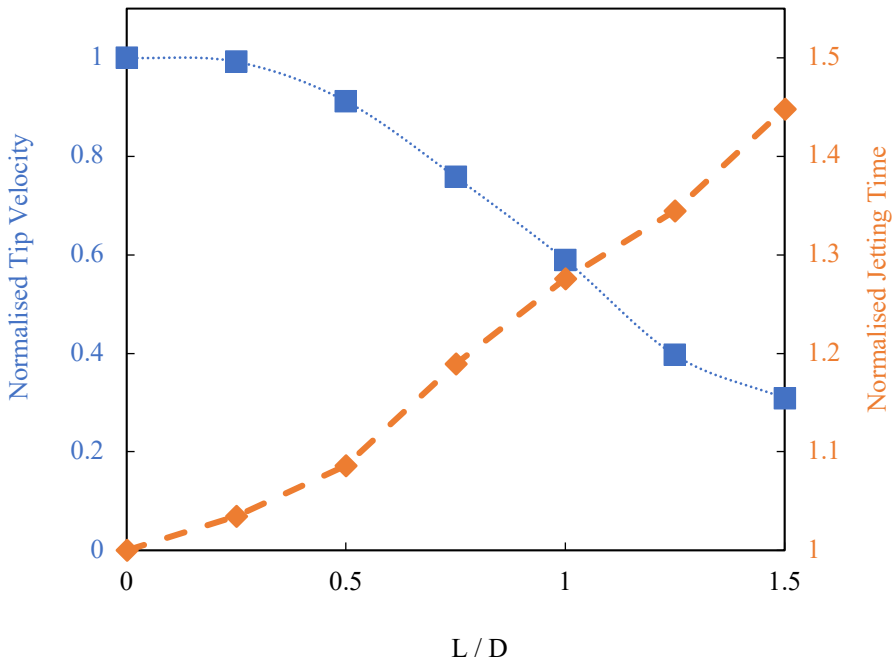

Figure 6-28. Normalised tip velocity and jetting time as a function of dual SAW offset

6.4 Summary

To summarise, the kinetic impacts of SAW-droplet interactions on an inclined slope have been investigated. It is found that, for a 1 µl droplet, an increase in SAW amplitude (power) corresponds to an increase in pumping velocity, for each slope angle. When the amplitude is fixed, the average droplet velocity is decreased as the incline angle is increased until it reaches a minimum at 90°. Increasing the slope angle further, results in the pumping velocity increasing once more with slope inclination. When examining SAW-droplet interactions with varying volume, it has been demonstrated that as SAW amplitude is enlarged, the increase in velocity is lesser in larger droplets as compared to the small droplets. Also, for the same amplitude, a smaller droplet will have a larger average pumping velocity, as compared to a bigger droplet, due to its lower contact area preventing droplet motion along the substrate.

Moreover, droplet impact on dry surfaces is examined without the presence of SAW interactions. Initially, a free impact droplet on a horizontal surface is assessed and compared to experimental data. The outcome suggests that maximum spreading diameter is largely insensitive to surface treatment, like experimental findings. Additionally, droplet impact on inclined surfaces with SAW interactions is studied. From the analysis it has been shown that the magnitude of applied SAW power has a significant impact on

rebound angle, contact time and maximum spreading diameter. It is also found that the initial impact velocity of the droplet plays an important role in the dynamics of droplet impact with SAW. Higher impact velocities can lead to more droplet spreading which results in a longer contact time.

Furthermore, dual SAW interactions on a droplet, from opposing sides, is scrutinised. Two perfectly aligned SAWs are initially tested, for a 10 µl droplet, at a variety of powers to determine their impact on aspects such as jet length, jet Weber number and velocity. The results indicate single droplet separation from the substrate is achieved at $We_j > 0.07$, with a linear trend observed for average droplet velocity in this regime. Additional testing at various volumes was initiated and a similar outcome observed as with all volumes a single droplet jet was witnessed at $We_j > 0.07$. These findings agree with those published in the literature.

Finally, the effect of dual SAW configuration on droplet deformation and dynamics is examined. A variety of SAW offsets are considered, and their influence analysed. The findings suggest that as the offset is increased, the tip velocity is decreased resulting in a longer jetting time. The offset between SAWs has been shown to produce a circulatory flow pattern, around the Z axis, reducing the vertical motion in the droplet. At L/D = 1, the circulation inside the droplet is at a peak value which reduces as the offset is further increased due to less SAW interaction.

Chapter 7– Multi-component Multi-phase Multi-Pseudopotential lattice Boltzmann model

7.1 Introduction

Multi-component multi-phase (MCMP) systems are analogous with nature and industrial systems, with either a liquid-gas, liquid-solid or gas-solid configuration depending on the state of the component or phase. Systems can be generally classified as miscible where the components or phases are able to dissolve and combine to make a homogenous solution i.e., ethanol and water, or immiscible where the components or phases are unable to mix resulting in a dispersion of one in another i.e., oil and water.

There has been significant development of MCMP models over the past decades, focusing on a variety of scientific problems such as fluid flow in porous media [165,210], boiling and condensing [211,212]. Traditional CFD methodologies have gained most attention, predominantly classified as either front tracking [213–215] or front capturing [216,217]. Front tracking models actively track the location of the interface between components, to determine the free surface curvature. Alternatively, front capturing schemes monitor the movement of the fluid and reconstruct the interface afterwards from the single continuum fluid. While tracking and capturing of components/phases is relatively simple, for highly dynamic cases, it can be challenging and computationally expensive due to rapid changes in mesh generation. The LBE, on the other hand, can capture phase segregation without the need for interface capturing or tracking. Microscale interparticle forces allow surface tension in multiphase fluid flow to emerge naturally.

In this chapter, a newly developed multi-component multi-phase multi-pseudopotential (MCMP MPI) LB model is introduced. The model is initially analysed by conventional benchmark tests, in comparison to the SCMP MPI model, to determine thermodynamic consistency, surface tension, dynamic oscillation, and fluid-solid implementation.

7.2 Model description

7.2.1 Multi-component Multi-phase lattice Boltzmann model

Considering the single relaxation-time BGK collision operator, the evolution of density distribution function for MCMP flow can be expressed as [218]

$$f_{i,\sigma}(\boldsymbol{x}+c_i\delta t, t+\delta t) = f_{i,\sigma}(\boldsymbol{x},t) - \frac{1}{\tau_\sigma}\left(f_{i,\sigma}(\boldsymbol{x},t) - f_{i,\sigma}^{eq}(\boldsymbol{x},t)\right) + \delta t F_{i,\sigma} \qquad 7\text{–}1$$

where $f_{i,\sigma}(\boldsymbol{x},t)$ is the density distribution function with its corresponding equilibrium $f_{i,\sigma}^{eq}(\boldsymbol{x},t)$, $\boldsymbol{x}$ is the spatial position, $\boldsymbol{c}_i$ is the discrete particle velocity along the *i*th direction, δ_t is the time step, τ_σ is the non-dimensional relaxation-time, $F_{i,\sigma}$ denotes the forcing term (described in Section 7.2.4) and σ signifies to the component. For a D2Q9 LB model, the equilibrium distribution function is obtained from,

$$f_{i,\sigma}^{eq} = \rho_\sigma \omega_i \left[1 + \frac{c_i \cdot u_\sigma^{eq}}{c_s^2} + \frac{(c_i \cdot u_\sigma^{eq})^2}{2c_s^4} - \frac{(u_\sigma^{eq})^2}{2c_s^2}\right] \qquad 7\text{–}2$$

where c_s is the lattice speed of sound $\left(c_s = \frac{\Delta x}{\Delta t\sqrt{3}}\right)$, with lattice weights and discrete velocities as,

$$[c_0, c_1, c_2, c_3, c_4, c_5, c_6, c_7, c_8] = \begin{bmatrix} 0 & 1 & 0 & -1 & 0 & 1 & -1 & -1 & 1 \\ 0 & 0 & 1 & 0 & -1 & 1 & 1 & -1 & -1 \end{bmatrix} \qquad 7\text{–}3$$

$$w_i = \begin{cases} 4/9, & i = 0 \\ 1/9, & i = 1,2,3,4 \\ 1/36, & i = 5,6,7,8 \end{cases} \qquad 7\text{–}4$$

The above framework can be applied to 3D flows, with the D3Q15, D3Q19 and D3Q27 lattice definitions being most favoured in the LB community. Similar to the single component method, the local mass density and velocity for each component are acquired from,

$$\rho_\sigma = \sum_\sigma f_{i,\sigma} \qquad 7\text{–}5$$

$$u_\sigma = \frac{1}{\rho}\sum_\sigma f_{i,\sigma}\, c_i \qquad 7\text{–}6$$

The kinematic viscosity of each component is defined as,

$$\upsilon_\sigma = \left(\tau_\sigma - \frac{1}{2}\right) c_s^2 \Delta t \qquad 7\text{–}7$$

thus, the viscosity can be altered if a different relaxation-time is chosen for each different component.

The fundamental dissimilarity comes in the definition of the equilibrium distribution function $f_{i,\sigma}^{eq}$, where density ρ_σ is the component density and velocity u_σ^{eq} is the velocity of the fluid mixture [104]. According to Guo, the description of u_σ^{eq} involves the use of a barycentric velocity, which is second order accurate in time and space, to define not only the equilibrium velocity but also the physical velocity of the fluid mixture, expressed as [104]

$$u_b = \frac{1}{\rho}\sum_\sigma \left(\sum_i f_{i,\sigma} c_i + \frac{\boldsymbol{F}_\sigma \delta t}{2}\right), \quad \rho = \sum_\sigma \rho_\sigma, \quad u_\sigma^{eq} = u_b \qquad 7\text{–}8$$

7.2.2 Fluid-fluid interactions

In the present model, the multi-pseudopotential interaction scheme (MPI) is extended to multiple components. In a multi-component fluid there exist two interactions; one responsible for interactions of particles within the same component and the other for interactions between particles in different components [218]. In the following, components for liquid and gas will be designated as subscripts 1 and 2, respectively. The MPI model, constructed of multiple pseudopotentials, is implemented to describe the particle interactions within the liquid component. In multi-component form, the equations are expressed as,

$$\boldsymbol{F}_{\sigma\sigma}^{MPI} = \boldsymbol{F}_{\sigma\sigma}^{1} + \boldsymbol{F}_{\sigma\sigma}^{2} + \cdots + \boldsymbol{F}_{\sigma\sigma}^{n} \qquad 7\text{–}9$$

$$\boldsymbol{F}_{11}^{MPI} = \sum_{j=1}^{n} -G_{j11}\psi_{j1}(\boldsymbol{x}) \sum_{i=1}^{N} w(|\boldsymbol{c_i}|^2)\psi_{j1}(\boldsymbol{x} + c_i\delta_t)c_i \qquad 7\text{–}10$$

For the water (liquid) component, the effective mass is calculated according to,

$$\psi_{j1} = \left(\frac{\rho_1}{\lambda_j \varepsilon_j + C_j \rho_1}\right)^{1/\varepsilon_j} \quad 7\text{–}11$$

which allows the introduction of various EOS to describe the composition of the multiphase liquid. $G_{j\sigma\sigma}$ in Eq. 7–10 is responsible for phase segregation, of which the value for each potential is set according to the EOS adopted. As for the air component (gas), the original SC model is employed to define the pseudopotential, expressed in exponential form,

$$\psi_2 = \rho_0 \left(1 - \exp\left(-\frac{\rho_2}{\rho_0}\right)\right) \quad 7\text{–}12$$

$$\boldsymbol{F_{22}} = -G_{22}\psi_2 \sum_{i=1}^{N} w(|\boldsymbol{c_i}|^2)\psi_2(\boldsymbol{x} + c_i\delta_t)c_i \quad 7\text{–}13$$

In this instance, the air (gas) component phase is assumed as ideal with no segregation, hence the value for $G_{22} = 0$. To introduce particle interaction between different components, the following equations are implemented,

$$\boldsymbol{F}_{\sigma\bar{\sigma}} = -G_{\sigma\bar{\sigma}}\psi_\sigma \sum_{i=1}^{N} w(|\boldsymbol{c_i}|^2)\psi_{\bar{\sigma}}(\boldsymbol{x} + c_i\delta_t)c_i \quad 7\text{–}14$$

where $G_{\sigma\bar{\sigma}}$ controls the strength of the interaction between components. It has been noted in the literature that the strength of interaction between components must be sufficiently large to enable immiscibility in binary mixtures [219]. In this study, the strength is set to $G_{12} = G_{21} = 0.1$ which is large enough to minimise the dissolution of one component into the other. To maintain simplicity, the effective mass is described by the original SC model through,

$$\psi_\sigma = \rho_\sigma \quad 7\text{–}15$$

Hence, the total interaction, for the liquid component, in the multi-component model is found from,

$$\boldsymbol{F}_{\mathbf{1},int} = \boldsymbol{F}_{11}^{MPI} + \boldsymbol{F}_{\mathbf{12}} \tag{7–16}$$

with the gas component established from,

$$\boldsymbol{F}_{\mathbf{2},int} = \boldsymbol{F}_{\mathbf{22}} + \boldsymbol{F}_{\mathbf{21}} \tag{7–17}$$

7.2.3 Fluid-solid interactions

Incorporating adhesive effects in the MCMP model is relatively straightforward due to its similarity to SCMP schemes. This can be achieved through additional forcing terms in the LBE which can mimic the fluid-solid interaction. As mentioned previously, there have been several methods proposed, for pseudopotential models, classified as density-based, pseudopotential-based, and modified pseudopotential-based. More recently, the geometric formulation has been adapted from the phase-field method to the pseudopotential model which has enhanced accuracy and flexibility.

For density-based MCMP models, the adhesive force acting on the σth component can be defined as [165,220]

$$\boldsymbol{F}_{\sigma,ads} = -G_{\sigma,ads}\rho_{\sigma}\sum_{i=1}^{N} w(|\boldsymbol{c_i}|^2)s(\boldsymbol{x} + c_i\delta_t)c_i \tag{7–18}$$

where $s(\boldsymbol{x} + c_i\delta_t)$ acts as a switch function that is equal to either 0 or 1 for solid and bulk fluid nodes, respectively. The strength of interaction between the fluid and solid wall can be adjusted through $G_{\sigma,ads}$ with positive and negative values signifying non-wetting and wetting surfaces, respectively. Intuitively, the value of $G_{\sigma,ads}$ for component 2 will have an opposing value to component 1 i.e., if $G_{1,ads} = 0.5$ then $G_{2,ads} = -0.5$.

A similar adjustment to the geometric formulation is required when extending to multiple components, with opposing values required between fluids. Unlike the above, no additional forcing terms are introduced with this method, only the density distribution near the solid boundaries is altered. Looking at the implementation in two dimensions

$$\rho_{\sigma,i,0} = \rho_{\sigma,i,2} + \tan\left(\frac{\pi}{2} - \theta_{\sigma}\right)\left|\rho_{\sigma,i+1,1} - \rho_{\sigma,i-1,1}\right| \tag{7–19}$$

the prescribed angle, θ_σ, for each component is defined by the user, with $\theta_\sigma \not\equiv \theta_{\bar{\sigma}}$. Here the value of prescribed angle for component 2 can be calculated from $\theta_2 = (180° - \theta_1)$, thus if $\theta_1 = 45°$ then $\theta_2 = (180° - 45°) = 135°$. As with the SCMP model, this technique can be applied to 3D flows following a similar procedure to Section 4.3.3.

7.2.4 Discrete forcing in the MPI

Incorporating a discrete forcing scheme into the pseudopotential LB can alleviate some unfavourable lattice effects inherent in the shifted velocity method, first proposed by Shan and Chen. Following [158], these discrete effects can be integrated into the MCMP MPI through,

$$F_{i,\sigma} = 3w_i\delta_t\left(1 - \frac{1}{2\tau_\sigma}\right)\left[\frac{(\boldsymbol{c_i} - \boldsymbol{u})}{c^2} + \frac{3(\boldsymbol{c}_i - \boldsymbol{u})\boldsymbol{c}_i}{c^4}\right]\boldsymbol{F} + \frac{3w_i\delta_t}{2c^4}\sum_j^n\left[\frac{s_j}{\tau_\sigma\psi_{j\sigma}^2}\left(3\left(\boldsymbol{F}_{j\sigma}\cdot\boldsymbol{c}_i\right)^2 - c^2\left(F_{j\sigma,x}^2 + F_{j\sigma,y}^2\right)\right)\right] \quad 7\text{–}20$$

where s_j are arbitrary constants. From the above it is apparent that the first term follows the Guo et al. [154] method, with corrections developed by Li et al. [153]. In the proposed model, both the liquid and gas components are subject to this modification however only the liquid part incorporates the additional term in Eq. 7–20, which is responsible for the correction in the MPI.

7.3 Model evaluation and validation

In the subsequent sections, the newly proposed methodology will be evaluated through established benchmark tests, comparing it to analytical solutions, published data and the single component model. In the study, the D2Q9 lattice structure will be employed to examine the performance of the model in two dimensions.

The PR EOS is chosen for the liquid in all cases unless stated otherwise. For liquid water, the parameters a, b and R are set to $a = 1/100$, $b = 2/21$ and $R = 1$, respectively, with the acentric factor $\omega = 0.344$. A summary of the MPI parameters for the PR EOS can be found in Appendix C. The non-dimensional relaxation-time (τ_σ) for each component is set to 1, hence the dynamic viscosity is equal to the density ratio $\mu_l/\mu_g = \rho_l\upsilon_l/\rho_g\upsilon_g = \rho_l/\rho_g$. To provide fair comparison, for the SCMP model, the above EOS parameters are also chosen, with a non-dimensional relaxation time of 1.

7.3.1 Evaluation of thermodynamic consistency

To assess the thermodynamic consistency of the model, the numerically obtained coexistence curves are compared against the analytical Maxwell construction through simulating flat interfaces.

A domain size of $N_x \times N_y = 100 \times 100$ is implemented for the 2D case, with periodic boundary conditions applied in all directions. The density fields are initialised as,

$$\rho_\sigma(x,y) = \rho_{\sigma,out} + \frac{\rho_{\sigma,in} - \rho_{\sigma,out}}{2}[\tanh(y_1) - \tanh(y_2)] \qquad 7\text{–}21$$

where $\rho_{\sigma,in}$ and $\rho_{\sigma,out}$ represents the densities of component σ inside and outside of the flat interface region, respectively, $y = 2(y - 25)/W$ and $y_2 = 2(y - 75)/W$, with $W = 5$ as the initial interface thickness. Again following [159], to approach thermodynamic consistency, the free parameter ε_j can be split into two separate quantities. In this approach, slight adjustment of the value can lead to significantly more agreeable results. Similar to [159], $\varepsilon_{forcing,j} = 0.89\ \varepsilon_{EOS,j}$ is provides optimal thermodynamic consistency across the range of reduced temperatures.

Additionally, for the free drop case, the same lattice structure and setup is chosen with the density field initialised as,

$$\rho_\sigma(x,y) = \frac{\rho_{\sigma,in} + \rho_{\sigma,out}}{2} - \frac{\rho_{\sigma,in} - \rho_{\sigma,out}}{2}\tanh\left[\frac{2(R - R_0)}{W}\right] \qquad 7\text{–}22$$

where $\rho_{\sigma,in}$ and $\rho_{\sigma,out}$ represents the densities of component σ inside and outside of the droplet, respectively, R_0 is the initial droplet radius ($R_0 = 30$), $W = 5$ and $R = \sqrt{(x - x_0)^2 + (y - y_0)^2}$ in which (x_0, y_0) is the central location of the domain.

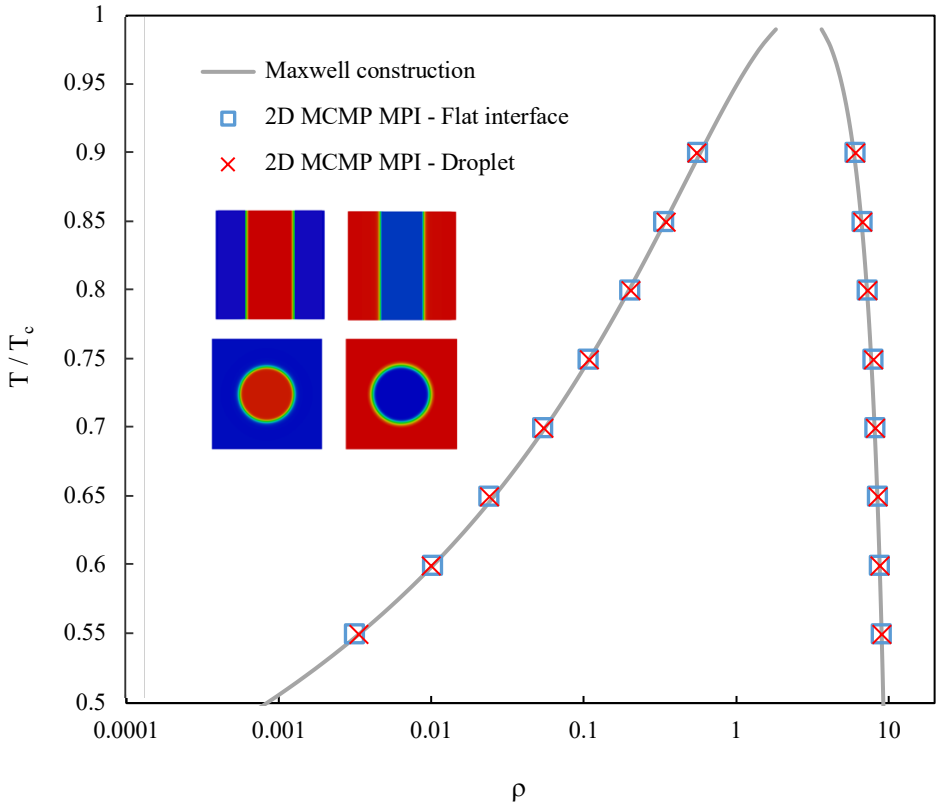

Figure 7-1. Comparison of numerically obtained coexistence densities with the analytical curve predicted by Maxwell construction for 2D MCMP MPI. Image inserts display density distributions for water (left) and air (right) components

As demonstrated in Figure 7-1, the simulated coexistence densities agree well with the analytical Maxwell construction, exhibiting compliance even at high density ratios. The proposed multi-component model has exhibited good thermodynamic consistency, both in simulating flat interfaces and free liquid drop surrounded by gas. A representative density cross section for water droplet in air, at high density ratio ($\rho_l/\rho_g \approx 800$), is shown in Figure 7-2. As demonstrated, the distribution for the multi-component model matches well with the single component MPI model, especially in the liquid. The SCMP does however display a larger density ratio between liquid and vapour ($\rho_l/\rho_g \approx 1170$) in this instance.

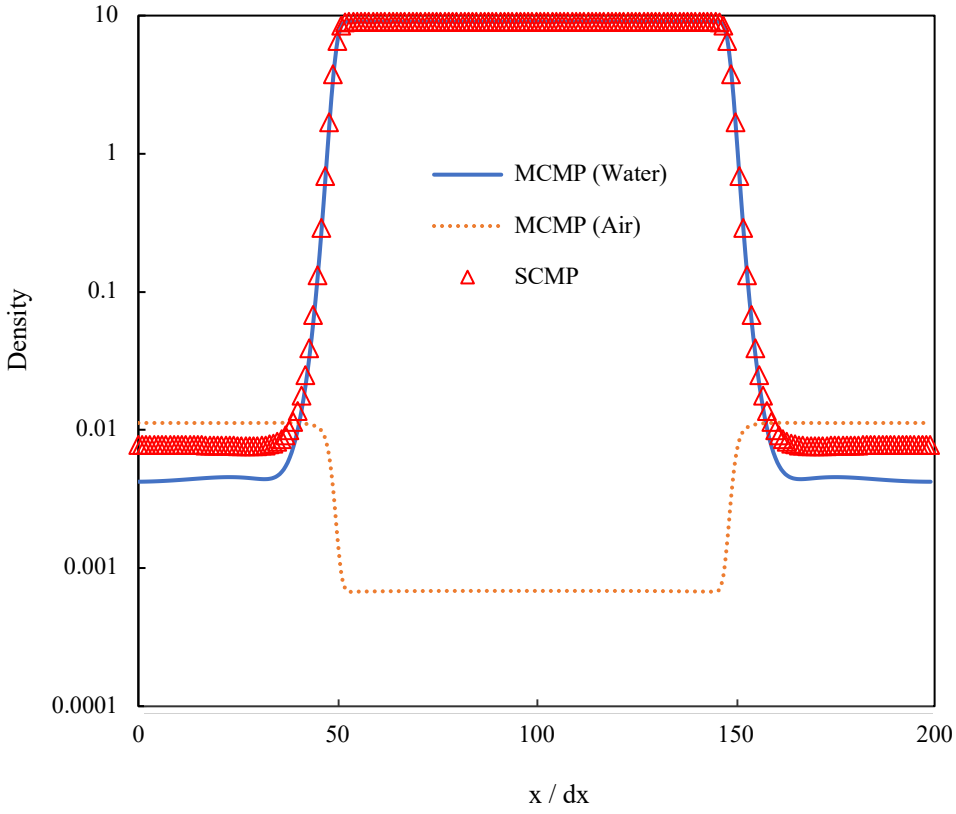

Figure 7-2. Density distribution comparison between single component (SCMP) and multi-component (MCMP) MPI models at high density ratio (T_R = 0.55)

7.3.2 Evaluation of spurious velocities

Spurious velocities are an inescapable by-product of multiphase LB models which affect accuracy and stability. The generation of these parasitic velocities is attributed to discretisation errors in the forcing scheme employed, manifesting near curved interfaces., especially at high density ratios There has been much study in this topic, providing analysis and solutions to the problem [221,222].

The current model is evaluated to determine the magnitude of spurious velocities, for a free water droplet surrounded by air, at high density ratio. As before, the results for the MCMP model are compared to the SCMP to evaluate any similarities and differences. As demonstrated in Figure 7-3, the largest velocities are found in the gas phase, outside of the droplet, for both models. The peak value for the MCMP is approximately 1.7 x 10^{-3} (lattice units) which is decreased significantly as the position is progressed towards the interface region and into the droplet. In contrast, the SCMP displays considerably larger peak values (around 2.3 x 10^{-2}) which is approximately one order of magnitude difference. This disparity can be attributed to the higher density ratio (lower vapour phase density)

which can drastically increase the level of spurious velocities as a consequence of the large density gradient.

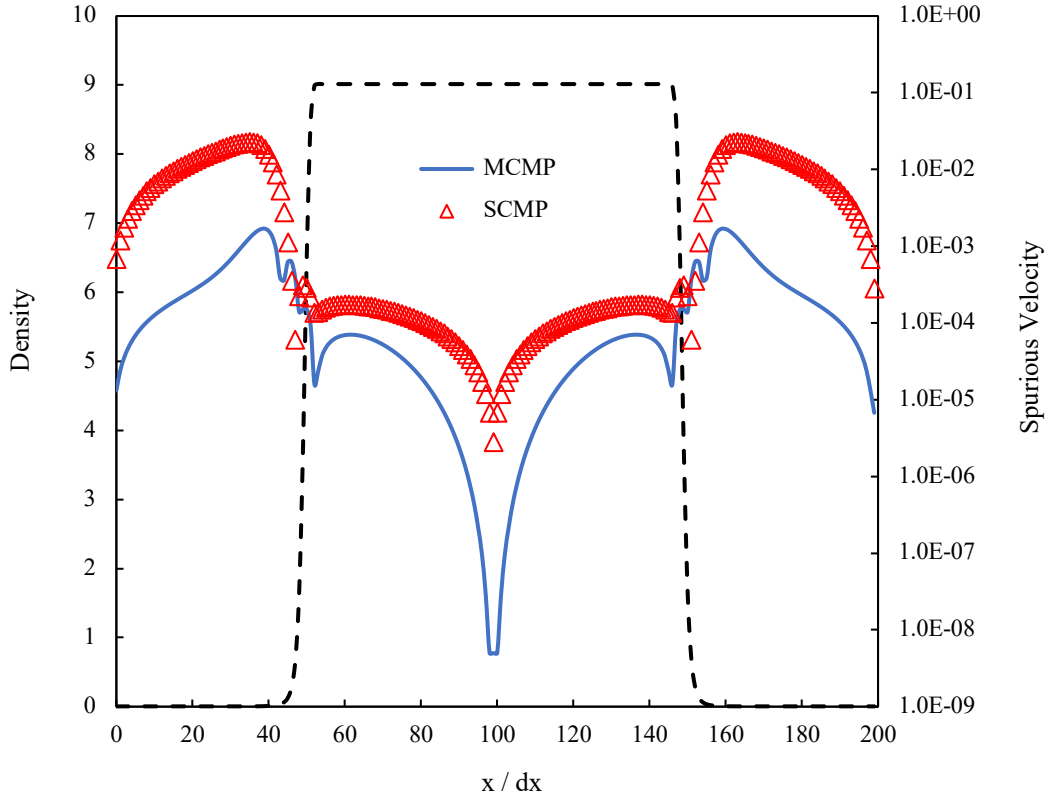

Figure 7-3. Velocity distribution through centre of domain, for SCMP and MCMP MPI models, at high denisty ratio (T_R = 0.55). Black dashed line represents droplet location.

7.3.3 Evaluation of interaction force

A further assessment of the MCMP model, in comparison to its SCMP counterpart, is in the form of examining the interaction force, specifically Fx or Fxii in the case of the MCMP. As the proposed model is based on the SCMP, the magnitude of the forcing should be the same as it is solely a consequence of the EOS employed (pseudopotentials), of which is identical for both models. To evaluate the forcing terms, the free droplet case described in Section 7.3.2 is selected.

As expected, the forcing distributions in the x-direction matches precisely for both models. Figure 7-4 provides a visual comparison, focusing on the left-hand-side of the droplet, at the interface region. Additionally, the insert plot specifies the total distribution across the width of the domain, showing symmetrical positive and negative forces at opposite sides of the droplet.

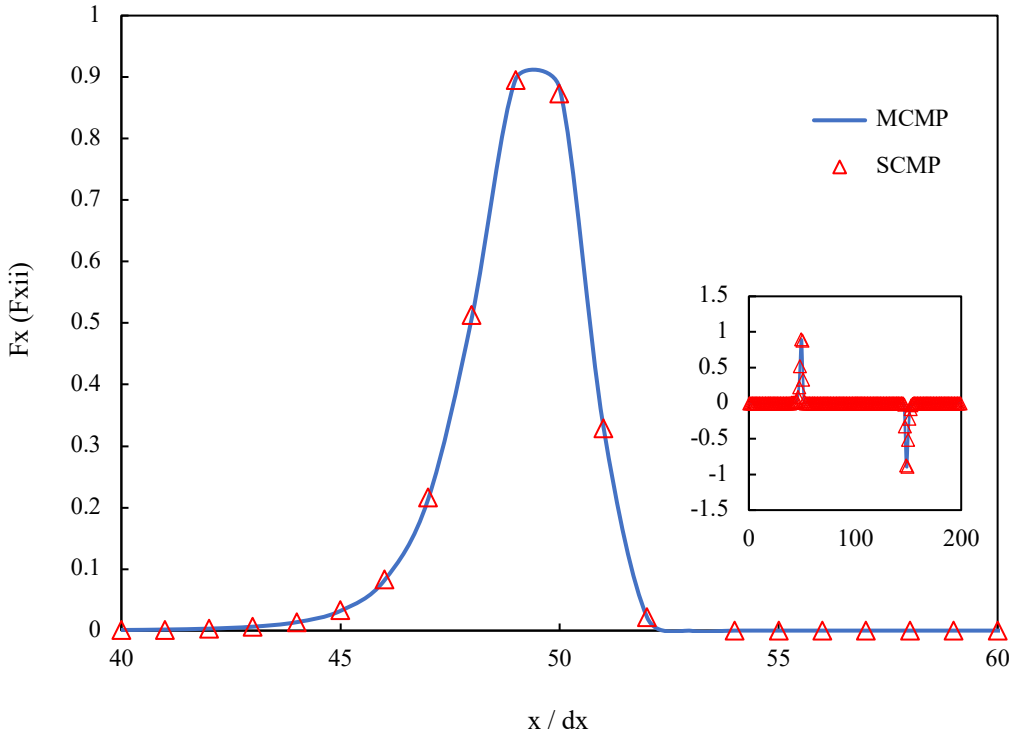

Figure 7-4. Interaction force at left-hand-side of droplet for MCMP and SCMP MPI. Insert illustrates total forcing distribution over width of the domain.

This outcome further supports the implementation of the proposed model, validating the interaction forces which play a significant role in stability and accuracy of multiphase LB models.

7.3.4 Evaluation of Laplace law

Laplace's law is employed to validate the simulation of droplets of different radii. According to Laplace's law, the pressure difference across the interface of a circular or spherical drop is related to the interfacial tension and the radius of the drop. In two-dimensions, the law is given by $\delta p = p_{in} - p_{out} = \gamma/R$, where p_{in} and p_{out} are the fluid pressures inside and outside of the drop, respectively, and R is the droplet radius. Once the interfacial tension is given, the pressure difference will be proportional to $1/R$.

To test the relationship numerically, the radius of the droplet is varied within $20 < R < 30$, and the pressure difference obtained. A domain size of $N_x \times N_y = 100 \times 100$ is selected for the examination, at a reduced temperature of $T_R = 0.65$. As illustrated in Figure 7-5, a linear relationship is confirmed for both the MCMP and SCMP models, with a coefficient of determination of 0.9999178 and 0.9999728, respectively. There are minor

differences in the values however the value of surface tension, for the two models, is very similar (0.231 for MCMP compared with 0.237 for SCMP case). This outcome provides evidence that the behaviour of the proposed model closely matches that of the single component MPI.

From the data, the model demonstrates a proportional relationship between the pressure difference inside and outside of the drop, and the inverse of drop radius therefore Laplace's law is substantiated.

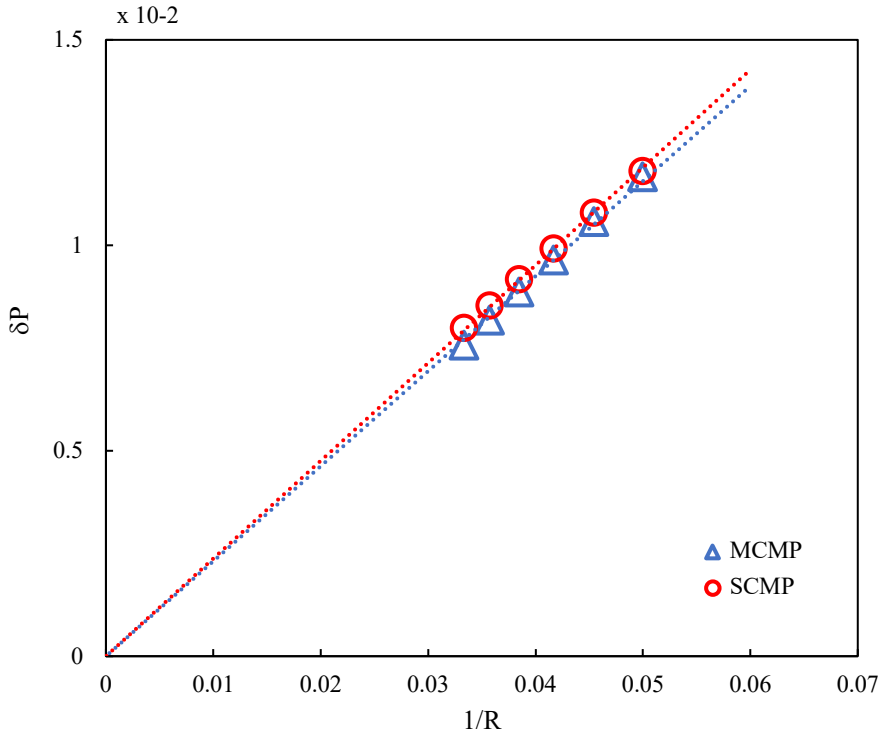

Figure 7-5. Comparison of Laplace's law validation for MCMP and SCMP MPI. Dashed lines represent linear best fit to data sets.

Furthermore, the relationship between surface tension and reduced temperature is compared against the Guggenheim theoretical relation [223] for the proposed MCMP model. From Figure 7-6, it is demonstrated that the numerical data closely matches the theoretical relation ($\gamma = \kappa(1 - T/T_c)^{1.22}$), established in [223], thus providing further proof of the consistency of the presented model.

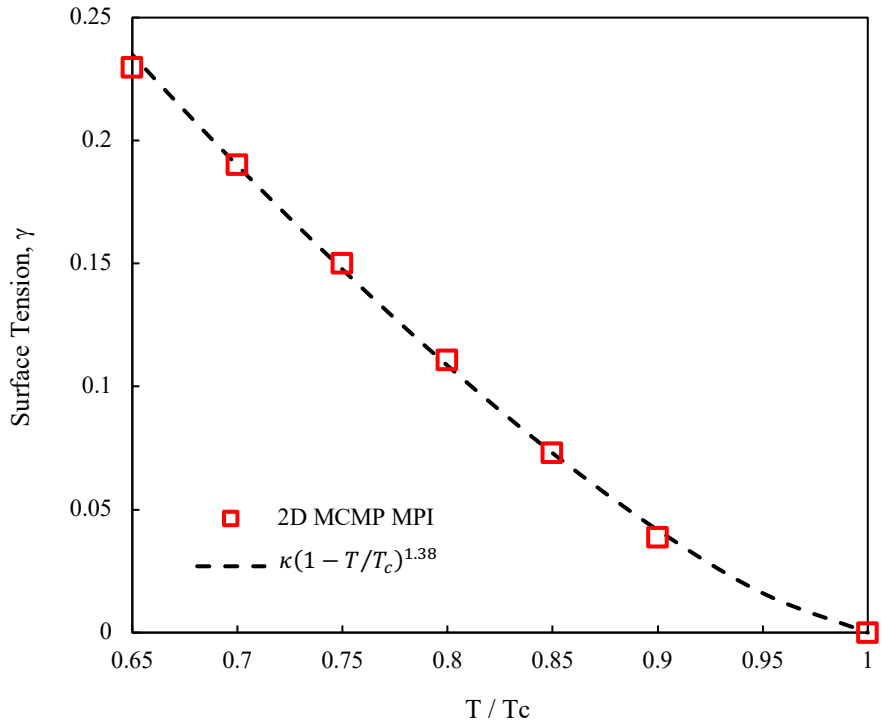

Figure 7-6. Relation for surface tension against reduced temperature

7.3.5 Evaluation of contact angle

As previously described, there are several techniques developed in the LB community to mimic fluid-solid adhesion. In this section, the geometric formulation will be examined as part of the proposed MCMP MPI model to determine its effectiveness and accuracy in simulating droplets on a surface of varying wetting properties.

In the 2D simulations, a stationary semi-circular droplet of radius $R = 40$ is initially placed on a flat surface with no body force applied. A lattice size of $N_x \times N_y = 300 \times 100$ is adopted, with periodic boundary conditions applied in the x direction, while a no-slip condition is added to the upper and lower boundaries. As previous, the reduced temperature is set to $T_R = 0.65$. A selection of numerically obtained images is provided in Figure 7-7, at various surface wettability, to illustrate the ability of the model.

θ ~ 30º θ ~ 90º θ ~ 150º

Figure 7-7. Numerically obtained images, for different levels of surface wettability, for 2D MCMP MPI

The results in Figure 7-8 are in good agreement with the analytical solution demonstrating the capability of the model to simulate static contact angles accurately. Additionally, as seen in Table 7-1, the discrepancy between the prescribed and measured contact angle is almost negligible, with a maximum error of ~1.3%.

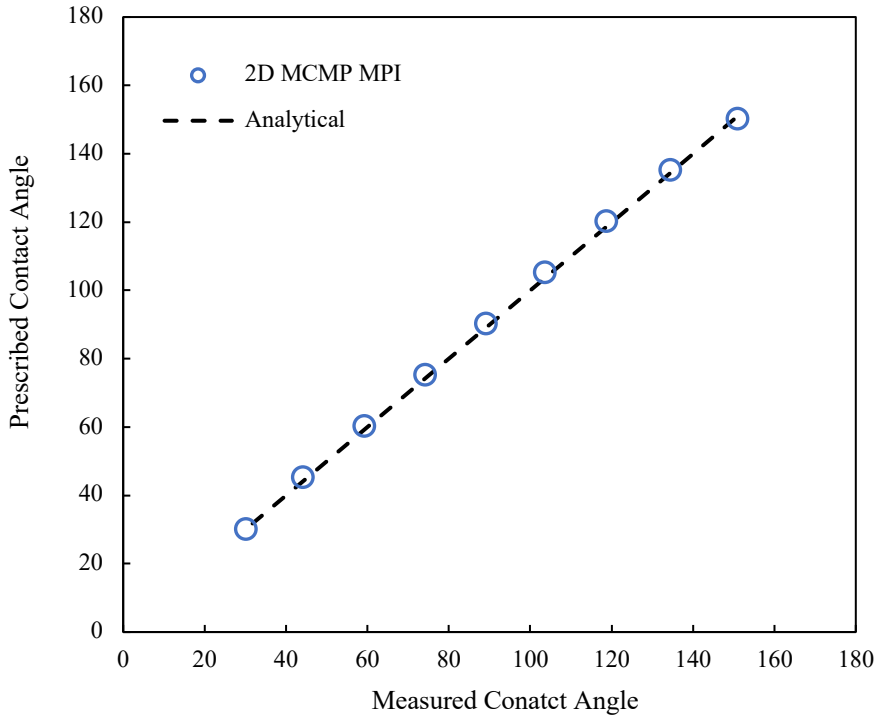

Figure 7-8. Measured contact angles for 2D MCMP MPI with geometric formulation at high density ratio (Tr = 0.65)

Table 7-1. Error in measured equilibrium contact angle for 2D MCMP MPI

Prescribed Contact Angle	Measured Contact Angle	% Error
150	151.0708334	-0.713889
135	134.6449421	0.263006
120	118.9016802	0.915266
105	103.7923138	1.150177
90	89.33172601	0.742527
75	74.35989719	0.853470
60	59.39213596	1.013107
45	44.39556409	1.343191
30	30.27308037	-0.910268

Additionally, validation of the schemes ability to accurately implement static contact angles, through scrutinising the equilibrium shape of the drop, is examined. As previously mentioned, Dupont and Legendre [178] demonstrate that, in the absence of gravity, it is possible to geometrically calculate the equilibrium quantities of the droplet via expressions described in Eq. 3–25. The numerical values for dimensionless wet length (L/R_0) and height (e/R_0) against the static contact angle θ_s are presented in Figure 7-9. The numerical data agrees well with the analytical solution for the range of angles considered.

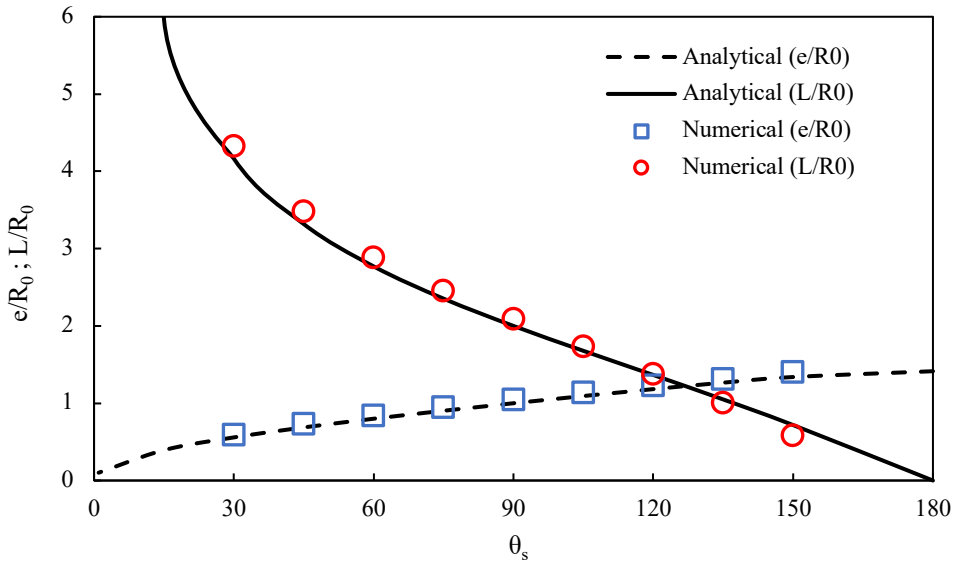

Figure 7-9. Dimensionless wet length L/R_0 and height e/R_0 of a droplet at equilibrium as a function of static contact angle θ_s for 2D MCMP MPI

7.3.6 Evaluation of droplet oscillation

To assess the dynamic condition of the model, a validation case is presented where a droplet, which is initially placed at the centre of the domain and deformed to an ellipsoidal shape, is allowed to oscillate to reach equilibrium due to interfacial tension and viscous dampening. The initial droplet is deformed to an ellipsoidal shape by,

$$\frac{(x-x_0)^2}{R_0^2}+\frac{(y-y_0)^2}{(0.8R_0)^2}=1 \qquad 7\text{–}23$$

where (x_0, y_0) is the centre of the domain and R_0 is the initial radius of the drop, set to $R_0 = 40$. Figure 7-10 demonstrates the evolution of the normalised droplet radius (droplet radius, at each timestep, as compared to equilibrium droplet radius R_e) in both the horizontal (W/W_0) and vertical directions (H/H_0). At the intersection of the solid and dashed lines, the droplet is spherical in shape.

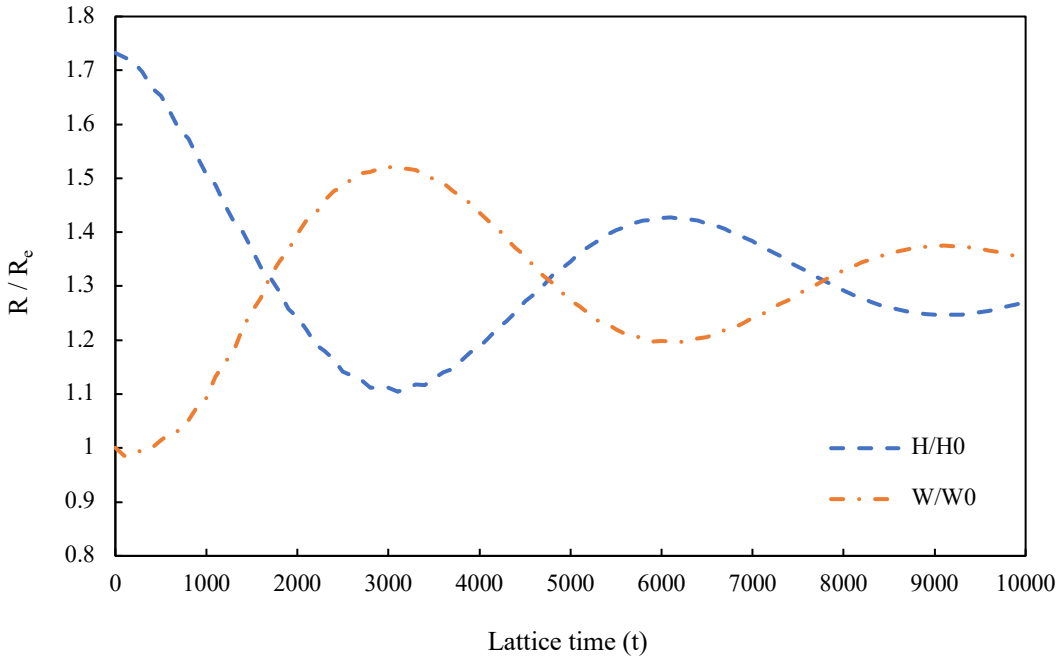

Figure 7-10. Normalised radius of oscillatory droplet as a function of time for 2D MCMP MPI

Following Eq's. 4–18 - 4–20, the analytical solution for time period $T = 2\pi/\omega_n$ for the second mode (n = 2) can be calculated and compared to the numerically obtained results. The analytical oscillatory period is found as $T_a = 3237$, while the numerical oscillation period is $T_{LBM} = 3300$, giving a relative error approximately 2%. The outcome

demonstrates the capability of the developed model in dynamic simulations involving multiple components at high density ratio.

7.4 Summary

A new MCMP LB has been proposed based on the MPI framework. The model is examined against the SCMP model and verified through use of conventional benchmarking examinations. The preliminary results indicate good agreement with the analytical solutions for static cases including thermodynamic consistency, Laplace law, and contact angle in addition to dynamic scenarios such as droplet oscillation.

A comparison with the SCMP reveals several key similarities however there are also some differences. The proposed MCMP model demonstrates excellent agreement with the SCMP in liquid phase density however the gas component/phase is slightly different hence the eventual density ratios are dissimilar. This exacerbates the magnitude of spurious velocities experienced in the SCMP model due to higher density ratio, thus the MCMP generates significantly lower values, on the order of one magnitude lower. Upon close inspection of the interaction force implemented, it is revealed that is matches the SCMP MPI, signifying correct forcing is applied in the model. Finally, a comparison of surface tension values unveils another close match between the SCMP and MCMP, which further validates the underlying assumptions made in the proposed model.

Chapter 8 – Conclusions and Future Work

8.1 Summary of thesis

The objective of this thesis was to develop a new modelling technique, based on the pseudopotential LBM, for the study of complex acoustic interactions in microscale sessile droplets, to provide insight and understanding of the underlying mechanisms which govern SAW-droplet interactions.

Initially, the pseudopotential LB method was investigated focusing on the effects of employing different forcing schemes, different EOS's and different EOS implementation to determine the most appropriate configuration for the current acoustofluidic application. It is revealed that, depending on the desired application, the choice of the above is not inconsequential. The original SC forcing leads to dependence of density on non-dimensional relaxation-time, hence it is advised to adopt the Guo or EDM in single relaxation time models whilst the multiple relaxation time models exhibit intrinsic independence of relaxation parameters and density.

Model stability, in the pseudopotential scheme, is inescapably linked to the magnitude of spurious velocities. Of the approaches tested, the Yuan Schaefer method demonstrated the lowest spurious velocities throughout the whole domain, whereas the piecewise linear method revealed the lowest values when only the inside of the liquid droplet is inspected. For a SAW-droplet application, due to the dynamic nature of the system, maintaining low spurious velocities in the vapour phase can reduce the chance of an unstable computation. However, lower spurious velocities inside the droplet will provide less resistance against the SAW interaction hence more accurate streaming patterns can be visualised.

The implementation of solid adhesion into the pseudopotential model was investigated. The geometric formulation is found to demonstrate superior compliance, over the fluid-solid interactions, when examining equilibrium contact angles and density profiles near solid boundaries. The effect of contact angle and droplet size, on spurious velocities, was investigated for several EOS implementations, applying the geometric formulation. The outcome suggests that contact angle and droplet size do not play an important role in creation of spurious velocities, with little deviation being witnessed over the ranges tested.

Based on the outcomes, a three-dimensional multiple relaxation time pseudopotential model for SAW interactions in microscale sessile droplets, on a $LiNbO_3$ substrate, has been constructed. Simulation results are validated against experimental data, evaluating mixing, pumping and jetting modes. A good agreement between simualtions and experiments is achieved. It is observed that there is a threshold wave amplitude at each frequency, at which the aformentioned modes can be achieved. Analysis of the data reveals the transition of mixing to pumping state at $We > 0.02$, $Ca > 3\text{x}10^{-4}$ and $Re > 60$, with the onset of jetting mode at $We > 0.1$, $Ca > 1.2\text{x}10^{-3}$ and $Re > 230$.

The impact of model variables, including surface treatment, viscosity ratio and interfacial tension has been analysed. It is found that on hydrophilic surfaces, the energy transfer from the SAW to the droplet is impeded by the large interfacial tension force. This is in opposition to hydrophobic surfaces where the droplet is moved and ejected from the substrate more easily. Also, it is revealed that viscosity ratio can play a role in delaying the ejection of the droplet from the surface. Movement of the liquid-gas/vapour interface is slowed resulting in a longer jetting time. Modification of the interfacial tension can lead to different droplet dynamics being witnessed. At larger interfacial tension, the droplet resists the deformation from the acoustic wave propogation, maintaining its spherical balloon shape. Alternatively, a reduction in interfacial tension allows the droplet to deform more along the Rayleigh angle, resulting in a longer jet to be seen. These findings provide the community with a range of outcomes according to initial conditions, circumventing the need for extensive real world experimental testing.

Due to the overwhelming presence of spurious velocities in the constructed model, an extensive investigation was carried out in to determine the effect of adjusting the free relaxation parameters in the MRT model. It was established that the choice of these parameters is not incosequenctial, with large fluctuations in spruious velocity magnitude with minor alteration of the free relaxation parameter values. The data suggests setting s_q, s_{xyz} and s_ε = 1.0 provides a balanced result, with a substantial reduction in spurious velocities in gas phase and minor in the liquid phase.

Additionally, the effect of CAH on droplet dynamics and behaviours has been studied. Interestingly, adopting a CAH window of $(\theta_R, \theta_A) = (95,105)$ has been shown to have a positive effect on simulated results, reducing the error against experimental data by up to 20%, compared to the original constructed model. The influence of EOS

implementation on SAW-droplet interactions was also examined. In all tests, the YS method produced shorter pumping distances and more droplet deformation in pumping scenarios, and longer jetting times being reported in jetting cases. Intriguingly, out of the three EOS's examined, the only method to provide a consistent density ratio over the duration of the simulation is the piecewise linear method. These recommendations are proposed to help guide potential scholars looking to exploit the simplicity of the model in acoustofluidic research.

The kinetic impacts of SAW-droplet interactions on an inclined slope have also been studied. The results show that an increase in SAW amplitude (power) corresponds to an increase in pumping velocity, for each slope angle. SAW-droplet interactions with varying droplet volume indicate that as the SAW amplitude is enlarged, the increase in velocity is lesser in larger droplets as compared to the small droplets. Also, for the same amplitude, a smaller droplet will have a larger average pumping velocity, as compared to a bigger droplet, due to its lower contact area preventing droplet motion along the substrate.

Moreover, droplet impact on dry surfaces is examined with and without SAW interactions. For a free impact drop, the outcome suggests that maximum spreading diameter is largely insensitive to surface treatment, like experimental findings. When SAW is applied, it has been shown that the magnitude of applied SAW power has a significant impact on rebound angle, contact time and maximum spreading diameter. It is also found that the initial impact velocity of the droplet plays an important role in the dynamics of droplet impact with SAW.

Furthermore, dual SAW interactions on a droplet, from opposing sides, is scrutinised. For two perfectly aligned SAWs the results indicate single droplet separation from the substrate is achieved at $We_j > 0.07$, with a linear trend observed for average droplet velocity in this regime. Also, the effect of dual SAW configuration on droplet deformation and dynamics was examined. The findings suggest that as the offset is increased, the tip velocity is decreased resulting in a longer jetting time. The offset between SAWs has been shown to produce a circulatory flow pattern, around the Z axis, reducing the vertical motion in the droplet. At L/D = 1, the circulation inside the droplet is at a peak value which reduces as the offset is further increased due to less SAW interaction.

Finally, a new MCMP LB is proposed based on the MPI framework. The model is investigated and verified through use of conventional benchmarking examinations. The preliminary results indicate good agreement with the analytical solutions for static cases including thermodynamic consistency, Laplace law, and contact angle in addition to dynamic scenarios such as droplet oscillation. Comparison to the SCMP MPI model reveals lower spurious velocities are generated in the proposed model, which is due to a slightly higher gas/vapour being realised. Close inspection of the interaction force implementation shows they are analogous whilst similar surface tension values are exposed for both models.

8.2 Future work

The microfluidics community is moving at a high pace, with new and interesting materials and configurations being applied in the pursuit of ever smaller LOC technologies. Since the newly constructed 3D model has been extensively tested for a $LiNbO_3$ substrate, it would be interesting to further analyse its capabilities for a variety of substrate materials.

The application to more complex systems involving ever more complicated geometries lends itself to the LB scheme due to its inherent simplicity in dealing with regular solid boundaries. Introducing flexible substrates which can be moulded into fascinating shapes is a possible continuation of this work, where moving boundaries could be implemented to replicate the physical experiments.

The final step in the model development would be the introduction of thermal impacts during SAW-droplet interactions. It has recently been demonstrated that the SAW power (energy) is mostly converted to heat, with only a small proportion providing internal streaming of the liquid. The heat generated not only causes the substrate to heat up but also the droplet and eventually the surrounding air. This added heat can be an unwanted by-product, especially in applications involving DNA cells for example. Determining the underlying mechanisms and thus providing enhanced understanding through modelling, can provide benefit to designers and researchers in the microfluidics field.

Additionally, as the proposed MCMP MPI model is still in its infancy, further development and analysis is required before it can be accepted as a genuine alternative to the conventional MCMP pseudopotential models which exist currently. Much attention has been focused on the phase-field models which is justified due to its superior

performance in certain areas, however the simplicity of the pseudopotential model still makes it a useful tool especially when investigating complex geometries and phase segregation scenarios.

APPENDIX A

The transformation matrix $\boldsymbol{M}$ for a D3Q15 model is expressed as [116,185];

$$\boldsymbol{M} = \begin{bmatrix} 1 & 1 & 1 & 1 & 1 & 1 & 1 & 1 & 1 & 1 & 1 & 1 & 1 & 1 & 1 \\ -2 & -1 & -1 & -1 & -1 & -1 & -1 & 1 & 1 & 1 & 1 & 1 & 1 & 1 & 1 \\ 16 & -4 & -4 & -4 & -4 & -4 & -4 & 1 & 1 & 1 & 1 & 1 & 1 & 1 & 1 \\ 0 & 1 & -1 & 0 & 0 & 0 & 0 & 1 & -1 & 1 & -1 & 1 & -1 & 1 & -1 \\ 0 & -4 & 4 & 0 & 0 & 0 & 0 & 1 & -1 & 1 & -1 & 1 & -1 & 1 & -1 \\ 0 & 0 & 0 & 1 & -1 & 0 & 0 & 1 & 1 & -1 & -1 & 1 & 1 & -1 & -1 \\ 0 & 0 & 0 & -4 & 4 & 0 & 0 & 1 & 1 & -1 & -1 & 1 & 1 & -1 & -1 \\ 0 & 0 & 0 & 0 & 0 & 1 & -1 & 1 & 1 & 1 & 1 & -1 & -1 & -1 & -1 \\ 0 & 0 & 0 & 0 & 0 & -4 & 4 & 1 & 1 & 1 & 1 & -1 & -1 & -1 & -1 \\ 0 & 2 & 2 & -1 & -1 & -1 & -1 & 0 & 0 & 0 & 0 & 0 & 0 & 0 & 0 \\ 0 & 0 & 0 & 1 & 1 & -1 & -1 & 0 & 0 & 0 & 0 & 0 & 0 & 0 & 0 \\ 0 & 0 & 0 & 0 & 0 & 0 & 0 & 1 & -1 & -1 & 1 & 1 & -1 & -1 & 1 \\ 0 & 0 & 0 & 0 & 0 & 0 & 0 & 1 & 1 & -1 & -1 & -1 & -1 & 1 & 1 \\ 0 & 0 & 0 & 0 & 0 & 0 & 0 & 1 & -1 & 1 & -1 & -1 & 1 & -1 & 1 \\ 0 & 0 & 0 & 0 & 0 & 0 & 0 & 1 & -1 & -1 & 1 & -1 & 1 & 1 & -1 \end{bmatrix}$$

with the inverse matrix $\boldsymbol{M^{-1}}$ defined as,

$$\boldsymbol{M^{-1}} = \begin{bmatrix} \frac{1}{15} & -\frac{1}{9} & \frac{2}{45} & 0 & 0 & 0 & 0 & 0 & 0 & 0 & 0 & 0 & 0 & 0 & 0 \\ \frac{1}{15} & -\frac{1}{18} & -\frac{1}{90} & \frac{1}{10} & -\frac{1}{10} & 0 & 0 & 0 & 0 & \frac{1}{6} & 0 & 0 & 0 & 0 & 0 \\ 16 & -\frac{1}{18} & -\frac{1}{90} & -\frac{1}{10} & \frac{1}{10} & 0 & 0 & 0 & 0 & \frac{1}{6} & 0 & 0 & 0 & 0 & 0 \\ \frac{1}{15} & -\frac{1}{18} & -\frac{1}{90} & 0 & 0 & \frac{1}{10} & -\frac{1}{10} & 0 & 0 & -\frac{1}{12} & \frac{1}{4} & 0 & 0 & 0 & 0 \\ \frac{1}{15} & -\frac{1}{18} & -\frac{1}{90} & 0 & 0 & -\frac{1}{10} & \frac{1}{10} & 0 & 0 & -\frac{1}{12} & \frac{1}{4} & 0 & 0 & 0 & 0 \\ \frac{1}{15} & -\frac{1}{18} & -\frac{1}{90} & 0 & 0 & 0 & 0 & \frac{1}{10} & -\frac{1}{10} & -\frac{1}{12} & -\frac{1}{4} & 0 & 0 & 0 & 0 \\ \frac{1}{15} & -\frac{1}{18} & -\frac{1}{90} & 0 & 0 & 0 & 0 & -\frac{1}{10} & \frac{1}{10} & -\frac{1}{12} & -\frac{1}{4} & 0 & 0 & 0 & 0 \\ \frac{1}{15} & \frac{1}{18} & \frac{1}{360} & \frac{1}{10} & \frac{1}{40} & \frac{1}{10} & \frac{1}{40} & \frac{1}{10} & \frac{1}{40} & 0 & 0 & \frac{1}{8} & \frac{1}{8} & \frac{1}{8} & \frac{1}{8} \\ \frac{1}{15} & \frac{1}{18} & \frac{1}{360} & -\frac{1}{10} & -\frac{1}{40} & \frac{1}{10} & \frac{1}{40} & \frac{1}{10} & \frac{1}{40} & 0 & 0 & -\frac{1}{8} & \frac{1}{8} & -\frac{1}{8} & -\frac{1}{8} \\ \frac{1}{15} & \frac{1}{18} & \frac{1}{360} & \frac{1}{10} & \frac{1}{40} & -\frac{1}{10} & -\frac{1}{40} & \frac{1}{10} & \frac{1}{40} & 0 & 0 & -\frac{1}{8} & -\frac{1}{8} & \frac{1}{8} & -\frac{1}{8} \\ \frac{1}{15} & \frac{1}{18} & \frac{1}{360} & -\frac{1}{10} & -\frac{1}{40} & -\frac{1}{10} & -\frac{1}{40} & \frac{1}{10} & \frac{1}{40} & 0 & 0 & \frac{1}{8} & -\frac{1}{8} & -\frac{1}{8} & \frac{1}{8} \\ \frac{1}{15} & \frac{1}{18} & \frac{1}{360} & \frac{1}{10} & \frac{1}{40} & \frac{1}{10} & \frac{1}{40} & -\frac{1}{10} & -\frac{1}{40} & 0 & 0 & \frac{1}{8} & -\frac{1}{8} & -\frac{1}{8} & -\frac{1}{8} \\ \frac{1}{15} & \frac{1}{18} & \frac{1}{360} & -\frac{1}{10} & -\frac{1}{40} & \frac{1}{10} & \frac{1}{40} & -\frac{1}{10} & -\frac{1}{40} & 0 & 0 & -\frac{1}{8} & -\frac{1}{8} & \frac{1}{8} & \frac{1}{8} \\ \frac{1}{15} & \frac{1}{18} & \frac{1}{360} & \frac{1}{10} & \frac{1}{40} & -\frac{1}{10} & -\frac{1}{40} & -\frac{1}{10} & -\frac{1}{40} & 0 & 0 & -\frac{1}{8} & \frac{1}{8} & -\frac{1}{8} & \frac{1}{8} \\ \frac{1}{15} & \frac{1}{18} & \frac{1}{360} & -\frac{1}{10} & -\frac{1}{40} & -\frac{1}{10} & -\frac{1}{40} & -\frac{1}{10} & -\frac{1}{40} & 0 & 0 & \frac{1}{8} & \frac{1}{8} & \frac{1}{8} & -\frac{1}{8} \end{bmatrix}$$

APPENDIX B

Table B-1. Physical and lattice parameters used in conversion

	Physical	Lattice
Length	2.67 mm	80 lu
Relaxation-time	-	0.5077
Kinematic viscosity	1.004 $m^2 s^{-1}$	2.567x10^{-3} $lu^2 tu^{-1}$
Density	998.2 kg m^{-3}	0.454 mu lu^{-3}
Interfacial tension	0.072 kg s^{-2}	-

Physical parameters are related to lattice units through unit conversion. Firstly, a suitable length conversion is found using

$$L_{phy} = C_l L_{LB} \rightarrow C_l = \frac{L_{phy}}{L_{LB}} = \frac{2.67x10^{-3}}{80} \approx 3.3375x10^{-5}\ m$$

The next stage involves calculating the time conversion factor. For this, the kinematic viscosities are used, with

$$\upsilon = \left(\tau - \frac{1}{2}\right) c_s^2 \Delta t, \quad c_s^2 = \frac{1}{3}\frac{\Delta x^2}{\Delta t^2} \quad \rightarrow \quad \upsilon = \frac{\left(\tau - \frac{1}{2}\right)}{3}\frac{{C_l}^2}{C_t}$$

where $\Delta x = C_l$ and $\Delta t = C_t$ represent the physical quantities and $\widetilde{\Delta x} = \widetilde{\Delta t} = 1$ are the lattice representations. From this relationship the time conversion is calculated

$$C_t = \frac{\left(\tau - \frac{1}{2}\right)}{3}\frac{{C_l}^2}{\upsilon_{phy}} = \frac{\left(0.5077 - \frac{1}{2}\right)}{3}\frac{(3.3375x10^{-5})^2}{1.004x10^{-6}} \approx 2.85x10^{-6}\ s$$

and hence the velocity conversion

$$C_u = \frac{C_l}{C_t} = \frac{3.3375x10^{-5}}{2.85x10^{-6}} \approx 11.72\ ms^{-1}$$

To check the consistency of the conversion, the physical Reynolds number (*Re*) is compared to lattice equivalent. Taking an arbitrary streaming velocity of $u = 0.07\ ms^{-1}$, the physical Reynolds number is found to be

$$Re_{phy} = \frac{u_{phy} L_{phy}}{\upsilon_{phy}} = \frac{0.07x2.67x10^{-3}}{1.004x10^{-6}} \approx 186.16$$

Comparing to the lattice counterpart

$$Re_{LB} = \frac{u_{LB}L_{LB}}{\upsilon_{LB}} = \frac{\frac{u_{phy}}{C_u}L_{LB}}{\upsilon_{LB}} = \frac{\frac{0.07}{11.72}x80}{2.567x10^{-3}} \approx 186.16$$

they are equivalent hence the conversion is robust.

Another check concerns the consistency in conversion when interfacial tension is involved, i.e., Weber and capillary numbers. An important parameter in the conversion is the relaxation, ${s_v}^{-1}$, as this dictates the size of the time conversion factor. Awkwardly, setting the value inappropriately will affect the consistency between physical and lattice. As the interfacial tension in the pseudopotential LB model is an emergent quantity, it is measured rather than set. hence it is advised to adjust the value until the converted interfacial tension matches the measured value obtained from the Laplace tests. As this is a known value, after conversion, the same value should be found provided the correct conversion parameters have been chosen.

Initially, a density conversion is found from

$$\rho_{phy} = C_\rho \rho_{LB} \rightarrow C_\rho = \frac{\rho_{phy}}{\rho_{LB}} = \frac{998.2}{0.454} \approx 2198.68\ kg\ m^{-3}$$

To translate between the physical interfacial tension and the lattice equivalent, an interfacial tension conversion is then calculated

$$C_\gamma = \frac{C_\rho (C_l)^3}{(C_t)^2} = \frac{2198.68\ (3.3375x10^{-5})^3}{(2.85x10^{-6})^2} \approx 10.08\ kg\ s^{-2}$$

hence the lattice equivalent interfacial tension, after conversion, is found to be

$$\gamma_{LB} = \frac{C_\gamma}{\gamma_{phy}} = \frac{0.072}{10.08} \approx 0.00714\ mu\ tu^{-2}$$

Comparing the converted value with the one found from Laplace Law test ($0.00729\ mu\ tu^{-2}$), it is evident that they are comparable, therefore the conversion is satisfactory. Again, a sanity check can be made using the streaming velocity used previously, however this time comparing the Weber number (*We*).

$$We_{phy} = \frac{\rho_{phy}\left(u_{phy}\right)^2 L_{phy}}{\gamma_{phy}} = \frac{998.2x(0.07)^2x2.67x10^{-3}}{0.072} \approx 0.181$$

$$We_{LB} = \frac{\rho_{LB}(u_{LB})^2 L_{LB}}{\gamma_{LB}} = \frac{0.454x\left(\frac{0.07}{11.72}\right)^2 x80}{0.00714} \approx 0.181$$

APPENDIX C

The thermodynamic consistency of the 3D MRT MPI model is evaluated by comparing the numerically obtained coexistence curves against the analytical Maxwell construction through simulating flat interfaces.

As presented in [159], thermodynamic consistency can be approached in MRT MPI models by splitting the free parameter ε_j into two separate quantities, thus the multi-pseudopotential is modified from Eq. 3–8 to the following,

$$\psi_j(\rho) = \left(\frac{\rho}{\lambda_j \varepsilon_{EOS,j} + C_j \rho} \right)^{1/\varepsilon_{EOS,j}} \tag{C-1}$$

This alteration provides the necessary flexibility in the model to adjust the density ratio without affecting the EOS implemented in the MPI. In the 2D tests carried out in [159], good agreement with the Maxwell construction was achieved through $\varepsilon_{forcing,j} = 0.89\ \varepsilon_{EOS,j}$. However, in the 3D investigations conducted as part of this work, $\varepsilon_{forcing,j} = 0.98\ \varepsilon_{EOS,j}$ is set to achieve suitable thermodynamic consistency.

The coexistence curves shown in the figure below agree well with the Maxwell construction, demonstrating the schemes capability of capturing the saturate phase behaviour of the fluid, even at large density ratios.

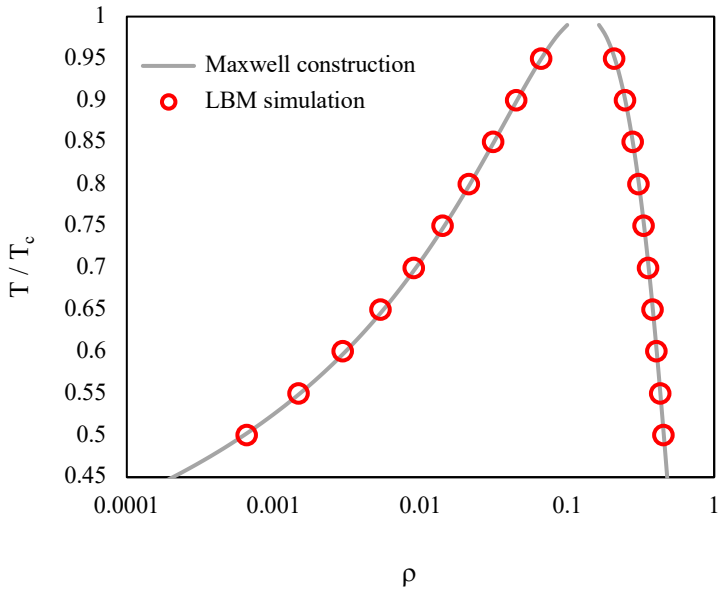

Figure C-1. Comparison of numerically obtained coexistence densities with the analytical curve predicted by Maxwell construction for 3D MPI

APPENDIX D

Unlike the original pseudopotential models, the MPI employs numerous potentials to try and better describe the flow of realistic fluids. In doing so, the cubic equations of state such as VW, CS, PR and SRK must be mapped on to the MPI to take advantage of the additional potentials. Taking the PR EOS as an example, in its original form it is expressed as,

$$p_{EOS,PR} = \frac{\rho T}{1-b\rho} - \frac{a\alpha\rho^2}{1+2b\rho-b^2\rho^2}$$

$$\alpha = \left[1 + (0.37464 + 1.54226\omega - 0.26992\omega^2) \times \left(1 - \sqrt{T/T_c}\right)\right]^2 \qquad \text{(D-1)}$$

According to [158], the EOS can be rearranged into the following arrangement

$$p_{EOS,PR} = \frac{\rho T}{1-b\rho} + \left(\frac{\alpha a}{2b\sqrt{2}}\right)\frac{\rho}{1+b\left(1+\sqrt{2}\right)\rho} - \left(\frac{\alpha a}{2b\sqrt{2}}\right)\frac{\rho}{1+b\left(1-\sqrt{2}\right)\rho} \qquad \text{(D-2)}$$

Hence, the shape is now appropriately matched to the MPI EOS and each corresponding pseudopotential parameter provided in the Table D-I below.

Table D-I. MPI parameters in PR EOS

EOS	jth pseudopotential	G_j	ε_j	λ_j	C_j
PR	1	$-\frac{2}{3}$	2	$\frac{1}{2}$	0
	2	$T\frac{2}{c^2}$	2	$\frac{1}{2}$	$-b$
	3	$\left(\frac{\alpha a}{2b\sqrt{2}}\right)\frac{2}{c^2}$	2	$\frac{1}{2}$	$b\left(1+\sqrt{2}\right)$
	4	$-\left(\frac{\alpha a}{2b\sqrt{2}}\right)\frac{2}{c^2}$	2	$\frac{1}{2}$	$b\left(1-\sqrt{2}\right)$

For full in-depth derivation and associated MPI forcing parameters for other EOS's mentioned, refer to [158].

REFERENCES

[1] D. Figeys and D. Pinto, *Lab-on-a-Chip: A Revolution in Biological and Medical Sciences*, Analytical Chemistry.

[2] R. F. Service, *Coming Soon: The Pocket DNA Sequencer*, Science (80-.). **282**, 399 (1998).

[3] D. Mark, S. Haeberle, G. Roth, F. von Stetten, R. Zengerle, F. Von Stetten, and R. Zengerle, *Microfluidic Lab-on-a-Chip Platforms: Requirements, Characteristics and Applications*, Chem. Soc. Rev. **39**, 1153 (2010).

[4] C. Y. Lee, C. L. Chang, Y. N. Wang, and L. M. Fu, *Microfluidic Mixing: A Review*, Int. J. Mol. Sci. **12**, 3263 (2011).

[5] K. Ward and Z. H. Fan, *Mixing in Microfluidic Devices and Enhancement Methods*, J. Micromechanics Microengineering **25**, (2015).

[6] K. Kang, L. J. Lee, and K. W. Koelling, *High Shear Microfluidics and Its Application in Rheological Measurement*, Exp. Fluids **38**, 222 (2005).

[7] A. Wixforth, *Acoustically Driven Planar Microfluidics*, Superlattices Microstruct. **33**, 389 (2003).

[8] J. Friend and L. Y. Yeo, *Microscale Acoustofluidics: Microfluidics Driven via Acoustics and Ultrasonics*, Rev. Mod. Phys. **83**, 647 (2011).

[9] X. Ding, P. Li, S.-C. S. Lin, Z. S. Stratton, N. Nama, F. Guo, D. Slotcavage, X. Mao, J. Shi, F. Costanzo, and T. J. Huang, *Surface Acoustic Wave Microfluidics*, Lab Chip **13**, 3626 (2013).

[10] L. Y. Yeo and J. R. Friend, *Surface Acoustic Wave Microfluidics*, Annu. Rev. Fluid Mech. **46**, 379 (2014).

[11] P. Delsing, A. N. Cleland, M. J. A. Schuetz, J. Knörzer, G. Giedke, J. I. Cirac, K. Srinivasan, M. Wu, K. C. Balram, C. Bäuerle, T. Meunier, C. J. B. Ford, P. V Santos, E. Cerda-Méndez, H. Wang, H. J. Krenner, E. D. S. Nysten, M. Weiß, G. R. Nash, L. Thevenard, C. Gourdon, P. Rovillain, M. Marangolo, J.-Y. Duquesne, G. Fischerauer, W. Ruile, A. Reiner, B. Paschke, D. Denysenko, D. Volkmer, A. Wixforth, H. Bruus, M. Wiklund, J. Reboud, J. M. Cooper, Y. Fu, M. S. Brugger, F. Rehfeldt, and C. Westerhausen, *The 2019 Surface Acoustic Waves Roadmap*, J. Phys. D. Appl. Phys. **52**, 353001 (2019).

[12] Y. Zhao, J. Fang, H. Wang, X. Wang, and T. Lin, *Magnetic Liquid Marbles: Manipulation of Liquid Droplets Using Highly Hydrophobic Fe3O4 Nanoparticles*, Adv. Mater. **22**, 707 (2010).

[13] T. Taniguchi, T. Torii, and T. Higuchi, *Chemical Reactions in Microdroplets by Electrostatic Manipulation of Droplets in Liquid Media*, in *Lab on a Chip*, Vol. 2 (2002), pp. 19–23.

[14] Y. Zhao, H. Gu, Z. Xie, H. C. Shum, B. Wang, and Z. Gu, *Bioinspired Multifunctional Janus Particles for Droplet Manipulation*, J. Am. Chem. Soc. **135**, 54 (2013).

[15] L. Sun, F. Bian, Y. Wang, Y. Wang, X. Zhang, and Y. Zhao, *Bioinspired Programmable Wettability Arrays for Droplets Manipulation*, Proc. Natl. Acad. Sci. U. S. A. **117**, 4527 (2020).

[16] G. M. Whitesides, *The Origins and the Future of Microfluidics*, Nature **442**, 368 (2006).

[17] S. Y. Teh, R. Lin, L. H. Hung, and A. P. Lee, *Droplet Microfluidics*, Lab on a Chip.

[18] J. Khandurina, T. E. McKnight, S. C. Jacobson, L. C. Waters, R. S. Foote, and J. M. Ramsey, *Integrated System for Rapid PCR-Based DNA Analysis in Microfluidic Devices*, Anal. Chem. **72**, 2995 (2000).

[19] H. A. Stone, A. D. Stroock, and A. Ajdari, *Engineering Flows in Small Devices: Microfluidics Toward a Lab-on-a-Chip*, Annu. Rev. Fluid Mech. **36**, 381 (2004).

[20] P. Abgrall and A. M. Gué, *Lab-on-Chip Technologies: Making a Microfluidic Network and Coupling It into a Complete Microsystem - A Review*, J. Micromechanics Microengineering **17**, (2007).

[21] X. Y. Du, Y. Q. Fu, S. C. Tan, J. K. Luo, A. J. Flewitt, W. I. Milne, D. S. Lee, N. M. Park, J. Park, Y. J. Choi, S. H. Kim, and S. Maeng, *ZnO Film Thickness Effect on Surface Acoustic Wave Modes and Acoustic Streaming*, Appl. Phys. Lett. **93**, 94105 (2008).

[22] Lord Rayleigh, *On Waves Propagated along the Plane Surface of an Elastic Solid*, Proc. London Math. Soc. **s1-17**, 4 (1885).

[23] A. A. Oliner, *Acoustic Surface Waves*, Vol. 24 (Springer Berlin Heidelberg, Berlin, Heidelberg, 1978).

[24] R. Tao, G. Mchale, J. Reboud, J. M. Cooper, H. Torun, J. T. Luo, J. Luo, X. Yang, J. Zhou, P. Canyelles-Pericas, Q. Wu, and Y. Fu, *Hierarchical Nanotexturing Enables Acoustofluidics on Slippery yet Sticky, Flexible Surfaces*, Nano Lett. **20**, 3263 (2020).

[25] S. K. R. S. Sankaranarayanan and V. R. Bhethanabotla, *Design of Efficient Focused Surface Acoustic Wave Devices for Potential Microfluidic Applications*, J. Appl. Phys. **103**, 64518 (2008).

[26] M. K. Tan, J. R. Friend, and L. Y. Yeo, *Interfacial Jetting Phenomena Induced by Focused Surface Vibrations*, Phys. Rev. Lett. **103**, (2009).

[27] J. Li, N. Xu, L. Dong, J. Li, M. H. Biroun, R. Tao, H. Torun, N. Xu, M. Rahmati, Y. Li, Y. Fu, R. Tao, C. Fu, J. Luo, Y. Wang, J. Xie, and D. Gibson, *Wide Range of Droplet Jetting Angles by Thin-Film Based Surface Acoustic Waves*, J. Phys. D.

Appl. Phys. **53**, 355402 (2020).

[28] P. J. Feenstra, Modeling and Control of Surface Acoustic Wave Motors, Univeristy of Twente, Enschede, 2005.

[29] S. Shiokawa, Y. Matsui, and T. Ueda, *Liquid Streaming and Droplet Formation Caused by Leaky Rayleigh Waves*, in *Proceedings., IEEE Ultrasonics Symposium* (IEEE, 1989), pp. 643–646.

[30] S. Shiokawa, Y. Matsui, and T. Ueda, *Study on Saw Streaming and Its Application to Fluid Devices*, Jpn. J. Appl. Phys. **29**, 137 (1990).

[31] R. J. Shilton, L. Y. Yeo, and J. R. Friend, *Quantification of Surface Acoustic Wave Induced Chaotic Mixing-Flows in Microfluidic Wells*, Sensors Actuators, B Chem. **160**, 1565 (2011).

[32] M. K. Tan, J. R. Friend, and L. Y. Yeo, *Microparticle Collection and Concentration via a Miniature Surface Acoustic Wave Device*, Lab Chip **7**, 618 (2007).

[33] R. J. Shilton, M. Travagliati, F. Beltram, and M. Cecchini, *Nanoliter-Droplet Acoustic Streaming via Ultra High Frequency Surface Acoustic Waves*, Adv. Mater. **26**, 4941 (2014).

[34] Y. J. Guo, H. B. Lv, Y. F. Li, X. L. He, J. Zhou, J. K. Luo, X. T. Zu, A. J. Walton, and Y. Q. Fu, *High Frequency Microfluidic Performance of LiNbO3 and ZnO Surface Acoustic Wave Devices*, J. Appl. Phys. **116**, 24501 (2014).

[35] P. Brunet, M. Baudoin, O. B. Matar, and F. Zoueshtiagh, *Droplet Displacements and Oscillations Induced by Ultrasonic Surface Acoustic Waves: A Quantitative Study*, Phys. Rev. E - Stat. Nonlinear, Soft Matter Phys. **81**, (2010).

[36] S. P. Zhang, J. Lata, C. Chen, J. Mai, F. Guo, Z. Tian, L. Ren, Z. Mao, P. H. Huang,

P. Li, S. Yang, and T. J. Huang, *Digital Acoustofluidics Enables Contactless and Programmable Liquid Handling*, Nat. Commun. **9**, (2018).

[37] J. Eggers, *Nonlinear Dynamics and Breakup of Free-Surface Flows*, Rev. Mod. Phys. **69**, 865 (1997).

[38] L. Y. Yeo and J. R. Friend, *Ultrafast Microfluidics Using Surface Acoustic Waves*, Biomicrofluidics **3**, 1 (2009).

[39] N. Akesson, W. Steinke, and W. Yates, *Spray Atomization Characteristics as a Function of Pesticide Formulations and Atomizer Design*, J. Environ. Sci. Heal. Part B **29**, 785 (1994).

[40] P. Spanoghe, M. De Schampheleire, P. Van der Meeren, and W. Steurbaut, *Influence of Agricultural Adjuvants on Droplet Spectra*, Pest Manag. Sci. **63**, 4 (2007).

[41] C. O'Callaghan and P. W. Barry, *The Science of Nebulised Drug Delivery*, Thorax **52**, S31 (1997).

[42] A. E. Rajapaksa, J. J. Ho, A. Qi, R. Bischof, T. H. Nguyen, M. Tate, D. Piedrafita, M. P. McIntosh, L. Y. Yeo, E. Meeusen, R. L. Coppel, and J. R. Friend, *Effective Pulmonary Delivery of an Aerosolized Plasmid DNA Vaccine via Surface Acoustic Wave Nebulization*, Respir. Res. **15**, 60 (2014).

[43] C. S. Lee, S. W. Park, and S. Il Kwon, *An Experimental Study on the Atomization and Combustion Characteristics of Biodiesel-Blended Fuels*, Energy and Fuels **19**, 2201 (2005).

[44] H. K. Suh and C. S. Lee, *Effect of Cavitation in Nozzle Orifice on the Diesel Fuel Atomization Characteristics*, Int. J. Heat Fluid Flow **29**, 1001 (2008).

[45] D. C. K. Rao, S. Karmakar, and S. Basu, *Atomization Characteristics and*

Instabilities in the Combustion of Multi-Component Fuel Droplets with High Volatility Differential, Sci. Rep. **7**, (2017).

[46] S. P. Newman, *Drug Delivery to the Lungs: Challenges and Opportunities*, Ther. Deliv. **8**, 647 (2017).

[47] M. Kurosawa, T. Watanabe, A. Futami, and T. Higuchi, *Surface Acoustic Wave Atomizer*, Sensors Actuators A Phys. **50**, 69 (1995).

[48] A. Qi, L. Yeo, J. Friend, and J. Ho, *The Extraction of Liquid, Protein Molecules and Yeast Cells from Paper through Surface Acoustic Wave Atomization*, Lab Chip **10**, 470 (2010).

[49] J. Ho, M. K. Tan, D. B. Go, L. Y. Yeo, J. R. Friend, and H. C. Chang, *Paper-Based Microfluidic Surface Acoustic Wave Sample Delivery and Ionization Source for Rapid and Sensitive Ambient Mass Spectrometry*, Anal. Chem. **83**, 3260 (2011).

[50] M. Alvarez, L. Y. Yeo, J. R. Friend, and M. Jamriska, *Rapid Production of Protein-Loaded Biodegradable Microparticles Using Surface Acoustic Waves*, in *Biomicrofluidics*, Vol. 3 (2009), p. 14102.

[51] H. Li, J. R. Friend, and L. Y. Yeo, *Surface Acoustic Wave Concentration of Particle and Bioparticle Suspensions*, Biomed. Microdevices **9**, 647 (2007).

[52] P. R. Rogers, J. R. Friend, and L. Y. Yeo, *Exploitation of Surface Acoustic Waves to Drive Size-Dependent Microparticle Concentration within a Droplet*, Lab Chip **10**, 2979 (2010).

[53] R. V. Raghavan, J. R. Friend, and L. Y. Yeo, *Particle Concentration via Acoustically Driven Microcentrifugation: MicroPIV Flow Visualization and Numerical Modelling Studies*, Microfluid. Nanofluidics **8**, 73 (2010).

[54] Z. Tengfei, W. Chaohui, N. Dong, J. Weitao, S. Yongsheng, Y. Lei, C. Bangdao,

L. Hongzhong, and D. Yucheng, *Exploitation of Surface Acoustic Waves to Drive Nanoparticle Concentration within an Electrification-Dependent Droplet*, RSC Adv. **4**, 46502 (2014).

[55] J. Shi, X. Mao, D. Ahmed, A. Colletti, and T. J. Huang, *Focusing Microparticles in a Microfluidic Channel with Standing Surface Acoustic Waves (SSAW)*, Lab Chip **8**, 221 (2008).

[56] J. Shi, H. Huang, Z. Stratton, Y. Huang, and T. J. Huang, *Continuous Particle Separation in a Microfluidic Channel via Standing Surface Acoustic Waves (SSAW)*, Lab Chip **9**, 3354 (2009).

[57] M. Wu, Z. Mao, K. Chen, H. Bachman, Y. Chen, J. Rufo, L. Ren, P. Li, L. Wang, and T. J. Huang, *Acoustic Separation of Nanoparticles in Continuous Flow*, Adv. Funct. Mater. **27**, (2017).

[58] Q. Y. Huang, Q. Sun, H. Hu, J. L. Han, and Y. L. Lei, *Thermal Effect in the Process of Surface Acoustic Wave Atomization*, Exp. Therm. Fluid Sci. **120**, (2021).

[59] D. Lee, N. Lee, G. Choi, and H. H. Cho, *Heat Transfer Characteristics of a Focused Surface Acoustic Wave (F-SAW) Device for Interfacial Droplet Jetting*, Inventions **3**, (2018).

[60] M. Mehmood, Experimental Investigation of Thermal and Kinetic Impacts of Surface Acoustic Waves on Water Droplet, Heriot-Watt University, 2020.

[61] M. Ciofalo, M. W. Collins, and T. R. Hennessy, *Modelling Nanoscale Fluid Dynamics and Transport in Physiological Flows*, Med. Eng. Phys. **18**, 437 (1996).

[62] J. Wu, *Acoustic Streaming and Its Applications*, Fluids **3**, 108 (2018).

[63] W. L. Nyborg, *Acoustic Streaming Due to Attenuated Plane Waves*, J. Acoust. Soc. Am. **25**, 68 (1953).

[64] W. L. Nyborg, *Acoustic Streaming near a Boundary*, J. Acoust. Soc. Am. **30**, 329 (1958).

[65] J. J. Campbell and W. R. Jones, *Propagation of Surface Waves at the Boundary Between a Piezoelectric Crystal and a Fluid Medium*, IEEE Trans. Sonics Ultrason. **17**, 71 (1970).

[66] J. Anderson, *Computational Fluid Dynamics* (Springer Berlin Heidelberg, Berlin, Heidelberg, 2009).

[67] R. J. LeVeque, *Finite Volume Methods for Hyperbolic Problems* (Cambridge University Press, 2002).

[68] H. K. Versteeg and W. Malalasekera., *An Introduction to Computational Fluid Dynamics: The Finite Volume Method* (Harlow: Prentice Hall, 2007).

[69] P. Zhou, *Finite Difference Method*, in *Numerical Analysis of Electromagnetic Fields* (Springer Berlin Heidelberg, Berlin, Heidelberg, 1993), pp. 63–94.

[70] M. N. Özişik, H. R. B. Orlande, M. J. Colaço, and R. M. Cotta, *Finite Difference Methods in Heat Transfer*, 2nd ed. (CRC Press, 2017).

[71] J. N. Reddy, *An Introduction to the Finite Element Method*, J. Press. Vessel Technol. **111**, 348 (1989).

[72] O. C. Zienkiewicz, R. L. Taylor, and J. Z. Zhu, *The Finite Element Method: Its Basis and Fundamentals* (Elsevier, 2013).

[73] C. . Hirt and B. . Nichols, *Volume of Fluid (VOF) Method for the Dynamics of Free Boundaries*, J. Comput. Phys. **39**, 201 (1981).

[74] M. Sussman, P. Smereka, and S. Osher, *A Level Set Approach for Computing Solutions to Incompressible Two-Phase Flow*, J. Comput. Phys. **114**, 146 (1994).

[75] D. Jacqmin, *Calculation of Two-Phase Navier–Stokes Flows Using Phase-Field Modeling*, J. Comput. Phys. **155**, 96 (1999).

[76] D. Köster, *Numerical Simulation of Acoustic Streaming on Surface Acoustic Wave-Driven Biochips*, SIAM J. Sci. Comput. **29**, 2352 (2007).

[77] H. Antil, A. Gantner, R. H. Hoppe, D. Koster, K. Siebert, and A. Wixforth, *Modeling and Simulation of Piezoelectrically Agitated Acoustic Streaming on Microfluidic Biochips*, in *Lecture Notes in Computational Science and Engineering*, Vol. 60 (2008), pp. 305–312.

[78] M. Alghane, B. X. Chen, Y. Q. Fu, Y. Li, J. K. Luo, and A. J. Walton, *Experimental and Numerical Investigation of Acoustic Streaming Excited by Using a Surface Acoustic Wave Device on a 128° YX-LiNbO3 Substrate*, J. Micromechanics Microengineering **21**, (2011).

[79] M. Alghane, Y. Q. Fu, B. X. Chen, Y. Li, M. P. Y. Desmulliez, and A. J. Walton, *Streaming Phenomena in Microdroplets Induced by Rayleigh Surface Acoustic Wave*, J. Appl. Phys. **109**, 114901 (2011).

[80] M. Alghane, B. X. Chen, Y. Q. Fu, Y. Li, M. P. Y. Desmulliez, M. I. Mohammed, and A. J. Walton, *Nonlinear Hydrodynamic Effects Induced by Rayleigh Surface Acoustic Wave in Sessile Droplets*, Phys. Rev. E - Stat. Nonlinear, Soft Matter Phys. **86**, 56304 (2012).

[81] A. Riaud, M. Baudoin, O. Bou Matar, J. L. Thomas, and P. Brunet, *On the Influence of Viscosity and Caustics on Acoustic Streaming in Sessile Droplets: An Experimental and a Numerical Study with a Cost-Effective Method*, J. Fluid Mech. **821**, 384 (2017).

[82] M. H. Biroun, M. T. Rahmati, M. Jangi, R. Tao, B. X. Chen, and Y. Q. Fu, *Computational and Experimental Analysis of Droplet Transportation/Jetting Behaviours Driven by Thin Film Surface Acoustic Waves*, Sensors Actuators, A

Phys. **299**, 111624 (2019).

[83] M. H. Biroun, M. Rahmati, R. Tao, H. Torun, M. Jangi, and Y. Fu, *Dynamic Behavior of Droplet Impact on Inclined Surfaces with Acoustic Waves*, Langmuir **36**, 10175 (2020).

[84] M. H. Biroun, J. Li, R. Tao, M. Rahmati, G. McHale, L. Dong, M. Jangi, H. Torun, and Y. Q. Fu, *Acoustic Waves for Active Reduction of Contact Time in Droplet Impact*, Phys. Rev. Appl. **14**, 24029 (2020).

[85] M. H. Biroun, M. Rahmati, M. Jangi, B. Chen, and Y. Q. Fu, *Numerical and Experimental Investigations of Interdigital Transducer Configurations for Efficient Droplet Streaming and Jetting Induced by Surface Acoustic Waves*, Int. J. Multiph. Flow **136**, 103545 (2021).

[86] D. Haydock and J. M. Yeomans, *Lattice Boltzmann Simulations of Acoustic Streaming*, J. Phys. A. Math. Gen. **34**, 5201 (2001).

[87] D. Haydock and J. M. Yeomans, *Lattice Boltzmann Simulations of Attenuation-Driven Acoustic Streaming*, J. Phys. A. Math. Gen. **36**, 5683 (2003).

[88] M. K. Tan and L. Y. Yeo, *Hybrid Finite-Difference/Lattice Boltzmann Simulations of Microchannel and Nanochannel Acoustic Streaming Driven by Surface Acoustic Waves*, Phys. Rev. Fluids **3**, 044202 (2018).

[89] S. M. Sheikholeslam Noori, M. Taeibi Rahni, and S. A. Shams Taleghani, *Numerical Analysis of Droplet Motion over a Flat Plate Due to Surface Acoustic Waves*, Microgravity Sci. Technol. **32**, 647 (2020).

[90] M. S. Noori, A. S. Taleghani, and M. T. Rahni, *Phenomenological Investigation of Drop Manipulation Using Surface Acoustic Waves*, Microgravity Sci. Technol. (2020).

[91] Q. Li, K. H. Luo, Q. J. Kang, Y. L. He, Q. Chen, and Q. Liu, *Lattice Boltzmann Methods for Multiphase Flow and Phase-Change Heat Transfer*, Prog. Energy Combust. Sci. **52**, 62 (2016).

[92] A. D. Angelopoulos, V. N. Paunov, V. N. Burganos, and A. C. Payatakes, *Lattice Boltzmann Simulation of Nonideal Vapor-Liquid Flow in Porous Media*, Phys. Rev. E **57**, 3237 (1998).

[93] C. Pan, M. Hilpert, and C. T. Miller, *Lattice-Boltzmann Simulation of Two-Phase Flow in Porous Media*, Water Resour. Res. **40**, 1 (2004).

[94] Y. Q. Zu, *Modelling of Migration of CO2 in Porous Media under Conditions of Saline Aquifers Using Lattice Boltzmann Method*, Procedia Eng. **126**, 471 (2015).

[95] H. W. Zheng, C. Shu, and Y. T. Chew, *A Lattice Boltzmann Model for Multiphase Flows with Large Density Ratio*, J. Comput. Phys. **218**, 353 (2006).

[96] L. Chen, Q. Kang, Y. Mu, Y.-L. He, and W.-Q. Tao, *A Critical Review of the Pseudopotential Multiphase Lattice Boltzmann Model: Methods and Applications*, Int. J. Heat Mass Transf. **76**, 210 (2014).

[97] H. Huang, M. C. Sukop, and X.-Y. Lu, *Multiphase Lattice Boltzmann Methods: Theory and Application* (John Wiley & Sons, Ltd, Chichester, UK, 2015).

[98] O. Filippova, S. Succi, F. Mazzocco, C. Arrighetti, G. Bella, and D. Hänel, *Multiscale Lattice Boltzmann Schemes with Turbulence Modeling*, J. Comput. Phys. **170**, 812 (2001).

[99] H. Yu, S. S. Girimaji, and L. S. Luo, *Lattice Boltzmann Simulations of Decaying Homogeneous Isotropic Turbulence*, Phys. Rev. E - Stat. Nonlinear, Soft Matter Phys. **71**, (2005).

[100] Y. Peng, W. Liao, L. S. Luo, and L. P. Wang, *Comparison of the Lattice Boltzmann*

and Pseudo-Spectral Methods for Decaying Turbulence: Low-Order Statistics, Comput. Fluids **39**, 568 (2010).

[101] T. Kataoka and M. Tsutahara, *Lattice Boltzmann Model for the Compressible Navier-Stokes Equations with Flexible Specific-Heat Ratio*, Phys. Rev. E - Stat. Nonlinear, Soft Matter Phys. **69**, (2004).

[102] T. Kataoka and M. Tsutahara, *Lattice Boltzmann Method for the Compressible Euler Equations*, Phys. Rev. E **69**, 056702 (2004).

[103] N. Frapolli, S. S. Chikatamarla, and I. V Karlin, *Entropic Lattice Boltzmann Model for Compressible Flows*, Phys. Rev. E - Stat. Nonlinear, Soft Matter Phys. **92**, (2015).

[104] T. Krüger, H. Kusumaatmaja, A. Kuzmin, O. Shardt, G. Silva, and E. M. Viggen, *The Lattice Boltzmann Method: Principles and Practice* (Springer International Publishing, Cham, 2017).

[105] S. Chapman and T. Cowling, *Mathematical Theory of Non-Uniform Gases an Account of the Kinetic Theory of Viscosity, Thermal Conduction and Diffusion in Gases*, 2nd ed. (1960).

[106] G. R. McNamara and G. Zanetti, *Use of the Boltzmann Equation to Simulate Lattice-Gas Automata*, Phys. Rev. Lett. **61**, 2332 (1988).

[107] S. Chen, H. Chen, D. Martinez, and W. Matthaeus, *Lattice Boltzmann Model for Simulation of Magnetohydrodynamics*, Phys. Rev. Lett. **67**, 5 (1991).

[108] P. L. Bhatnagar, E. P. Gross, and M. Krook, *A Model for Collision Processes in Gases. I. Small Amplitude Processes in Charged and Neutral One-Component Systems*, Phys. Rev. **94**, 511 (1954).

[109] X. He and L.-S. Luo, *Theory of the Lattice Boltzmann Method: From the*

Boltzmann Equation to the Lattice Boltzmann Equation, Phys. Rev. E **56**, 6811 (1997).

[110] S. Succi, I. V Karlin, and H. Chen, *Colloquium : Role of the H Theorem in Lattice Boltzmann Hydrodynamic Simulations*, Rev. Mod. Phys. **74**, 1203 (2002).

[111] E. T. Jaynes, *Gibbs vs Boltzmann Entropies*, Am. J. Phys. **33**, 391 (1965).

[112] D. D'Humieres, *Generalized Lattice-Boltzmann Equations, in Rared Gas Dynamics: Theory and Sim-Ulations, Prog.*, in *Prog. Astro. Aeor., Vol. 159, Edited by B. D. Shizgal and D. P. Weaver, AIAA, Washington, DC* (1992), pp. 450–458.

[113] P. Lallemand and L. S. Luo, *Theory of the Lattice Boltzmann Method: Acoustic and Thermal Properties in Two and Three Dimensions*, Phys. Rev. E - Stat. Physics, Plasmas, Fluids, Relat. Interdiscip. Top. **68**, 25 (2003).

[114] M. E. McCracken and J. Abraham, *Multiple-Relaxation-Time Lattice-Boltzmann Model for Multiphase Flow*, Phys. Rev. E - Stat. Nonlinear, Soft Matter Phys. **71**, (2005).

[115] Q. Li, Y. L. He, G. H. Tang, and W. Q. Tao, *Improved Axisymmetric Lattice Boltzmann Scheme*, Phys. Rev. E - Stat. Nonlinear, Soft Matter Phys. **81**, (2010).

[116] D. D'Humières, I. Ginzburg, M. Krafczyk, P. Lallemand, and L. S. Luo, *Multiple-Relaxation-Time Lattice Boltzmann Models in Three Dimensions*, in *Philosophical Transactions of the Royal Society A: Mathematical, Physical and Engineering Sciences*, Vol. 360 (2002), pp. 437–451.

[117] C. Zhen-Hua, S. Bao-Chang, and Z. Lin, *Simulating High Reynolds Number Flow in Two-Dimensional Lid-Driven Cavity by Multi-Relaxation-Time Lattice Boltzmann Method*, Chinese Phys. **15**, 1855 (2006).

[118] A. Fakhari and T. Lee, *Multiple-Relaxation-Time Lattice Boltzmann Method for*

Immiscible Fluids at High Reynolds Numbers, Phys. Rev. E - Stat. Nonlinear, Soft Matter Phys. **87**, (2013).

[119] K. N. Premnath and J. Abraham, *Simulations of Binary Drop Collisions with a Multiple-Relaxation-Time Lattice-Boltzmann Model*, Phys. Fluids **17**, 1 (2005).

[120] A. Fakhari and M. H. Rahimian, *Investigation of Deformation and Breakup of a Falling Droplet Using a Multiple-Relaxation-Time Lattice Boltzmann Method*, Comput. Fluids **40**, 156 (2011).

[121] P. Yang, Z. Wen, R. Dou, and X. Liu, *Effect of Random Structure on Permeability and Heat Transfer Characteristics for Flow in 2D Porous Medium Based on MRT Lattice Boltzmann Method*, Phys. Lett. A **380**, 2902 (2016).

[122] Q. Liu, X. B. Feng, Y. L. He, C. W. Lu, and Q. H. Gu, *Three-Dimensional Multiple-Relaxation-Time Lattice Boltzmann Models for Single-Phase and Solid-Liquid Phase-Change Heat Transfer in Porous Media at the REV Scale*, Appl. Therm. Eng. 319 (2019).

[123] Q. Liu, Y. L. He, Q. Li, and W. Q. Tao, *A Multiple-Relaxation-Time Lattice Boltzmann Model for Convection Heat Transfer in Porous Media*, Int. J. Heat Mass Transf. **73**, 761 (2014).

[124] I. Ginzburg, *Equilibrium-Type and Link-Type Lattice Boltzmann Models for Generic Advection and Anisotropic-Dispersion Equation*, Adv. Water Resour. **28**, 1171 (2005).

[125] I. Ginzburg, F. Verhaeghe, and D. dHumì eres, Two-Relaxation-Time Lattice Boltzmann Scheme: About Parametrization, Velocity, Pressure AndMixed Boundary Conditions, 2008.

[126] D. H. Rothman and J. M. Keller, *Immiscible Cellular-Automaton Fluids*, J. Stat. Phys. **52**, 1119 (1988).

[127] A. K. Gunstensen, D. H. Rothman, S. S. Zaleski, and G. Zanetti, *Lattice Boltzmann Model of Immiscible Fluids*, Phys. Rev. A **43**, 4320 (1991).

[128] D. Grunau, S. Chen, and K. Egger, *A Lattice Boltzmann Model for Multi-Phase Fluid Flows*, Phys. Fluids A Fluid Dyn. **5**, (1993).

[129] M. Latva-Kokko and D. H. Rothman, *Diffusion Properties of Gradient-Based Lattice Boltzmann Models of Immiscible Fluids*, Phys. Rev. E **71**, 056702 (2005).

[130] T. Reis and T. N. Phillips, *Lattice Boltzmann Model for Simulating Immiscible Two-Phase Flows*, J. Phys. A Math. Theor. **40**, 4033 (2007).

[131] M. R. Swift, W. R. Osborn, and J. M. Yeomans, *Lattice Boltzmann Simulation of Nonideal Fluids*, Phys. Rev. Lett. **75**, 830 (1995).

[132] M. Swift, E. Orlandini, W. Osborn, and J. Yeomans, *Lattice Boltzmann Simulations of Liquid-Gas and Binary Fluid Systems*, Phys. Rev. E **54**, 5041 (1996).

[133] T. Inamuro, N. Konishi, and F. Ogino, *Galilean Invariant Model of the Lattice Boltzmann Method for Multiphase Fluid Flows Using Free-Energy Approach*, Comput. Phys. Commun. **129**, 32 (2000).

[134] T. Inamuro, T. Ogata, S. Tajima, and N. Konishi, *A Lattice Boltzmann Method for Incompressible Two-Phase Flows with Large Density Differences*, J. Comput. Phys. **198**, 628 (2004).

[135] T. Inamuro, S. Tajima, and F. Ogino, *Lattice Boltzmann Simulation of Droplet Collision Dynamics*, Int. J. Heat Mass Transf. **47**, 4649 (2004).

[136] A. Fakhari and M. H. Rahimian, *Phase-Field Modeling by the Method of Lattice Boltzmann Equations*, Phys. Rev. E - Stat. Nonlinear, Soft Matter Phys. **81**, (2010).

[137] J. W. Cahn and J. E. Hilliard, *Free Energy of a Nonuniform System. I. Interfacial Free Energy*, J. Chem. Phys. **28**, 258 (1958).

[138] S. M. Allen and J. W. Cahn, *Mechanisms of Phase Transformations within the Miscibility Gap of Fe-Rich Fe-Al Alloys*, Acta Metall. **24**, 425 (1976).

[139] M. Geier, A. Fakhari, and T. Lee, *Conservative Phase-Field Lattice Boltzmann Model for Interface Tracking Equation*, Phys. Rev. E - Stat. Nonlinear, Soft Matter Phys. **91**, (2015).

[140] H. Liang, J. Xu, J. Chen, H. Wang, Z. Chai, and B. Shi, *Phase-Field-Based Lattice Boltzmann Modeling of Large-Density-Ratio Two-Phase Flows*, Phys. Rev. E **97**, 33309 (2018).

[141] X. Shan and H. Chen, *Lattice Boltzmann Model for Simulating Flows with Multi Phases and Components*, Phys. Rev. E **47**, 1815 (1993).

[142] H. Liu, Q. Kang, C. R. Leonardi, S. Schmieschek, A. Narváez, B. D. Jones, J. R. Williams, A. J. Valocchi, and J. Harting, *Multiphase Lattice Boltzmann Simulations for Porous Media Applications*, Comput. Geosci. **201156**, 1 (2015).

[143] H. A. Warda, S. H. Haddara, E. M. Wahba, and M. Sedahmed, *Lattice Boltzmann Simulations of the Capillary Pressure Bump Phenomenon in Heterogeneous Porous Media*, J. Pet. Sci. Eng. **157**, 558 (2017).

[144] Y. Hou, H. Deng, Q. Du, and K. Jiao, *Multi-Component Multi-Phase Lattice Boltzmann Modeling of Droplet Coalescence in Flow Channel of Fuel Cell*, J. Power Sources **393**, 83 (2018).

[145] H. Deng, K. Jiao, Y. Hou, J. W. Park, and Q. Du, *A Lattice Boltzmann Model for Multi-Component Two-Phase Gas-Liquid Flow with Realistic Fluid Properties*, Int. J. Heat Mass Transf. **128**, 536 (2019).

[146] Y. Hou, H. Deng, N. Zamel, Q. Du, and K. Jiao, *3D Lattice Boltzmann Modeling of Droplet Motion in PEM Fuel Cell Channel with Realistic GDL Microstructure and Fluid Properties*, Int. J. Hydrogen Energy **45**, 12476 (2020).

[147] H. Huang, M. Krafczyk, and X. Lu, *Forcing Term in Single-Phase and Shan-Chen-Type Multiphase Lattice Boltzmann Models*, Phys. Rev. E - Stat. Nonlinear, Soft Matter Phys. **84**, (2011).

[148] X. He and G. Doolen, *Thermodynamic Foundations of Kinetic Theory and Lattice Boltzmann Models for Multiphase Flows*, J. Stat. Phys. **107**, 309 (2002).

[149] X. Shan and H. Chen, *Simulation of Nonideal Gases and Liquid-Gas Phase Transitions by the Lattice Boltzmann Equation*, Phys. Rev. E **49**, 2941 (1994).

[150] X. Shan, *Analysis and Reduction of the Spurious Current in a Class of Multiphase Lattice Boltzmann Models*, Phys. Rev. E - Stat. Nonlinear, Soft Matter Phys. **73**, (2006).

[151] K. Connington and T. Lee, *A Review of Spurious Currents in the Lattice Boltzmann Method for Multiphase Flows*, Journal of Mechanical Science and Technology.

[152] M. Sbragaglia, R. Benzi, L. Biferale, S. Succi, K. Sugiyama, and F. Toschi, *Generalized Lattice Boltzmann Method with Multirange Pseudopotential*, Phys. Rev. E - Stat. Nonlinear, Soft Matter Phys. **75**, (2007).

[153] Q. Li, K. H. Luo, and X. J. Li, *Forcing Scheme in Pseudopotential Lattice Boltzmann Model for Multiphase Flows*, Phys. Rev. E - Stat. Nonlinear, Soft Matter Phys. **86**, 16709 (2012).

[154] Z. Guo, C. Zheng, and B. Shi, *Discrete Lattice Effects on the Forcing Term in the Lattice Boltzmann Method*, Phys. Rev. E - Stat. Physics, Plasmas, Fluids, Relat. Interdiscip. Top. **65**, 6 (2002).

[155] P. Yuan and L. Schaefer, *Equations of State in a Lattice Boltzmann Model*, Phys. Fluids **18**, (2006).

[156] A. L. Kupershtokh, D. A. Medvedev, and D. I. Karpov, *On Equations of State in a Lattice Boltzmann Method*, Comput. Math. with Appl. **58**, 965 (2009).

[157] S. Khajepor, J. Wen, and B. Chen, *Multipseudopotential Interaction: A Solution for Thermodynamic Inconsistency in Pseudopotential Lattice Boltzmann Models*, Phys. Rev. E - Stat. Nonlinear, Soft Matter Phys. **91**, 1 (2015).

[158] S. Khajepor and B. Chen, *Multipseudopotential Interaction: A Consistent Study of Cubic Equations of State in Lattice Boltzmann Models*, Phys. Rev. E **93**, 1 (2016).

[159] K. Pasieczynski and B. Chen, *Multipseudopotential Interaction Models for Thermal Lattice Boltzmann Method Simulations*, Phys. Rev. E **102**, 13311 (2020).

[160] N. F. Carnahan and K. E. Starling, *Equation of State for Nonattracting Rigid Spheres*, J. Chem. Phys. **51**, 635 (1969).

[161] D. Y. Peng and D. B. Robinson, *A New Two-Constant Equation of State*, Ind. Eng. Chem. Fundam. **15**, 59 (1976).

[162] Q. Li, K. H. Luo, and X. J. Li, *Lattice Boltzmann Modeling of Multiphase Flows at Large Density Ratio with an Improved Pseudopotential Model*, Phys. Rev. E - Stat. Nonlinear, Soft Matter Phys. **87**, (2013).

[163] X. Shan, *Pressure Tensor Calculation in a Class of Nonideal Gas Lattice Boltzmann Models*, Phys. Rev. E - Stat. Nonlinear, Soft Matter Phys. **77**, (2008).

[164] C. E. Colosqui, G. Falcucci, S. Ubertini, and S. Succi, *Mesoscopic Simulation of Non-Ideal Fluids with Self-Tuning of the Equation of State*, Soft Matter **8**, 3798 (2012).

[165] N. S. Martys and H. Chen, *Simulation of Multicomponent Fluids in Complex Three-Dimensional Geometries by the Lattice Boltzmann Method*, Phys. Rev. E - Stat. Physics, Plasmas, Fluids, Relat. Interdiscip. Top. **53**, 743 (1996).

[166] Q. Kang, D. Zhang, and S. Chen, *Displacement of a Two-Dimensional Immiscible Droplet in a Channel*, Phys. Fluids **14**, 3203 (2002).

[167] M. C. Sukop and D. Or, *Lattice Boltzmann Method for Modeling Liquid-Vapor Interface Configurations in Porous Media*, Water Resour. Res. **40**, 1 (2004).

[168] P. Raiskinmäki, A. Koponen, J. Merikoski, and J. Timonen, *Spreading Dynamics of Three-Dimensional Droplets by the Lattice-Boltzmann Method*, Comput. Mater. Sci. **18**, 7 (2000).

[169] Q. Li, K. H. Luo, Q. J. Kang, and Q. Chen, *Contact Angles in the Pseudopotential Lattice Boltzmann Modeling of Wetting*, Phys. Rev. E - Stat. Nonlinear, Soft Matter Phys. **90**, 53301 (2014).

[170] R. Benzi, L. Biferale, M. Sbragaglia, S. Succi, and F. Toschi, *Mesoscopic Modeling of a Two-Phase Flow in the Presence of Boundaries: The Contact Angle*, Phys. Rev. E - Stat. Nonlinear, Soft Matter Phys. **74**, 021509 (2006).

[171] H. Ding and P. D. M. Spelt, *Wetting Condition in Diffuse Interface Simulations of Contact Line Motion*, Phys. Rev. E - Stat. Nonlinear, Soft Matter Phys. **75**, (2007).

[172] Y. Yu, Q. Li, C. Q. Zhou, P. Zhou, and H. J. Yan, *Investigation of Droplet Evaporation on Heterogeneous Surfaces Using a Three-Dimensional Thermal Multiphase Lattice Boltzmann Model*, Appl. Therm. Eng. **127**, 1346 (2017).

[173] A. Hu, L. Li, R. Uddin, and D. Liu, *Contact Angle Adjustment in Equation-of-State-Based Pseudopotential Model*, Phys. Rev. E **93**, 53307 (2016).

[174] T. Akai, B. Bijeljic, and M. J. Blunt, *Wetting Boundary Condition for the Color-*

Gradient Lattice Boltzmann Method: Validation with Analytical and Experimental Data, Adv. Water Resour. **116**, 56 (2018).

[175] Q. Li, Y. Yu, and K. H. Luo, *Implementation of Contact Angles in the Pseudopotential Lattice Boltzmann Simulations with Curved Boundaries*, Phys. Rev. E **100**, 1 (2019).

[176] S. Khajepor, J. Cui, M. Dewar, and B. Chen, *A Study of Wall Boundary Conditions in Pseudopotential Lattice Boltzmann Models*, Comput. Fluids (2018).

[177] B. Wen, B. Huang, Z. Qin, C. Wang, and C. Zhang, *Contact Angle Measurement in Lattice Boltzmann Method*, Comput. Math. with Appl. **76**, 1686 (2018).

[178] J. B. Dupont and D. Legendre, *Numerical Simulation of Static and Sliding Drop with Contact Angle Hysteresis*, J. Comput. Phys. **229**, 2453 (2010).

[179] L. Wang, H. B. Huang, and X. Y. Lu, *Scheme for Contact Angle and Its Hysteresis in a Multiphase Lattice Boltzmann Method*, Phys. Rev. E - Stat. Nonlinear, Soft Matter Phys. **87**, 13301 (2013).

[180] H. B. Eral, D. J. C. M. 't Mannetje, and J. M. Oh, *Contact Angle Hysteresis: A Review of Fundamentals and Applications*, Colloid Polym. Sci. **291**, 247 (2013).

[181] K. Sritharan, C. J. Strobl, M. F. Schneider, A. Wixforth, and Z. Guttenberg, *Acoustic Mixing at Low Reynold's Numbers*, Appl. Phys. Lett. **88**, 1 (2006).

[182] Z. Wang and J. Zhe, *Recent Advances in Particle and Droplet Manipulation for Lab-on-a-Chip Devices Based on Surface Acoustic Waves*, Lab Chip **11**, 1280 (2011).

[183] A. Hospital, J. R. Goñi, M. Orozco, and J. Gelpi, *Molecular Dynamics Simulations: Advances and Applications*, Adv. Appl. Bioinforma. Chem. **8**, 37 (2015).

[184] Q. Li and K. H. Luo, *Achieving Tunable Surface Tension in the Pseudopotential Lattice Boltzmann Modeling of Multiphase Flows*, Phys. Rev. E - Stat. Nonlinear, Soft Matter Phys. **88**, 53307 (2013).

[185] A. Xu, T. S. Zhao, L. An, and L. Shi, *A Three-Dimensional Pseudo-Potential-Based Lattice Boltzmann Model for Multiphase Flows with Large Density Ratio and Variable Surface Tension*, Int. J. Heat Fluid Flow **56**, 261 (2015).

[186] P. G. De Gennes, *Wetting: Statics and Dynamics*, Rev. Mod. Phys. **57**, 827 (1985).

[187] M. Gross, F. Varnik, D. Raabe, and I. Steinbach, *Small Droplets on Superhydrophobic Substrates*, Phys. Rev. E - Stat. Nonlinear, Soft Matter Phys. **81**, (2010).

[188] C. A. Miller and L. E. Scriven, *The Oscillations of a Fluid Droplet Immersed in Another Fluid*, J. Fluid Mech. **32**, 417 (1968).

[189] H. Lamb, *Hydrodynamics* (Cambridge University Press, 1932).

[190] S. Ammar, G. Pernaudat, and J. Y. Trépanier, *A Multiphase Three-Dimensional Multi-Relaxation Time (MRT) Lattice Boltzmann Model with Surface Tension Adjustment*, J. Comput. Phys. **343**, 73 (2017).

[191] İ. Dinçer and C. Zamfirescu, *Drying Phenomena*, in *Theory and Applications*, 1st ed. (John Wiley & Sons, Ltd, Chichester, UK, 2015), pp. 457–459.

[192] R. Huang and H. Wu, *Third-Order Analysis of Pseudopotential Lattice Boltzmann Model for Multiphase Flow*, J. Comput. Phys. **327**, 121 (2016).

[193] K. N. Premnath and J. Abraham, *Three-Dimensional Multi-Relaxation Time (MRT) Lattice-Boltzmann Models for Multiphase Flow*, J. Comput. Phys. **224**, 539 (2007).

[194] M. P. Elizalde-González and L. E. García-Díaz, *Application of a Taguchi L16 Orthogonal Array for Optimizing the Removal of Acid Orange 8 Using Carbon with a Low Specific Surface Area*, Chem. Eng. J. **163**, 55 (2010).

[195] M. S. Noori, M. T. Rahni, and A. S. Taleghani, *Effects of Contact Angle Hysteresis on Drop Manipulation Using Surface Acoustic Waves*, Theor. Comput. Fluid Dyn. **34**, 145 (2020).

[196] Q. Li and K. H. Luo, *Thermodynamic Consistency of the Pseudopotential Lattice Boltzmann Model for Simulating Liquid-Vapor Flows*, Appl. Therm. Eng. **72**, 56 (2014).

[197] K. Pasieczynski and B. Chen, *Fluid–Fluid Interactions in Pseudopotential Lattice Boltzmann Models: Effects of Model Schemes and Fluid Properties*, Int. J. Numer. Methods Fluids **93**, 1578 (2021).

[198] Y. Wang, X. Tao, R. Tao, J. Zhou, Q. Zhang, D. Chen, H. Jin, S. Dong, J. Xie, and Y. Q. Fu, *Acoustofluidics along Inclined Surfaces Based on AlN/Si Rayleigh Surface Acoustic Waves*, Sensors Actuators, A Phys. **306**, (2020).

[199] Y. Wang, Q. Zhang, R. Tao, J. Xie, P. Canyelles-Pericas, H. Torun, J. Reboud, G. Mchale, L. E. Dodd, X. Yang, J. Luo, Q. Wu, and Y. Q. Fu, *Flexible/Bendable Acoustofluidics Based on Thin-Film Surface Acoustic Waves on Thin Aluminum Sheets*, ACS Appl. Mater. Interfaces **13**, 16978 (2021).

[200] N. Janardan and M. V. Panchagnula, *Effect of the Initial Conditions on the Onset of Motion in Sessile Drops on Tilted Plates*, Colloids Surfaces A Physicochem. Eng. Asp. **456**, 238 (2014).

[201] Š. Šikalo, C. Tropea, and E. N. Ganić, *Impact of Droplets onto Inclined Surfaces*, J. Colloid Interface Sci. **286**, 661 (2005).

[202] Y. H. Yeong, J. Burton, E. Loth, and I. S. Bayer, *Drop Impact and Rebound*

Dynamics on an Inclined Superhydrophobic Surface, Langmuir **30**, 12027 (2014).

[203] Z. Jin, D. Sui, and Z. Yang, *The Impact, Freezing, and Melting Processes of a Water Droplet on an Inclined Cold Surface*, Int. J. Heat Mass Transf. **90**, 439 (2015).

[204] K. M. Wisdom, J. A. Watson, X. Qu, F. Liu, G. S. Watson, and C. H. Chen, *Self-Cleaning of Superhydrophobic Surfaces by Self-Propelled Jumping Condensate*, Proc. Natl. Acad. Sci. U. S. A. **110**, 7992 (2013).

[205] S. S. Latthe, R. S. Sutar, V. S. Kodag, A. K. Bhosale, A. M. Kumar, K. Kumar Sadasivuni, R. Xing, and S. Liu, *Self – Cleaning Superhydrophobic Coatings: Potential Industrial Applications*, Prog. Org. Coatings **128**, 52 (2019).

[206] S. P. Dalawai, M. A. Saad Aly, S. S. Latthe, R. Xing, R. S. Sutar, S. Nagappan, C.-S. Ha, K. Kumar Sadasivuni, and S. Liu, *Recent Advances in Durability of Superhydrophobic Self-Cleaning Technology: A Critical Review*, Prog. Org. Coatings **138**, 105381 (2020).

[207] I. S. BAYER and C. M. MEGARIDIS, *Contact Angle Dynamics in Droplets Impacting on Flat Surfaces with Different Wetting Characteristics*, J. Fluid Mech. **558**, 415 (2006).

[208] Z. Yang, Y. Cai, Q. Li, H. Li, Y. Jiang, R. Lin, C. Zheng, D. Sun, and X. Gao, *Predicting Particle Collection Performance of a Wet Electrostatic Precipitator under Varied Conditions with Artificial Neural Networks*, Powder Technol. **377**, 632 (2021).

[209] J. L. Han, H. Hu, Q. Y. Huang, and Y. L. Lei, *Particle Separation by Standing Surface Acoustic Waves inside a Sessile Droplet*, Sensors Actuators, A Phys. **326**, 112731 (2021).

[210] J. Yang and E. S. Boek, *A Comparison Study of Multi-Component Lattice*

Boltzmann Models for Flow in Porous Media Applications, in *Computers and Mathematics with Applications*, Vol. 65 (2013), pp. 882–890.

[211] C. Zhang, P. Cheng, and W. J. Minkowycz, *Lattice Boltzmann Simulation of Forced Condensation Flow on a Horizontal Cold Surface in the Presence of a Non-Condensable Gas*, Int. J. Heat Mass Transf. **115**, 500 (2017).

[212] S. Zheng, F. Eimann, C. Philipp, T. Fieback, and U. Gross, *Single Droplet Condensation in Presence of Non-Condensable Gas by a Multi-Component Multi-Phase Thermal Lattice Boltzmann Model*, Int. J. Heat Mass Transf. **139**, 254 (2019).

[213] S. Shin and D. Juric, *Modeling Three-Dimensional Multiphase Flow Using a Level Contour Reconstruction Method for Front Tracking without Connectivity*, J. Comput. Phys. **180**, 427 (2002).

[214] J. Hua and J. Lou, *Numerical Simulation of Bubble Rising in Viscous Liquid*, J. Comput. Phys. **222**, 769 (2007).

[215] J. Hua, J. F. Stene, and P. Lin, *Numerical Simulation of 3D Bubbles Rising in Viscous Liquids Using a Front Tracking Method*, J. Comput. Phys. **227**, 3358 (2008).

[216] H. Huang, P. Meakin, and M. Liu, *Computer Simulation of Two-Phase Immiscible Fluid Motion in Unsaturated Complex Fractures Using a Volume of Fluid Method*, Water Resour. Res. **41**, 1 (2005).

[217] D. Jain, J. A. M. Kuipers, and N. G. Deen, *Numerical Study of Coalescence and Breakup in a Bubble Column Using a Hybrid Volume of Fluid and Discrete Bubble Model Approach*, Chem. Eng. Sci. **119**, 134 (2014).

[218] J. Bao and L. Schaefer, *Lattice Boltzmann Equation Model for Multi-Component Multi-Phase Flow with High Density Ratios*, Appl. Math. Model. **37**, 1860 (2013).

[219] M. L. Porter, E. T. Coon, Q. Kang, J. D. Moulton, and J. W. Carey, *Multicomponent Interparticle-Potential Lattice Boltzmann Model for Fluids with Large Viscosity Ratios*, Phys. Rev. E **86**, 036701 (2012).

[220] H. Huang, D. T. Thorne, M. G. Schaap, and M. C. Sukop, *Proposed Approximation for Contact Angles in Shan-and-Chen-Type Multicomponent Multiphase Lattice Boltzmann Models*, Phys. Rev. E - Stat. Nonlinear, Soft Matter Phys. **76**, (2007).

[221] A. J. WAGNER, *THE ORIGIN OF SPURIOUS VELOCITIES IN LATTICE BOLTZMANN*, Int. J. Mod. Phys. B **17**, 193 (2003).

[222] S. Leclaire, N. Pellerin, M. Reggio, and J.-Y. Trépanier, *An Approach to Control the Spurious Currents in a Multiphase Lattice Boltzmann Method and to Improve the Implementation of Initial Condition*, Int. J. Numer. Methods Fluids **77**, 732 (2015).

[223] E. A. Guggenheim, *The Principle of Corresponding States*, J. Chem. Phys. **13**, 253 (1945).